Photoactive polymer – carbon nanotubes hybrid nanostructures

Felipe Wasem Klein

UNIVERSITÉ DE STRASBOURG

ÉCOLE DOCTORALE de Physique et Chimie Physique

[Institut Charles Sadron – UPR 22]

THÈSE présentée par :

[Felipe WASEM KLEIN]

soutenue le : **28 janvier 2021**

pour obtenir le grade de : **Docteur de l'université de Strasbourg**

Discipline/ Spécialité : Chimie Physique

Nanostructures hybrides polymères photoactifs - nanotubes de carbone mono et bi-feuillets

THÈSE dirigée par :

[Dr. PETIT Pierre]	Directeur de Recherche, Université de Strasbourg

RAPPORTEURS :

Dr. LOISEAU Annick	Directeur de Recherche, Onera
Dr. CAMPIDELLI Stéphane	Directeur de Recherche, DRF/IRAMIS/NIMBE

Examinateur :

Dr. BINIEK Laure	Chargée de Recherche, Université de Strasbourg

Acknowledgements

First of all, I would like to thank all the members of the jury and specially the reviewers (Dr. Annick Loiseau and Dr. Stéphane Campidelli) that took their time to review this manuscript and the final presentation, as well as for the interesting and helpful discussion that followed. Thanks to the proposed corrections this manuscript is now more complete and will be registered with a better quality. I hope we can work together in the future for improving even more the obtained results.

I would like to thank my thesis supervisor, Dr. Pierre Petit, for introducing me to the very interesting research topic of carbon nanotubes, for all the discussions during these three years of thesis, and for the time spent in the elaboration of this manuscript. I also thank you for introducing me for many people in the field and helping me in my academic and professional path.

I also thank Dr. Philippe Mesini who coordinated the chemistry part of this thesis and welcomed me to the ICS for an internship that led to this thesis. Your coordination was a guidance in how to become a better chemist and will help me for my entire career.

Speaking of chemistry, I need to thank Jean-Philippe Lamps for his instruction in the lab, his incredible stories and experiences as a chemist and most importantly, for developing the synthesis of the polymers used in this thesis. Without you this thesis would have never even started.

The main topic of this thesis was the characterization of the nanohybrids. Many people of the Institute participated in this more or less deeply, and I thank them all:

Prof. Matthias Pauly for the training in UV-Vis Spectroscopy, which provided the most amount of data for this thesis.

Dr. François Schosseler, who not only taught me Fluorescence Spectroscopy but also was present in most presentations and major discussions of this thesis. Your collaboration was invaluable, and I cannot thank you enough for your insights.

Catherine Foussat and Dr. Melanie Legros for SEC analysis and help with characterization experiments.

Dr. Marc Schmutz for his experience in electronic microscopy and his help that allowed me to advance in the analysis of the complex systems I studied in this thesis

Christian Blanck for his time for training me in TEM and for obtaining such good images that the reader can see in this manuscript. I thank him also for his good humor and being able to motivate me to go out for a run even in the cold winter.

Christophe Contal for the AFM analysis that helped advance more the project.

Dr. Laure Biniek for the many discussions in everything related to P3HT, help in the understanding of many results and of course, for the good company in the BJC and the Football team

This thesis would advance without our collaborators from the Laboratoire Charles Coulomb in Montpellier, especially Matthieu Paillet that gave his time to perform a great number of characterization experiments and brought his expertise in the analysis of the data. I thank him also for his warm welcome and guidance during the many times I stayed in Montpellier. I am thrilled for being able to work at your side in the near future.

Also from the L2C I thank Dr. Jean-Louis Salvajol for his expert knowledge in Raman spectroscopy that allowed us to understand the small changes we observed between our systems; Dr. Ahmed Zahab for his warm welcome and Dr. Romain Parret for taking his time for helping me attain the final goal of this thesis in obtaining the preliminary results of photocurrent studies.

I need to thank also Prof. Sylvie Choua, Prof. Claire Courson, Prof. Rene Luzz and Julien BOEHLER for letting me join their team for Chemical Engineering classes at IUT Robert Schumann. It was very fun and this experience really pushed me forward becoming a professor one day.

The work performed would not have been possible without the help from the administration of the ICS, a hand that guided me through this labyrinth of bureaucracy and were often open for a short break when the computer screen started to get tiring.

Following on this not so scientific path, I need to thank the BJC members, who are always working for making the ICS a better place for all its members, especially those on a short-term contract. The coffees held every fortnight were a good medicine after the whole week of work, and the events were some of the great memories I have from at the ICS. The same goes for the members of the two football teams, for there is not a better way of relieving stress that kicking a ball very hard (and having a beer after for the Friday night games).

Life in the Institute would not have a meaning without the friends made along the way. There we have Leandro and Christian that responsible for me not losing completely any hold I have of my native language. Jean and Javid, always happy and with a lot of energy for joining in all sport activities. Randy, Morgane, Swann, Eirini, Eulalie, Nicolas, Charchit, Othmene, the list goes on and on, thank you all.

Finally, I would like to thank the people from outside of the Institute that supported me (in both senses). My family for all the laughs, the holidays and the sharing. And for the last but far from the least, my girlfriend Anne, that lived the last four years with me, sharing all these moments and making me the happiest person on Earth.

Table of contents

Introduction

Mankind search for performance has led us to different materials for varying applications: light metal alloys for planes and other structures, semi-conducting materials for electronics, and the list goes on. Between those, carbon nanotubes (CNTs) have been in focus since their discovery due to their excellent properties for different applications, such as their high thermal and electric conductivity (better than copper) and exceptional tensile strength (higher than steel).

More recently, photoluminescence and photoconductivity properties have been also revealed, motivating their integration in optoelectronic devices. However, these applications are hindered by some technological issues, such as the diversity of properties of an as synthesized sample of carbon nanotubes. In fact, samples of carbon nanotubes are not constituted of a unique species: their synthetic procedures result in a more or less diverse population of different carbon nanotubes species that may exhibit a broad range of optical and electronic properties.

A strategy for circumventing this problem could be incorporation of CNTs into hybrid materials. It allows one to combine the remarkable properties of CNTs cited above with those of another material. This second material ideally would be easily synthesized, have interesting and well-defined optical properties such as a strong optical absorption, and interact synergistically with the CNTs. For example, in a typical carbon nanotube optoelectronic device, the added material could act as an antenna, being the component that interacts with light and acts on the device.

Materials that behave just as this include conjugated polymers, from which as notable example is poly(3-hexylthiophene) (P3HT). Its strong absorbance in the visible, p-type semiconducting behavior and relative good stability to air have made it one of the most studied polymers for application in optoelectronic devices.

This thesis inscribes itself in a larger project which searches to improve carbon nanotube optoelectronic devices by functionalizing them with optically active materials. Its strategy is based on covalent functionalization, due to its versatility and effectiveness. For doing this, a new copolymer of P3HT which contains an active group at the end of its side chains was synthesized. This polymer allows for an original single step functionalization of the CNTs, without the need for one or more intermediate steps. These intermediate steps create an excess of uncontrolled defects onto the CNTs surface, degrading their properties more than necessary.

Another part of the strategy for improving the optoelectronic performance of CNTs is the use of double-walled carbon nanotubes (DWNTs). It is expected that, upon covalent functionalization, the outer layer of these coaxial structures would act as a sacrificial layer while the properties of the inner layer would

remain intact. Because of this possibility, preliminary tests with DWNTs were included in this thesis, although we did not reach the point of functionalization of devices made from DWNTs.

For attaining the final goal of functionalizing CNTs devices with the P3HT copolymer, many steps were needed. These include first the synthesis of the copolymer, followed by the understanding of the interaction of the CNTs with the polymer chains with and without the covalent bond. Only after all these we were finally able to functionalize devices. The results of this work are exposed in this manuscript, which is divided in four main chapters.

The first chapter searches to introduce the reader to fundamental concepts required for understanding what is presented in the following chapters. As we deal with two materials in this thesis, it is separated in two main sections. The first one starts with a simple description of the electronic structure of carbon nanotubes and how their singular structure can be analyzed by spectroscopic methods. After understanding their properties as individual species, it is shown how they can be modified by their interaction with neighboring molecules (non-covalent and covalent functionalization). This part finishes with a brief overview of how DWNTs behave in comparison to single walled carbon nanotubes (SWNTs), establishing the foundations to work with these more complex structures.

The second part of the first chapter introduces briefly our photoactive polymer, P3HT. The properties of this material depend not only on that of a single polymer chain, but on how these interact between themselves under the form of aggregates. For this, a model from the literature that links the structure of the aggregates to its optical and electronic properties is presented. This model is the basis for many of the interpretations in this thesis.

Chapter 2 presents the synthesis of the polymers and copolymers used in this thesis, the latter being developed by Dr. Philippe Mésini and Jean-Philippe Lamps prior to the beginning of this thesis. It is followed by the route chosen for obtaining the most important reproducibility in our results. We describe the elaboration of non-covalent nanohybrids used as precursors for the covalent functionalization, which description and effectiveness close the chapter.

Chapter 3 is also divided in two main parts: non-covalent and covalent functionalization of CNTs. The former was initially studied for optimizing the conditions for the latter, and in order to get references to distinguish the effects of each type of functionalization. However, the procedure chosen for the non-covalent functionalization led to interesting results related to the organization of the polymer chains onto the carbon nanotubes and to the formation of polymers aggregates, and more in-depth studies were performed in order to understand these results. As such, these studies became an important part of this manuscript.

The second part of this Chapter introduces the results of covalent functionalization, as analyzed by spectroscopy techniques. Raman spectroscopy in particular, through studies performed with Dr.

Matthieu Paillet and Dr. Jean-Louis Sauvajol, has proven to be important tools in the characterization of the obtained systems. Interestingly, covalent functionalization leads to a different polymer chain configuration at the nanotube-polymer interface than the one observed in the non-covalent nanohybrids.

Following the successful functionalization of CNTs with the obtained copolymer, their application in devices such as field-effect transistors comes as a natural follow-up of the project. Chapter 4 presents the preliminary results of these studies, performed besides Dr. Matthieu Paillet and Dr. Romain Parret.

This work led to some new insights about the behavior of the hybrid system, but also finished with some open questions for further studies. All these are shortly resumed in a general conclusion at the end of this manuscript.

Chapter 1: State of the art

1. Carbon nanotubes

1.1 Electronic structure

Carbon nanotubes were put on the spotlight in 1991 after their identification by IIjima[1], who observed them via TEM in by-products of the synthesis of C_{60} via arc-discharge[2] (first observations dating back to 1952[3]). Since then, many studies, from fundamental physics up to applied sciences, have been performed around these materials.

Electronic structure was already predicted in 1992 for single-walled carbon nanotubes (SWNTs)[4,5], even before their first observation in 1993.[6,7] A first evaluation of the electronic structure of carbon nanotubes can be derived from the electronic structure of the 2D graphene sheet, considering the nanotube one it is rolled up following a $\mathbf{C_h}$ vector as in **Figure 1**. The rolling-up vector defines a couple of indexes (*n, m*), whose values refer to the number of times the lattice parameters $\mathbf{a_1}$ and $\mathbf{a_2}$ are repeated to build it. The unit cell along the nanotube is also defined by the vector **T**, being the smallest perpendicular vector to $\mathbf{C_h}$ that ends in a carbon atom.[8]

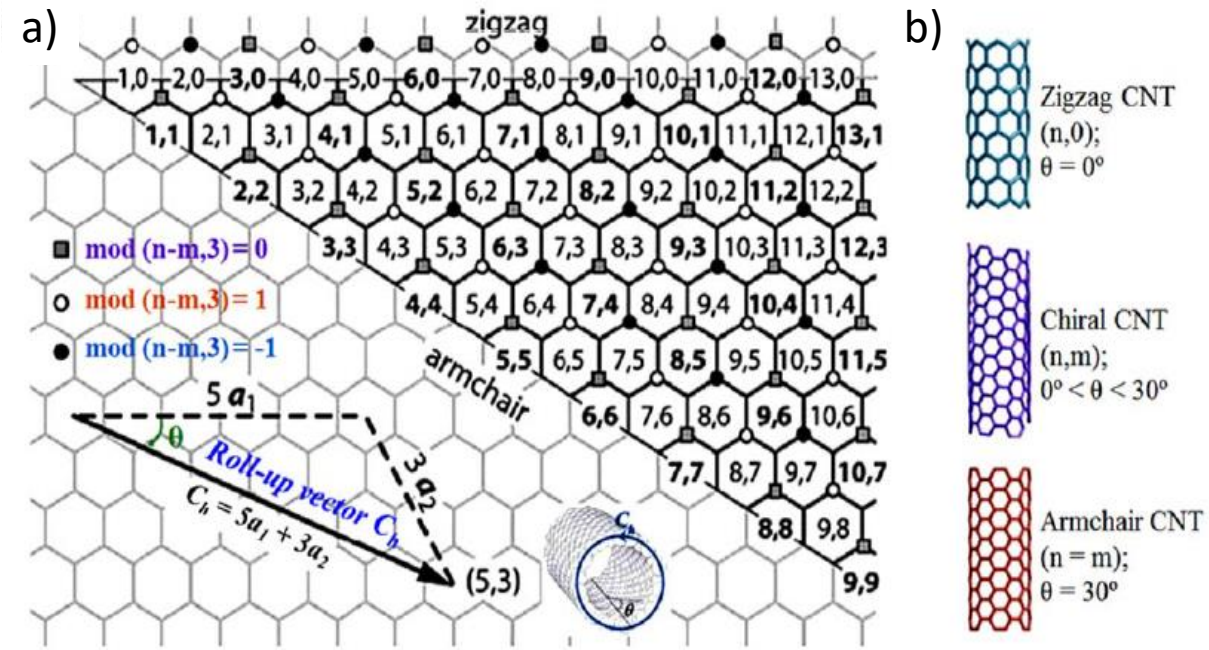

Figure 1: a) Diagram showing the different configurations of the roll-up vector $\mathbf{C_h}$ for different chirality. This diagram also represents the different rolling angles with the horizontal line (0°) representing zigzag nanotubes and the line at 30° to it

representing armchair nanotubes. Pair Numbers in bold are metallic nanotubes. The arrows below the diagram represent the construction of a (5, 3) nanotube roll-up vector; b) Representation of the three types of carbon nanotubes. [8]

The (*n, m)* indexes allow the determination of the tube diameter and the angle between the $\mathbf{C_h}$ vector and the $\mathbf{a_1}$ lattice vector. Based on their values, we can distinguish three geometries (**Figure 1b**).

- Armchair carbon nanotubes ($n = m$, $\theta = 30°$)
- Zigzag carbon nanotubes ($m = 0$, $\theta = 0°$)
- Chiral nanotubes

The basis of construction of the electronic structure is the hybridization of sp^2 in plane orbitals and p_z orbitals perpendicular to the graphene sheet. In a tight binding approximation, we obtain respectively strong σ bonds and, more importantly, a π-system that governs the electronic properties. In fact, the gap between the π and π* bands decreases with increasing size of the graphene layer and vanishes for large enough sheets, resulting in a semi-metal at 0 K (see **Figure 2**).

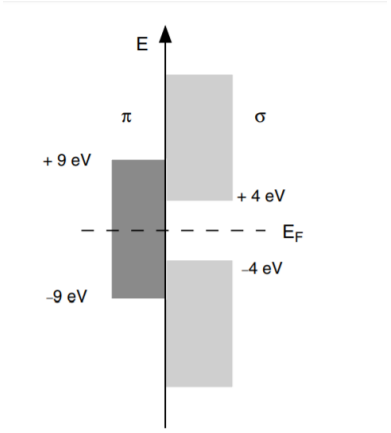

Figure 2: Schematic energy band diagram for graphene[9]

The band structure for carbon nanotubes is obtained from the graphene band structure by imposing periodic boundary conditions along the circumference of the tube, which quantify the number of allowed electronic states of the graphene electronic structure. As a consequence, depending on the (*n, m*) indexes of the rolling vectors, the nanotubes may be either metallic or semi-conducting. It can be shown that the nanotubes are metallic if *n-m* is a multiple of three, otherwise it is semi-conducting.

The method used for determining the characteristics above does not consider rehybridization of orbitals due to curvature. Thus, it is not a good approximation for very small nanotubes. For larger diameter nanotubes ($d > 1$ nm) these effects of curvature can be neglected.

1.2 Optical properties

Because of their 1D nature, the density of states of carbon nanotubes is marked by Van Hove singularities, corresponding to the extrema in the band dispersion relations and defining the gap for the semiconducting nanotubes. For metallic nanotubes the Van Hove singularities are located at the edges of a plateau with a non-zero density of states centered at the Fermi level (**Figure 3**).

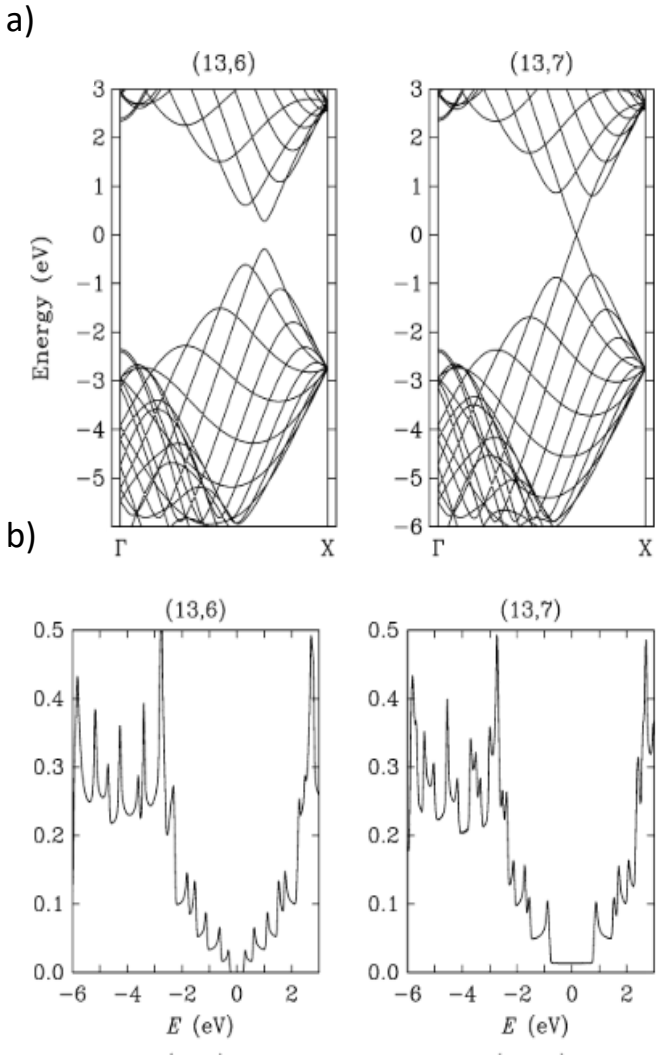

Figure 3: a) Band structure of two different chiral carbon nanotubes: (13, 6), a semi-conducting nanotube; and (13,7), a metallic nanotube; b) Corresponding density of states. Both graphs were obtained through a tight binding model.[10]

Direct experimental observation of the density of states can be made by STM.[8]. Selection rules for the band to band transitions impose that allowed transitions take place only between symmetric Van Hove singularities (called E_{ii}). As the firsts E^{S}_{11} and E^{S}_{22} transitions of semi-conducting nanotubes and E^{M}_{11} of metallic nanotubes are located in the UV-Vis-NIR range, optical absorption spectroscopy is generally used to probe the electronic structure of carbon nanotubes (**Figure 4**).

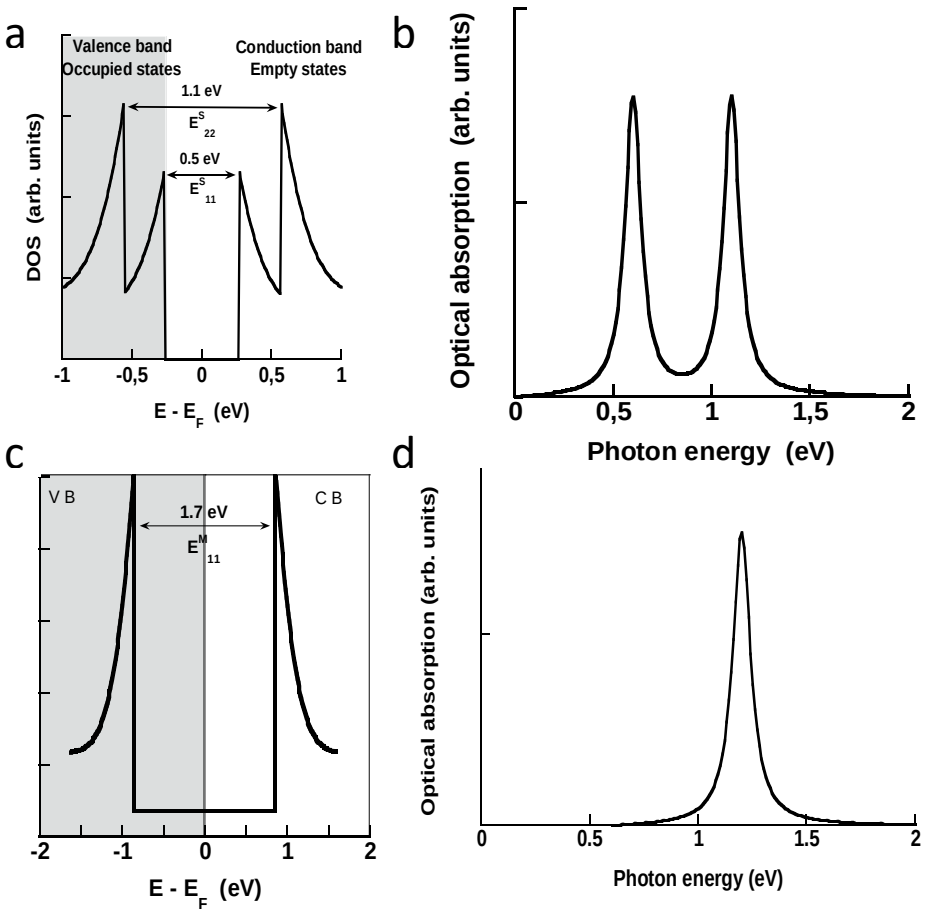

Figure 4: a) Density of states of a semi-conducting SWNTs (diameter of about 1.4 nm) showing E^S_{11} and E^S_{22} optical transitions; b) Corresponding absorption peaks; c) Density of states of a metallic SWNTs showing its E^M_{11} optical transition; d) Corresponding absorption peak.[11]

The representation of the energy between the Van Hove singularities as a function of the diameter of SWNTs is known as Kataura's plot (**Figure 5**), from the publication of Kataura *et al.*[12], who calculated these values from the tight binding approximation. Other plots can be obtained from other calculation methods which consider the trigonal warping effect, the excitonic nature of transitions or from experimental determinations. It can be observed in these graphs that the optical transition energy is inversely proportional to the nanotube diameter. Also, for nanotubes of similar diameter, the transitions E^S_{11} and E^S_{22} are of lower energy than E^M_{11}.

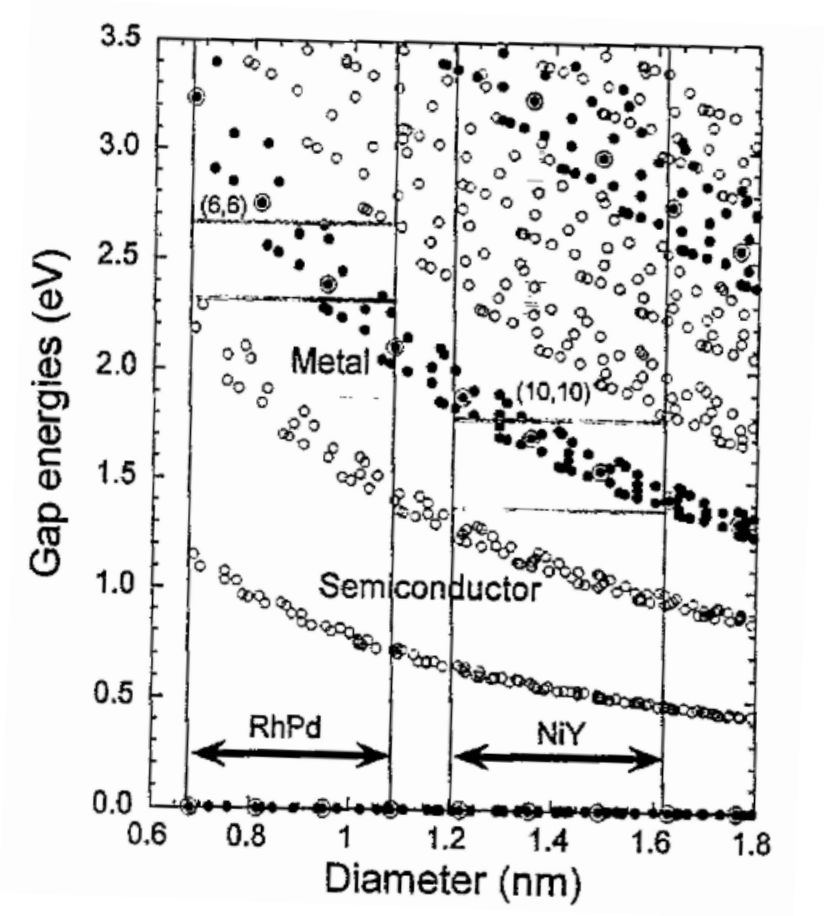

Figure 5: Kataura plot obtained from a tight binding model. Open circles represent semi-conducting carbon nanotubes while closed circles represent metallic nanotube. RhPd and NiY represent different catalysts used for the CNTs synthesiss.[12]

As synthesized SWNTs are generally organized in a close packed triangular lattice[13] due to the strong Van der Walls interactions between tubes. These bundles may contain different types of carbon nanotubes, which results in an absorption spectrum made of the superposition of the spectra of all individual species, broadened due to inter-tube interactions. (**Figure 6**).[14–18]

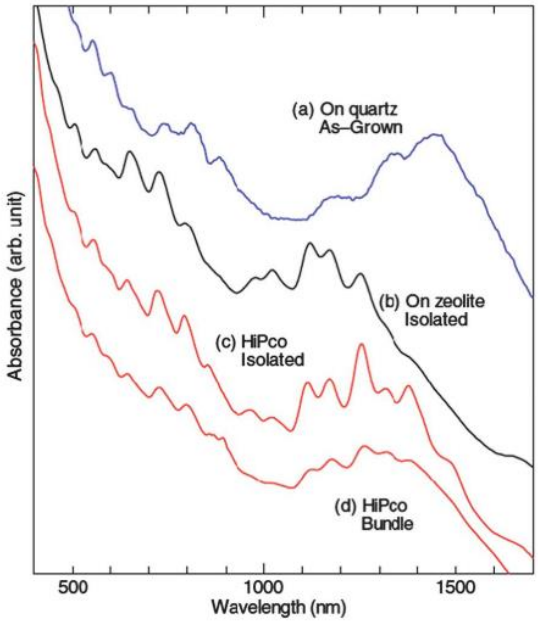

Figure 6: Absorption spectra a) CVD carbon nanotubes directly grown on a quartz substrate; b) CVD carbon nanotubes synthesized on small metal catalyst particles deposited on zeolite, then dispersed in D_2O with SDS then ultracentrifuged for eliminating bundles; c) HiPCO SWNTs dispersed in D_2O with SDS then ultracentrifuged for eliminating bundles; d) The same from c, but without ultrasonication.[19]

Experimentally, the absorption spectra of carbon nanotubes also present a background whose main origin is the π-plasmon, a collective excitation of the pi electrons under irradiation. This π-plasmon absorption band has a Lorentzien lineshape, which, for the large wavelengths usually used in our study, can be approximated as a variation in $1/\lambda$. Other factors that affect the background include light scattering, especially from carbonaceous material and catalyst particles present in the sample.[20,21]

One can note that the medium (solvent, dispersant) may affect the position of the absorption peaks.[22,23]

1.3 Photoluminescence spectroscopy

Photoluminescence (PL) of carbon nanotubes was first observed in 2002[18] in semi-conducting carbon nanotubes.

Optical transitions in carbon nanotubes were shown to be of excitonic nature. This means that, upon excitation, the generated electron-hole pair is not free, but bound by a force of coulombic nature, described by a quasi-particle named exciton. These quasiparticles induce a series of discrete energy levels (hydrogen like) up to a continuum of states in the electronic structure of nanotubes. As a consequence, upon excitation through the gap, the electron relaxes (non-radiative transition) from its excited state to a lower discrete excitonic level before recombination (radiative transition). The energy

of the lowest excitonic level corresponds to E^{S}_{11} diminished by the exciton binding energy. This exciton binding energy is high for carbon nanotubes (of the order of hundreds of meV due to their 1D nature and decreases when the nanotube diameter increases as $1/d^2$.

Due to selection rules, exciton recombination from the lowest excitonic state is non radiative (dark exciton). The PL of carbon nanotubes is thus originated from direct recombination from the upper excitonic state (bright exciton). As a consequence, the PL quantum yield of carbon nanotubes is low.[19,24–28]

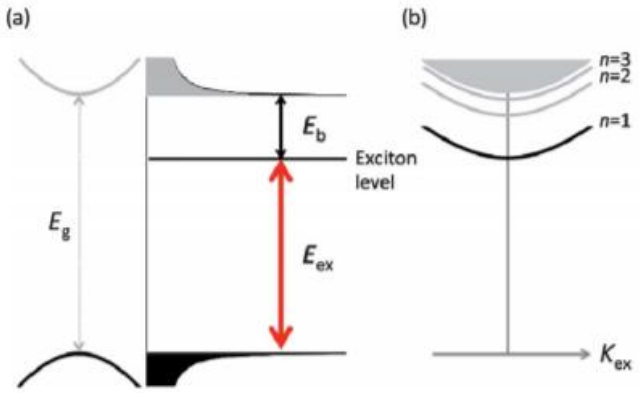

Figure 7: a) Schematic representation of the first sub-band structure of carbon nanotubes and its corresponding density of states with the position of its lowest energy exciton state (E_{ex}). E_g is the band to band energy gap (E^{S}_{11}), E_b the exciton binding energy; b) Schematic representation of the exciton energy levels up to its continuum of states, which corresponds to the nanotube inter-band transition.[19]

A sample of well dispersed SWNTs can be excited for example through E^{S}_{22} and emit light with an energy corresponding to its E^{S}_{11} red shifted by the energy difference between E^{S}_{11} and the emissive excitonic state(**Figure 8**). This fluorescence cannot be observed in bundles due to interactions with metallic carbon nanotubes, which allow charge recombination.[18]

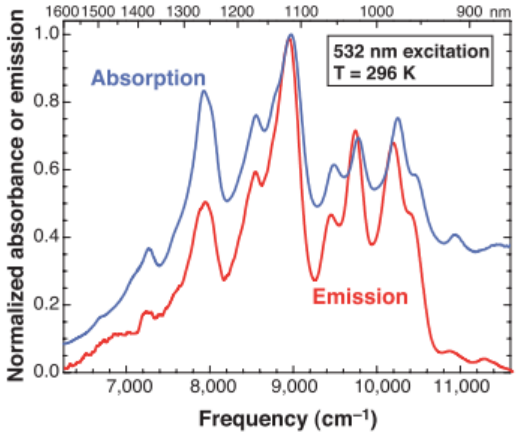

Figure 8: Comparison of the absorption and emission spectra on the E^{S}_{11} region for a suspension of HiPCO nanotubes dispersed in SDS micelles in D_2O[18]

In some cases, it is possible to observe energy transfer between nanotubes of different chirality (more specifically, from semiconducting tubes of large band-gap to other of narrower band-gap) through a Foster energy transfer mechanism. This happens if those tubes are close enough and in the absence of metallic nanotubes.[29,30]

1.4 Raman spectroscopy of carbon nanotubes

Raman spectroscopy is one of the most valuable techniques for the characterization of carbon nanotubes.[31]

Raman scattering is the inelastic scattering of photons by matter. In other words, the vibrations of the matter slightly modify the frequency of incident photons. These appear as a frequency shift on the scattered photons in relationship to that of the incident photons.

The observed vibrations are determined by selection rules, active modes being those that cause changes in the tube polarizability. In this way, only modes with specific symmetries can be observed, symmetries also related to the nanotube chirality. For example, **Figure 9** represents all different vibration modes for a (10,10) nanotube, while only those of symmetry A_{1g} being allowed.[9]

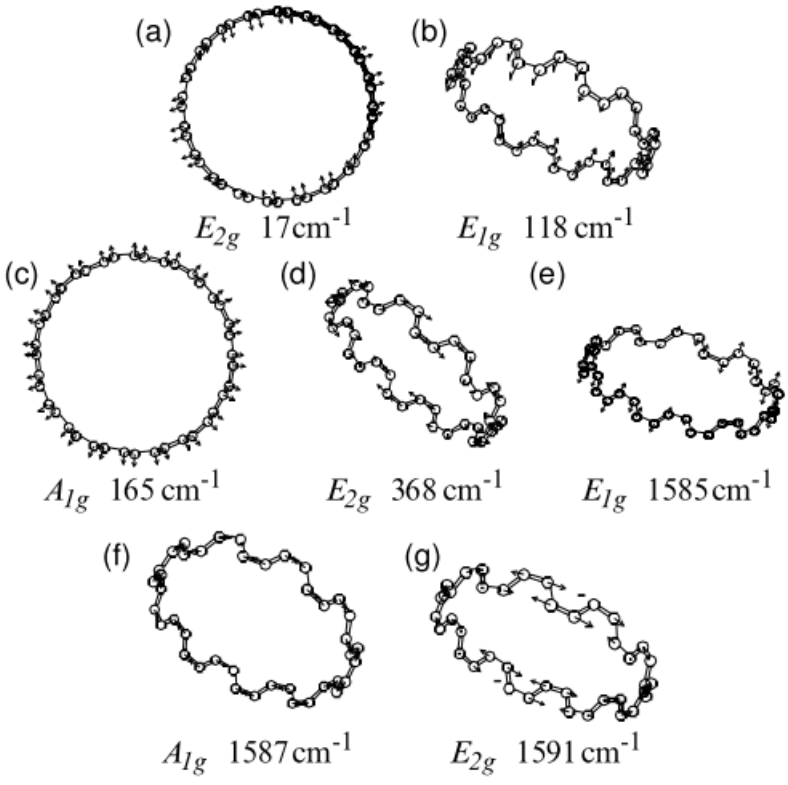

Figure 9: Vibrational modes of carbon nanotubes for a (10, 10) SWNT. Raman shifts are theoretical since only the A_{1g} modes displayed are active.[8]

For carbon nanotubes, the most important active modes are the radial breathing modes (RBM) and the tangential (G) modes.

Radial breathing modes have a A_{1g} (or A_1) symmetry, respectively for achiral and chiral nanotubes. These are symmetric radial extensions/contractions (as shown in **Figure 9c**). The frequency shift of these modes is inversely proportional to the diameter of the nanotubes and is found in the range 200-300 cm^{-1} (**Figure 10**).[32] However, this simple linear dependence may be affected by the surrounding medium of the nanotubes, such as their inclusion in bundles or by the solvent.

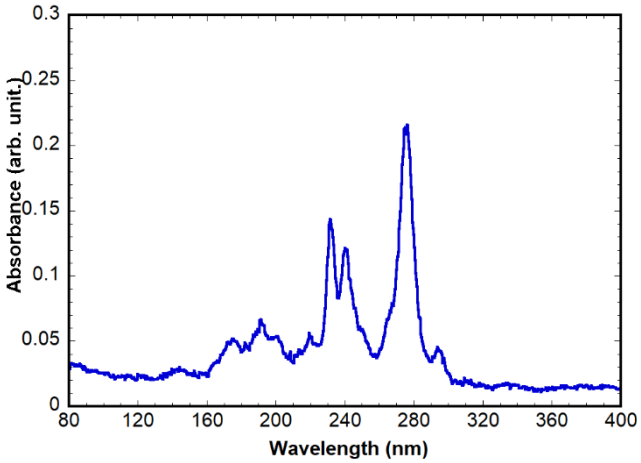

Figure 10: Raman spectrum (excitation 532 nm) of HiPCO SWNTs displaying its RBM modes

Tangential G modes are located between 1550 – 1600 cm^{-1} and come from in-plane vibrations of graphene (single peak). In carbon nanotubes, there are two active modes in this zone: the transversal (TO) and longitudinal (LO) modes, respectively along the tube circumference and along the nanotube axis. [32] These two modes have A_1 symmetry. They are called G^+ and G^-, respectively the one with higher and lower Raman shift. The correspondence between G^+/G^- and TO/LO designations depends on the chirality. While the G^+ mode is relatively independent of the diameter, the G^- one depends on it (see **Figure 11**). As the nanotube diameter increases, the two G modes frequencies approach. For sufficiently high diameters (as in MWNTs), only a single peak, with the same frequency as in graphene, is observed.[33]

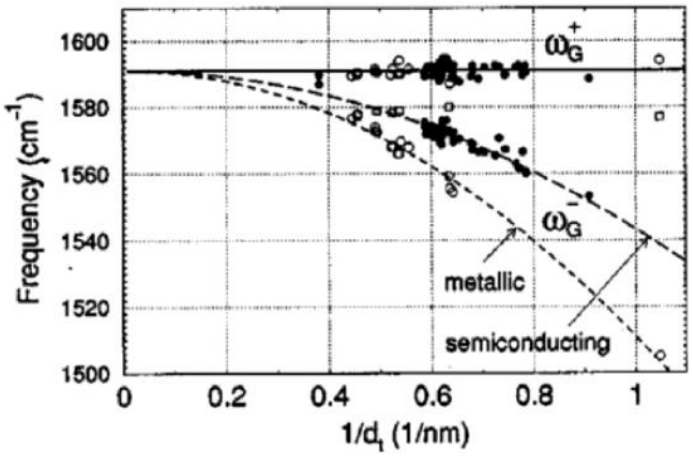

Figure 11: Diameter dependence of the G modes with the nanotube diameter. Only the low frequency component has a dependence on the tube diameter, which is slightly different between semi-conducting and metallic nanotubes.[33]

For semiconducting chiral SWNTs, the two modes are narrow and symmetric, being described by Lorentzien lineshapes. For metallic nanotubes, while the G^+ feature remains similar to the one observed for semi-conducting tubes, the G^- feature is a broad and asymmetric, being described by a specific lineshape called a Breit-Wigner-Fano (BWF) lineshape (**Figure 12**). This band is the result of interferences between the continuum of electronic states and the phonons. The frequency of this band increases with the nanotube diameter, while its width decreases.

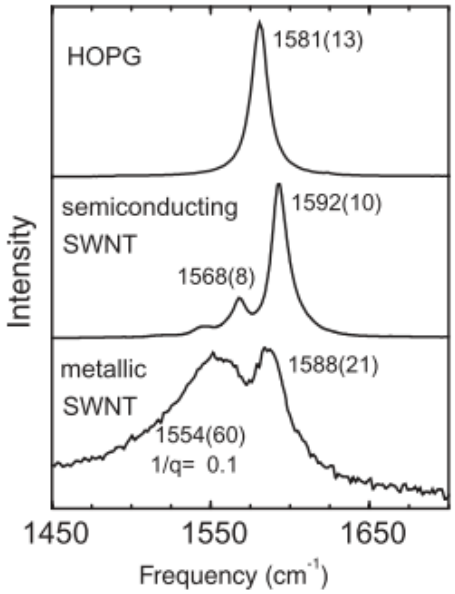

Figure 12: G band for HOPG (top), for chiral semiconducting (middle) and a chiral metallic (bottom) carbon nanotube. The semi-conducting chiral nanotube presents two G modes with a Lorentzian shape, while the G^- feature of the chiral metallic SWNT presents a broad and asymmetric lineshape. Excitation is 2.41 eV. [33]

The characteristics of the G-modes in the Raman spectra of are summarized in **Table 1**.[34]

Table 1: Summary of G band profiles as a function of the nature of SWNTs, as well as its designation as TO and LO. Adapted from [34].

Nanotube type	Number of components	Profile	G^-	G^+
Semiconducting chiral	2	LO + TO - Lorenzian	TO	LO
Metallic chiral	2	LO – Fano TO - Lorenzian	LO	TO
Armchair	1	Lorenzian		TO
Semiconducting zigzag	1	Lorenzian		LO
Metallic zigzag	1	Fano	LO	

Contrary to the RBM modes, the G modes are less affected by the environment in the absence of charge transfer, since tangential vibrations do not change the shape of the nanotube.

Another important feature in Raman spectroscopy of carbon nanotubes is the D band, observed between 1250 and 1450 cm^{-1}. Normally inactive, it is activated by the presence of defects in the sp^2 structure that allows elastic electron scattering. This band is dispersive, meaning that its frequency changes with the laser excitation energy (increasing with increasing the excitation energy).

Other modes, such as two-phonon modes (for example the G' mode observed at around 2600 cm^{-1}, are also observed but will not be further described.

Most importantly, the Raman spectra for carbon nanotubes is resonant: in this case the scattering is coupled with light absorption, which increases the signal a thousand-fold, allowing the observation of a signal even for individual nanotubes under the right conditions.[31] This allows one to select carbon nanotubes species by tuning the excitation wavelength (**Figure 13**). Resonance can happen with both incident and scattered photons.

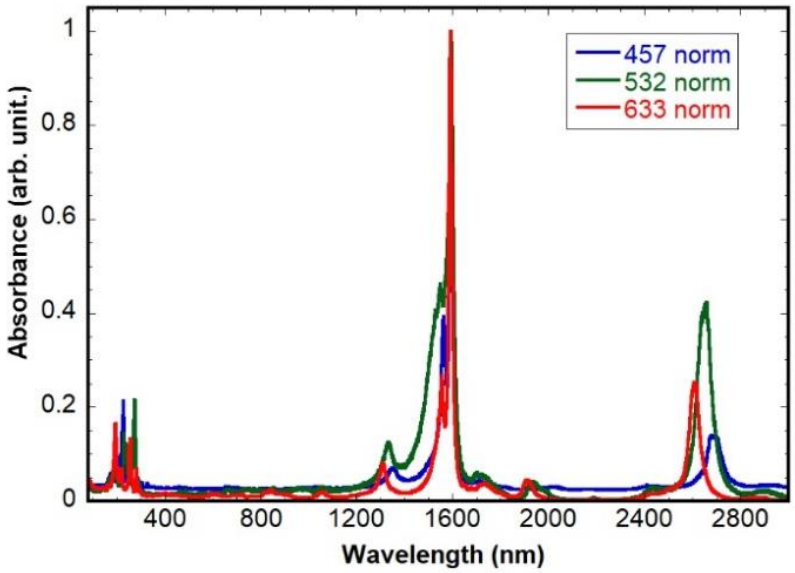

Figure 13: Raman spectra of HiPCO SWNTs used in this thesis obtained through excitation at different wavelengths. The spectra were normalized by the intensity of the G mode.

1.5 Charge transfer effects

Charge transfer affects the electronic properties of carbon nanotubes and results in changes that are analogous to results observed with non-covalent functionalization. This chapter describes briefly what is observed.

Charge transfer from or to single-walled carbon nanotubes shifts their Fermi energy level. This means that filled states in the valence band are depleted or empty states in the conductive band are filled, suppressing the corresponding optical transitions.

The effect of charge transfer has been studied since the end of the 90's by optical absorption and Raman spectroscopies. Petit *et al.* [35] studied the electronic or carbon nanotubes produced by laser ablation by tuning their Fermi level by exposure to solutions of given chemical potential (n-doping) or halogen vapors (p-doping). The authors observed that, by increasing (decreasing) the shift of the Fermi energy, the peaks up to the corresponding energy are suppressed **(Figure 14)**.[35]

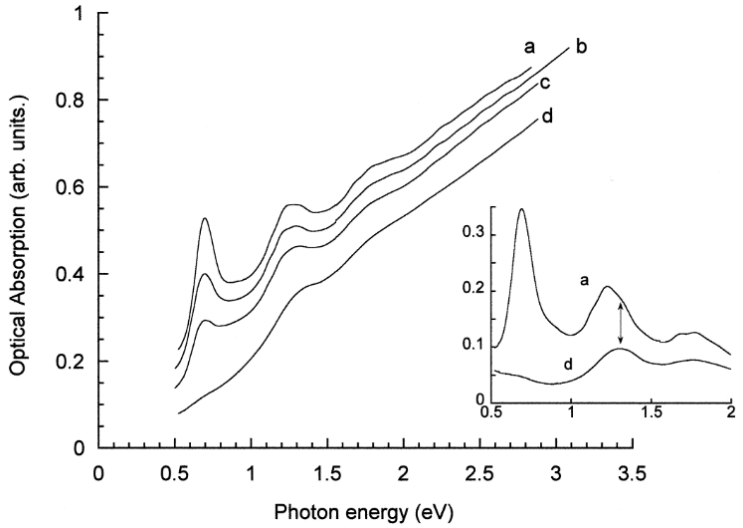

Figure 14 : Evolution of the absorption spectrum of SWNTs (a) to the exposure to molecules of different redox potentials: antraquinone-lithium for 1s (b) and 10s (c) and to fluorenone-lithium (d). Inset: curves a and d after π-plasmon correction.[35]

Doping of carbon nanotubes affects also the Raman spectrum of carbon nanotubes. Electron doping causes a downshift of the G^+ mode, while hole doping causes an upshift, due to lattice expansion and contraction respectively.[36]The Raman features are also affected by the loss of resonances originated by the suppression of optical transitions. In a sample of mixed nanotubes for example, increasing the doping causes the gradual disappearance of RBM peaks, as different chirality need different levels of doping for losing resonance.[9,33]

1.6 Non-covalent functionalization of carbon nanotubes

Dispersion of carbon nanotubes in most common solvents results in concentrations smaller than the ppm, and some better dispersants are not capable of breaking the strong Van der Waals interaction between them, causing dispersion of large bundles.[37,38]

Non-covalent functionalization comes as one of the best methods to allow solubilization and unbundling of carbon nanotubes. Specific interactions can be also used to tune some of the carbon nanotubes properties, allowing for charge or energy transfer. The fact that it does not disrupt the sp^2 network is an advantage over covalent functionalization.[39]

Both covalent and non-covalent functionalization of carbon nanotubes have been discussed in many reviews[39,40,49,50,41–48], so only more relevant cases will be presented.

1.6.1 Functionalization of carbon nanotubes with small molecules

Exohedral functionalization can be performed with molecules by different kind of interactions, such as π-stacking and hydrophobic interactions. The latter was initially used for the separation of carbon nanotubes bundles and allowed, for example, the first observation of carbon nanotubes photoluminescence.[18] Hydrophobic interactions can be more or less reversible, sometimes large excesses of the functionalizing agent is needed to assure stability.[47,51]

π-stacking on the other hand promotes a more intimate interaction between the carbon nanotubes and surrounding molecules, allowing selectivity, charge or energy transfer. These effects can be observed through changes in the properties of both the carbon nanotubes and of the molecules used to functionalize them, such as shifts on the optical absorption and PL spectra, quenching of emission and shifts of Raman spectra peaks.[51–56] Energy band alignment both species is important and may afford some selectivity of some chiral species.[53] Many different molecules can interact with carbon nanotubes through π-stacking, such as porphyrins,[51–53] carbocyanines,[54,55] perylenes,[57,58] pyrenes,[59] and other dyes,[56,60] between others.

Functionalization of carbon nanotubes by small molecules can also be endohedral, the filling being performed by diffusion of vapor phase of the filling material. Some of the molecules inserted in this way are oligothiophenes[61–63], β-carotene,[64] squaraines[65] and perylenes.[66] The diameter of the nanotubes as well as their electronic character may affect the electronic coupling, but in general energy transfer happen when the dye is excited.

1.6.2 Functionalization of carbon nanotubes with conjugated polymers

Besides small molecules, a diverse range of macromolecules are capable to interact with carbon nanotubes, allowing for its enhanced solubility. Besides this, some macromolecules such as DNA and some conjugated polymers can have different interactions with carbon nanotubes of different chirality, sometimes this difference being such that separation of these different chirality can be achieved.[67]

Conjugated polymers consist of chains of species that present alternating simple and double bonds. This allows for electronic delocalization of the π-electrons along the chain, resulting in semi-conducting materials with a band structure. Most of these conjugated polymers present aromatic units in their backbone, allowing for π-stacking onto the surface of carbon nanotubes.

These molecules are relatively complex, the stacking onto the carbon nanotubes being affected by many preparation parameters such as solvent, chain length, solubilizing side chains, etc. For example, P3HT

wraps around SWNTs in $CHCl_3$ solutions[68,69] or NMP,[69] but aggregates perpendicularly to the tube in anisole (see **Chapter 2.3**).[70,71] Wrapping is considered to be best configuration for stable dispersions (**Figure 15**).[67]

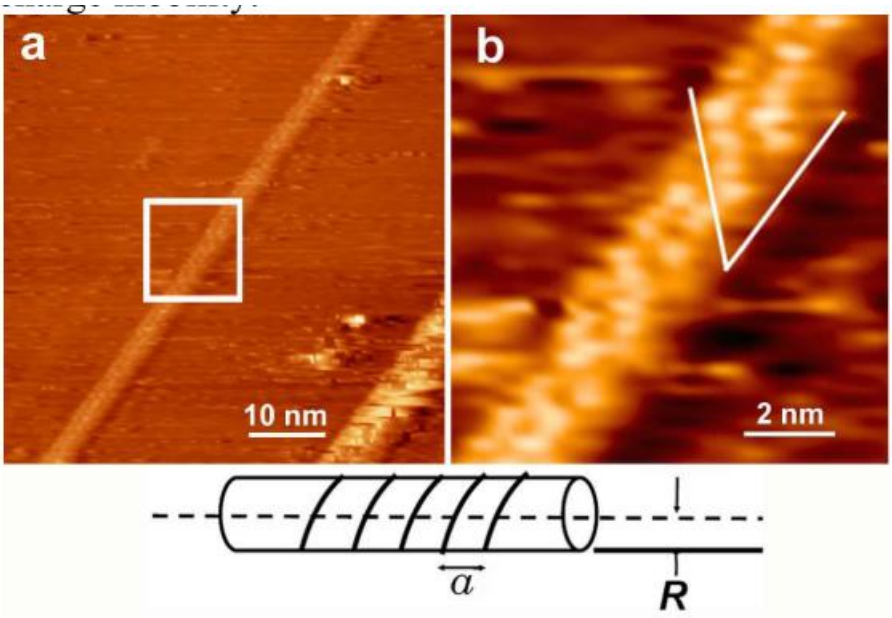

Figure 15: STM images of P3HT wrapped around SWNTs obtained from the drop-casting of a solution in $CHCl_3$[68]

1.6.2.1 Dispersibility

Because of the possibility of π-stacking, conjugated polymers were early though as possible dispersants for SWNTs. First evidences for dispersion of carbon nanotubes with conjugated polymers come from tests with poly(m-phenylenevinylene-co-2,5- dioctyloxy-p-phenylenevinylene) (PmPV).[72] Since then, a large variety of conjugated polymers have been used for the polymer wrapping (**Figure 16**).[73]

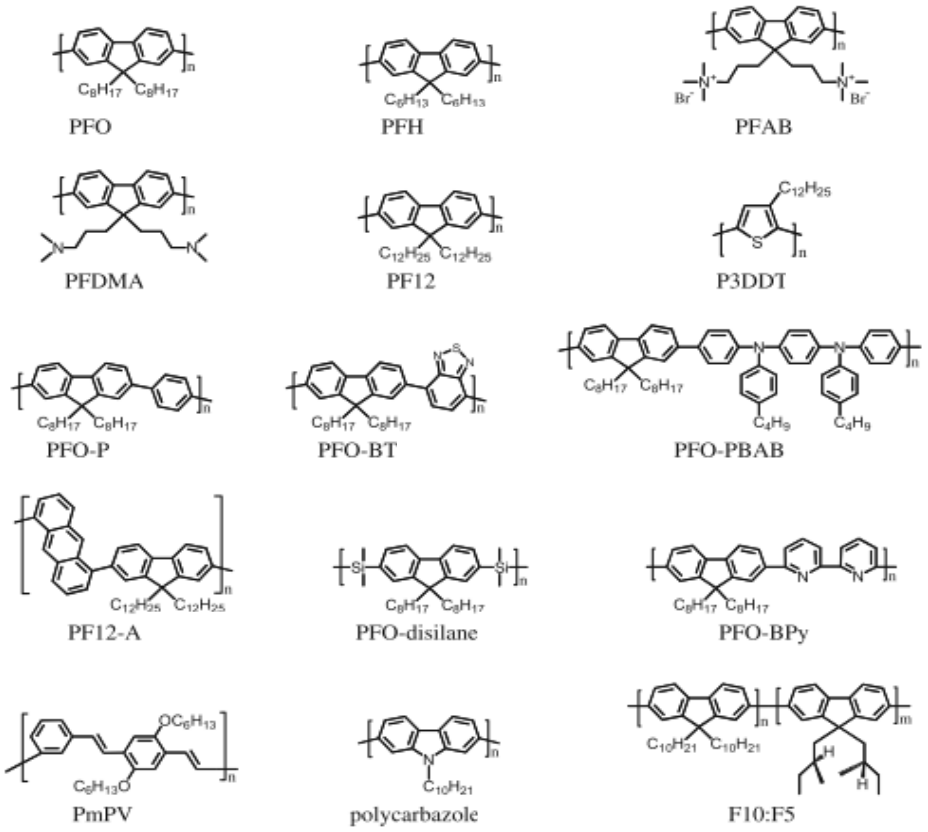

Figure 16: Structure of conjugated polymers showing selectivity towards carbon nanotubes.[73]

All these structures have been used principally for studying the optical properties of carbon nanotubes and the interaction between both components. The main problem of using these is that, due to the strong interactions between the components, their removal requires the use of harsh processes that may damage the nanotubes.[38] Some groups have tried to obtain polymer free selected nanotubes by using polymers that break upon action of specific chemical[74], by changing the folding configuration, by changing the solvent[75], or by the use of supramolecular polymers.[76,77]

An interesting exception is the possible exchange of PFO by P3HT on PFO-wrapped carbon nanotubes, due to the stronger interaction of P3HT than PFO with the carbon nanotubes.[78] The polymer wrapped around the nanotube can also bring some functionality to the system, as it can be more easily functionalized than the nanotube itself, allowing solubility control, introduction of switches, between others.[38,79]

1.6.2.2 Selectivity

While studying the dispersion of carbon nanotubes with conjugated polymers, it was discovered that some conjugated polymers are able to selectively functionalize carbon nanotubes, leading to suspensions

of pure species (normally semi-conducting). Polymer wrapping strategies are especially useful comparing to other techniques due to high yield, high concentration and relatively simple procedure.[67,80]

The effectiveness of the selection depends on many factors. For example, bad solvents for the polymer induces a more rigid chain that reduces its conformational freedom and increase the selectivity.[67,73,81,82] On the other hand, solvents that allow more flexible chain conformations decrease selectivity while increasing solubilization yield. Temperature plays similarly, with an optimum temperature range for dispersion and selectivity.[83] Concentration also needs to be optimized, such that there is only enough polymer for covering and solubilizing the species.[73,84–88]

Polymer parameters such as the composition of the backbone,[67,73,81,82] and of the side chain[73,89], as well as molecular weight[86–88,90,91] also affect the overall result. For example, polyfluorenes with larger alkyl chains are able to disperse nanotubes of larger diameters, increasing also the overall yield but losing selectivity in the process (**Figure 17**). [89] At the same time, an optimum for solubility was obtained for copolymer of polyfluorene, poly[2,7-(9,9-dioctylfluorene)-alt-2,5- (3-dodecylthiophene)] (PFT) (**Figure 18**). Low solubilization was attributed to weak interactions between polymer and nanotube for lower molecular masses and to polymer aggregation for higher.[88]

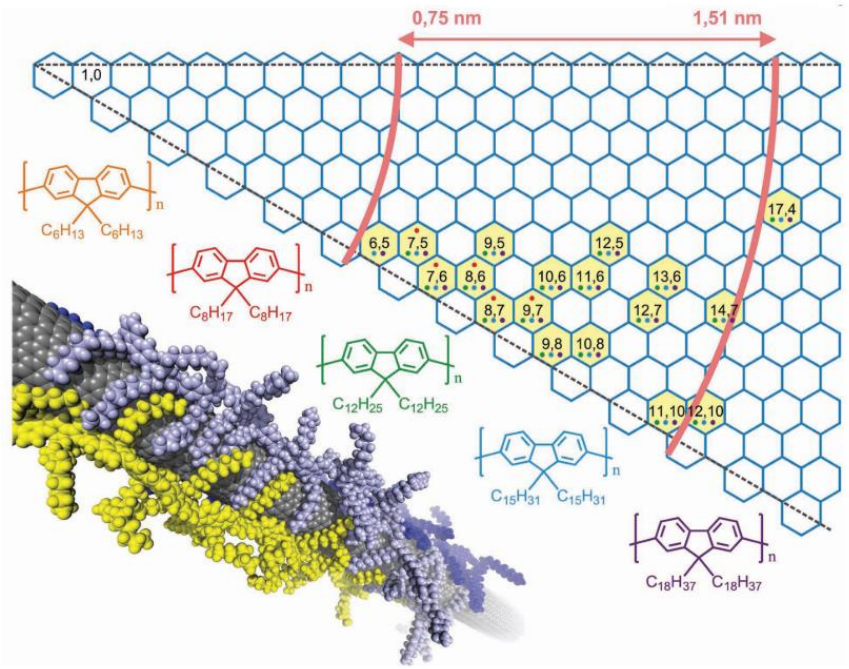

Figure 17 : Chirality map of wrapping for different alkyl side chain length on polyfluorene[89]

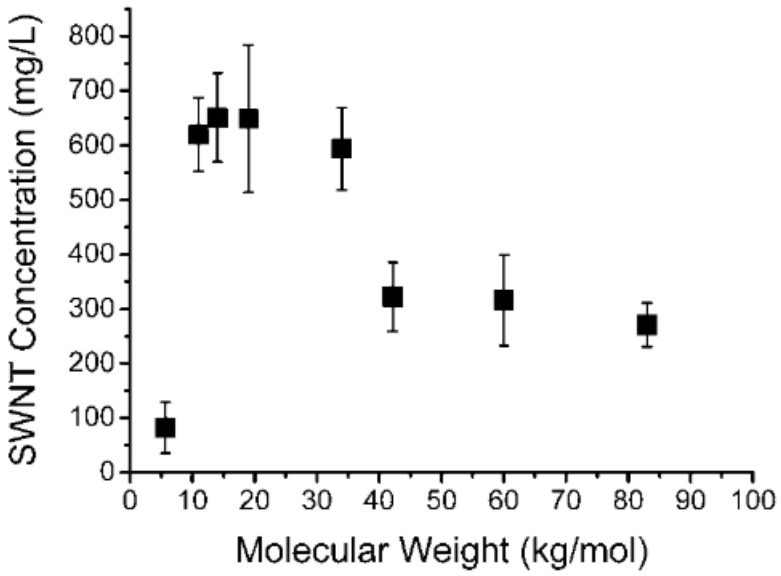

Figure 18: Concentration of dispersed SWNTs as a function of the molecular weight of PFT used for its dispersion at a fixed polymer concentration in THF.[88]

1.6.2.3 Devices

Beside dispersion and study of SWNTs, the main idea behind the dispersion of carbon nanotubes with conjugated polymers was the use of the carbon nanotubes as possible electron acceptors for organic photovoltaics. Reasoning for this includes the ability of carbon nanotubes to absorb in the near infrared, their high charge mobility compared to fullerenes, and their ease in forming percolation pathways for charge transport.[92,93] Upon irradiation, excitons are formed in the conjugated polymers. Contrary to inorganic semiconductors, these excitons have a high binding energy, so an intimate contact between phases is needed for allowing charge separation before recombination.[94] It is also important that the energy levels are correctly aligned, in what is called a type II heterojunction. In this type of heterojunction, both the HOMO and LUMO of the first component are at a respectively higher level than the HOMO and LUMO of the second component. In this kind of heterojunction, electrons and holes are confined to each material, avoiding charge recombination[94]

Some polymers like poly[2-methoxy-5- (2'-ethyl-hexyloxy)-1,4-phenylene vinylene] (MEHPPV), PFO, have been shown to have the good band alignment for direct exciton transfer to SWNTs, but not for charge separation.[94,95] Others, like P3HT, have a good band alignment for inducing exciton dissociation when the polymer or the nanotube is excited. However, although experiments show electron conductivity on the SWNTs and hole conductivity in the polymer upon excitation of any of the components,[92,96], some studies have found the opposite.[97]

Figure 19 shows a comparison of the energy levels of [6,6]-phenyl-C61-butyric acid methyl ester (PCBM, a fullerene modified with a solubilizing chain), semiconducting SWNTs, P3HT and PFO. P3HT in particular has a good energy band alignment for forming type II heterojunctions with SWNTs for application in solar cells.[67]

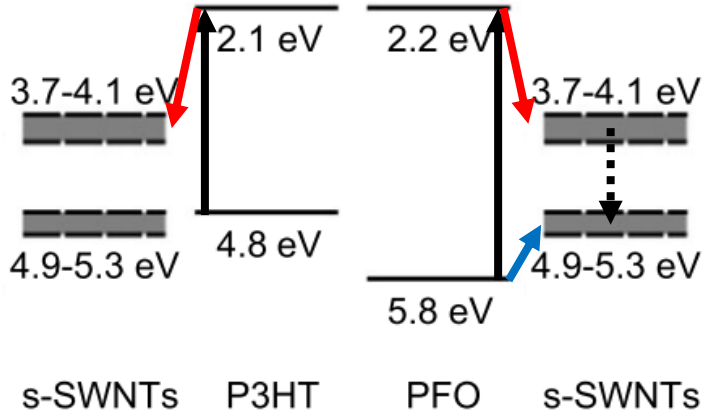

Figure 19: Energy levels of some common conjugated polymers and that of SWNTs, showing excitation of the polymer (black arrows). After excitation, an electron (red arrow) can be transferred from P3HT to the SWNTs, while the exciton (red and blue arrow) is transferred from PFO to SWNTs, where charge recombination (dashed black arrow) can happen.

In practice, solar cells made from conjugated polymers and SWNTs display low efficiency compared to what is now commonly obtained using organic solar cells.[98] One of the main reasons is the presence of metallic species that provide a pathway for charge recombination.[92]

1.7 Covalent functionalization of carbon nanotubes

Contrary to non-covalent functionalization, which requires the presence of specific components, covalent functionalization is extremely versatile, with all the toolbox of organic chemistry open to functionalize carbon nanotubes. However, covalent functionalization creates defects on the graphitic structure, affecting negatively some of the nanotubes properties such as their conductivity.[39]

This effect on the crystalline structure is easily observed on the electronic structure of the carbon nanotubes as well. As in the case of doping, optical transitions are extinguished.[15] In Raman spectroscopy, the main effect of the covalent functionalization is the increase of the D band with respect to the G band. Thus, the ratio between the integrated areas of the D and G bands are associated with the amount of defects present on the nanotubes and it is frequently used to estimate functionalization rates

(**Figure 20a**).[99–101]However, quantitative results may be hard to be achieved because of the dependence of I_D/I_G on the laser power and the excitation wavelength (**Figure 20b**). [99–101]

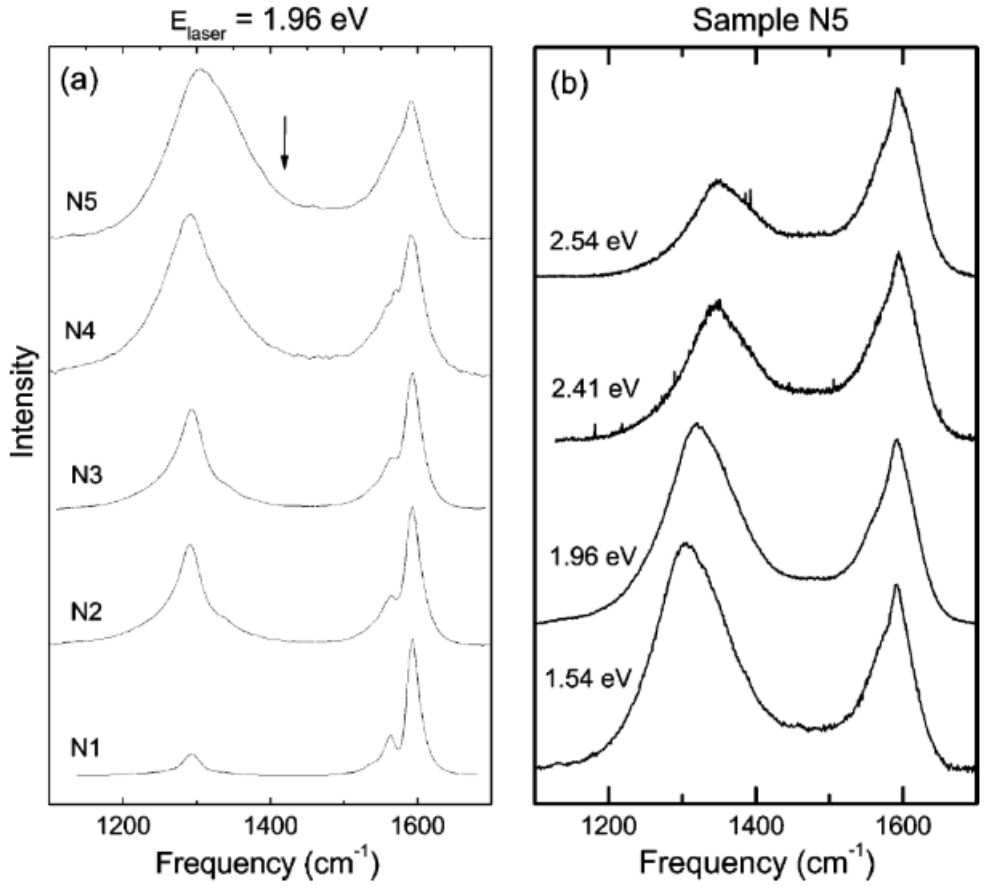

Figure 20: a) Raman spectra (excitation 1.96 eV) of SWNTs films with increasing functionalization raters (N1 - lower to N5 - higher); b) Changing the laser excitation energy for the sample N5[15]

Among direct methods for the functionalization of carbon nanotubes, the most useful are acid or ozone driven oxidation, which creates groups such as carboxylic acids (that can be further modified with $SOCl_2$ for promoting esterification or amidation reactions); cycloadditions of carbenes and nitrenes; and radicalar chemistry. Since we used the latter in our studies, it will be the only one described.[39]

1.7.1 Radicalar chemistry

One of the main methods used for carbon nanomaterials functionalization is the use of a diazonium decomposition reaction, generating phenyl radicals that bind to carbon nanotubes or graphene. The binding occurs because the carbon nanotubes are reductive enough for allowing an electron transfer to the diazonium salt, thus transforming it into an aryl radical. The mechanistic pathway includes first a fast adsorption of the diazonium cation followed by a slow electron transfer from the nanotube, causing

the diazonium decomposition and the binding of the phenyl radical (**Figure 21a**).[100,102] The grafted aryl radicals are then used for further reactions (**Figure 21b**).[103]

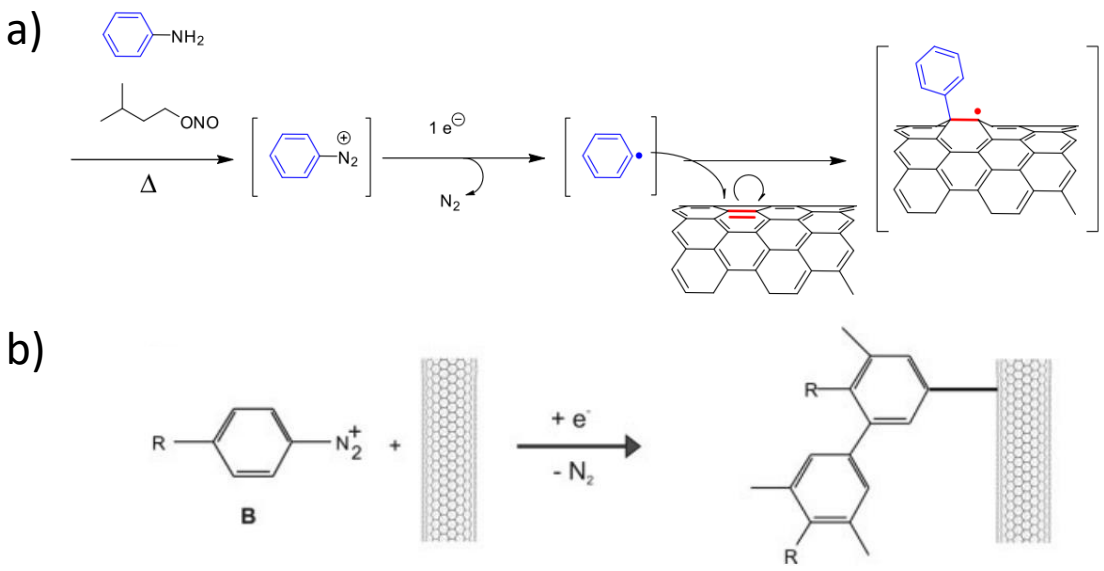

Figure 21: a) Mechanism of diazonium functionalization starting from an aniline. The diazonium is formed in situ (from [102]); b) Possible mechanism for polymer formation during diazonium functionalization (from [102]).

Bahr and Tour[104] introduced in 2001 a method for performing diazonium coupling with SWNTs by diazonium compounds generated in situ by the reaction of an aniline with isoamyl nitrite in THF at 80°C (**Figure 21a**). In their work, an excess of aniline derivative was used (4 NH_2 groups per carbon atom), resulting in the disappearing of the optical transitions of all species as well as a large increase of the D/G ratio in the Raman spectrum. The process was efficient for grafting para-functionalized anilines with halogen, alkyl, ester and nitro groups in the para- position; but failed at grafting p-aminobenzoic acid. The estimated functionalization rate was of 1 attached group per 30-40 carbon atoms.

This functionalization route is faster for metallic nanotubes **(Figure 22a** and **b**), allowing selective elimination of metallic pathways in random network devices if the concentration is controlled (**Figure 22c**).[100,105,106] This selectivity may take place in both the adsorption step of the diazonium (different affinities)[100,107] and during the electron transfer step (easier electron transfer from the tube to the diazonium from metallic species and low bandgap semiconducting ones).[102] This trend however can be inversed in basic conditions due to the formation of an electron rich intermediate that prefers to adsorb onto larger band gap nanotubes.[107]

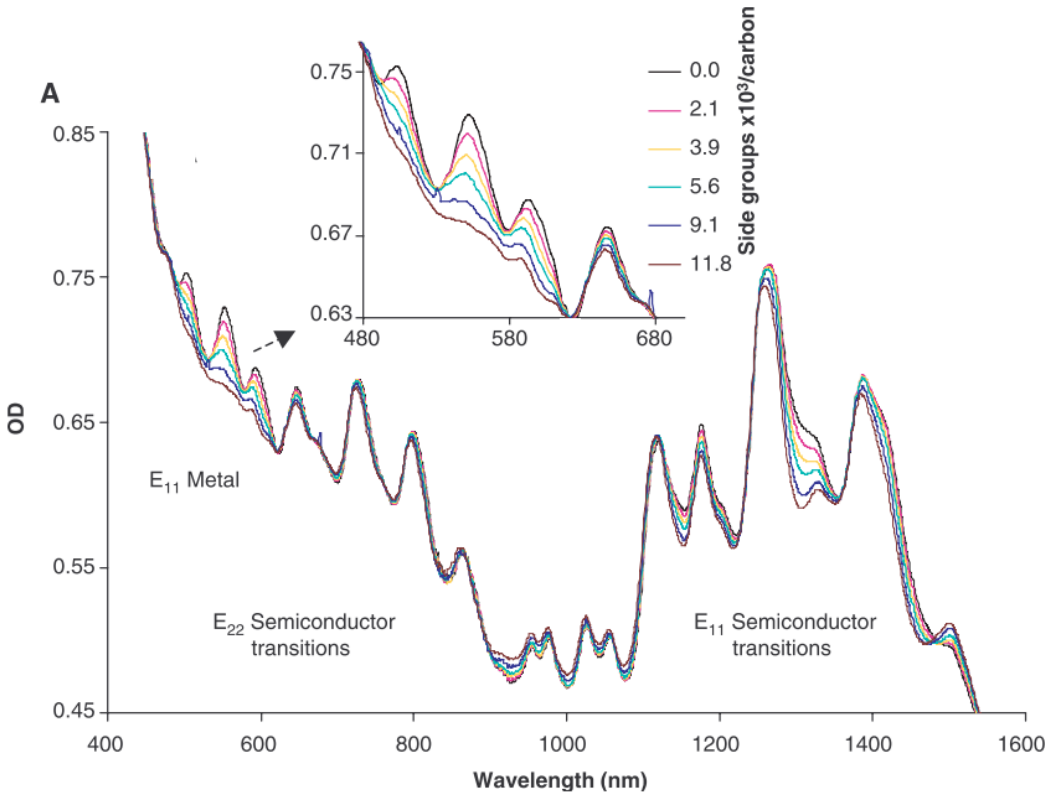

Figure 22: Optical absorption spectra of HiPCO carbon nanotubes functionalized through diazonium grafting (low functionalization rates of few defects per thousand carbon atoms) showing the reduction of metallic carbon nanotubes optical resonances while keeping semi-conducting species almost unchanged.[105]

This same process resulted in similar behavior when functionalizing SWNTs without solvent. The authors conclude that mechanical shear originated by the stirring bar was enough to expose large surfaces for the functionalization reaction. These conditions were used to functionalize MWNTs, despite their lower reactivity attributed to their larger diameters.[108]

A derived method consists in the utilization of aryldiazonium salts.[109] These reactions can be performed in aqueous media on SDS dispersed SWNTs, obtaining up to 1 added group every 9 carbons as determined by TGA. The Raman spectra confirmed the very high functionalization rates obtained, both by the D/G ratio and by the disappearance of the RBM modes. Solubility of the product in organic solvents was also enhanced compared to that of raw carbon nanotubes. The efficiency of this reaction can be increased by optical excitation of the carbon nanotubes, which generates heat locally and favors the reaction.[110]

While high functionalization rates are often aimed for solubilization, there is some interest in low functionalization rates. For example, Piao *et al.*[111] performed covalent functionalization of (6,5) SWNTs by aryl groups at very low functionalization rates. The presence of "isolated" defects can generate a new two-level state in the semi-conducting carbon nanotube band structure, associated with a new possible optical transition, E_{11}^{-}. Thus, mobile excitons can be channeled to and trapped in this new lower- energy

state, producing a new emission that is redshifted from the native E_{11} fluorescence. The low energy level generated by the defect competes with the low-lying dark exciton energy level that quenches carbon nanotube photoluminescence, allowing an increased emission quantum yield (**Figure 23**). Spatial localization of the exciton also increases the total PL lifetime.[112]

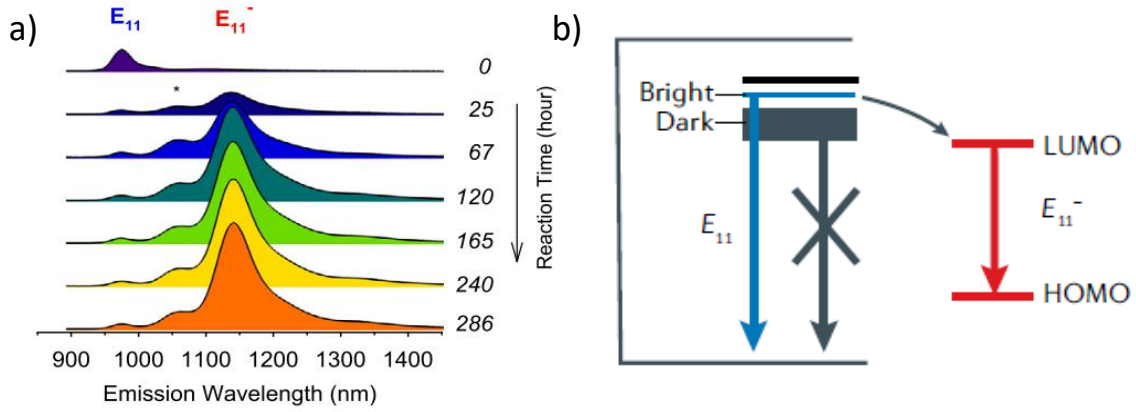

Figure 23: a) Evolution of the E_{11}- emission as a function of time during functionalization with p-nitrophenyldiazonium tetrafluoroborate[111] *b) Proposed energy level diagram of the organic color center. Excitation happens with the formation of a bright exciton. From there, there is a competition between the decay pathways: direct fluorescence, quenching via the dark exciton and energy transfer to the defect state.* [113]

These defects have been called sp^3 defects or organic color centers between other names and are natural room temperature single photon emitters.[114] Other possible applications involve the chemical sensing (through binding to the defects, changing its electron donating/withdrawing effects), imaging and promoting up-conversion luminescence.[113]

Lastly, while not being an example of radicalar chemistry, a cycloaddition based on azidodichloro-triazine is particularly interesting due to the rearrangement of chemical bonds after the cycloaddition step, recovering the π-conjugation of the carbon nanotube (**Figure 24**). The chlorine atoms can be further replaced by other groups.[47,115]

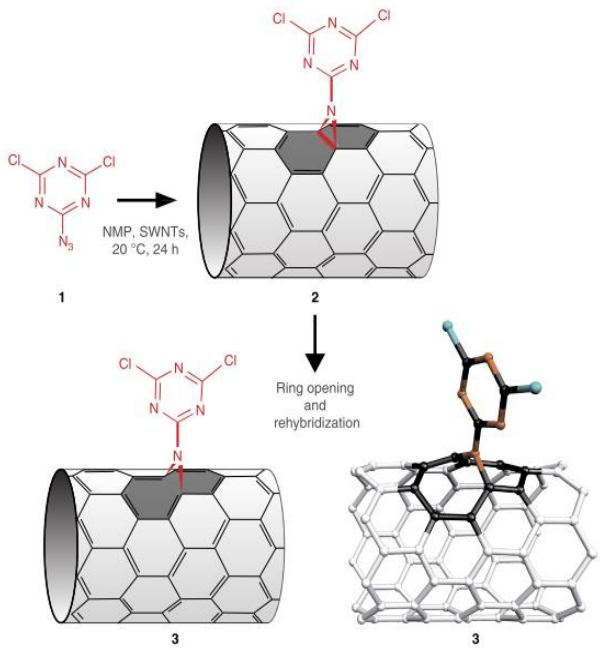

Figure 24: Functionalization of carbon nanotubes by [2+1] cycloaddition reaction. Cycloaddition is followed by ring opening and rehybridization, leading to the reestablishment of local π-conjugation[115]

1.7.2 Examples of functionalized carbon nanotubes

The grafting of some simple substituted aniline compounds can be followed by other reactions for more complex functionalization. One of the main methods is the utilization of acetylene groups in the p-position of the diazonium, allowing the use of the Huigsen 1,3-dipolar cycloaddition (or CuAAC – copper-catalyzed alkyne-azide cycloaddition), a copper(I) catalyzed cycloaddition between an azide and a terminal alkyne. This is the main reaction of the group that constitutes the click chemistry toolbox. The great advantage of this method is the high reactivity (by definition), allowing modification of (almost) all available functionalized groups, without secondary reactions. This allows for the grafting of high added value molecules onto the carbon nanotubes in a more efficient way than through direct diazonium chemistry, which requires large excess of the reactive.[99]

CuAAC was first used already in 2005 by Adronov *et al.*[45,116] for the grafting polystyrene onto the carbon nanotubes, leading in an increased solubility of the carbon nanotubes in THF and other organic solvents. Hay coupling provides an alternative but similar method for coupling more complex molecules to alkyne functionalized carbon nanomaterials, such as porphyrins,[117] between a series of others.[40]

Other attachment reactions include esterification (especially in previously oxidized carbon nanotubes), Hay coupling,[117] Sonogashira reaction[118], etc. Most reactional schemes show problems when functionalizing carbon nanotube in two steps due to crowding that may prevent complete coupling.[118]

Porphyrins were one of the most studied molecules functionalized through two step methods. Other coupled compounds include cyclodextrins,[40] gold nanoparticles,[40,47] amino-acids,[40] phtalocyanines,[99] coumarins[119] and polymers (these being more detailed in **Chapter 1.7.3**).[45] One of the main reasons for the functionalization is to create optoelectronic coupling, such as when phtalocyanines are used as antennas for exciting the carbon nanotubes. However, in most cases there is little difference between covalently grafted and non-covalent functionalized carbon nanotubes in terms of charge or energy transfer, the main gains being an increased solubility.

1.7.3 Functionalization of carbon nanotubes with polymers

One of the main reasons for polymer grafting onto the carbon nanotubes is to increase the solubility of carbon nanotubes in organic solvents or to increase the compatibility with a polymer matrix.[40,120]

Many types of functionalization of carbon nanotubes have been used. In general, polymers are grafted by coupling to active groups present on the carbon nanotubes surface (grafting to approach). An alternative is the growth from the carbon nanotubes after attachment of a suitable initiator (grafting from approach). It is important to note that most of the articles on this topics report polymers grafted to the nanotubes through their chain ends, independent of grafting to or grafting from.[41]

CuAAC has been used for attaching polystyrene onto carbon nanotubes previously functionalized by an alkyne bearing diazonium.[45,116] Radicalar approaches can be used to bind macroinitiators (azo-polymers, such as azo-PEGs) or living growing chains (PS, polycaprolactone), such as chain end-capped with a TEMPO group (**Figure 25**) or even radicals generated through γ irradiation (PEO, PE).[42]

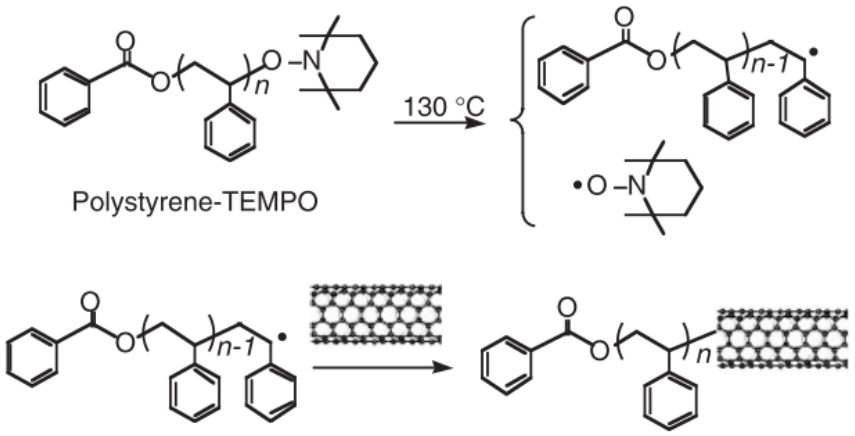

Figure 25: Grafting of living chains of polystyrene in a TEMPO polymerization mechanism through the addition of carbon nanotubes as radical scavenger[42]

Diazonium reaction can be used for direct synthesis of a poly(phenylene)-like coating containing different functional groups. Control of chain length can be obtained through the control of the concentration and the use of a reducing agent,[121] or through controlling the applied potential when SWNTs were deposited onto an electrode.[122]

Again, radical grafting of initiators onto the carbon nanotube surface is a good method for starting polymerizations directly from the nanotubes surfaces (grafting from). 1,1-Bis(t-butyldioxy)cyclohexane, for example, decomposes at high temperature, forming radicals that can be attached to carbon nanotubes. Controlled polymerization can also proceeds through attached groups, such as the attachment of initiating groups for ATRP for the growth of polymetracrylates, polyacrylic acid or PS (**Figure 26**)[40,42]

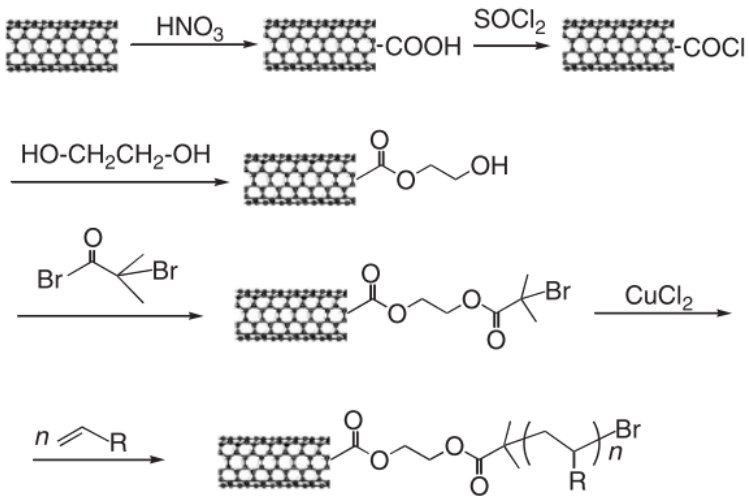

Figure 26: Scheme of attachment of an initiating group for ATRP[42]

Typical ionic methods can be also used, such as grafting of PVC onto carbon nanotubes through Friedel-Craft alkylation,[123] or by attaching ionic initiators.[42] Other examples of possible functionalization pathways and obtained hybrid materials are described in different reviews.[40–44,124]

In terms of conjugated polymers, there are relatively few studies. This may be caused by their relative expense and difficult synthesis compared to the more common polymers on the examples above.

Regioregular and regiorandom (see chapter 2) P3HT and poly(3-dodecylthiophene) (P3DDT) were grafted onto carbon nanotubes through esterification of acyl chloride groups present on oxidized carbon nanotubes with alcohol functions on the P3HT chain end. The obtained nanohybrids organized in structures that the authors called butterfly structure (P3HT) and stem-cell (P3DDT) structures, with the nanotube acting as the body/stem and P3HT crystals acting as wings/leaves (these crystals were formed by the covalently attached chains and the remaining chains present in the medium).[125] Another group used the same grafting reaction for functionalizing MWNTs. Notably a blue shift in the absorption of

the polymer was observed in both solution and thin film, ascribed to a distorted chain configuration. Photovoltaic performance was better for the covalent than for non-covalent hybrids.[126]

As a conclusion, although many polymers have been attached to carbon nanotubes, most of the studies focus only on the solubilization and compatibilization with polymer matrices. Functionalization happens in two steps for most cases, with a first addition of a small molecule that acts as an initiator (grafting from) or as anchoring point (grafting onto). In the first case, the method is limited mostly to vinylic monomers. The second case allows a larger scope but is limited by steric hindrance.

1.8 DWNTs

1.8.1 Electronic and optical properties

Carbon nanotubes may exist also as double-walled (DWNTs) and multi-walled carbon nanotubes (MWNTs), coaxial structures whose layers are separated by around 3.4 Å, similar to the distance between layers in graphite. The electronic structure is more complex for these compound systems, since it is influenced by the different combinations of carbon nanotubes (M@M, M@S, S@M and S@S for DWNTs, where M represents metallic and S represents semiconducting nanotubes and the notation is outer @ inner tube). Interlayer interactions also lead to a resulting electronic structure different to a simple sum of its parts.

Electronic coupling between the two carbon nanotubes varies. First of all, optical transitions of both layers are red-shifted compared to that of isolated nanotubes due to the dielectric screening. The coupling is also affected by the interlayer distance, with a red-shift for more separated tubes, but a possible blue-shift when the interlayer distance is small. Theory also predicts that the relative handedness of chiral nanotubes also affects this shift, which has been shown, although the formation of pairs of nanotubes of same handedness is more probable. These effects are more intense in the semi-conducting species that forms the DWNT.[127–129]

1.8.2 Photoluminescence spectroscopy

For a long time, the photoluminescence of DWNTs was an open discussion. Several groups reported emission from the inner tubes, sometimes enhanced compared to SWNTs of the same type. [22,130,131] On the other hand, other groups reported that there is no fluorescence from the inner tubes, attributing the

quenching to energy-transfer to the outer-tubes, resulting in the stronger luminescence from the latter. [132–136]

This debate was finally settled by the studies of Levshov *et al.*[31], which performed experiments with individual suspended DWNTs. PL of the inner tubes was observed, although with a low quantum yield of the order of 10^{-6}, which was attributed to energy transfer from the inner to the outer tube (and independent of the metallic or semi-conducting character of the outer tube). The emission of the inner tubes (which were identified by electron diffraction and Raman spectroscopy) was red-shifted from that of corresponding SWNTs, due to electronic coupling and dielectric screening between the two tubes. This red-shift was dependent on the chirality of both tubes. Inverse transfer from the outer to the inner tube was only observed in one chirality combination (inner tube semi-conducting (14,1), outer tube metallic (15,12)). The previously observed PL from the inner tubes was attributed to the extraction of these from the DWNTs by pre-treatment steps, such as ultrasonication and ultracentrifugation.[137]

From these results, we can agree that PL spectroscopy is not as useful a method for DWNTs as for SWNTs, being limited to probing the outer layer of the former. The emission of the outer tube is also limited by the setup due to their high wavelengths (for example by the absorption of D_2O above 1600 nm).

1.8.3 Raman spectroscopy

Coupling of the vibrations between the two layers in DWNTs affects their frequency shifts, so DWNTs spectra cannot be considered as the sum of individual SWNTs.

In individual DWNTs, two low frequency modes are observed: in-phase and out of phase vibrations, called radial-breathing-like modes (RBLM). These are dependent not only on the tubes diameters, but also on the interlayer distance (that is, the mechanical coupling) and the relative chirality. These modes are up-shifted in relation to the individual corresponding SWNTs. For a constant interlayer distance, the modes are down-shifted for increased diameter (as for SWNTs). The out-of-phase RBLM also down-shifts with increasing interlayer distance (**Figure 27a**). [34,128,138,139]

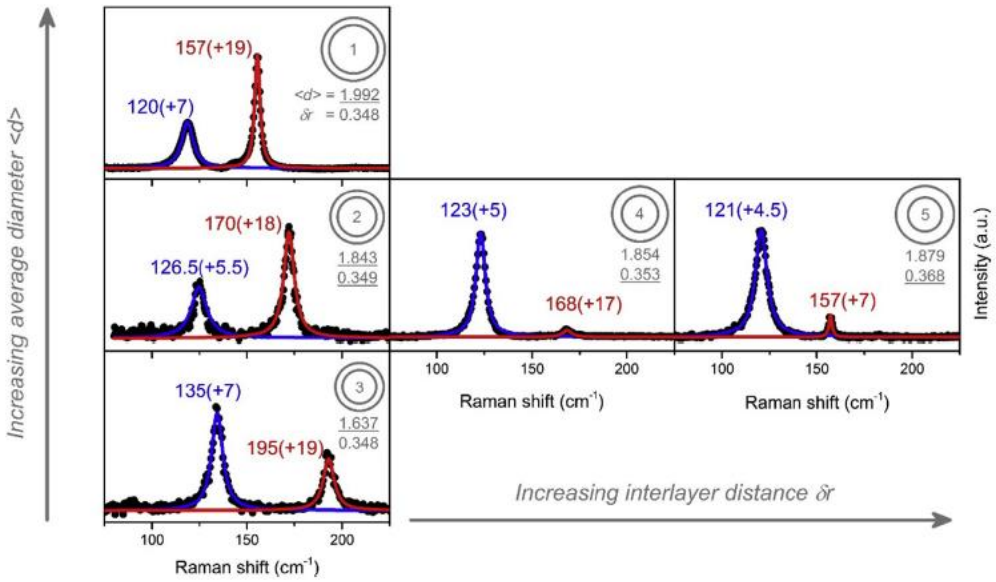

Figure 27: RBLM region of Raman spectra of different DWNTs. The vertical axis shows the dependence of RBLM with the diameter (keeping close inter-layer distances); The horizontal axis shows the variation of the interlayer distance for DWNTs with close average diameters[34]

In relation to the G modes, up to 4 peaks may be present in the Raman spectrum of DWNTs. The lineshapes follow the same criteria as for SWNTs. [34]

From theoretical[140] and experimental[34] results, it was shown that the G modes shift when comparing to those of the corresponding SWNTs. These shifts depend on the distance between the two layers of carbon nanotubes. When the distance is larger than the equilibrium distance (close to the interlayer distance between graphene layers in graphite), a negative pressure affects the inner tube, causing its expansion and a softening of its modes. A blue-shift is observed for small intertube distances. An opposite trend is observed for the outer layers.

Overall, changes in the vibration modes of the DWNTs compared to their corresponding SWNTs are weakly affected by the interlayer coupling between the both nanotubes and need to be taken into account when analyzing the spectra.

1.8.4 Charge transfer effects

The absorption spectra of the inner tubes are unchanged upon doping of DWNTs (for example, by thionyl chloride[135] (**Figure 28**) or ozone[17]) while the same treatment suppresses the E^{S}_{11} transition of SWNTs and attenuates or broadens the other transitions. The outer tubes are affected in the same way as SWNTs.

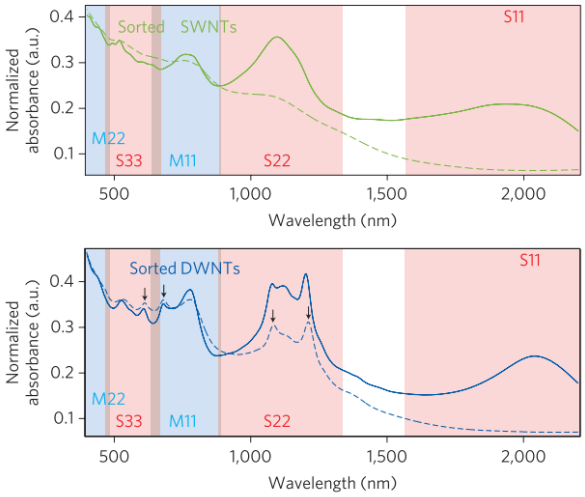

Figure 28: Optical absorption spectra of selected SWNTs (top) and selected DWNTs (bottom) before (continuous line) and after (dashed line) doping with thyonil chloride. [135]

Electrochemical doping was studied by Raman spectroscopy for DWNTs sorted by their outer wall electronic properties. Charge transfer between the tubes depended on the specific chirality, with the outer tube type determining the potential at which charge transfer occurs. The potential needed to observe it followed this trend: M@M < M@S < S@M < S@S with the notation outer @ inner. This happens because outer metallic tubes have a continuum of states that can be filled potential, while charge transfer from semi-conducting outer tubes requires a threshold potential corresponding to the E^S_{11} transition. In the same manner, metallic inner tubes accept charge transfer from any state of the outer tubes, while semi-conducting start to get doped only when potential reaches the value of the E^S_{11} transition (**Figure 29**).[141]

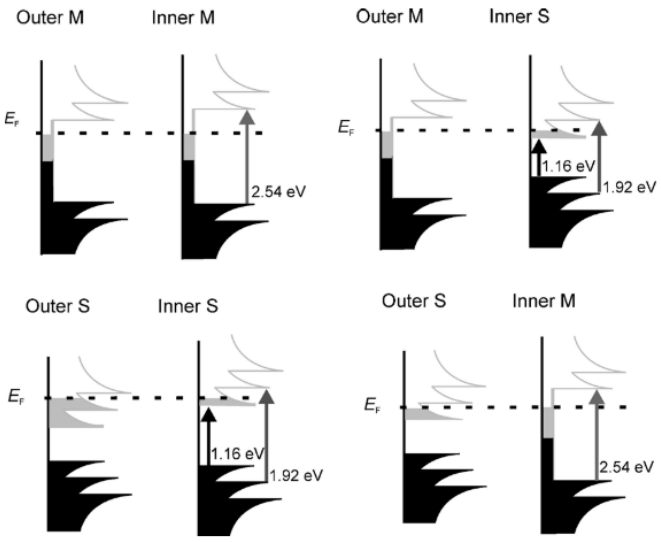

Figure 29: Schematic representation of the Fermi level shift (in gray) that must be obtained by application of an electrochemical potential for electron transfer from the outer to the inner tube. The arrows indicate the optical transitions probed in the cited study. [141]

In conclusion, charge transfer can happen between the two layers of DWNTs. Upon chemical doping the outer tubes are mostly affected while the inner tubes remain unchanged. This seems to be related to the relatively low doping potentials attained by this process, affecting mostly the low energy states of the outer tubes. On the other hand, the application of an electrochemical potential allows one to attain doping levels capable of affecting the optical transitions of the inner tubes due to the charge transfer from the outer tubes.

1.8.5 Non-covalent and covalent functionalization of DWNTs

Functionalization of DWNTs has been studied to check the effects of the functionalization of the outer tube on the properties of the inside tube. From first principles calculation, Lopez-Benzanilla found that the creation of sp^3 defects on the outer layer reduces the charge transport in both inner and outer tubes when they have a typical graphitic interlayer distance, but with no effects on the inner tubes if this distance is larger.[142]

Initial tests of functionalization of DWNTs indicate that the overall structure and properties of the inner tubes are not affected by functionalization. A high degree of fluorination for example causes the vanishing of the optical and Raman signals of the external tube while keeping those of the inner tube intact.[130,143] Similar results were obtained with functionalization with diazonium[144,145] and with ozone.[17]

Covalent functionalization with diazonium salts was used for probing the transport properties of both walls. Electronic conduction of the outer wall was completely lost after functionalization, but the inner tube properties remained intact (**Figure 30**). Field-effect transistors made with the functionalized DWNTs behave similarly to SWNTs ones, functionalization reducing conductivity but not suppressing it.[144,145] Sensors made from DWNTs presents an advantage over devices made from SWNTs, being capable of combining the selectivity of intact carbon nanotube sensors with the selectivity of chemically functionalized ones.[146]

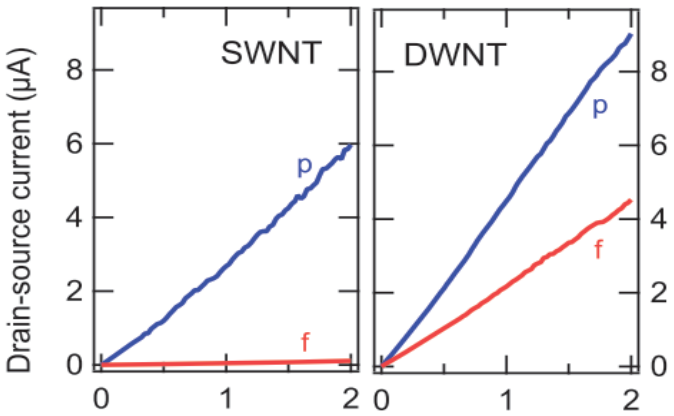

Figure 30: Electrical current as a function of drain voltage in devices made of pristine (p) and functionalized (f) SWNTs (left plot) and DWNTs (right plot).[144]

Most of the small molecule chemistry performed on DWNTs is similar to the one performed on SWNTs. Functionalization with dyes in particular was performed to study charge and energy transfer effects from the dye to the nanotube, in general happening only with the outer tube (for example, for perylenediimides,[147] porphyrins[10,148] and phtalocyanines[149]). An exception is the observation of photoelectron transfer from dimethylaminobenzene to the inner tubes of DWNTs.[150]

In conclusion, the structure of the inner tube remains intact upon chemical functionalization. The transport properties of these functionalized DWNTs are similar to those of non-functionalized SWNTs. This was shown to be especially useful in devices, as the sensitivity of the functionalized DWNT remains similar to that of unmodified SWNTs, but the functionalization allows the increase of the sensor selectivity. Energy transfer can occur between the two layers, but normally happens from the inner to the outer tube due to their band alignment.

2. Properties of poly(3-hexylthiophene) (P3HT)

2.1 Brief overview

Semiconducting polymers are the object of many studies due to their interesting optoelectronic properties. Among them, P3HT (structure in **Figure 31**) is one of the most studied due to its relatively easy and well described synthesis that allows good control of its chemical characteristics (low dispersity, control of molecular weight and chain ends, control of regioregularity), relative ease of scaling up, good solubility in common organic solvents (chloroform, tetrahydrofuran, orthodichlorobenzene, etc…) and relative good stability in air, making it widely available commercially. This makes P3HT one of the best

candidate for applications on organic electronic devices, such as organic field effect transistors (OFETs) and organic photovoltaics (OPV) .[151]

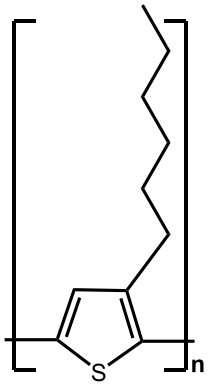

Figure 31: Chemical structure of P3HT

Electronic and optical properties of P3HT originate from the chemical structure of the polymer backbone. As the chain grows, delocalization of the π- and π* orbital wavefunctions delocalize over the chain. This reduces the optical gap defined by the electronic transition between these two orbitals, causing a red-shift of the observed spectrum (**Figure 32**).[151]

This electronic delocalization happens as long as all thiophene units remain in a single plan. However, as the chain grows the presence of defects (mislinkage or twists in the chain induced by thermal agitation) becomes more probable, and a maximum delocalization is attained. The length over which the electrons are delocalized is called effective conjugation length, which for P3HT in solution is estimated to be around 14 units.[152]

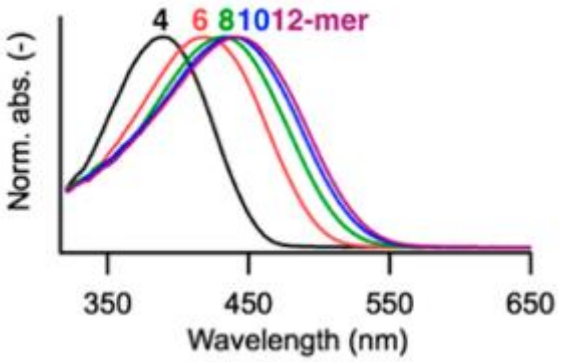

Figure 32: Optical absorption spectra of oligomers of 3-hexylthiophene of different lengths

Chain planarity depends on the solvent and is increased in solid state compared to that in solution.[151]

The presence of mislinkages in the polymer chain also breaks conjugation. Optimum electronic properties are attained for P3HT when monomer units are linked in what is called heat-to-tail (HT) configuration (**Figure 33**). This linkage reduces steric interactions between the polymer side-chains,

reducing deformation of the polymer backbone and thus increasing conjugation.[151,153,154] Thus, P3HT with majorly HT links is called a regioregular. Otherwise it is designated as regiorandom.

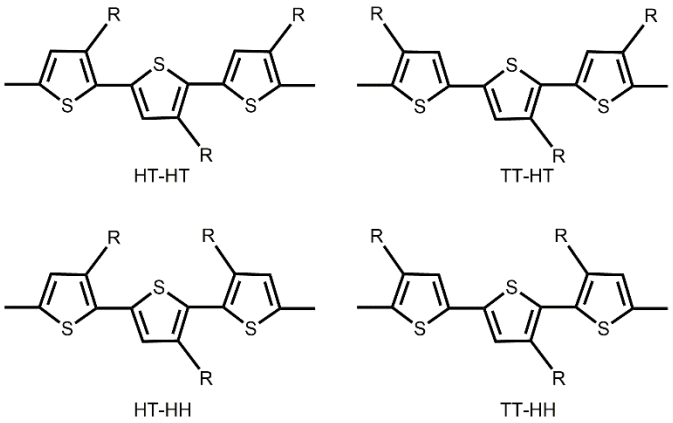

Figure 33: Triads demonstrating the possible monomer links. A P3HT (in which R = C_6H_{13}) is called regioregular when most of the units are linked in an HT configuration.

Electronic properties are also affected by the morphology of the polymer layer. The charge transport is more efficient in well-ordered crystalline domains. In the perfect case, 1D crystals growth due to π-π stacking interactions between the aromatic thiophene units.

Generally, P3HT aggregates in the form of nanofibers. The nanofiber axis (**b** axis), which may be few μm long, is originated by the π-π stacking of the polymers. In such a structure, both polymer back bones and side chains are perpendicular to the b axis. The height of the fibers contains only few P3HT layers (along the **a** axis). Their width (along the **c** axis) grows linearly with the molecular weight, up to around 10 kg/mol, above which chain folding occurs. (**Figure 34a**).[151,155] A perfect morphology cannot be obtained however, as the rigidity of the chains and the presence of flexible side chains lead to the formation of amorphous regions between crystalline domains, which contains chain ends, chain folds and tie-polymer chains

The crystalline domains of P3HT may organize in two possible structural cells, called form I and form II (**Figure 34b**), which differ in the side chain packing.[151] Single crystals can be obtained only in the second form, mainly because the larger interdigitation of the alkyl chains in this form leads to a lower internal energy than form I.[156]

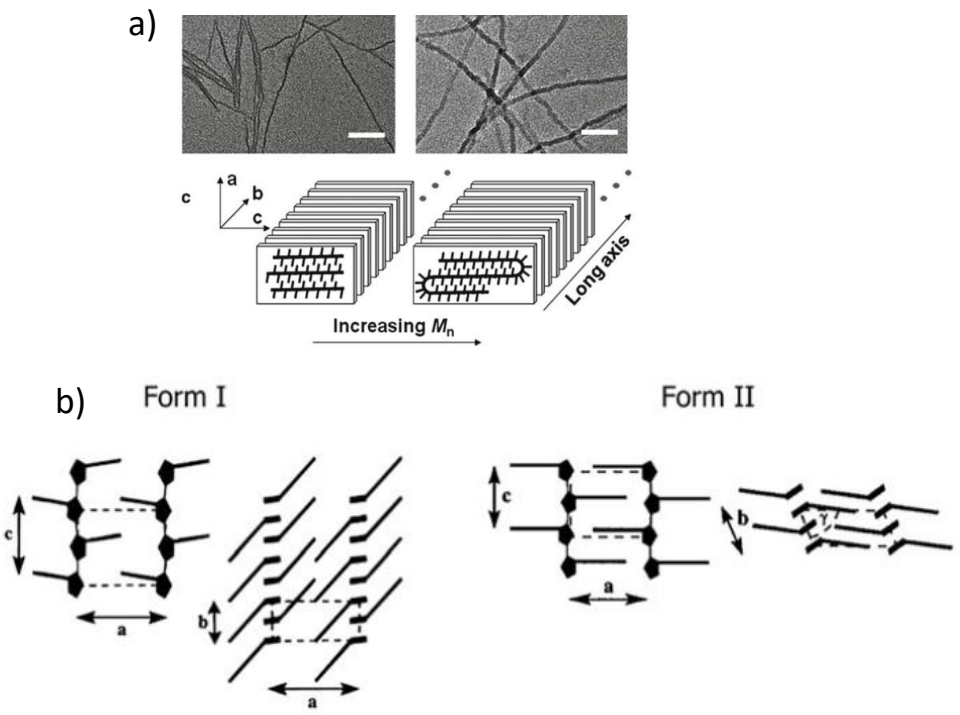

Figure 34: a) TEM images of nanofibers of P3HT of different molecular weights and the corresponding schematic arrangement of polymer chains in the fibers; [151] *b) Crystal structure of both forms of P3HT.*[151]

For device application, a P3HT film is usually formed through deposition from solution. The deposited chains usually adopt two orientations relative to the substrate: edge-on, with π-staking parallel to the surface of the substrate; and face-on, with π-staking perpendicular to surface of the substrate (**Figure 35**).A third form, flat-on or chain standing, is rare, happening only in specific conditions.[157] The edge-on chains are generally formed, but face-on can be obtained under rapid drying conditions.[151] Faster charge transport occurs in the chain axis and the π-staking axis, making edge-on orientation adapted for OFET devices (high in-plane charge transport), with field effect mobility more than one hundred times higher than that for face-on films. On the other hand, face-on configuration is more adapted for OPV devices.[151,158]

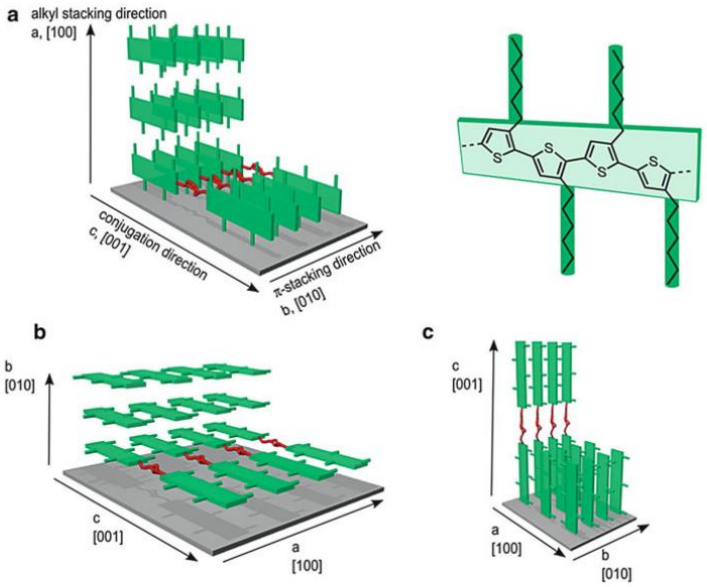

Figure 35: Molecular orientation of P3HT in thin layers deposited on a substrate. a) Edge-on; b) Face-on; c) Flat-on[151]

The extended polymer backbone promotes anisotropic light absorption and charge transport. Charge transport is affected by the extension of the π-conjugation, intermolecular interactions and finally the morphology of the system. In relation to the molecular weight, passing from 4 to 36 kg/mol increases charge carrier mobility from 10^{-6} to 10^{-2} cm^2/Vs. Chain mobility is mainly limited by the amorphous matrix. For P3HT of high molecular weight, the long chains can tie the boundaries between grains (tie chains), increasing the conductivity, despite the overall less crystallinity. Saturation is reached for high molecular weights, where defects in the crystalline structure compensates the increase in the fraction of tie-chains.[151,155,159–161]

More details on the different P3HT morphologies and crystalline structures can be found in the literature.[151,155,162]

An introduction to the concept of H and J-type aggregates will be given in **Chapter 2.2**, which relates the degree of chain ordering to the optical spectra of the polymer and thus to its electronic properties. In **Chapter 2.3**, some strategies for increasing the chain ordering will be given.

2.2 Introduction to Spano's model

Absorption and emission spectra of aggregated P3HT chains are generally made of several bands. These bands correspond to allowed optical transitions from the electronic ground state to upper electronic excited states originated by coulomb interaction between neighboring chromophores and by the coupling with vibrational modes in the absorption spectra. In the emission spectra, they are due to the

recombination of the excitation from the lowest electronic excited state to the vibrational modes of the ground state. These features in the spectra depend on both interchain interaction and intrachain conformation.

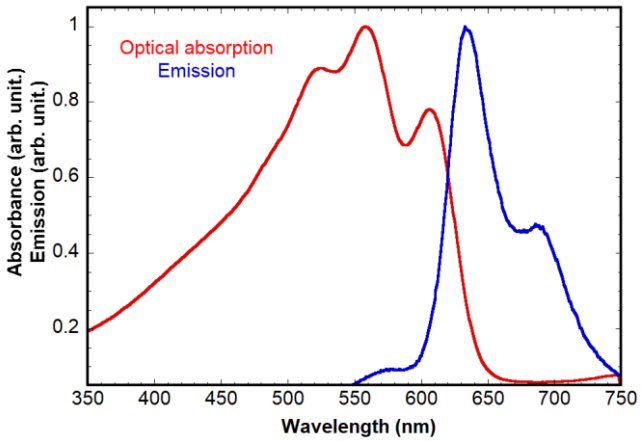

Figure 36: Normalized optical absorption and emission spectra (excitation 520 nm) of P3HT aggregates obtained by cooling a solution in THF

The model developed by Spano and coworkers in a series of papers[163–169] allows for interpreting absorption and emission spectra in regard to the relative effects of interchain aggregation and intrachain conformation. This model comes from the theory of excitonic coupling first developed by Kasha and coworkers[170,171] for aggregates of relatively small molecules, translated into a semi-classical vector model for the electrostatic interaction between transition dipole moments.

For an asymmetric chromophore, the electron distribution leads to a dipole moment (polarization vector) given by $\sum \mathbf{r}_i$ ($\mathbf{r}_i$ is the position of electron i in the molecule). Upon excitation, the transition between the ground state $|g\rangle$ (S_0) and the excited one $|e\rangle$ (oS_1) defines the transition dipole moment of the molecule (**Equation 1**)

$$\boldsymbol{\mu} = \langle e|\sum \mathbf{r}_i|g\rangle \qquad (1)$$

The electronic structure of a dimer of non-interacting molecules is made of two degenerated localized excited states. The intermolecular coulomb interaction between the transition dipole moments lifts the degeneracy leading to the formation of two delocalized excited states (excitons), linear symmetric and anti-symmetric combinations of the two localized excited states, separated by $2|J_0|$, with J_0 defined **in Equation 2**.

$$J_0 = ((\boldsymbol{\mu}_1.\boldsymbol{\mu}_2)-3(\boldsymbol{\mu}_1.\mathbf{r}).(\boldsymbol{\mu}_2.\mathbf{r})) / 4\pi\varepsilon R^3 = \mu^2(3\cos^2\theta - 1)/ 4\pi\varepsilon R^3 \qquad (2)$$

Where **μ**1 and **μ**2 are the dipole moments corresponding to the |g> →|e> ($S_0 \rightarrow S_1$) transition of molecules "1" and "2", respectively, **R** =R**r** is the displacement vector connecting the molecular mass centers, and ε is the dielectric constant of the medium (**Figure 37a**).

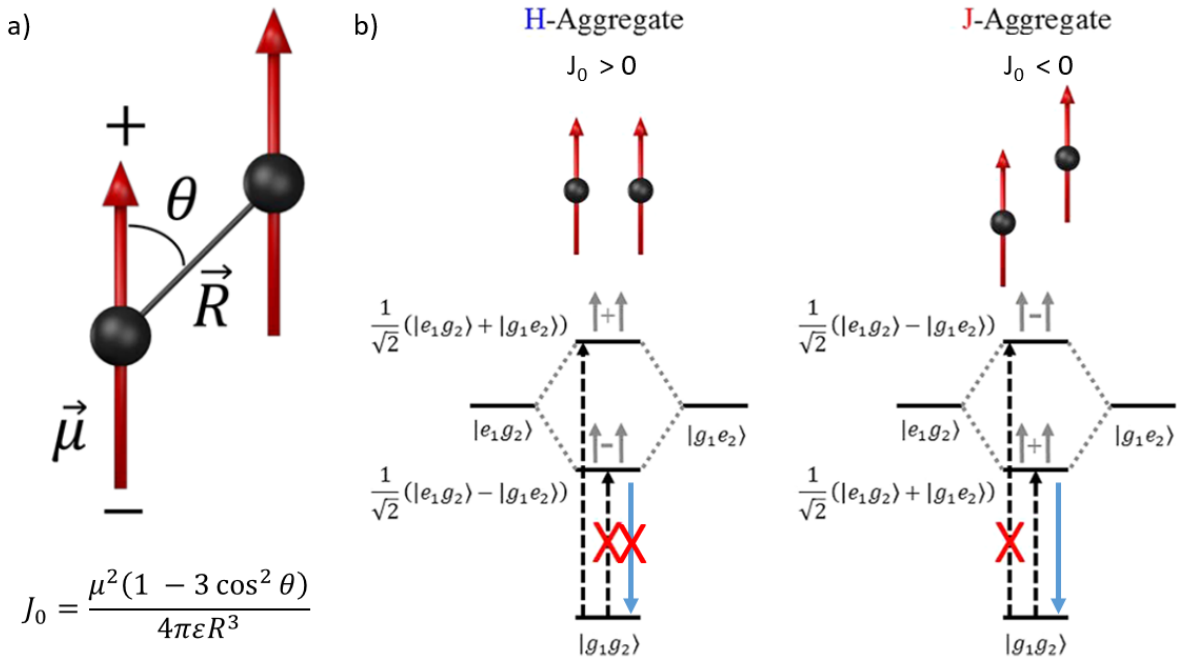

Figure 37: a) Relative orientation of transition dipole moments defining a J-aggregate ($\theta < \theta_M$) and H-aggregate ($\theta_M < \theta < \pi/2$). The magic angle θ_M is 54.7 degrees; b) Energy level diagram for H- and J-dimers. For H-aggregates absorption is allowed only to the top state and emission is forbidden. For J-aggregates absorption and emission are allowed from the bottom excited state.

The energy of the symmetric state is shifted by J_0 with respect to the excited state of the monomer, the one of the anti-symmetric state by $-J_0$.

To deduce the selection rule for light absorption, one must take the vector sum of the transition dipoles for the given exciton state. It naturally turns out that only in-phase arrangements of dipoles give allowed exciton states, which is necessary, since the wavelength of the light used for electronic excitation of molecules is much greater than molecular dimensions of ordinary molecules. Thus, in the symmetric state, the transition dipole moments are in-phase and the transitions from the ground state allowed. In the anti-symmetric state, the transition dipole moments cancel and the transitions from the ground state forbidden, and, as a consequence, excitation recombination from the anti-symmetric state is non radiative

If $J_0 > 0$, transitions occur to the upper excited state, the aggregate is called H-aggregate (from the hypsochromic shift from the excited state of the monomer). If $J_0 < 0$, transitions occur to the lower excited state, the aggregate is called J-aggregate, referring to the work of E.E. Jelley,[172] who observed

bathochromic shift in the aggregates in his works. For H-dimers, this simple two molecule description results in a blue-shift of the absorption spectrum (compared to the single molecule case), with non-radiative exciton recombination. For J-aggregates, the absorption is red-shifted and exciton recombination is emissive.

For many π-conjugated chromophores, the dipole-allowed $S_0 \rightarrow S_1$ electronic transition is strongly coupled to the C=C vibrational mode (vinylic stretch). In the two molecules description, it results that some otherwise forbidden emissive recombination of the exciton become allowed due to this coupling to the vibrational modes, as shown in **Figure 38**.

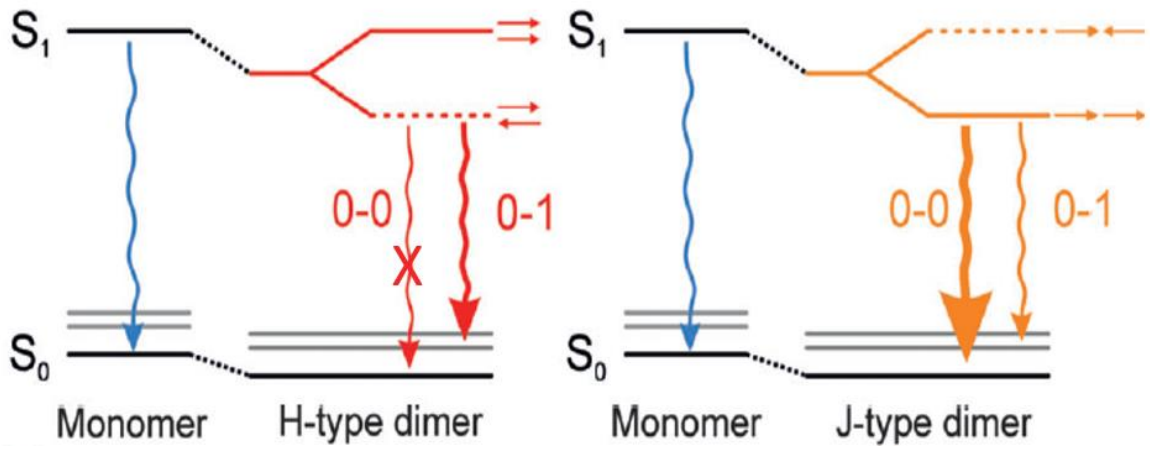

Figure 38: H- and J- type coupling for molecular dimers, showing the first vibrational levels of the ground state. The energy of the dimer states is lower than that of an individual molecule due to Van der Waals stabilization. The thickness of the arrows represents the relative emissivity from the lowest excited state to the first vibrational level. Adapted from [173]

Considering the case of N non-interacting molecules, the electronic structure is made of N degenerated excited levels. After the electrostatic perturbation caused by the intermolecular dipole-dipole interaction of transition dipoles, an exciton band of N discrete exciton states is produced with a band width of $2J_0$. In the case of conjugated polymers, there is a strong coupling between the optical transition and the ring stretching mode around 1400 cm^{-1}, which increases the complexity of the spectra by involving vibronic transitions. The final lineshape of the spectra depends on the strength of the exciton coupling J_0. If the coupling is weaker than the separation between the vibrational levels, we may see different vibronic peaks in the absorption spectra (top of **Figure 39**); if coupling is larger than this separation, we observe only one absorption peak (bottom of **Figure** 39).[166,168]

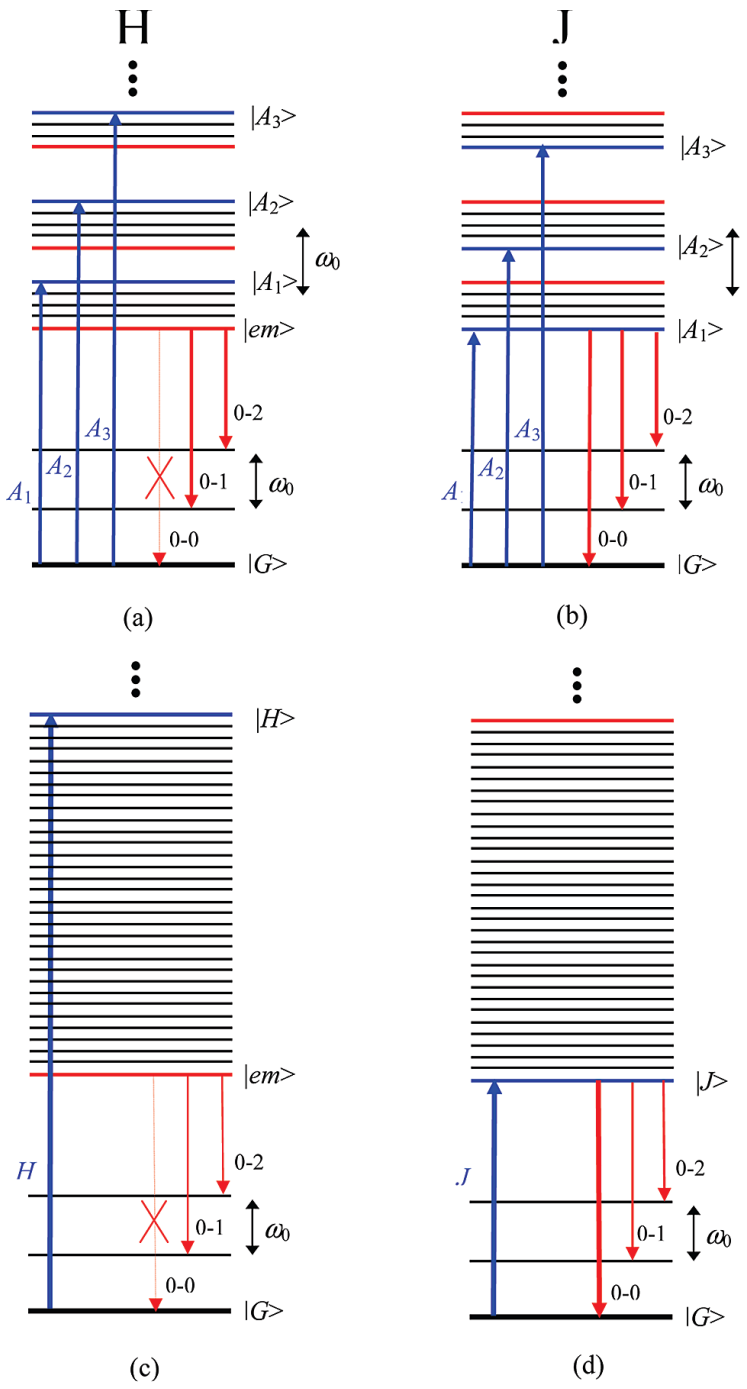

Figure 39: Energy level diagrams depicting absorption (blue arrows) and emission (red arrows) in ideal H- and J-aggregates in the weak exciton coupling regime (a,b) and the strong exciton coupling regime (c,d).

In the case of conjugated polymers, the two types of aggregation (J-type intrachain aggregation, and H-type interchain aggregation) compete. The interplay between both types of interactions defines the photophysical properties of the polymer (**Figure 40a** and **b**). The study is complicated by the fact that aggregation causes chain planarization in relation to the melt/solution state, inducing a red-shift on the optical properties. Because of this, spectral shifts are not enough for defining the dominant behavior in these materials.

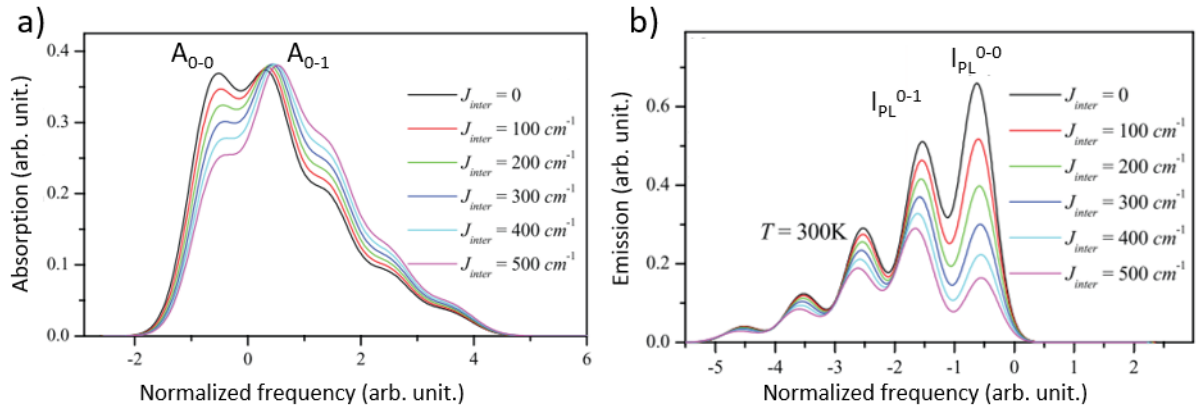

Figure 40: Calculated a) absorption and b) PL spectra of a polymer aggregate with a fixed intra-chain coupling strength (J_{intra}) for increasing value of inter-chain coupling strength (J_{inter}). The ratios of $A_{0\text{-}0}/A_{0\text{-}1}$ and $I^{PL}{}_{0\text{-}0}/I^{PL}{}_{0\text{-}1}$ transitions decrease with increasing interchain coupling. Adapted from [164].

The model developed by Spano and coworkers[163,164] introduces a way to the use of spectroscopic features to estimate the chain conformation and the corresponding exciton coupling strength. For a given polymer, considering similar interchain ordering, it is shown that an increase in conjugation length causes a decrease in interchain exciton coupling, increasing J-type like behavior.[174] This exciton coupling can be estimated from the ratios $A_{0\text{-}0}/A_{0\text{-}1}$ and $I_{PL}{}^{0\text{-}0}/I_{PL}{}^{0\text{-}1}$.

This model shows that generally P3HT behaves as a weakly-coupled H-aggregate (coupling of lower energy than the separation between vibrational levels), so its spectra are characterized by a series of vibronic bands. In this case, the ratio $A_{0\text{-}0}/A_{0\text{-}1}$ is less than 1 and decreases when intrachain order (conjugation length) decreases. In the PL spectra at room temperature, the ratio $I_{PL}{}^{0\text{-}0}/I_{PL}{}^{0\text{-}1}$ also decreases when intrachain order increases. We will use these results when interpreting the obtained spectra for our nanohybrids, comparing the degrees of intrachain order based on the spectral features of our systems.

2.3 Obtaining high ordering of P3HT: homogeneous and heterogeneous nucleation

As commented above, obtaining a highly ordered structure for P3HT and other semiconducting polymers can be quite difficult due to the rigidity of the backbone and entanglements in more concentrated solutions, meaning that a high potential barrier needs to be overcome for conformation changes.[155]

At this point it is important to distinguish two similar concepts that will be used in the following: crystallinity and aggregation. Crystallinity is a long range structural ordering of the polymer chains. Aggregation, in the present manuscript, means a low range ordering of polymer chains, in theory requiring only two interacting polymer chains (or a single folded one, the folding being a defect that

decouples the electronic states of the two linked oligomers). Larger aggregates in a highly ordered state may be equivalent to a crystal.[173]

2.3.1 Crystals of P3HT

When we talk about crystallinity in P3HT, we normally talk about the crystalline domains on the semi-crystalline films obtained by deposition on a substrate. These domains, organized in form I, are usually small and are not isolable.[151]

Self-seeding is one method to obtain P3HT single crystals. This technique is based on thermal treatment and leads to crystals of P3HT in form II.[175] Single crystals of this form displays remarkable optical properties comparing to the usual form I obtained in thin films (**Figure 41**). This is explained as due to the chain being in a fully extended configuration, maximizing intra-chain order.

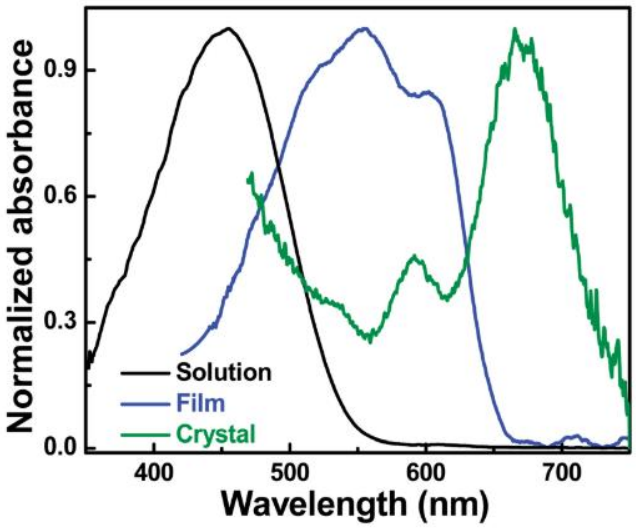

Figure 41: Normalized optical absorption spectrum of P3HT in solution in 3-hexylthiophene, of a spin-cast thin film (blue) and of a single crystal (green).[176]

2.3.2 Aggregates of P3HT

One way to obtain P3HT aggregates is by cooling a solution of free polymer. In solution, absorption and emission peaks are similar to those observed in the melt, in which we observe a coiled state characterized by torsional defects along the polymer chain. In this state, spectral features change with temperature as with other conjugated polymers – a decrease in temperature causes the increase in conjugation length

(by reducing thermal defects on the chain), thus increasing oscillator strength and red-shifting the absorption maximum.[177,178]

Below a given temperature an order-disorder transition occurs. The temperature at which this happens depends on the chain length: the longer the chain, the higher the temperature of transition (**Figure 42**). This transition is characterized by the formation of weakly interacting H-type aggregates.[178]

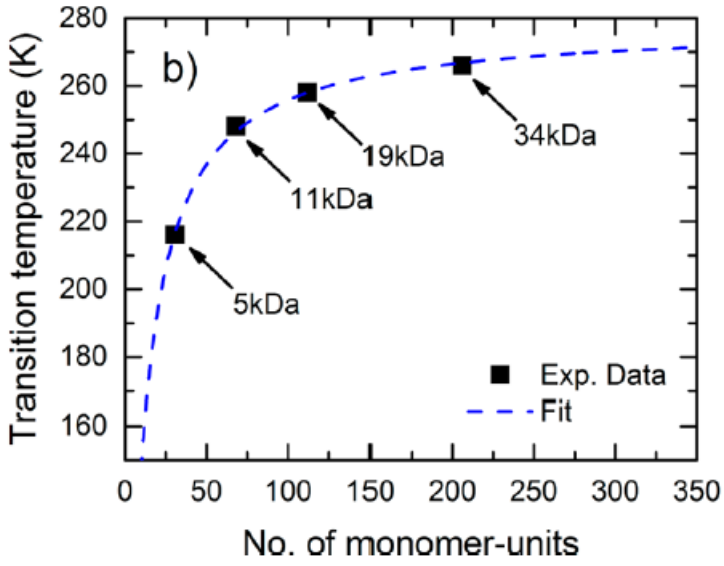

Figure 42: Dependence of the order-disorder transition temperature of P3HT in THF as a function of the number of monomer units[178]

Another way is to form thin films obtained by drying a solution of free P3HT. In this case, H-type aggregates are usually observed (**Figure 43a**). Slowing down the aggregation process, such as evaporation from a solvent of high boiling point[163] or vapor phase annealing[155], allows for reducing the number of defects and increases intra-chain order.[167] Higher intrachain order has been correlated to better mobility and performance in OFET devices.[163,174,179,180]

First J-like aggregates were obtained by slowly cooling a solution of P3HT of high molecular weight in toluene (**Figure 43b**). [181] This slow cooling allows for fractionation of chain lengths, reducing the disorder of the formed fibers. These J-like aggregates present a slightly modified crystalline structure of form I, with more compacted chains and more planar chains. [181,182]

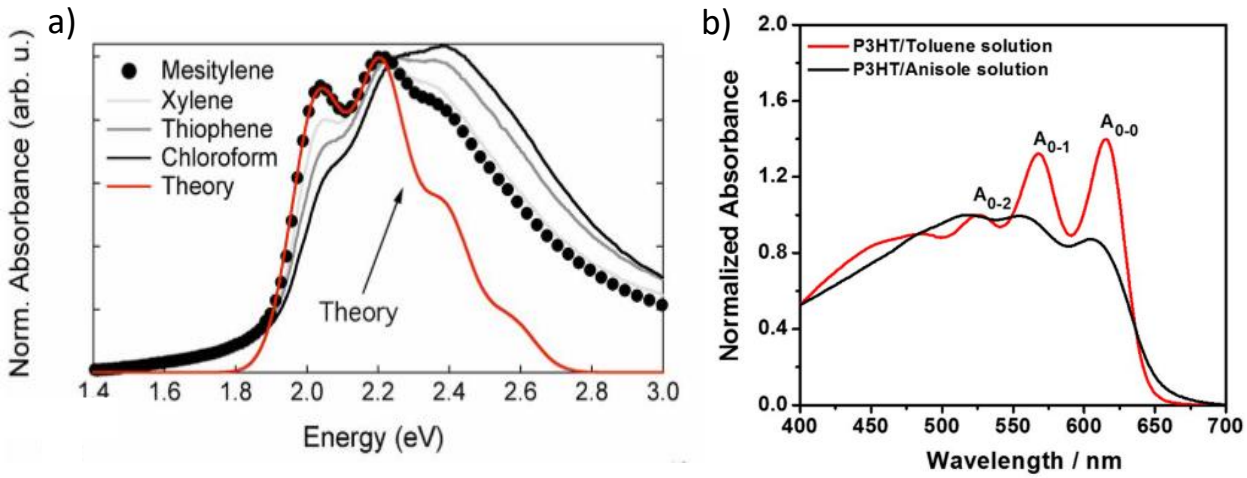

Figure 43: a) Absorption spectra of P3HT thin films obtained from d. The red curve corresponds to a theoretical curve obtained from H-aggregate theory[163] *b) UV-Vis absorption spectra normalized at the A_{0-2} absorption feature for suspensions of P3HT aggregates formed in toluene and anisole*[182]

More recently, ultrasonication[183] ,light pulsing[184], crystallization in solvent interfaces[180,185] and slow cooling of solution of other solvents[179] also allowed obtaining of these structures.

Besides homogeneous nucleation, diverse methods of heterogeneous nucleation can be used to improve the ordering of P3HT. Carbon nanotubes with different number of walls are known to nucleate P3HT in a marginal solvent, such as decalin and anisole. The resulting structures are "shish-kebab" where CNT play the role of the "shish" (**Figure 44**).[70,71] This aggregation is said to happen because of the hexagonal aromatic structure of carbon nanotubes and is observed also in boron nitride nanotubes.[186] Nanowires and nanoribbons of P3HT can grow in any kind of graphitic structure.[187]

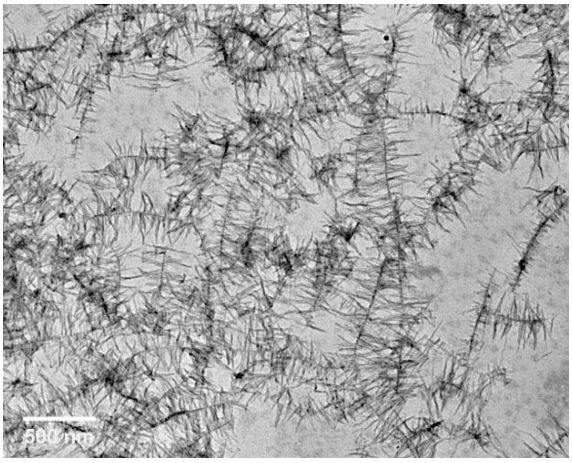

Figure 44: TEM image of a shish-kebab structures obtained by adding SWNTs onto P3HT in solution in anisole.

These shish-kebab nanostructures can also be formed around organogelators as perylene tetracarboxydiimide (PDI), [188,189] a sorbitol derivative [190,191] and fibrillary structures of highly self-assembled polypeptides.[192]

Chapter 2: Synthesis of copolymer and elaboration of nanohybrids

The present chapter describes all the experimental synthetic procedures, from the synthesis procedure for obtaining poly(3-hexylthiophene) (P3HT) and its derivative copolymer (PHTcoAHT) to the elaboration of the nanohybrids (non-covalent and covalent).

The synthetic route for obtaining P3HT is not new, so a brief bibliographic review on the synthetic procedure is described in **Section 1.1**. The synthesis of the copolymer follows (**Section 1.2**), and the list of the synthesized homo- and copolymers used for understanding the physico-chemical and optoelectronic properties of the obtained nanohybrids is given (1.3). The CNTs used in this work are then briefly described (**Section 2**). In **Section 3**, we report two routes for the elaboration of the non-covalent nanohybrids. A first one allows one to get nearly pure suspension of nanohybrids by solvent extraction (**Section 3.1**). However, as this method works only for two macromolecules of comparable length and only SWNTS, a second one, more crude, allowing the formation of nanohybrids whatever the macromolecule and type of CNTs is given (**Section 3.2**). The main advantages of this second route is that it allows for good reproducibility and a better control of the total quantities of material in the ending solution. Lastly, the synthesis of the covalent nanohybrids is presented in **Section 4**.

Once the copolymer was obtained, two types of nanohybrids were synthesized with the carbon nanotubes of different number of walls. Only the synthetic procedures and a brief overview is given in this chapter, with more details on the physico-chemical properties of the obtained nanohybrids given in **Chapter 3**.

1. Synthesis of poly(3-hexylthiophene) and derivate copolymers (P3HT and PHTcoAHT)

The copolymers we targeted (PHTcoAHT) have a P3HT backbone with a controlled fraction of the hexyl side chains functionalized with aniline groups at their end. The aniline group can react with the CNTs by Tour's reaction:[104] the aniline is converted *in situ* to its diazonium, which alkylates the CNTs (**Scheme 1**). The synthetic pathway was designed also good regioregularity and control of the polymer molecular weight.

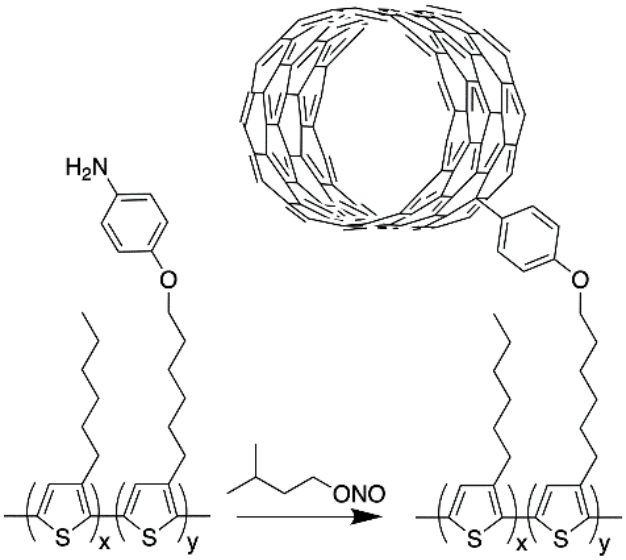

Scheme 1: Reaction pathway for the functionalization of nanotubes with PHTcoAHT

Unmodified P3HT of different molecular weights were also synthesized for comparison with the systems obtained with the copolymer.

A brief description of the syntheis and the obtained polymers and copolymers is described in the following. Details of the synthesis can be found in **Annex 1**.

1.1 Synthesis of P3HT – General mechanism

Polythiophene is a conjugated polymer first obtained through electrochemical synthesis. Although presenting interesting electronic properties, this material is insoluble in all common solvents and non-meltable, severally limiting its applicability. This is solved by adding alkyl chains to the thiophene rings, achieving solubility in common organic solvents for chains longer than butyl.[193–195]

For these alkyl substituted polythiophenes (P3ATs), the linking of the monomers is especially important in defining its properties. It has been shown that a high fraction of connections of HT-HT type (*head-to-tail-head-to-tail*, meaning the polymer is regioregular – see **Figure 45**) results in better electronic properties (for example, conductivity of a regioregular film can be more than a hundred times higher than that of a regiorandom one[154,196]). The reason for this is that HT links avoid steric hindrance between alkyl chains, increasing chain planarity and thus conjugation length. HH coupling on the other hand increases torsional angle and destroys conjugation.[151,153,154]

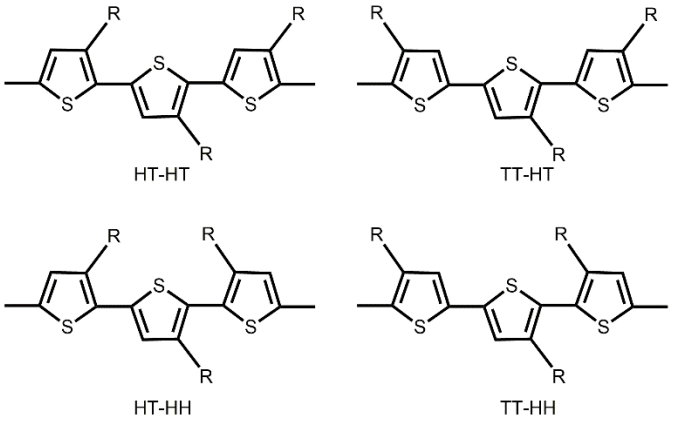

Figure 45: Possible triads for P3HT polymerization

Historically, synthesis of polythiophenes was performed by oxidative methods (through addition of $FeCl_3$)[193] or electrochemical methods, being still used today for specific applications. Oxidative polymerization can result in relatively high HT linkages when controlling the amount of catalyst added (slow addition resulting in up to 94 % regioregularity).[196,197] Usually the values of the regioregularity are between 50-60 % though, reproducibility is low, a good control of molecular weights is difficult, dispersities varying between 1.3 and 5.[195]

The first reliable syntheses of regioregular P3ATs came with catalytic methods starting from 2,5-dihalogen-3ATs. Addition of activated zinc[198] or a Grignard compound[153,154] followed by a nickel catalyst resulted in regioregularities higher than 90 %. This second method is today known as Kumada Catalyst Transfer Polymerization (KCTP or Grignard Metathesis (GRIM) Polymerization. It increased regioregularity (higher than 98 %) and gives a good control of the molecular weight and low dispersity (Đ).[199,200] This control is related to the fact that thiophene is an electron-rich monomer, resulting in a good association between the growing chain and the nickel catalyst, avoiding termination and keeping the growing chains "alive".[199,200]

The mechanism for the KCTP was first thought to proceed by a step growth mechanism.[199,200] However, studies by McCullough[201,202] and Yokozawa groups[203,204] have resulted in the currently accepted quasi-living chain growth mechanism.

The mechanism starts with a transmetallation reaction on the magnesium chloride in position 5 of the thiophene (preferably metallated by the Grignard compound because of steric hindrance on position 2, which also inhibits their addition during the polymerization step – this is further affected by a stabilizing effect of the alkyl chains[205]) and further coupling with another monomer in a tail-to-tail fashion. This means that all polythiophene chains always have at least one TT coupling. The nickel-catalyst is reduced in this step and can then combine with this dimer through oxidative addition, which is the first reaction of a catalytic cycle including a transmetallation and reductive elimination, as can be seen in **Scheme 2**.[159] The catalyst has been shown to be able to move randomly inside the chain during propagation (so

the TT defect is not necessarily found on the chain end, although it is mostly the case). This ring walking is necessary during the polymerization, as it enables migration to the chain end.[206–208]

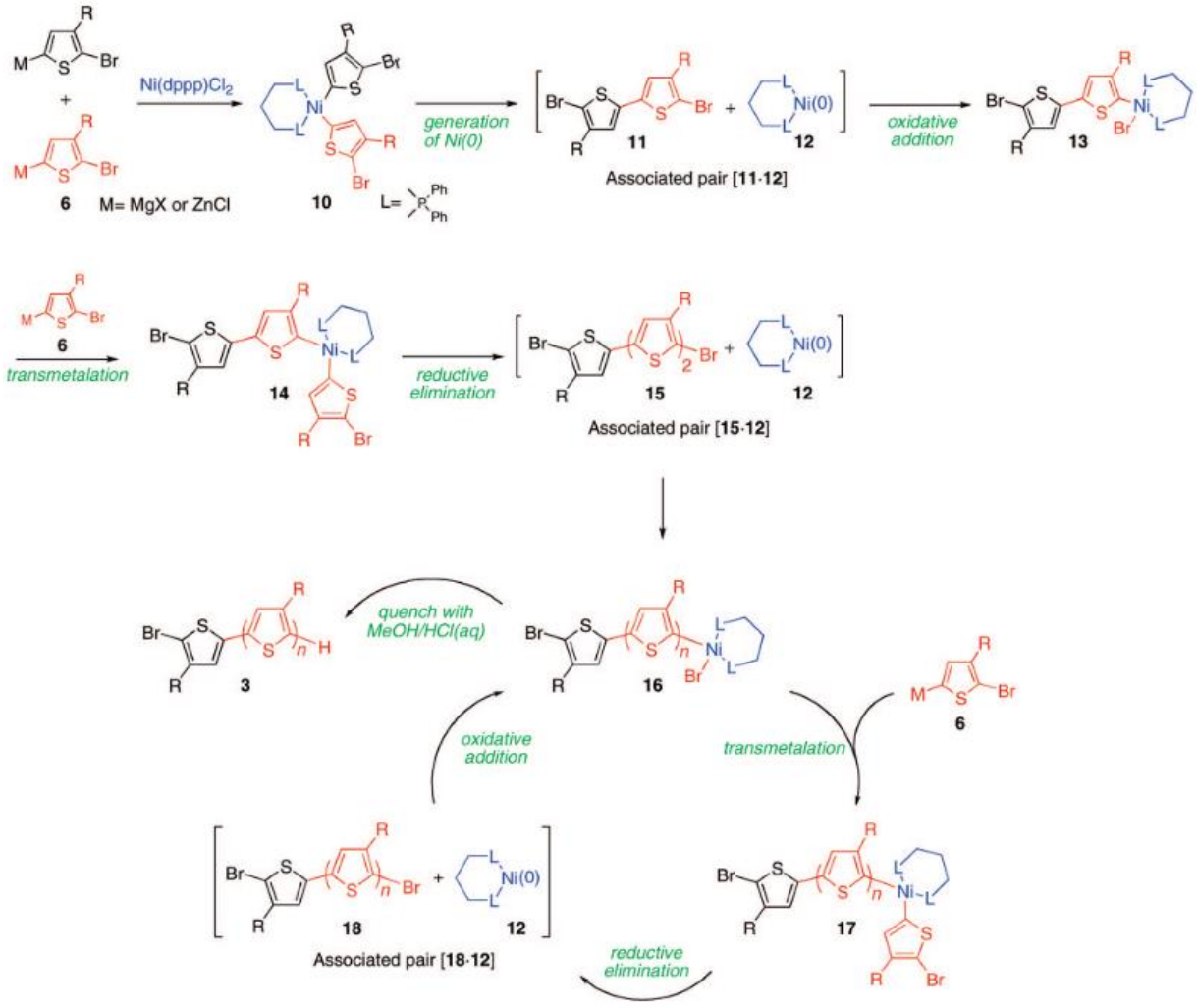

Scheme 2: Mechanism of P3HT polymerization[159]

Chain end and molecular weight control is affected by non-stoichiometric Grignard compound addition. The mechanism described above results in H/Br ending for P3HT upon quenching with a proton source. If there is starting Grignard compound (RMgCl) in the mixture, H/H and H/R endings are also observed, whose ratio increases with reaction time. This excess can also cause termination, increasing the dispersity.[209]

1.2 Synthesis of the copolymer PHTcoAHT

The targeted copolymers were synthesized by GRIM polymerization. Attempts to copolymerize hexylthiophene with monomers bearing an aniline side groups failed, even when aniline was protected.

Therefore, we synthesized a brominated copolymer that was transformed in aniline derivatives in afterward (**Scheme 3**).[210,211]

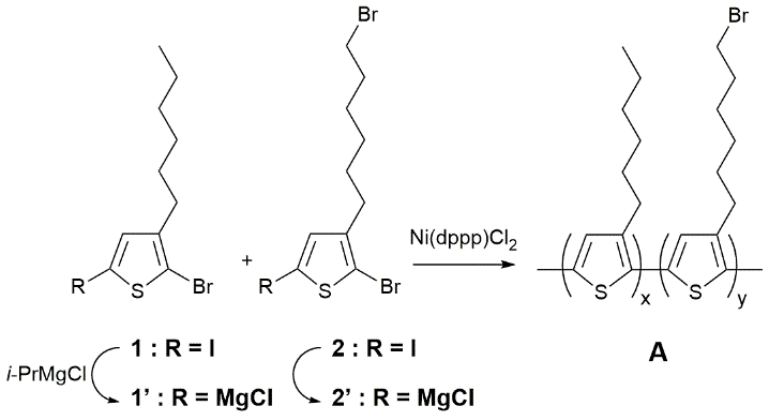

Scheme 3: Polymerization of monomers 1 and 2 into our functionalized copolymer precursor

Alkylthiophene monomers bearing a bromine at the end of the side chains have been successfully polymerized by this method. As expected, no side reaction occurs at the bromide of the side chains.[210,211] and the resulting copolymer is statistical.[212] We have copolymerized the 5-iodo 2-bromo monomers **1** and **2**. Their structures differ only by the bromine on the end of side chain. The iodo group in position 5 enhances regioregularity being more reactive towards metalation, increasing regioregularity of the final product.[213]

For initial tests we fixed the molar proportion of 2 at 15%. This should lead at maximum to a few covalent links per thousand SWNT carbon atoms (distance between defects corresponding to 2.5 nm estimated from the size of thiophene oligomers[214], a nanotube of diameter equal to 1 nm having 120 C atoms/nm).

Before the polymerization itself, **1** and **2** are metallated by the exchange of iodine with i-PrMgCl to yield the monomers **1'** and **2'**. We have measured the conversion rate of this step by the method described by Catala.[213,215] After metallation, an aliquot of the solution was quenched with CD_3OD and observed by NMR. The alcoholysis of **1'** and **2'** forms the corresponding compounds deuterated in position 5, identified by a singlet at 6.78 ppm. Beside this major compound, the NMR spectra also show unreacted **1** or **2** (singlet at 6.95 ppm), and 3-alkyl-2-bromothiophene (doublet at 7.17 ppm) coming from the hydrolysis of **1'** or **2'** by protonated impurities in the reaction medium (**Figure 46**). This analysis provides the rate of active monomer (ca 90 %), and the required amount of catalyst for the targeted degree of polymerization. It also proves that the bromide on the side chain is not affected by the organomagnesium and that metallation takes place only at position 5.

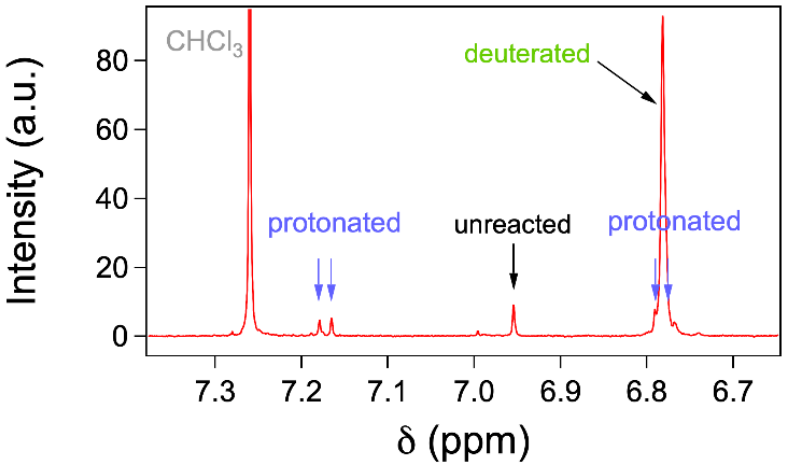

Figure 46: NMR analysis of the mixtures of monomers. The monomers are metallated with i-PrMgCl. The observed aliquot has been hydrolyzed by CD_3OD.

The regioregularity of the copolymer was estimated by comparing the intensity of the signals of the proton 4 of the thiophene, according to the assignment of the literature[153,198,216]. Especially, the signal for the proton thiophene at 6.97 ppm, assigned to HT-HT triads, represents more than 99% of the signal.

Copolymerization was conducted with different feed rates of **2** (5%, 16% and 25%) for checking the monomer distribution along the chain. At a conversion rate < 10% (determined by optical spectroscopy – **Figure 47a**), a sample was taken from the reaction medium, hydrolyzed with CD_3OD, precipitated in cyclohexane and analyzed by NMR. We determined that the molar fraction of units **2** in the polymer follows the feed ratio (**Figure 47b**), showing that the comonomers have close reactivities and yield random copolymers.

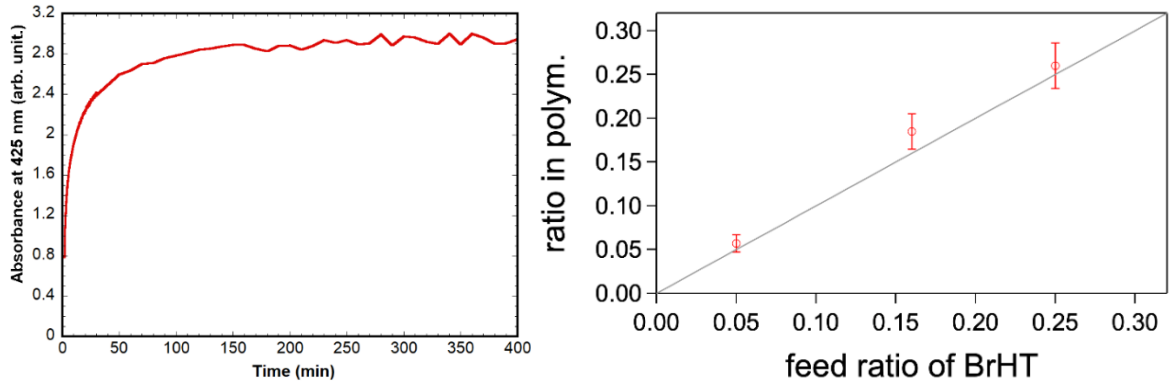

Figure 47: a) Kinetics of polymerization of P3HT followed by its optical absorption at 425 nm; b) Molar fraction of monomer 2 in the polymer vs molar fraction of the monomer 2 in the feed.

Our first results showed a bimodal SEC profile for some of the synthesized polymers (**Figure 48**). We determined it is a result from our quenching, which promoted chain-chain coupling. More acidic conditions (replacement of methanol by HCl 5 M) were capable to solve this issue, as already described in the literature.[209] This problem is less sensible for high molecular weights; as longer chains reduce the

probability of chain-end encounters.[199,207,209] We observed a lower dispersity notably for our synthesized P3DDT.

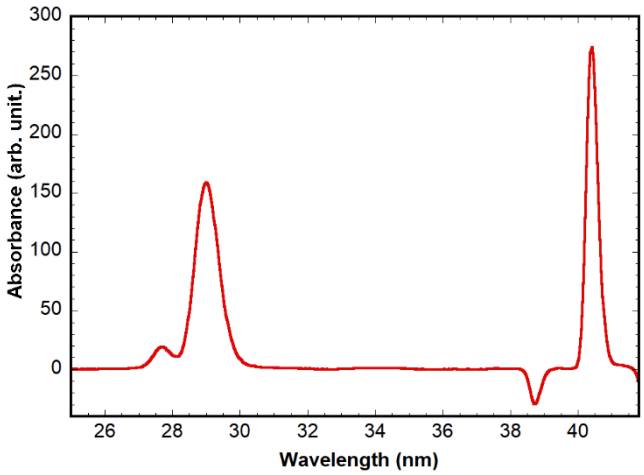

Figure 48: Example of a bimodal SEC profile

In the precursor brominated copolymer, the bromide was substituted by *p*-hydroxyaniline protected as its diphenylmethylenimine (copolymer B in **Scheme 4**). This functionalization yield is higher than 98 % under phase transfer catalyst conditions. The rate of substitution of the bromine was estimated by NMR (**Figure 49**) by the comparison of the integrals of the CH_2O protons at 3.87 and the residual integral at 3.43 ppm (shift of the CH_2Br protons). The imine could not be hydrolyzed by acid catalysis in H_2O/THF mixture because it led to phase separations during the reaction. Therefore, the aniline was deprotected by aminolysis with hydroxylamine yielding the reacting copolymer PHTcoAHT (**Scheme 4**).[217,218]

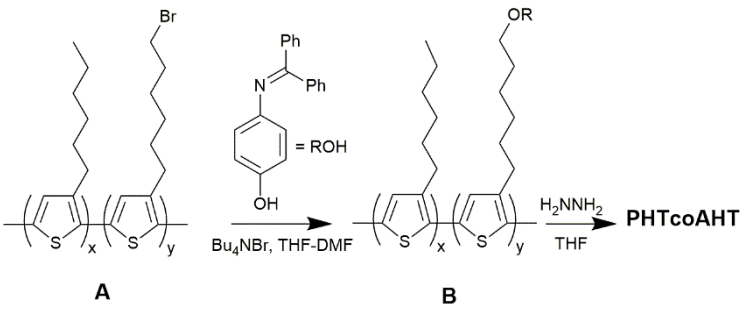

Scheme 4: Modification of the copolymer A leading to PHTcoAHT

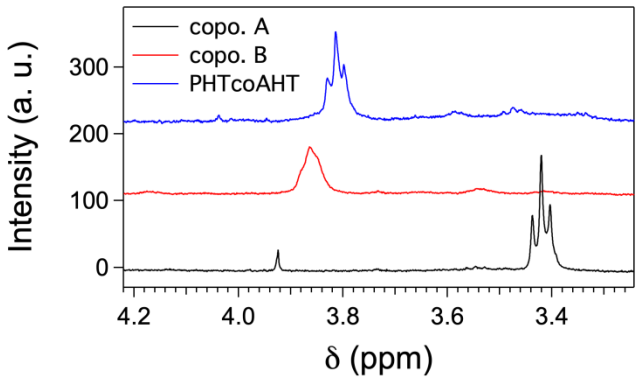

Figure 49: Comparison of the NMR spectra of copolymers A, B and PHTcoAHT (M_n = 36000 g/mol) between 3.2 and 4.3 ppm.

1.3 Synthesized polymers and copolymers

Following the described steps above, we synthesized P3HT of 3 different molecular masses, PHTcoAHT of two different molecular masses, an aminated homopolymer of two different molecular masses and P3DDT of one molecular mass. A summary of all those polymers is presented in **Table 2**.

Table 2: Characteristics of the synthesized polymers and copolymers

Adopted name	**Type of polymer**	**M_n(g/mol)**	**Average Length (nm)[c]**	**Đ**	**Ratio of comonomer**
P44	P3HT	44000[a]	110	1.86[a]	0 %
P21	P3HT	21000[a]	53	1.11[a]	0 %
P7	P3HT	7400[a]	19	1.34[a]	0 %
CP36	PHTcoAHT	36000[a]	84	1.41[a]	18 %
CP5	PHTcoAHT	4700[a] [3700][b]	11	1.29[a] [1.12][b]	14 %
FP17	Aminated P3HT	17500[a]	30	1.26[a]	100 %
FP8	Aminated P3HT	7800[a]	13	1.47[a]	100 %
PD18	P3DDT	17900[a]	30	1.02	0 %

[a] Determined by SEC; [b] Determined by MALDI-TOF; [c] Average length of a stretched polymer chain of mass M_n

From this point thereafter, unless it is specified, all polymers and copolymers will be called by their name given in the first column of table.

Molar mass was determined by SEC. At this point we note that molecular weight for P3HT and thus its modified versions tend to be overestimated due to the chain rigidity compared to the PS molecular

weight standard. For lower molecular weight, MALDI-TOF (Matrix Assisted Laser Desorption Ionization - Time of Flight) could be utilized for more accurate determinations, but this technique cannot be implemented for longer chains, because their lower desorption from the matrix, and their lower ionization efficiency.[219]

The two totally aminated polymers were very little studied due to their extreme sensibility to oxidation of all the pendant chains, forming completely insoluble aggregates.

The synthesis of P3DDT was performed due to their increased capacity of dispersing carbon nanotubes relative to P3HT.[220] The synthesis of the respective copolymer, PDDTcoADDT was tried but only finished in October 2020, so further studies were not performed.

2. Carbon nanotubes used in this study

HiPCO SWNTs (mean diameter 1.0 +/- 0.2nm) have been purchased from NanoIntegris. They were dried at 250 °C under vacuum prior to use.

DWNTs were provided by Emmanuel Flahaut. Statistics from HRTEM studies show that around 77 % of the nanotubes were DWNTs with around 18 % were SWNTs, with the remaining having three walls. The inner and outer diameters range from 0.53 to 2.53 nm and from 1.23 to 3.23 nm, respectively. The median inner diameter is 1.35 nm and the median outer diameter is 2.05 nm.[221]

These carbon nanotubes could not be dispersed in usual solvent, such as THF, even with long sonication times, flocculation happening spontaneously after dispersion. These flocculates consist of unorganized knotted bundles of carbon nanotubes, whose optical density when deposited on a lacey carbon film is very heterogeneous (**Figure 50a**). Less dense zones consist mostly of large bundles for SWNTs (**Figure 50b**) and smaller bundles for DWNTs (**Figure 50c**). We also observe a large amount of residual catalyst particles for SWNTs, while not many for DWNTs.

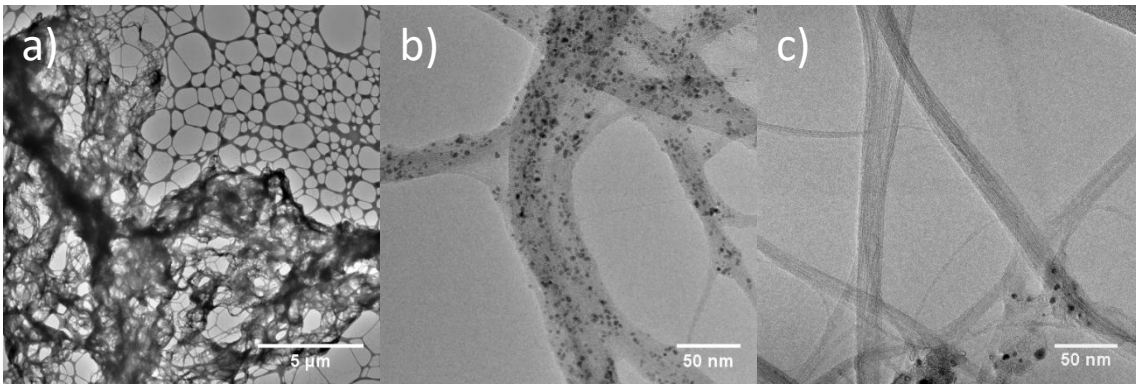

Figure 50: a) Low magnification TEM images of SWNTs sonicated for 5 min in THF and deposited on lacey carbon films. The nanotubes flocculate immediately after sonication; b) High magnification image of a less dense zone inside a large flocculate. Large bundles are observed, with individualized nanotubes being rarely detected; c) High magnification image of DWNTs sonicated in THF. Also a less dense zone is imaged. Bundles for this sample are smaller, individual nanotubes being more often observed. Black spots in b) and c) are residual catalyst particles.

3. Elaboration of non-covalent nanohybrids

The present chapter describes the elaboration of non-covalent nanohybrids. These were initially synthesized to act as blanks for the characterization of the covalent nanohybrids described in **Section 3**.

3.1 Elaboration of non-covalent nanohybrids via a solvent extraction method

This method was introduced by Schuettfort *et al*.[222] for the solubilization of CoMoCat and HiPCO SWNTs in THF with the use of regioregular P3HT of M_n between 25 and 35 kg/mol. After adding SWNTs in a P3HT solution, the suspension is sonicated (15 min) and centrifuged to eliminate bundles and impurities. Toluene is then added to the supernatant, causing the precipitation of the P3HT coated SWNTs. The authors explain this precipitation as due to the lower solubility of carbon nanotubes in toluene than in THF.[37] We disagree with this interpretation and believe that the P3HT interacting with the SWNTs have a different conformation in each of these solvents. The precipitate is then collected, dispersed in toluene and centrifuged. This procedure is repeated until complete elimination of the polymer in the supernatant (checked by UV-vis). **Figure 51** presents the described steps as a flowchart.

We followed this method to get solutions of pure nanohybrids (without excess of free polymer) for characterization and for further covalent functionalization tests.

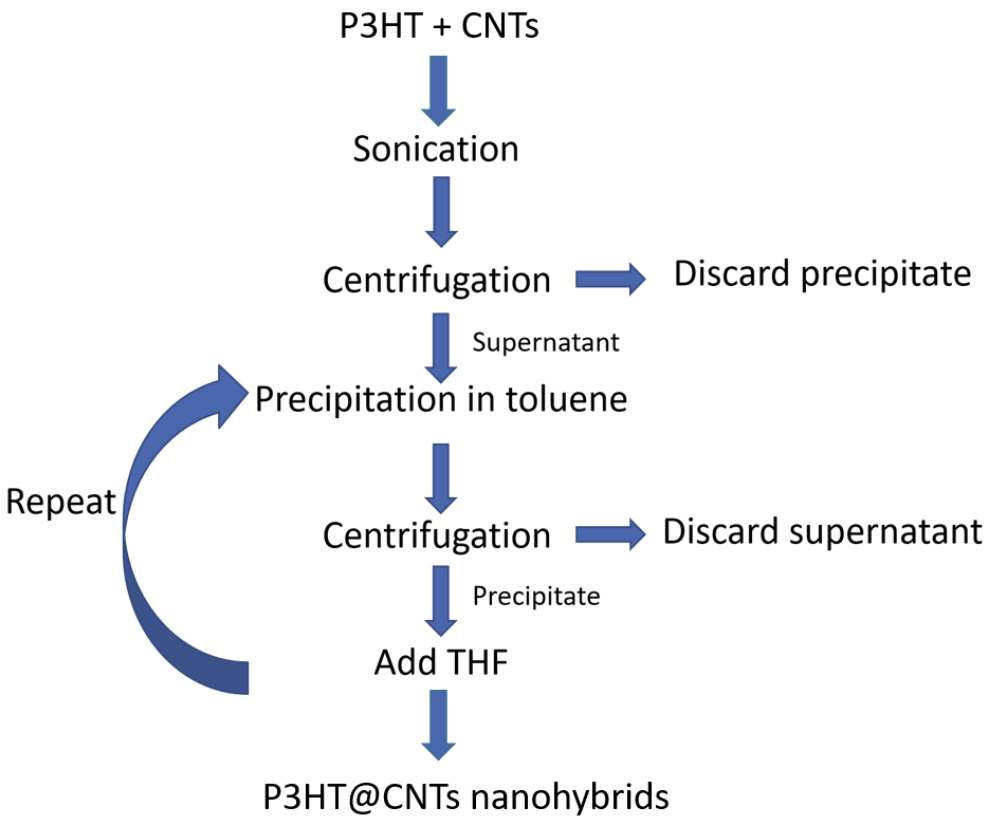

Figure 51: Flowchart of the steps of the solvent extraction method. Addition of toluene is stopped when no soluble polymer is present in the supernatant.

We could obtain a suspension of nanohybrids using the homopolymer P21, which as a similar molecular weight than the one used in reference 222. However, to obtain satisfying results, sonication has to be extended up to 30 min using a tip sonicator (Fischer Scientific Model FB-505, Power 500 W, used at 20 % of total power) with a polymer/SWNTs ratio three times higher than the one reported.

We also observed that the absolute concentration of carbon nanotubes is an important parameter. Positive results were obtained for concentrations in the range 0.125 to 0.38 mg/mL, while respecting the polymer excess condition. Higher concentrations caused a total sedimentation already at the first centrifugation step. This is possibly due to entanglement of the bundles together with the more dispersed nanotubes, the bundles acting like a net that carry all the nanotubes down. Lower concentrations contain too few material and are hard to work with.

At least 6 redispersion steps were needed for eliminating the polymer. As we advanced in the polymer elimination, the polymer spectra observed on the supernatant is not in its dissolved state, but in aggregated state.

The UV-vis spectrum of the final nanohybrids is shown on **Figure 52**. The concentration of SWNTs in the last dispersion is about twice that of the SDS suspension, as estimated from the E^{S}_{11} transitions.

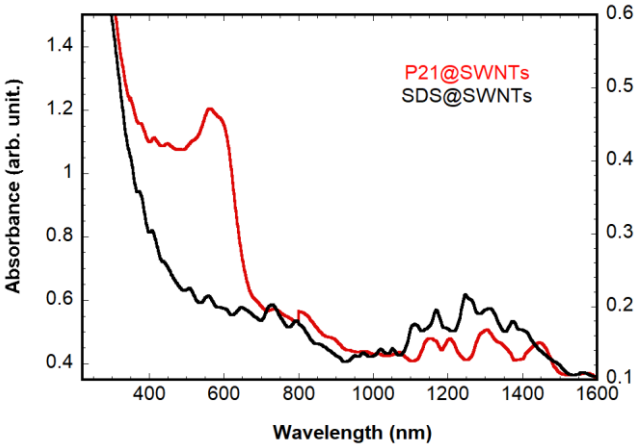

Figure 52: Spectra of P21@SWNTs in THF (red, left-scale) obtained by the solvent extraction method compared to SDS@SWNTs in D_2O (black, right scale)

The spectrum of the isolated non-covalent nanohybrids is fully consistent with the one reported in [1]. It clearly shows the superposition of the absorption spectra of PHTcoAHT aggregates, characterized by a band around 500 - 650 nm, and of carbon nanotubes red shifted in the region 1000 – 1500 nm compared to the SDS suspension. The red shift of the optical transitions of the non-covalently functionalized SWNTs is characteristic of strong electronic interactions at the SWNT-copolymer interface (see **Chapter 3**) However, the structure of carbon nanotubes absorption peaks observed all along the spectrum is close to that in the SDS suspension, suggesting no selectivity towards the different carbon nanotubes species.

Fluorescence spectroscopy of the final solution indicates there are still some remaining free polymer in solution in concentrations too low for detection by optical absorption spectroscopy. No emission of the aggregates is visible. We can assume the observed signal comes from polymer not interacting with the carbon nanotubes since the fluorescence of P3HT in interaction with carbon nanotubes is quenched (**Figure 53,** detailed discussion in **Chapter 3**).

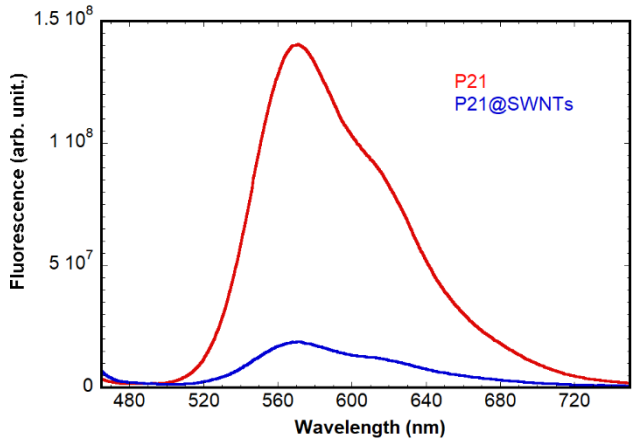

Figure 53: Emission spectra (excitation 450 nm, triangular cell) of P21 and of P21@SWNTs nanohybrids obtained by adding SWNTs onto the P21 solution.

TEM images (holey grid) show a carbon nanotubes network consisting mainly in individualized or small bundles of carbon nanotubes dispersed in a suspended polymer film (respectively the black and the white arrow in **Figure 54**). This is in agreement with what is observed by optical absorption spectroscopy, where we observe a residue of polymer and small bundles of carbon nanotubes. The origin of this film of polymer is possibly due to the drying conditions when preparing the grid.

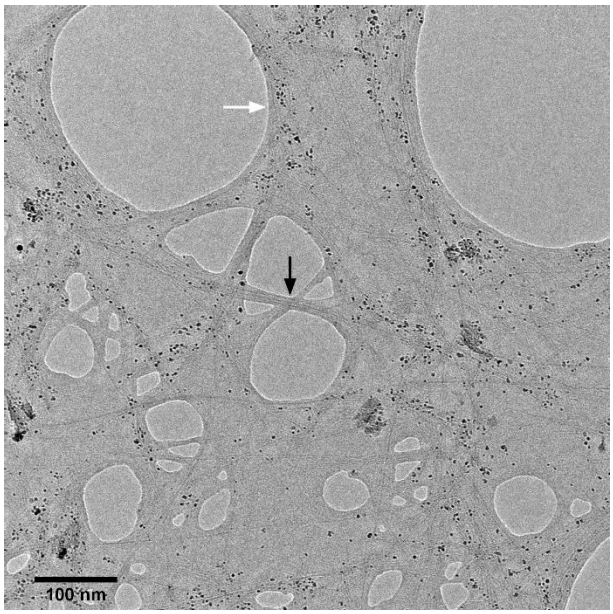

Figure 54: TEM image of P21@SWNTs nanohybrids deposited onto a lacey carbon film. Black arrow indicates a more individualized carbon nanotube covered in polymer, while the white arrow indicates a thicker polymer film.

The molecular weight of the polymer is an important parameter for achieving dispersion of the carbon nanotubes. For both homopolymer P7 and copolymer CP5, after mixing with SWNTs, the amount of dispersed nanotubes is very low compared to what can be obtained with P21. Moreover, after the first centrifugation step, we did not observe any nanotube in suspension after the first centrifugation step, the supernatant consisting of only a well solubilized polymer solution with no trace of aggregates. On the other extreme, P44 also did not form stable suspensions with the carbon nanotubes in these conditions, and, after the first centrifugation step, the supernatant consisted of a violet solution with spectral features of polymer aggregates and of free polymer, but with no trace of carbon nanotubes.

Besides P21, only the copolymer CP36 led to nanohybrids that could be isolated from the excess of polymer. It is noticeable that these two polymers are the only ones having a degree of polymerization (taking into account the relative masses of thiophene and aniline terminated thiophene) similar to those used in the study that inspired this process.[222] This optimum dispersion with intermediate molecular weights is in agreement with the results obtained with PFT@SWNTs dispersions.[88]

However, the presence of the comonomer bearing the aniline group has an impact on both the dispersibility of SWNTs and the amount of aggregated polymer onto the tubes (of about 1/50 the one

obtained with P21). The obtained nanohybrids are stable for few days for P21@SWNTs and few hours for CP36@SWNTs.

In the conditions of the study, the solvent extraction method does not work for DWNTs. No material remains in suspension after centrifugation, suggesting a weaker interaction between both species. The higher density of DWNTs certainly also plays a role in the failure of this method.

In conclusion, the solvent extraction method allows for obtaining nearly pure suspensions of P21@SWNTs and CP36@SWNTs. It does not work however for the other polymers nor using DWNTs suggesting that the couple (homo-copolymer length / CNTs diameter) has an impact on the nature of the nanohybrids. Moreover, although a relative important concentration of the nanohybrids could be obtained, especially in the case of P21, the total obtained yield is low, with less than 5 % of the initial material (both SWNTs and polymer) mass added remaining in the final nanohybrids. Actually, this method could probably work with other polymers and CNTs but would need find the right parameters for each, which was not compatible with the timescale of our project.

3.2 Elaboration of non-covalent nanohybrids without further purification

One of the objectives of this thesis is to obtain perfectly quantitative and reproducible results. Using this method, if one has the control of the initial materials used, we do not control what we obtain at the end. Moreover, as it will be discussed in **Chapter 3**, the solvent extraction method does not work for the nanohybrids after covalent functionalization. This led us to choose another operating mode.

First of all, this method is simple, without extra steps after mixing in order to eliminate the excess polymer, the counterpart being the remaining of bundles in the system. Secondly, it allows for good reproducibility and a better control of the total quantities of material in the ending solution.

A typical mother suspension of SWNTs was made by adding 0.7 mg of SWNTs to 4 mL of THF by sonication (5 minutes). The used mother suspension of DWNTs made by adding 0.48 mg of DWNTs to 4 mL THF by sonication (5 minutes). Sonication was repeated for 30 s before each use. A tip sonicator Fischer Scientific Model FB-505 (500 W) was used for all sonication steps at 20% power level.

Preparation of non-covalent nanohybrids was performed by adding a determined volume of the mother suspension to 4 mL to a solution of pure polymer and by sonicating the mixture for 5 min. The obtained mixture is immediately characterized by optical absorption and fluorescence spectroscopies. The same procedure is repeated for each addition until flocculation of the obtained nanohybrids happens instantaneously after the sonication step. The procedure is schematically represented in **Figure 55**.

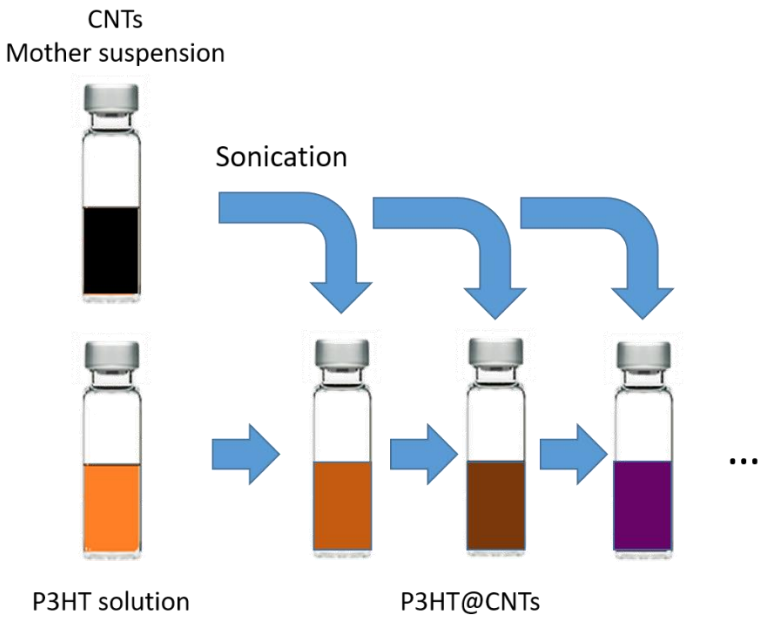

Figure 55: Scheme of the method used for producing nanohybrids suspensions. A small fraction of a mother suspension of CNTs is added to a solution of P3HT. The mixture is then sonicated and analyzed. This procedure is repeated until flocculation is instantaneous.

Using this procedure, all polymers and copolymers are able to form non covalent nanohybrids with CNTs. However, drastic differences in the dispersibility of CNTs, their stability and in the kind of polymer aggregates formed onto the CNTs are obtained depending on the polymer used. It will be shown in chapter 3 that these differences come from the differences in the conformation of the polymers in solution.

4. Covalent functionalization of carbon nanotubes

4.1 Diazonium reaction

The covalent nanohybrids were prepared by carrying out Tour's reaction (see **Scheme 1** and see **Chapter 1 Section 1.6** for mechanism) using non-covalent nanohybrids as precursors.

They were elaborated with both copolymers CP5 and CP36. We chose a SWNTs/copolymer concentration ratio of 0.2 for CP36 and 0.05 for CP5. This concentration ratio is well below the critical SWNTs/copolymer concentration ratio above which spontaneous flocculation occurs for non-covalent nanohybrids, ensuring the dispersion of the nanohybrids.

After sonication, the nanohybrids suspension was transferred to a sealed Schlenk's vial, to which were added 10 equiv. of isoamyl nitrite with respect to the amine groups. The mixture was finally put under argon through vacuum-argon cycling before being heated to 60 °C for 12 h under stirring.

After the reaction, the system was redispersed by sonication and the final product was then centrifuged for 5 minutes at 25000 g. The supernatant was recovered and characterized.

Unlike the non-covalent nanohybrids, the covalent ones do not show a red-shift of the optical absorption bands compared to SDS@SWNTs, indicating that the interaction of the copolymer at the with the nanotubes is different for both kinds of nanohybrids. Moreover, covalent nanohybrids are stable for two months whatever the copolymer (CP5 and CP36) and the kind of nanotubes (SWNTs and DWNTs). Also, contrary to the non-covalent nanohybrids, the covalent ones do not precipitate when toluene is added to the suspension (when trying to isolate them through the solvent extraction method). Our interpretation is that the polymer organization on the nanotubes surface is different for the covalent nanohybrids than for the non-covalent ones, the aniline group acting as a spacer between the nanotubes and the polymer backbone. This interpretation will be detailed in **Chapter 3**.

Sadly, the obtained amounts are very low, for CP36 being lower than that of the non-covalent nanohybrids. This, coupled to the relative difficulty in obtaining large amount of the copolymer, prevents analyses that require larger amounts of sample, such as TGA and XPS.

4.2 Effect of the temperature of Tour's reaction on the suspension of the non-covalent hybrid.

As Tour's reaction is performed at 60°C, we have checked by fluorescence the effect of the temperature on the non-covalent nanohybrid used as a precursor.

Temperature variation was performed using a Peltier module. To ensure a good thermal contact between the optical cell and the system, a square 10 mm x 10 mm cell was used. The nanohybrids solution was diluted about 100 times to avoid the saturation of the signal and reabsorption effects.

Upon heating up to 60 °C, the fluorescence increases rapidly and after 15 minutes reaches a plateau meanwhile some flocculation becomes observable. This probably corresponds to a modification of the adsorption-desorption equilibrium between the nanohybrids and the surrounding copolymer solution (**Figure 56**). This experiment shows that the copolymer re-dissolves at least partially, leading to a possible change in the orientation of the aniline group relative to the nanotubes in the suspension, favoring the reaction.

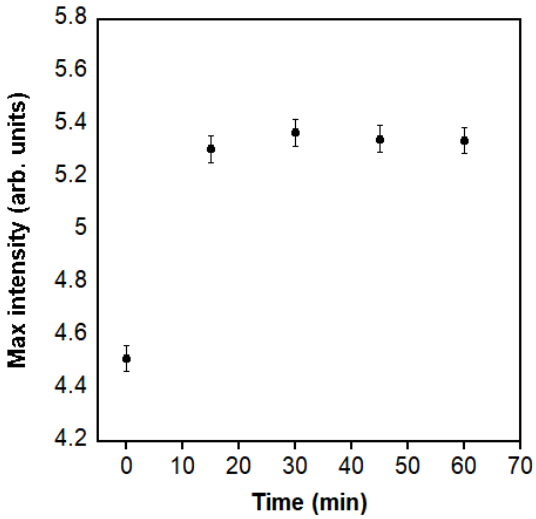

Figure 56: Evolution of the fluorescence intensity measured at the maximum of emission (568 nm) of SWNT/PHTcoAHT 36000 at 60°C. The first measurement corresponds to the fluorescence at room temperature.

4.3 Effect of the reaction conditions on the copolymer

Another question arose about a possible interaction of the oxidant agent with the polymer. To check the stability of the polymer against the conditions used for Tour's reaction, a blank reaction was performed using a CP5 solution (3.5 mg dissolved in 4 mL of THF) mixed with the same amount of isoamyl nitrite (10 eq. relative to the amine groups) used in the reaction with the carbon nanotubes. This mixture was heated up to 60 °C for 12 h. The resulting product was precipitated in methanol and its molecular mass analyzed by MALDI-TOF (**Figure 57**). We found that the mean molecular mass was not significantly changed between before and after reaction, remaining centered at about 3400 Da. This shows that the chains are uncleaved by the reaction conditions, nor it leads to oxidative coupling of the chains.

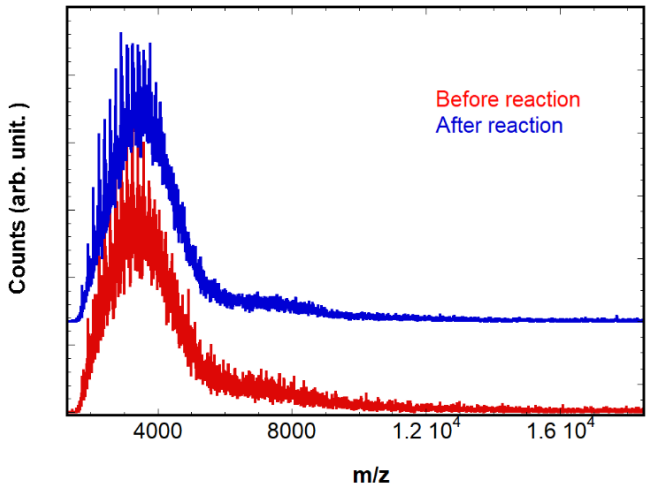

*Figure 57: MALDI-TOF MS spectra of **CP5** (red) and of the same polymer after 12 h at 60 ° C with isoamyl nitrite in THF (blue).*

NMR spectra revealed that no changes occurred in the peaks corresponding to the thiophene backbone (singlet at 6.99 ppm) and the α-CH_2 (at 2.81 nm, the position on the alkyl chain most prone to oxidation), both keeping the same integral ratio. Features related to the aniline group of CP5 (doublets at 6.73 and 6.62) disappeared, which is possibly due to deamination[223], leading to the overlap of the protons with the $CHCl_3$ and the thiophene. There is also a shift on the massif corresponding to C**H**$_2$-OC_6H_4-NH_2, also observed for other arylamine ethers, also in agreement with the deamination of the aniline.[224]

UV-Vis, fluorescence and Raman spectra (**Figure 58**) also remain unchanged. The resulting copolymer was still able to form non-covalent nanohybrids with SWNTs.

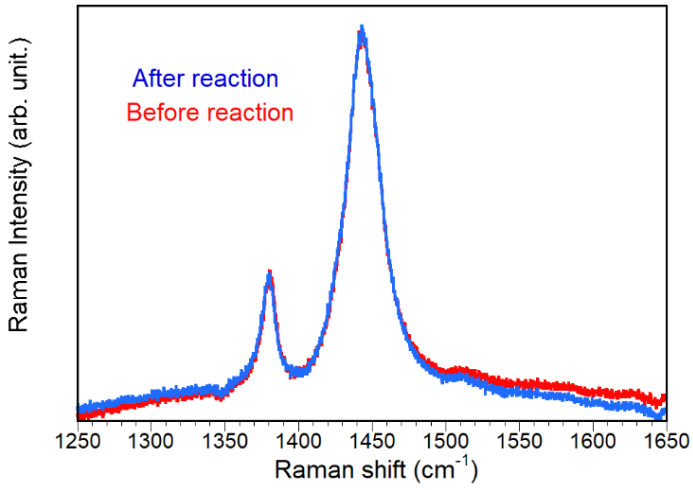

Figure 58: Raman spectra before and after reaction.

We conclude that, under the conditions used for Tour reaction with SWNTs, the polymer backbone remains unchanged, with modifications happening only on the aniline group.

The results obtained in this section show the efficiency of Tour's reaction to functionalize CNTs with our P3HTcoAHTs.

5. Conclusion

Having in mind that the ultimate goal of this work is the elaboration of P3HT – CNTs nanohybrids having possible interesting optoelectronic properties, no more than eight homo- and copolymers have been synthesized at the ICS during this work. Their synthesis is described as well as the route for the elaboration of the non-covalent nanohybrids used as precursors in the syntheses of the covalent ones and necessary for the understanding of both covalent and non-covalent systems.

The key point of this chapter is the successful functionalization of CNTs by a novel copolymer consisting of a P3HT backbone with a controlled fraction of its hexyl side chains functionalized with an aniline group. Thanks to the work of the chemists of the Institute, Jean-Philippe Lamps, Mohamed Raoui and Philippe Mésini, who developed the synthetic route of this copolymer prior to my PhD, it is the first time that a direct single-step functionalization of raw CNTs by the side chains of a polymer is reported, previously reported functionalization having been performed on previously oxidized CNTs.[225] The physico-chemical characterizations of the obtained non-covalent and covalent nanohybrids are given in **Chapter 3**, and their application in functionalized devices in **Chapter 4**.

Chapter 3: Physico-chemical characterizations of the nanohybrids

In this chapter, we report optical absorption spectroscopy, fluorescence spectroscopy, microscopy and Raman spectroscopy studies performed on the different nanohybrids elaborated from the different homo and copolymers synthesized and the two kinds of nanotubes. To try to be the most readable possible, we firstly present the results obtained onto the non-covalent nanohybrids elaborated, detailing deeply those concerning P21@SWNTs. We then study and compare the effects of the different parameters, the polymer mass, the presence of the comonomer, the length of the alkyl chains, the solubility and the type of nanotubes. The obtained results reveal drastic differences in the organization of the polymers adsorbed onto the tubes as well as on the kinetics of their adsorption. It is shown that these differences are due to the difference in solubility of the different polymers, leading to different kinds of aggregation.

Finally, the characterizations of the covalently functionalized nanohybrids and their comparison with their precursors are reported, showing that copolymers interacting with the nanotubes are in a more disordered state compared to the respective non-covalent nanohybrids.

1. Characterization of P21@SWNTs nanohybrids

P21@SWNTs nanohybrids were chosen as reference samples for describing the physico-chemical properties of the non-covalent nanohybrids. This polymer has an intermediate chain length and was the most successfully isolated by the solvent extraction method (**Chapter 2**, **Section 3.1**), which gave preliminary signs of the formation of polymer aggregates on the nanotubes surfaces. We mention right here that, as it will show in the following section, that aggregation of P21 onto SWNTs occurs spontaneously and that they are not affected by sonication (no re-dissolution).

The systems described here were prepared by adding successive fractions of a mother suspension of carbon nanotubes to a solution of the polymer. Description of the method is given in **Chapter 2**, **Section 3.2**. After each addition, optical absorption and fluorescence spectroscopies were performed on the system. This method allows one to estimate the conformation of the polymer chains in the aggregates by using the model introduced in **Chapter 1**, **Section 2.2**.

1.1 Optical absorption

Upon adding SWNTs in the polymer solution, we observe an increase of the broad band characteristic of P3HT aggregates (500 to 650 nm) (**Figure 59**). Concomitantly, the absorption band of the free polymer at 450 nm decreases while those of SWNTs increase. Upon increasing the amount of SWNTs, the suspensions become less and less stable. After the last addition of SWNTs, the system destabilized instantaneously after sonication. The isosbestic point observed near 500 nm is indicative that there is a change in the polymer upon interaction with the carbon nanotubes. Two polymer species coexist in the system, free P3HT in solution and P3HT aggregates.

Moreover, a pure solution of P21 with the same concentration (26.2 µg/mL) does not show any trace of aggregation within the timescale of few days as well as no change are observable when the solution is sonicated in the absence of carbon nanotubes, excluding sonocrystallization effects.[183] This indicates that the presence of the carbon nanotubes is responsible of the change in the absorption spectra.

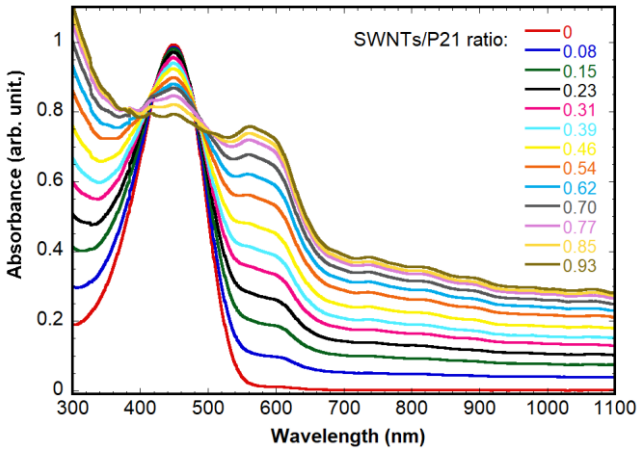

Figure 59: Evolution of the absorption spectrum of a solution of P21 with successive additions of SWNTs. Each addition of SWNTs corresponds to an increase on the SWNTs/P21 mass ratio of 0.08.

To better analyze the changes in the absorption spectra, the carbon nanotubes background due to π-plasmons is subtracted using a $1/\lambda$ variation. As we observed that at 700 nm there is no absorption band originated by the polymer nor by the nanotubes, the absorption value at this wavelength was chosen to define the proportionality factor A. A linear increase of this factor up to a total amount of SWNTs close to 0.06 mg shows the pertinence of this analysis. Deviation from the linearity is explained by the progressive destabilization of the solutions which reduces the total absorbance (**Figure 60a**). The resulting spectra are shown in **Figure 60b**.

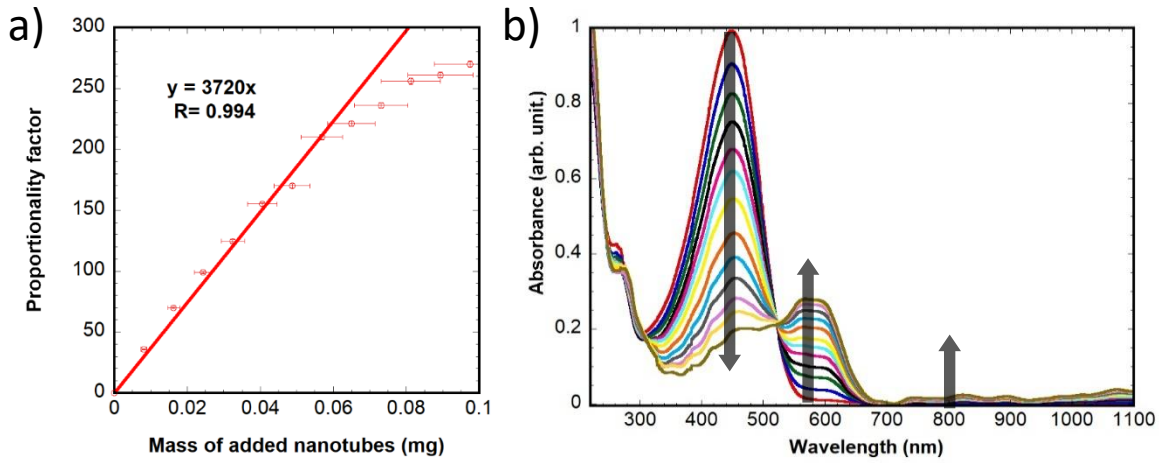

*Figure 60: a) Proportionality factor of the background correction of the curves displayed in **Figure 59**; b) Evolution of the absorption spectrum of a solution of P21 with successive additions of SWNTs after background correction.*

At wavelengths higher than the isosbestic point, the absorption feature is localized at the same place than absorption of pure P3HT aggregates. However, the feature is too poorly resolved to distinguish the $A_{0\text{-}0}$ and $A_{0\text{-}1}$ vibronic peaks, which suggest a low number of interacting units in the aggregates.

Considering that two polymer species coexist, from the curves in **Figure 60b** and using the first recorded spectrum (before addition of carbon nanotubes) as a reference spectrum, we can estimate the amount of free polymer in solution. This is done by scaling the pure P3HT spectrum until it has the same amplitude at the low wavelength side (between 350 and 400 nm) as that of the P21@SWNTs for each spectrum (**Figure 61a**).

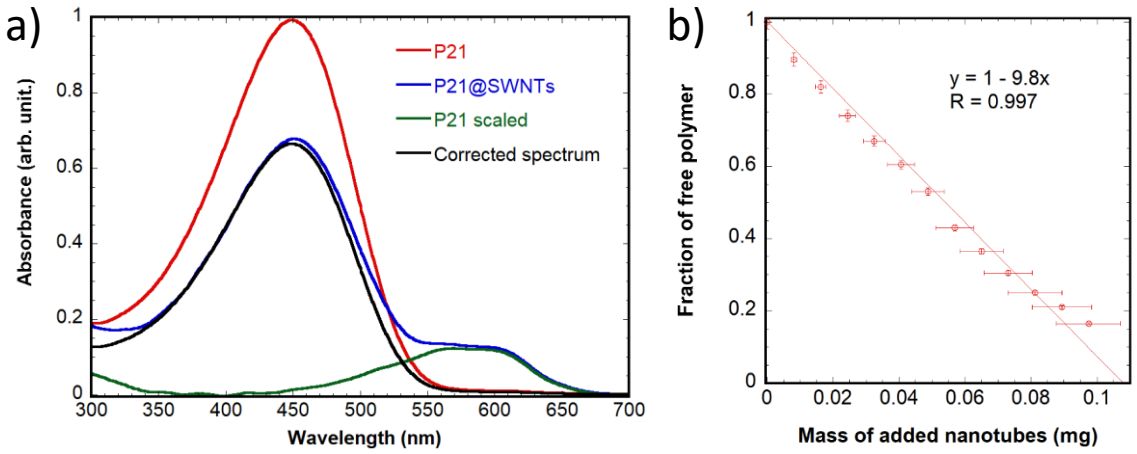

Figure 61: a) Example of spectral decomposition used to obtain the amount of free polymer; b) Free polymer correction factors as a function of the amount of carbon nanotubes added;

Figure 61b shows that the amount of free polymer decreases linearly with the amount of carbon nanotubes added to the suspension. Thus, we can reasonably assume that the same amount of polymer interacts with the carbon nanotubes for any given concentration. This suggests that the aggregates

formed on an isolated tube or bundle are approximatively constant in number and size. It also suggests that flocculation occurs between the nanohybrids, due to the increase in their concentration in the solution.

Using the slope given by a linear fit, we can estimate the mass of polymer adsorbed onto the carbon nanotubes surface. Considering that 0.9% of the amount of polymer in this suspension covers every µg of carbon nanotubes, and that the total amount of the polymer is 105 µg, we calculate and adsorbed ratio of 1.02 mg of polymer/mg of carbon nanotubes, corresponding roughly to 0.4 3-hexylthiophene units per carbon hexagon. This value, incompatible with a single uniform coating of the surface of the nanotubes, is in agreement with the formation of aggregates of P3HT on the tubes (all the more it is undervalued as it does not take into account the mass of residual catalyst and amorphous carbon).

The overall variation of the absorption spectrum after subtracting the contribution of the free polymer is shown in **Figure 62**. According to the model of Spano, the poor resolution in the aggregates region suggests that the number of interacting units is low in the aggregates.[169] Moreover, the constant shape of the aggregates peaks indicates that this number of interacting units does not depend on the SWNTs/P21 mass ratio.

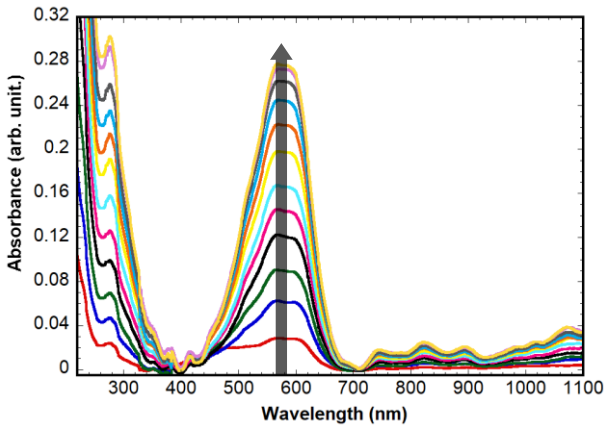

Figure 62: Spectra obtained from subtracting the free polymer contribution from the background corrected spectra of ***Figure 61b***

An attempt to estimate the values of $A_{0\text{-}0}$, $A_{0\text{-}1}$ and $A_{0\text{-}2}$ can however be made by the decomposition of the last recorded spectrum. This was done by using four Gaussian curves, three for the vibronic transitions and one for possible residual contribution of the free polymer. The same Gaussian width has been used to fit the three vibronic peaks, the parameters corresponding to the amplitude and position of the peaks being free. The width and position of the free polymer peak were fixed to the values of the free polymer spectrum. The resulting peaks for each component and the overall fit are displayed in **Figure 63**.

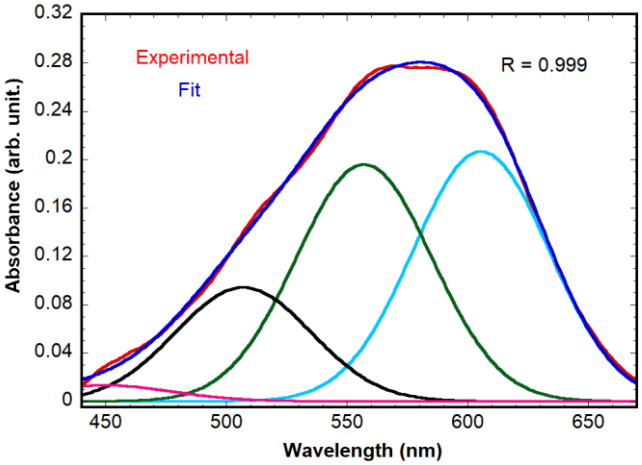

Figure 63: Fit of the aggregate part of the last recorded spectrum of P21@SWNTs

Despite the crudeness of this method, the best fit gives equidistant position of the vibronic transitions, in agreement with a classic Franck-Condon distribution. It is noticeable that this distance between the peaks is of 1440 ± 50 cm^{-1}, in perfect agreement with the measured value for the dominant vibration of 1450 ± 5 cm^{-1} for well-ordered P3HT.[226] The obtained value for $A_{0\text{-}0}/A_{0\text{-}1}$ is clearly overvalued (1.05 ± 0.05), however, the important point is that this value is close to 1, as it is observed in the experimental spectrum. These results strongly suggest a dominant J-like behavior and thus that the aggregates have a high degree of intrachain order (extended chains).

Comparing one of the spectra of **Figure 62** to that of SDS@SWNTs in D_2O (**Figure 64**), a red shift of the absorption bands is observed. This red-shift, measured on the E_S^{22} transitions, is of the order of 20 nm (0.05 ± 0.01 eV), which is close to the values obtained for P3HT@CoMoCat nanotubes of 0.06 eV[227] and of other compounds π-stacking on carbon nanotubes, such as porphyrins.[52] The change of the dielectric environment does not account for such a high change as shown by studies in solvents of different dielectric constant,[228] so part of the shift must be caused by the electronic interactions between both components.

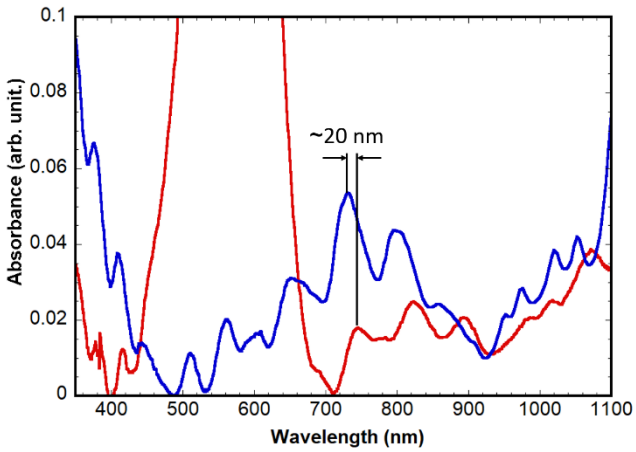

Figure 64: Comparison between spectra corrected from the π-plasmons contribution of P21@SWNTs and the same nanotubes suspended with SDS in D_2O. A red-shift of around 20 nm is observed for the Es^{22} transitions.

These optical absorption experiments reveal the strong interaction between P21 and SWNTs in the non-covalent nanohybrids. This interaction is capable of partially unbundle the SWNTs and to keep them dispersed for a few hours after sonication, although the chain conformation onto the nanotubes, driven by the π-stacking of the thiophene units and hydrophobic interactions of the alkyl chains, does not completely avoids flocculation of the nanohybrids. Based on the estimation of the amount of adsorbed polymer per carbon nanotube, the polymer chains stack in small aggregates on the carbon nanotubes. The SWNTs are responsible for this aggregation acting as a template that leads to aggregates with a dominant intrachain ordering (J-like behavior).

1.2 Fluorescence spectroscopy

Fluorescence spectra (**Figure 65a**) were recorded on the same samples than those used for optical absorption spectroscopy using a triangular cell in order to avoid internal absorption effects. The main effect observed here is the quenching of the free polymer emission by the addition of the carbon nanotubes. We can estimate the variation of free polymer in solution from these experiments, as we did by optical absorption spectroscopy, and we observe a good agreement between both estimations (**Figure 65b**).

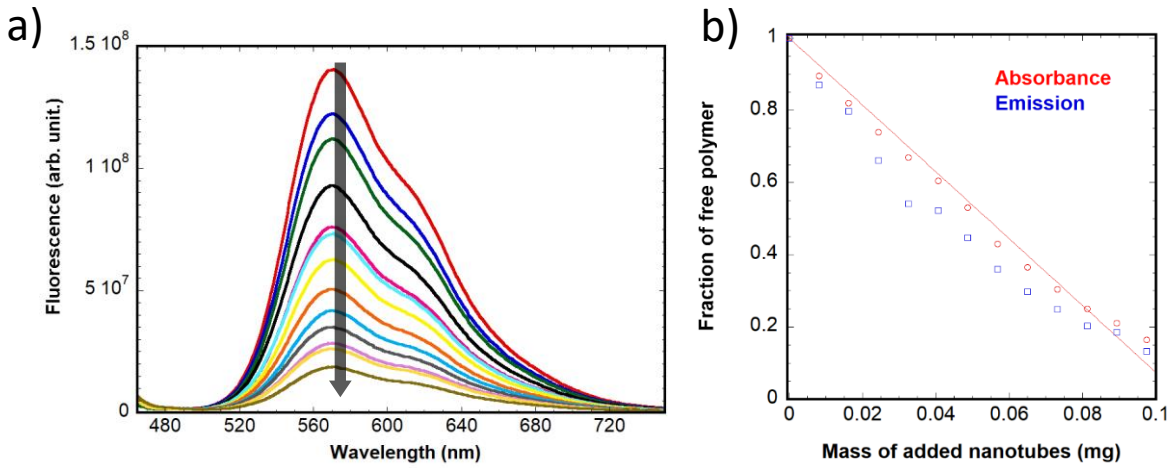

Figure 65 : a)Fluorescence measurements for P21@SWNTs nanohybrids as a function of the amount of added SWNTs to the P21 solution. Excitation was performed at 450 nm; b) Comparison between absorption and emission of P21@SWNTs as a function of the amount of added SWNTs

In these emission spectra excited at 450 nm, no signature of emission from aggregates is observable even when normalizing the emission spectra by their maximum (**Figure 66**). To increase the possible contribution of the emission of aggregates, we performed experiments at excitation wavelengths of 520 nm (and 560) (figures not shown), but still no trace of emission of the aggregates is observed.

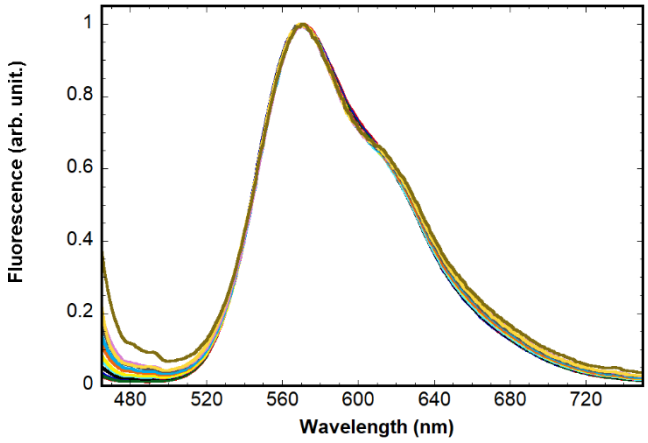

*Figure 66: Fluorescence spectra (excitation 450 nm) of P21@SWNTs nanohybrids shown in **Figure 65a**. normalized by the maximum emission intensity;*

Photoluminescence spectroscopy (PL) allows one to study charge or energy transfer under light irradiation. On well dispersed semi-conducting SWNTs, band-to-band optical transitions leads to the creation of a bound electron-hole pair (exciton), whose recombination may be radiative (bright exciton) or non-radiative (dark exciton). Each carbon nanotube species has an individual emission wavelength whose intensity is maximum when the excitation wavelength corresponds to a band-to-band transition (usually performed at E^{S}_{22}). Scanning both excitation and emission wavelengths allows one to obtain a PL map in which each spot corresponds to a single nanotube species (**Figure 67a**).

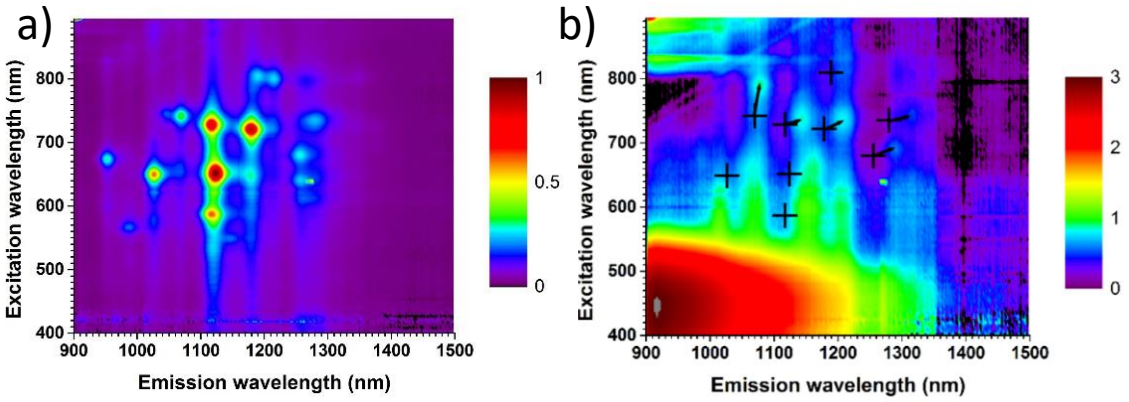

Figure 67: a) Photoluminescence map of SDS@SWNTs; b) Photoluminescence map of P21@SWNTs nanohybrids. The PL signal of the nanotubes is weak, indicating that the SWNTs are not completely individualized as in SDS. The bottom left corner is dominated by the free polymer signal.

For our P21@SWNTs nanohybrids (**Figure 67b**), we observe that both excitation and emission wavelengths are red-shifted (respectively 20 – 30 nm and 25 – 35 nm) compared to that of the same species dispersed by SDS in D_2O. This is in agreement with what is observed for the corresponding optical absorption spectrum and is explained by a change in the local dielectric constant and by the π-π interactions between SWNTs and P3HT.

We also observe emission from all SWNTs species when the excitation energy corresponds to that of the polymer aggregates absorption (between 550 and 650 nm). This is a sign of energy transfer from the polymer aggregates to the carbon nanotubes. The band alignment between the polymer aggregates and the SWNTs is expected to be that of a type II heterojunction (as shown in **Chapter 1**, **Section 1.6**), which would lead only to electron transfer from the polymer aggregates to the SWNTs, and thus to no emission from the latter. This suggests that this energy transfer occurs via a Förster resonance energy transfer mechanism.[229] This mechanism predicts energy transfer (exciton transfer) from an excited chromophore to an acceptor. The efficiency of this transfer is proportional to the overlap between the emission of the donor (between 600 and 750 nm for polymer aggregates) and the absorption of the acceptor (between 550 and 750 nm for SWNTs species, see **Figure 67a**). The efficiency also depends on the distance d between the donor and the acceptor, decreasing as $1/d^6$. In our case, energy transfer efficiency is revealed by the stronger emission of the SWNTs when exciting the polymer aggregates than when excited directly through E^S_{22}.

The results above show that nanotubes are responsible of the aggregation of the polymer. They show that strong π - π interactions exist between the thiophene units and the aromatic rings of the nanotubes and are in agreement with the wrapping of the chains around SWNTs. Moreover, the estimated amount of adsorbed polymer suggests that this wrapping could be made of few stacked chains of copolymers.

This is in agreement with the absence of fluorescence emissivity from the aggregates, whose emission is quenched by energy transfer to the SWNTs.

1.3 Microscopy

Microscopic characterization was mainly performed by TEM. Two types of grids were prepared: regular carbon grids and lacey carbon films (holey grids). The objective of using the second type of grids is to improve contrast, since carbon nanotubes are hardly visible over the amorphous carbon coating of the regular carbon grids.

Figure 68 shows selected TEM images of the grids obtained by deposition of 5 µL of P21@SWNTs on lacey carbon films. The deposited droplets were dried with the help of a filter paper. The difference between grids obtained from systems obtained by the addition method and by the solvent extraction method is that we observe more isolated nanotubes and less catalyst particles in the purified systems, but the overall results are similar.

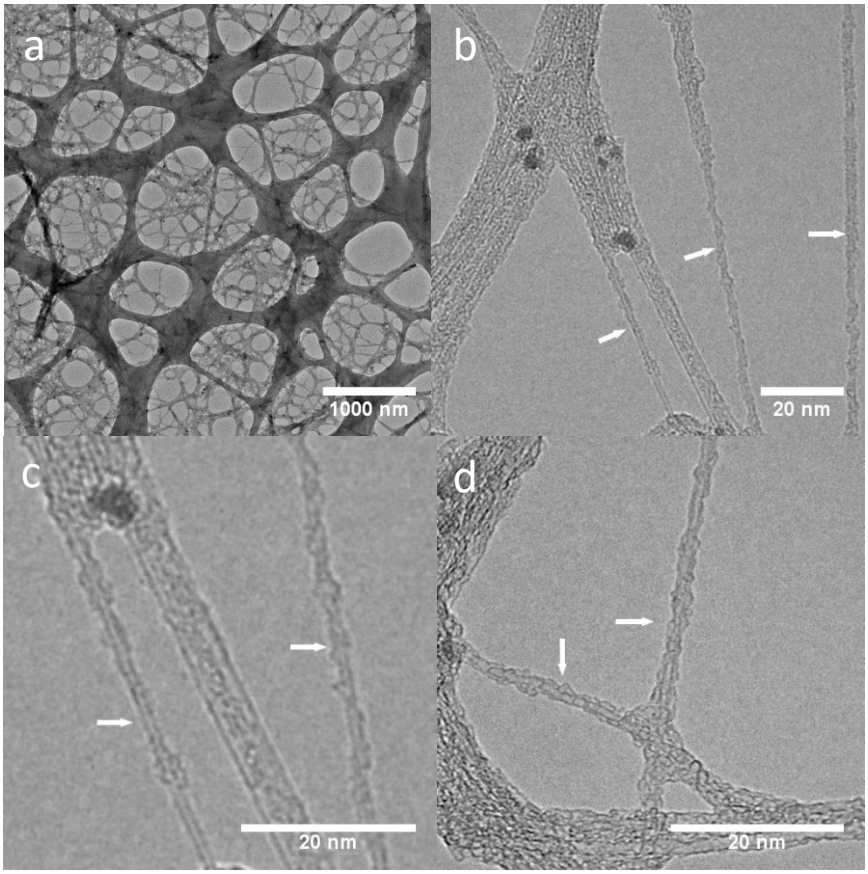

Figure 68: Selected representative images of the non-covalent P21@SWNTs (SWNTs/P21 ratio = 0.93) system deposited on a lacey carbon grid. a) Low magnification; b) Medium magnification image showing a zone in which many individualized carbon nanotubes (white arrows) are present; c) Zoom on some individualized carbon nanotubes, in agreement with polymer wrapping around the carbon nanotubes; d) High magnification image of another zone.

Figure 68a show a low magnitude image, showing that many bundles and aggregates are present in the sample, with isolated nanotubes bridging some points of the nets. Two explanations can be given: the first is that some flocculation happens in solution, as observed by the suspension stability. The second is that aggregation occurs during the grid preparation, the drying front causing aggregation of the nanohybrids. The fact that most of the observed bundles are relatively thin favors the second explanation. **Figure 68b** shows a zone with individualized carbon nanotubes. Zones like this are found often on the grid.

Figure 68c and **d** show selected typical images of nanohybrids. The surface of the nanotubes is covered by the polymer. Looking closely, we can see that the polymer seems to wrap around the nanotubes. The wrapping is not uniform, with some regions having a thicker cover of polymer than others. This shows that, despite the average size of aggregates being constant (as shown by optical absorption spectroscopy), aggregates of different size may form, their size being limited to a few polymer layers. This wrapping behavior is very similar to the one observed for similarly prepared grids of PFO@SWNTs[29] or P3HT@SWNTs in $CHCl_3$ or DCB.[230]

Similar images are obtained when the solutions are deposited onto a carbon grid (**Figure 69**). We observe on the whole surface of the grid many isolated nanotubes or small bundles, both covered with polymer, although the low contrast of images obtained in this type of grid hinders more detailed observation of the morphology.

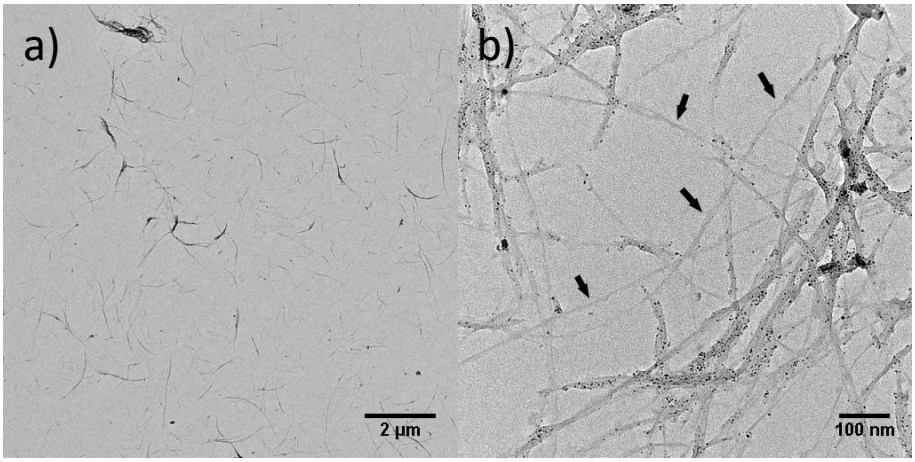

Figure 69: a) Low magnification and b) High magnification TEM images of P21@SWNTs nanohybrids (SWNTs/P21 ratio = 1.02) deposited on a carbon grid. Black arrows point to isolated nanotubes or small bundles covered with polymer.

Cryo TEM experiments confirmed the results above (**Figure 70**): P21 disperses the carbon nanotubes, but some bundles still remain in solution. The polymer forms a small layer around the carbon nanotubes, which is compatible with the wrapping of the polymer backbone around the nanotube surface.

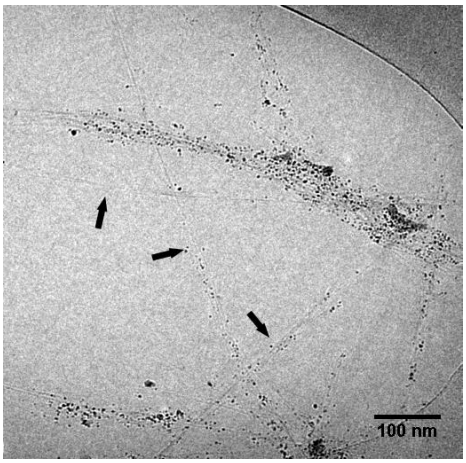

Figure 70: Cryo TEM image of P21@SWNTs nanohybrids (SWNTs/P21 ratio = 1.02). Black arrows point to individual carbon nanotubes or small bundles covered with polymer.

Based on all microscopy experiments performed on these samples, we conclude that the polymer P21 wraps the surface of the SWNTs. This is supported by the fact the signature of shish-kebab structures (in which aggregates point out from the carbon nanotube surface) has never been observed. Considering the results obtained by optical absorption spectroscopy, this wrapping leads to the formation of small polymer aggregates, consisting of a few aggregated polymer chains. These aggregates are tightly adsorbed on the SWNTs surface due to π-stacking and hydrophobic interactions (respectively the backbone and the polymer side chains) the latter being responsible for the relatively low stability of the dispersions.

1.4 Conclusion

While in solution, a long conjugated polymer chain is relatively flexible, being in a relatively disordered coil conformation. Upon Van der Waals interaction with a carbon nanotube (π-π interactions), a part of the chain adsorbs onto its surface, the rest remaining possibly in solution. In the present case of P21, its high entropy of mixing competes with Van der Waals interactions with the nanotubes leading to a small amount of adsorbed polymer chains. π-π interactions along the nanotube also competes with the entropy of conformation of the polymer leading to an energetically favorable adsorption of the entire chain. The wrapped configuration of the polymer is the most favorable as it is the less constraint. The template effect of the carbon nanotubes leading to this wrapping leads to an extended conformation of the polymer backbone (no chain folding as in typical P3HT nanofibers). The resulting electronic structure of the aggregates is dominated by intrachain interactions (J-type character of the aggregates). Moreover, the wrapping structure around the tubes increases the diameter of the nanohybrid as the number of

successive wrapping chains increases. This results into a mismatch between thiophene units in successive stacked chains in the aggregates weakening the contribution of interchain interactions.

2. Effect of the polymer molecular weight

As reported in **Chapter 2** the solvent extraction method shows that the interaction of the polymers with the nanotubes depends on their molecular weight, leading to different morphologies, solubility and selectivity towards different carbon nanotubes species.

It is important here to underline here that for P44, opposite to all other polymers and copolymers used in this work, the growth of polymer aggregates onto SWNTs occurs within a long timescale. Moreover, the aggregates in P44@SWNTs redissolve, at least partially under sonication, opposite to P21@SWNTs and P7@SWNTs, in which they are stable under sonication. The results reported in this section on P44@SWNTs must then be considered only as trends. A detailed analysis of this system is given in **Section 6.1**.

Figure 71 compares the optical absorption spectra of nanohybrids obtained with the addition of SWNTs to solutions of homopolymers of different molecular masses. For the three polymer masses, similar initial concentrations of polymer (P7: 34 µg/mL; P21: 26 µg/mL; P44: 17 µg/mL) and similar amounts of SWNTs added each time (P7: 9.9 µg; P21 8.1 µg; P44: 8.5 µg) were used. The spectra were recorded immediately after each addition of SWNTs. **Table 3** shows the critical SWNTs/polymer ratio before spontaneous flocculation and the estimated amount of adsorbed thiophene units (obtained following the procedure described in **Section 1.2**). For the latter estimation, the extinction coefficient is considered independent of the polymer molecular weight (as an approximation).[231].

Table 3: Characteristics of the solutions of homopolymer @ SWNTs hybrid solutions

Polymer	SWNTs/polymer critical ratio	Adsorbed polymer (mg polymer/ mg SWNTs)	Adsorbed polymer (hexyl thiophene units/carbon hexagon)
P7	0.27 ± 0.12	0.58 ± 0.01	0.25 ± 0.01
P21	2.16 ± 0.10	1.00 ± 0.01	0.44 ± 0.01
P44	0.63 ± 0.08	1.54 ± 0.08	0.67 ± 0.05

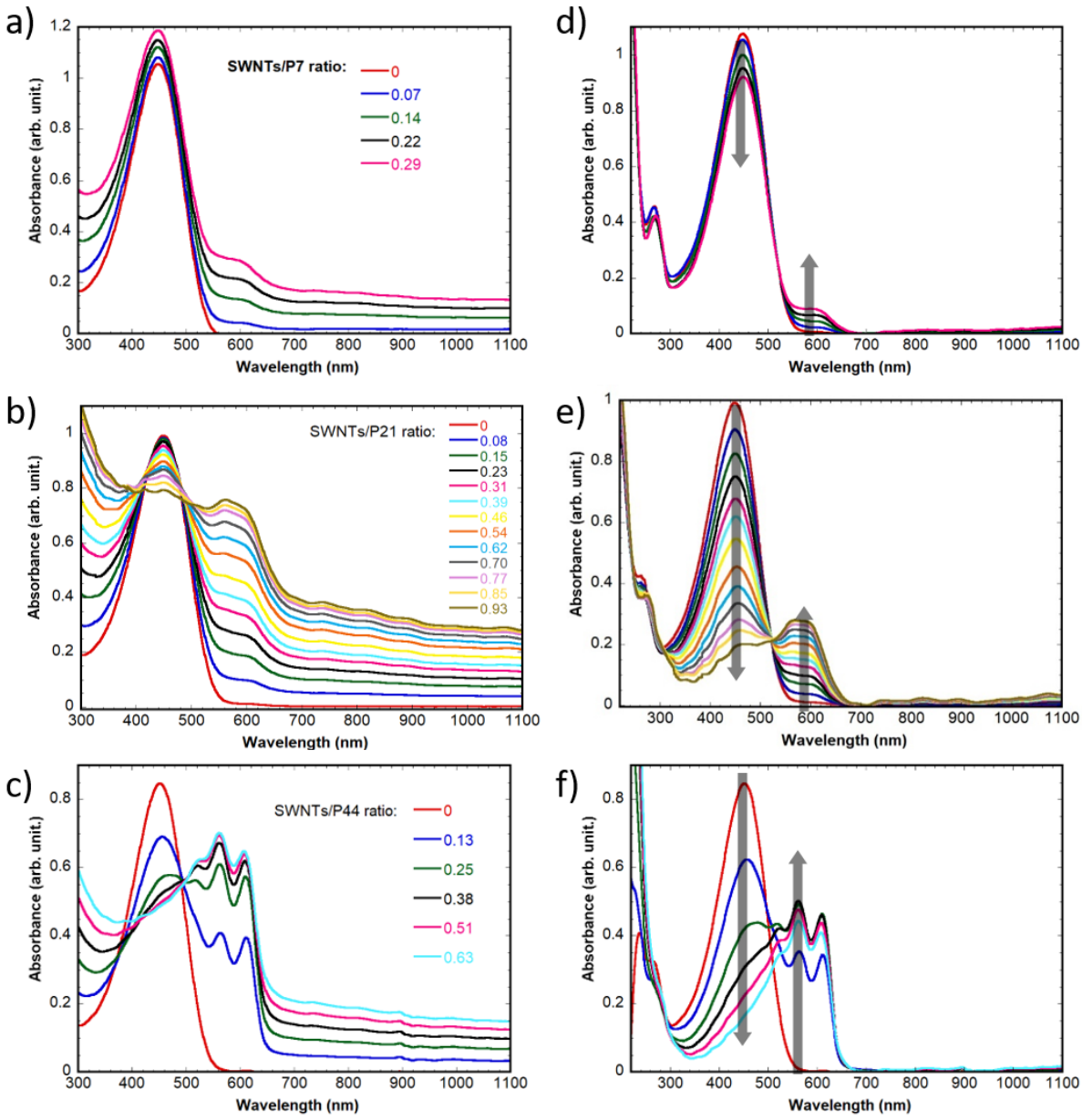

Figure 71: Comparison between optical spectra of the nanohybrids of polymers of different molecular mass as a function of the amount of added SWNTs. On the left side: raw spectra of a) P7@SWNTs; b) P21@SWNTs; c) P44@SWNTs nanohybrids. On the right side: Spectra corrected by the π-plasmon absorption of d) P7@SWNTs; e) P21@SWNTs; f) P44@SWNTs nanohybrids

From these experiments, two observations may be drawn:

- Increasing the mass of the polymer leads to an increase of the amount of thiophene units in the aggregates adsorbed onto the tubes and thus to an increase in the resolution of the vibronic peaks.

- The maximum amount of nanotubes dispersed before flocculation depends on the polymer mass. This amount of dispersed nanotubes is maximum for P21 (**Table 3** and **Figure 72** below).

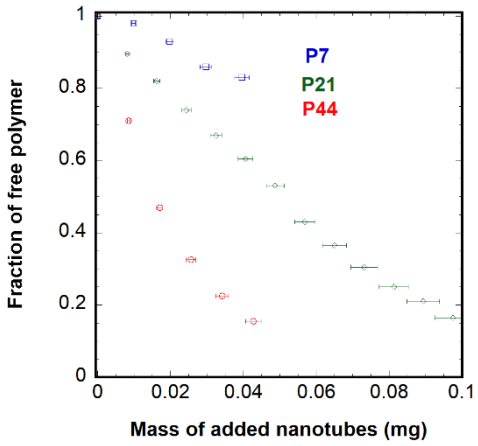

Figure 72: Fraction of free polymer remaining in solution as a function of the added mass of SWNTs to a solution of P44 (red), P21 (green) and P7 (blue). Mass of free polymer is P7: 138 µg; P21: 105 µg; P44: 68 µg

The variation of the fluorescence spectra of P44@SWNTs observed for the same suspensions that those used for optical absorption experiments, when exciting at 450 nm, is similar to what observed for P21@SWNTs (**Figure 65**) and P7@SWNTs (data not shown). It decreases as the amount of aggregated polymer chains increases. This variation is in good agreement with the one observed from optical absorption **(Figure 73a**), However, opposite to what is observed for P21 and P7, when exciting at higher wavelengths, where the polymer aggregates absorb, we clearly observe their emission(**Figure 73b**).

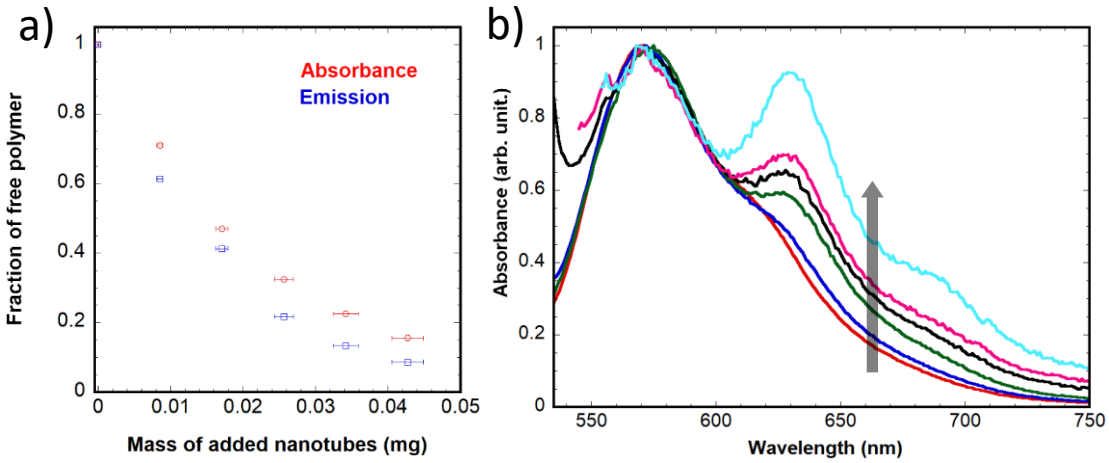

*Figure 73: a) Fraction of free polymer calculated from optical absorption (red) and from emission (blue, excitation 450 nm) data as a function of the mass of added carbon nanotubes; b) Normalized emission (excitation 520 nm) for P44@SWNTs nanohybrids (absorption spectra given in **Figure 71b**) ;*

As mentioned in the introduction of this section, the results obtained for the amount of adsorbed thiophene units for P44@SWNTs are undervalued due to spectra being obtained before the system reached its equilibrium, as it can take many hours for this to happen (see **Section 6.1**). However, it is

clear that the coverage for this system is higher than for P21@SWNTs and P7@SWNTs. This higher coverage corresponds to the presence of larger aggregates on the surface of the nanotubes. Their larger size leads to less efficient energy transfer from the polymer chains in the exterior of the aggregates to the nanotubes, which leads to radiative exciton recombination in the aggregates and observation of their emission.

From these optical absorption and fluorescence experiments, we can already state that the polymer mass has a drastic influence on the nature of the polymer aggregates and their interactions with the nanotubes.

TEM images of P7@SWNTs present similar results to that of P21@SWNTs and will not be further discussed.

P44@SWNTs on the other hand seems to form a different kind of structure when observed by TEM (**Figure 74**). Deposited on a lacey carbon grid, a thick polymer film is formed around the carbon nanotubes (individualized or in bundles (**Figure 74a** and **b**). The observed structures are compatible with helical wrapping, but in this case more chains would overlap forming larger aggregates than for P21@SWNTs.

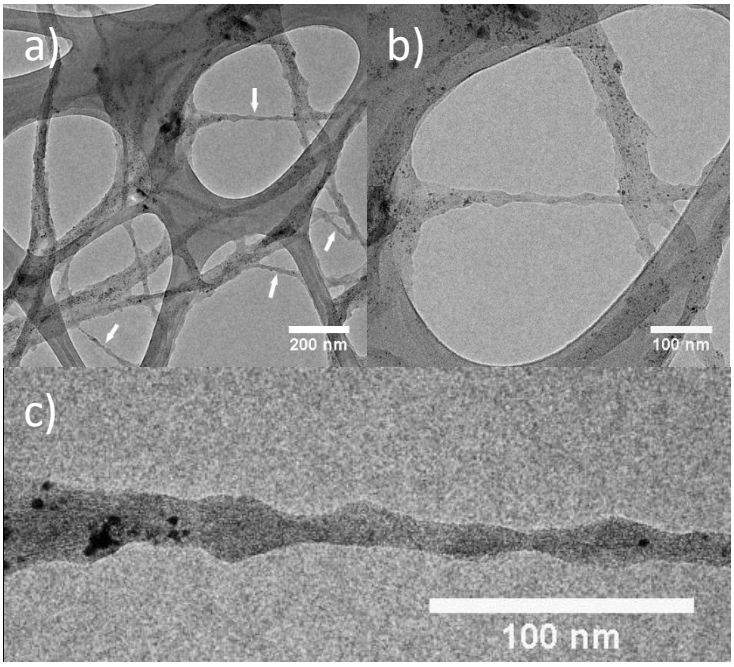

Figure 74: TEM images of P44 @ SWNTs nanohybrids (SWNTs/P44 ratio = 0.13) deposited on a lacey carbon grid (a few minutes after sonication); a) Low magnification image representing the general aspect of the sample; b) Medium magnification image with a single nanotube or a small bundle covered by polymer; c) High magnification image of the nanotube/bundle described in b, showing a structure that could be compatible with helical wrapping;

Deposition of the suspension onto carbon grids show a different morphology. We observe the presence of linear fibers perpendicular to the nanotube axis (**Figure 75** in a shish-kebab type structure (as observed in bad solvents).

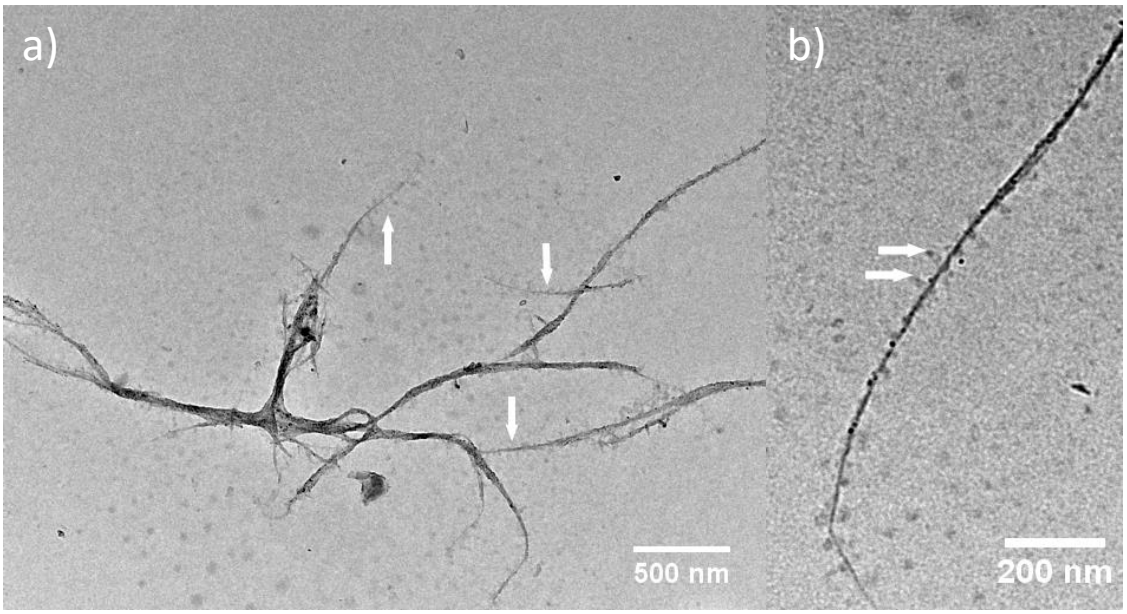

Figure 75: a) Low magnification TEM image of P44@SWNTs nanohybrids (SWNTs/P44 ratio = 0.28) deposited on carbon grids (few minutes after sonication), showing a bundle reuniting many smaller bundles and individual nanotubes b) High magnification TEM image of a small dispersed bundle. In both images, arrows point to zones were polymer fibers grow from the carbon nanotubes.

To be sure of the structure actually adopted by the system in solution, Cryo-TEM experiments were performed on these samples (**Figure 76**). We observe in these images structures similar to those observed on carbon films. This result suggests that what is observed on lacey carbon grids is the collapse of the fibers due to the drying of the grid.

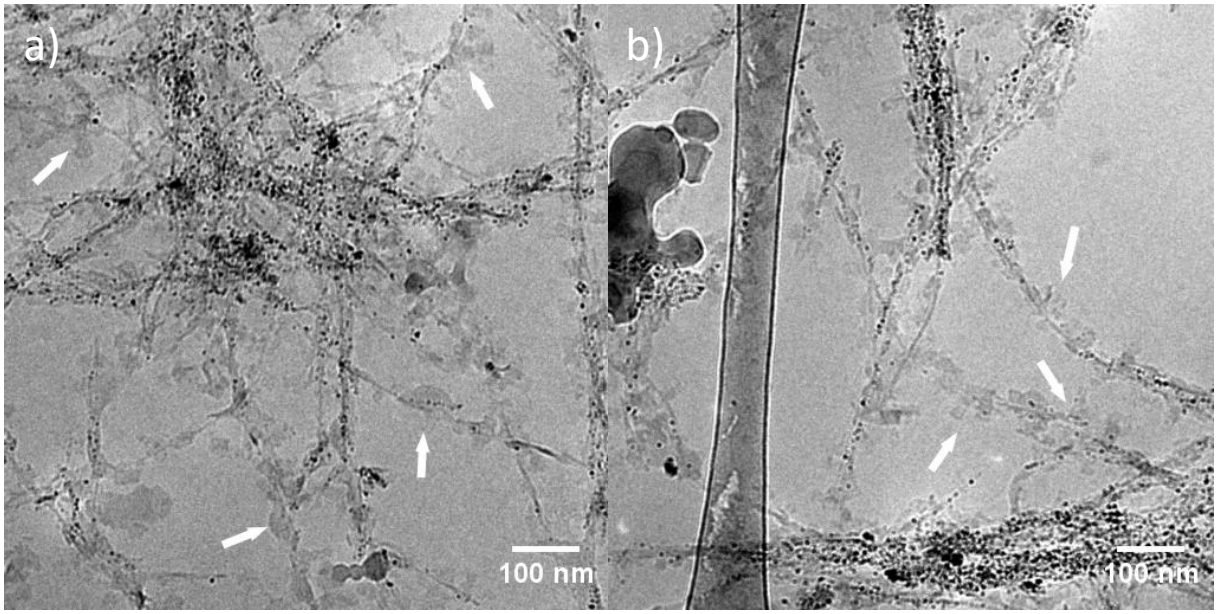

Figure 76: Cryo-TEM images of P44@SWNTs nanohybrids (SWNTs/P44 ratio = 0.28). Arrows show small polymer fibers grew from the nanotubes surfaces

Our interpretation about the formation of the shish-kebab structure is the following. Due to the high mass of the polymer, only a small fraction of the chain length adsorbs onto a nanotube or a small bundle of nanotubes, the rest staying in solution. The parts of neighboring chains adsorbed on the same tube which remain in solution aggregate (in an extended configuration perpendicular to the tube axis) due to their low solubility. They form seeds which nucleate the aggregation of the polymer chains in the solution. As in pure P3HT solutions, further aggregation is governed by interchain π-π interactions between the polymer backbones units and fibers grow perpendicularly to the tube axis, on one or on either side of the tubes because of steric effects. This interpretation will be refined in view of the kinetics study of aggregation of P44 with the tubes.

In conclusion, the polymer mass has a drastic effect on the dispersion and morphology of the nanohybrids. P7 have short length and high solubility leading to an extended helical configuration when adsorbed onto the tubes. Compared to P21, the higher solubility of P7 leads to a weaker number of aggregates as well as a smaller amount of chains within these aggregates and to a lower amount of dispersed nanotubes. The chain length of P44 does not lead to the adsorption of the entire chain onto the tube. The remaining parts in solution of neighboring adsorbed molecules aggregate to form seeds from which fibers grow perpendicular to the tube axis.

3. Effect of the comonomer

Although our copolymers contained only around 15 % of comonomer, we have tested the influence of the bulky aniline group on the polymer organization. The SWNTs/CP36 critical mass ratio for stability in solution is lower than for P21@SWNTs, estimated to 1.36 ± 0.30 mg of SWNTs/mg of CP36. This was expected from the results from the solvent extraction method (**Chapter 2**).

Plasmon corrected spectra of CP36@SWNTs are displayed on **Figure 77a**. Doing the same treatment as the one on **Figure 61a**, we can estimate the amount of adsorbed thiophene units onto the SWNTs for CP36 (**Figure 77b**). The obtained value is 1.21 ± 0.13 mg CP36/ mg SWNTs (or 0.55 ± 0.06 3-hexylthiophene groups per hexagon), which is slightly higher than the one obtained for P21@SWNTs (1.00 mg P21/ mg SWNTs). The higher resolution of the polymer aggregate peaks is in agreement with a higher number of interacting units.

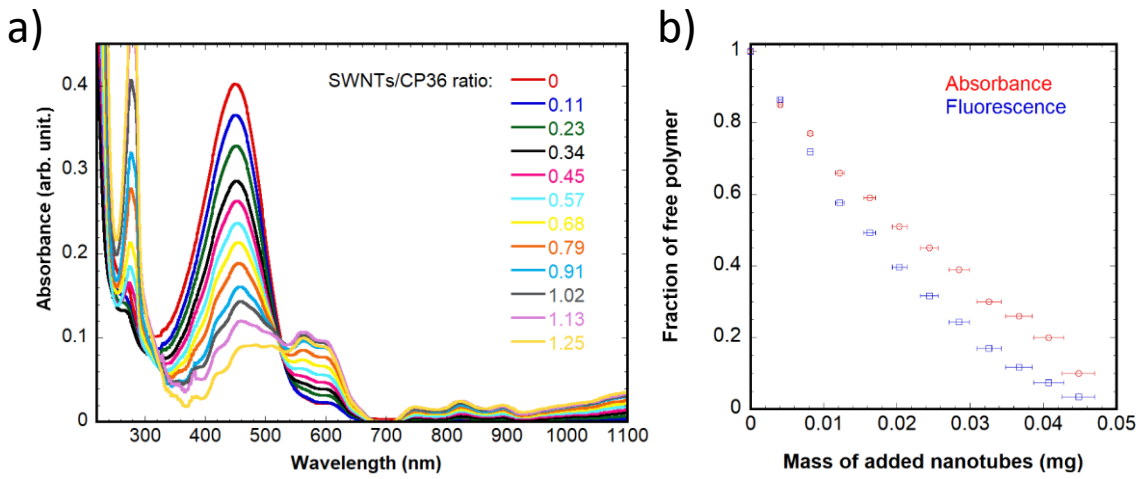

Figure 77: a) Plasmon corrected curve of CP36@SWNTs nanohybrids; b) Fraction of CP36 as a free polymer as a function of the mass of added nanotubes. The red dots were obtained through fitting a well dissolved polymer curve into the CP36@SWNTs spectra corrected by the plasmon, as was done for P21 in ***Figure 61****; the blue dots were obtained by comparing the emission maximum for different amounts of carbon nanotubes.*

The optical spectra of the CP36@SWNTs show a lower $A_{0\text{-}0}/A_{0\text{-}1}$ ratio than P21@SWNTs, suggesting lower polymer intrachain order (**Figure 77a**). The estimated ratio is 0.91 ± 0.02, being lower than the 0.99 ratio of the P7 and P21 homopolymers.

The appearance of CP36@SWNTs observed by TEM is very similar to that of P21@SWNTs. Moreover, the absence of emission of the aggregates lead us to the conclusion that CP36 adopts the same wrapping configuration in the nanohybrids than P21. The same is true for the couple CP5@SWNTs and P7@SWNTs.

A few tests were performed with the polymer containing all functionalized side chains (FP17). Sonicating a small fraction of carbon nanotubes with a solution of this polymer in THF did not form a stable dispersion of carbon nanotubes. The obtained material tended to flocculate and float even during sonication. Further experiments were abandoned due to this behavior.

From the above results, it difficult to conclude about the effect of the comonomer. It seems that the number of thiophene units in the aggregates in CP36@SWNTs is slightly larger than the one in P21@SWNTs). The decrease of the J-type character of the aggregates may come from the disorder induced by the presence of the aniline.

4. Effect of the alkyl side chain

As for the polymer molecular weight, the solubilizing side chain was shown in the literature to display an important effect on the dispersibility and selectivity of the polymer towards carbon nanotubes.

To check this effect and possibly obtain more stable nanohybrids, tests with an homopolymer with dodecyl side chains (PD18) were performed.

Results are shown for a PD18 solution (4 mL, 25.4 µg/mL) to which fractions of 50 µL of SWNTs mother suspension (0.42 mg/mL, 21 µg per fraction) were added (**Figure 78a**). Critical ratio for precipitation was of 1.45 ± 0.05, inferior only to that of P21@SWNTs nanohybrids. The polythiophene backbone for PD18 would be equivalent of that of a P3HT of molecular weight of only 11 kg/mol, suggesting a positive effect of the side chain on the solubility of the nanohybrids. The nanohybrids are stable only for a few hours nonetheless.

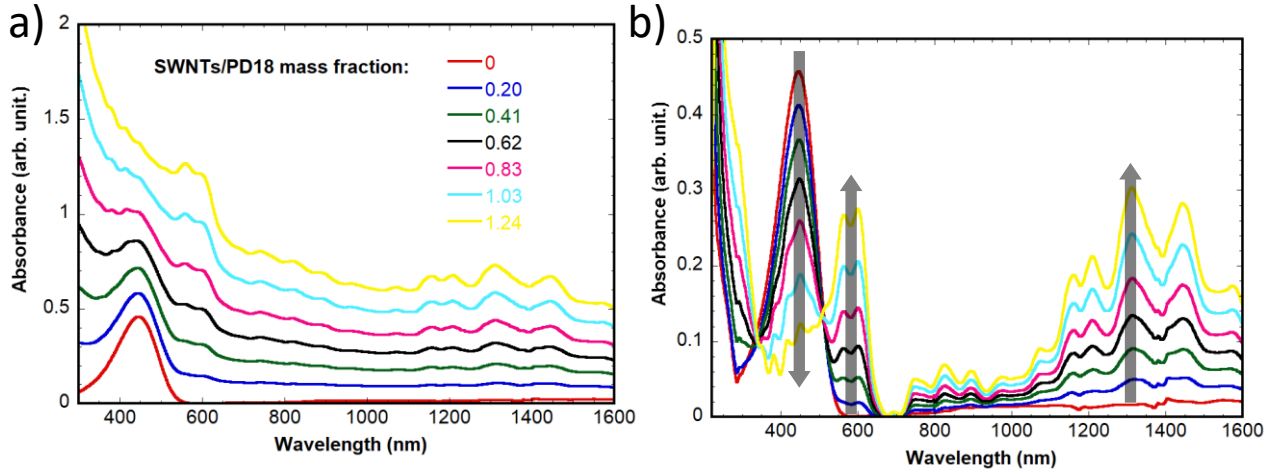

Figure 78: a) Optical absorption spectra of PD18@SWNTs nanohybrids as a function of the amount of SWNTs added to a PD18 solution (25.4 µg/mL). Each SWNTs addition corresponds to an increase of 0.20 on the SWNTs/PD18 ratio; b) Spectra corrected by the π-plasmon absorption (fit in 1/λ).

Although this polymer presents a higher solubility than the similar mass polymer P21, we observe well resolved aggregate peaks (**Figure 78b**), which suggests larger aggregates. It is also clearly observable that the $A_{0\text{-}0}/A_{0\text{-}1}$ ratio is superior to 1 (1.03 for the last curve), suggesting the highest intrachain order between the studied systems.

The amount of adsorbed thiophene units is however lower than the one obtained for P21, attaining only 0.64 ± 0.05 mg PD18/ mg SWNTs (0.18 ± 0.02 3-dodecylthiophene units). This follows the tendency of chain length shown in **Section 2**, although such a low coverage is surprising considering the high resolution of the polymer peaks.

The obtained systems only show emission of the free polymer, as for the other polymers except P44, suggesting that the emission of the aggregates is completely quenched due to energy transfer to the carbon nanotubes.

5. Effect of the type of carbon nanotube

Another interesting effect is that of the diameter of the nanotubes. As it was mentioned in **Chapter 1**, many conjugated polymers have some kind of selectivity on the nanotube diameter, and most of those lose completely their ability of solubilizing the nanotubes when their diameter increases. Increasing the chain length is one of the methods of increasing the solubility of tubes of larger diameters, as well as using longer alkyl chains, so we expect the longer polymers and the poly(3-dodecylthiophene) to better solubilize nanotubes of larger diameter

Figure 79 shows the absorption spectra of P21@DWNTs nanohybrids.. . The different configurations of SWNT@SWNT in DWNTs (leading to different Van der Waals interactions between them) and the large dispersity in diameter of the DWNTs lead to large variety of the π-plasmon. Their contribution to the optical spectra cannot be estimated by a simple 1/λ approximation and only the raw spectra can be analysed.

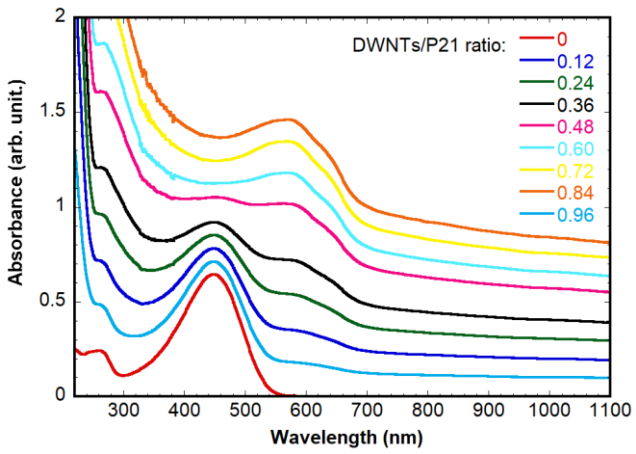

Figure 79: Absorption spectra of P21@DWNTs nanohybrids. Each addition corresponds to 9.6 µg of DWNTs, the solution containing a total of 79.8 µg of P21.

From **Figure 79**, we observe an overall behavior similar to what observed for P21@SWNTs.

We can see however that the value of $A_{0\text{-}0}/A_{0\text{-}1}$ for this system is lower than for P21@SWNTs (estimated to be of about 0.8-0.9). As it can be seen in **Figure 80**Figure 80: TEM image of isolated nanohybrids P21@DWNTS (DWNTs/polymer ratio = 0.9)**.,** the polymer adsorbed onto the DWNTs adopts the same configuration than P21@SWNTs. The decrease of the ratio $A_{0\text{-}0}/A_{0\text{-}1}$ is consistent with a better matching of thiophene units of two stacked chains in the aggregates due to the flatter surface of DWNTs compared

to SWNTs. This better matching increases the interchain interactions, increasing the relative H-type character of the aggregates. The P21@DWNTs nanohybrids are stable in suspension up to a critical concentration ratio of 0.96 ± 0.12 mg DWNTs/ mg P21, which is less than half the one obtained for P21@SWNTs nanohybrids. DWNTs presents lower specific surface ratio than SWNTs, which would suggest they require less polymer to obtain the same surface coverage. This suggests that they are even less stable than indicated by the critical concentration ratio above and ca be taken as another effect of the different conformation of the polymer aggregates on the DWNTs compared to SWNTs.

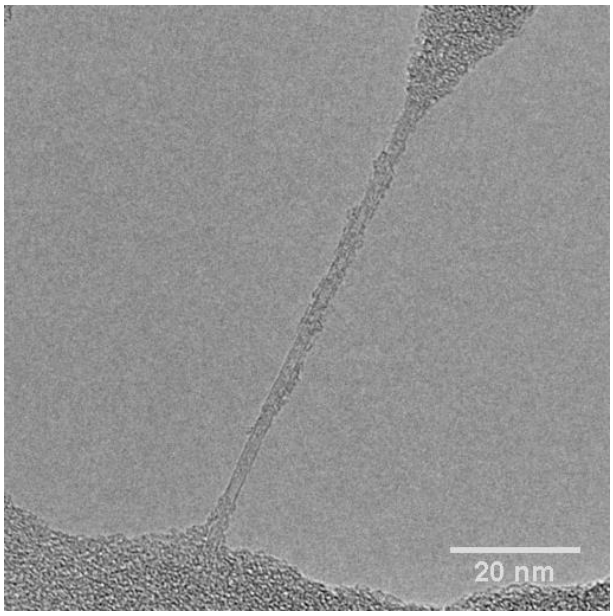

Figure 80: TEM image of isolated nanohybrids P21@DWNTS (DWNTs/polymer ratio = 0.9).

The results obtained for P44@DWNTs are similar to those obtained for P21@DWNTs (**Figure 81**). As in the case for P44@SWNTs, results shown here are not obtained in equilibrium, a kinetics of growth of aggregates being observed.

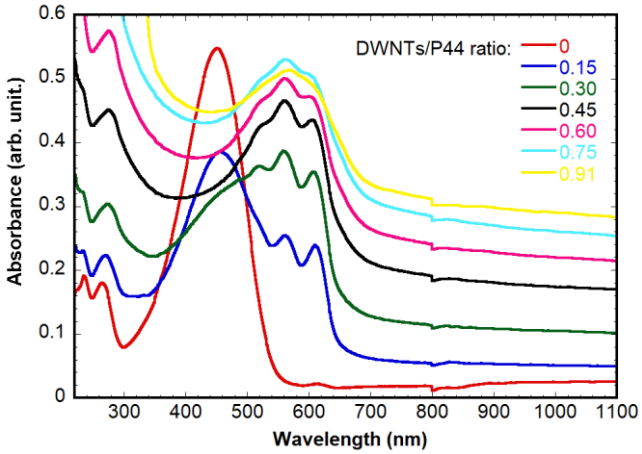

Figure 81: Absorption spectra of P44@DWNTs. Each addition corresponds to 10 µg of DWNTs into a solution containing 68 µg of P44

The total amount of dispersed nanotubes actually increases compared to P44@SWNTs, passing to 0.91 ± 0.11 mg DWNTs/ mg P44 (0.63 ± 0.08 for P44@SWNTs). The increase in the dispersibility of DWNTs compared to SWNTs can be related to the slower aggregation kinetics (see **Section 6**). Because of the slowly growing aggregates, more polymer remains in solution at a given time, being available to DWNTs on posterior additions.

TEM shows that DWNTs behave as SWNTs in P21@CNTs nanohybrids and P44@CNTs. (**Figure 80**). P21@DWNTs wraps onto the tubes while P44 forms shish-kebab structures

Fluorescence measurements are in agreement with these TEM observations, aggregates being emissive only for the P44@DWNTs shish-kebab structure.

This effect of the diameter of the tube is fully consistent with the observed effect of the polymer mass. It is the couple (polymer mass – nanotube diameter) which governs the aggregation in the nanohybrids.

6. Effect of the solvent

As observed with the mass effect, the morphology of the nanohybrids seems to be dominated by the solubility of the polymer. This could explain why shish-kebab structures can be obtained when carbon nanotubes are added to solutions of P3HT in bad solvents.[9,16]

To test this hypothesis, we started with a P21 solution in anisole (13 µg/mL). At this concentration, P21 is not soluble at room temperature. Complete dissolution is attained when heating the solution up to 70 °C, point at which it becomes bright orange. Still, aggregation happens when the solution is cooled back to room temperature. In these conditions, aggregation is complete in less than 15 min after the solution is cooled to room temperature, resulting in a dark red suspension of polymer fibers.

By adding a fraction of SWNTs (25 µg, final concentration 6.3 µg/mL) to the P21 solution in anisole at 70 °C and sonicating at this temperature, we observed the same changes in the optical absorption spectrum (**Figure 82**) as when we add SWNTs to a solution of P21 in THF at room temperature, *i.e.* the appearance of the broad band attributed to P3HT aggregates.

However, when cooled to room temperature, the absorption of the polymer aggregates increases, while little free polymer remains in solution. However, contrary to the aggregates' bands observed at 70°C (or when performing the experiment in THF), we clearly distinguish the vibronic peaks of the polymer aggregates. This suggests a larger number of interacting polymer chains in the aggregates for this system. Also, contrary to pure P21 solution in anisole, aggregation was complete at the moment of the

first analysis (about 5 min upon the solution is taken out of the heat bath), implying a faster aggregation kinetics due to the presence of the SWNTs.

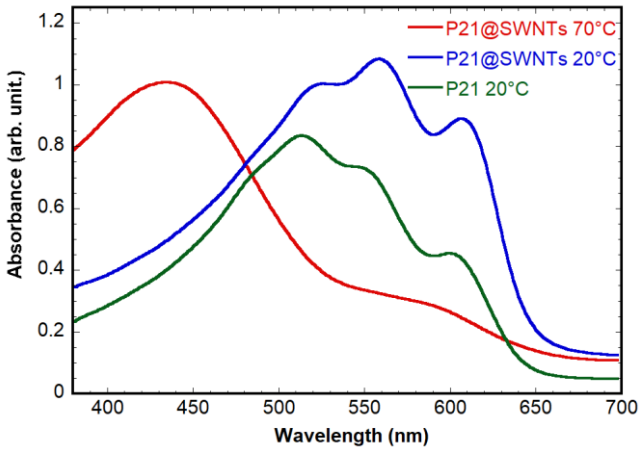

Figure 82: Optical absorption spectra of P21@SWNTs in anisole at 70 °C (red) and 20 °C (blue). The spectra of P21 in anisole at 20 °C is shown (green) as a reference.

The $A_{0\text{-}0}/A_{0\text{-}1}$ ratio is higher for the aggregates formed on the carbon nanotubes than for those obtained by homogeneous nucleation. This implies a stronger intra-chain ordering of the polymer chains in the aggregates due to a template effect of the carbon nanotubes surfaces.

TEM images (**Figure 83**) of the suspensions deposited on a carbon grid reveal that the nanohybrids have a shish-kebab morphology, similar to those observed for P44@SWNTs nanohybrids in THF.

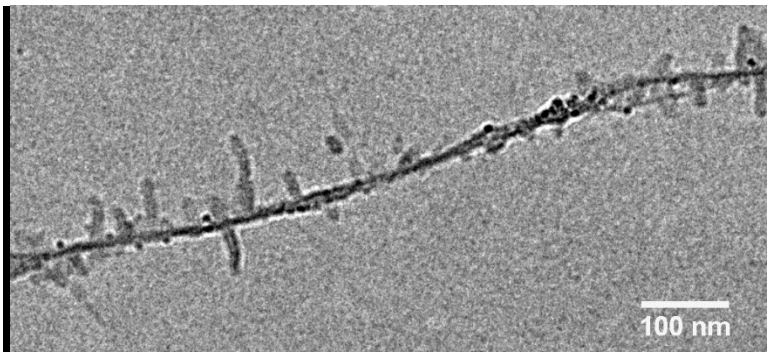

Figure 83: TEM image of P21@SWNTs nanohybrids prepared in anisole deposited onto a carbon grid.

To confirm the results above are not an effect of the procedure rather than of the solubility, the same experiments were performed in THF. A solution of similar concentration (13 µg/mL) was heated to 50 °C (limited by the boiling point of THF). Then, a volume of SWNTs mother suspension was added to the solution followed by sonication. Finally, it was cooled back to room temperature. The obtained spectra as well as the observed morphology were similar to those of nanohybrids prepared directly at room temperature, thus the thermal treatment could not be the reason for this result.

In conclusion, the morphology of the nanohybrids is dependent on the solubility of the polymer chains in the system. Aggregation in a bad solvent is similar to that of longer chains, originating shish-kebab structures. This happens because polymer-polymer interactions stabilize more the system than the solvation of the chains and its gain of entropy.

7. Study of the kinetics of aggregation of P3HT due to heterogeneous nucleation with carbon nanotubes

Heterogeneous nucleation of P3HT by carbon nanotubes is reported in the literature when the latter are introduced into a super-saturated solution of the former in a bad solvent.[71] This leads to the growth of fiber like structures moving away from the carbon nanotubes, in what is called shish-kebab structures (the shish being the CNT, the kebab being the polymer fibers)..

These structures are similar to those obtained for P44@SWNTs, which also displayed a kinetics of polymer aggregation. However, our solutions of P3HT are not in a supersaturated phase, no polymer aggregation being observed at room temperature in the concentrations studied, even with application of sonication. Thus, the study of the behavior of P44@CNTs, and its comparison with P21@CNTs (which did not display any aggregation kinetics) can be useful for complementing our understanding of these systems.

7.1 Study of the kinetics of aggregation for P44

A phenomenon of polymer aggregation with time was observed when we were preparing P44@CNTs nanohybrids. Because of its high molar mass (M_n = 44 kg/mol, Đ = 1.86), which means it has lower solubility than shorter chains and that aggregation phenomena are more probable with this polymer.

A typical evolution of the optical absorption spectrum of P44@SWNTs is shown on **Figure 84**. (SWNTs/P44 ratio of 0.28, initial P44 concentration of 0.19 µg/mL). We observe the increase of the band corresponding to P3HT aggregates with time after addition of SWNTs to the solution, together with a reduction on the absorption of the free polymer at 450 nm. At the end of the experiment, no traces of flocculation are observable. We point out that the beginning of the kinetics is unfortunately missing due to the operating mode. The first spectrum of **Figure 84** has been recorded about 5 minutes after sonication of the mixture P44 and SWNTs. The absorbance of the free P44 of the starting solution is of 0.83.

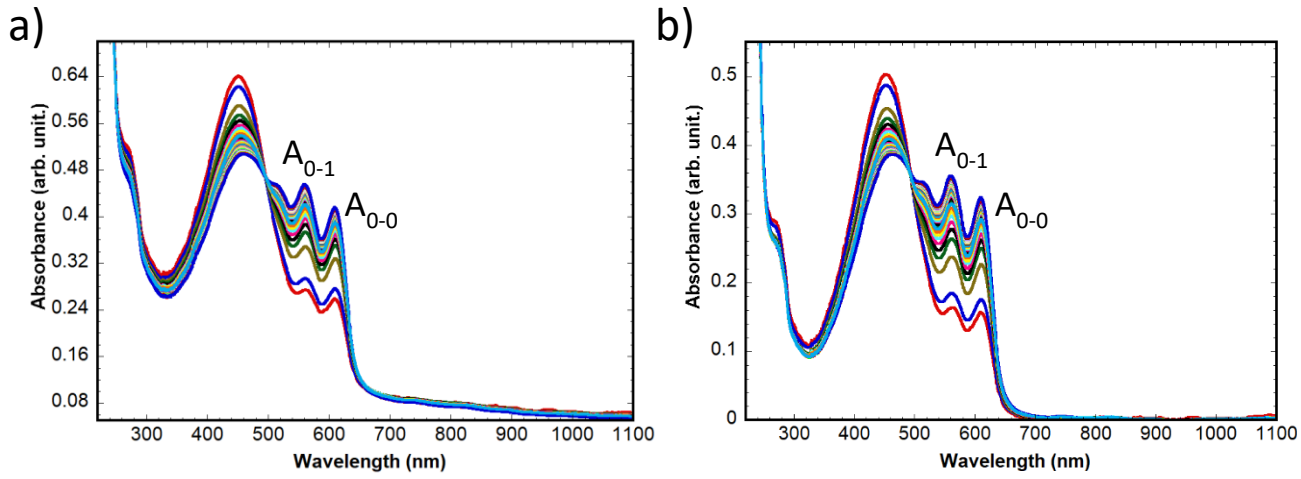

Figure 84: Kinetics of P44 aggregation upon addition of SWNTs. The curves are spaced of 30 min each. SWNTs/P44 ratio is 0.28 for this experiment (75 µg of P44 in 4 mL of solution). a) Raw curves; b) Corrected by the π-plasmon absorption

Taking the amount of free (dissolved) polymer to be proportional to the absorption at 450 nm we can fit the evolution of the absorbance at this wavelength as a function of time by a stretched exponential, called Avrami's equation in this field (see **Equation 3**), (**Figure 85a**). This same function also fits well the absorptions $A_{0\text{-}0}$ and $A_{0\text{-}1}$ of the polymer aggregates (**Figure 85b**).

$$A = A_{inf} + A_0 e^{-\left(\frac{t}{\tau}\right)^{\alpha}} \qquad \textbf{(3)}$$

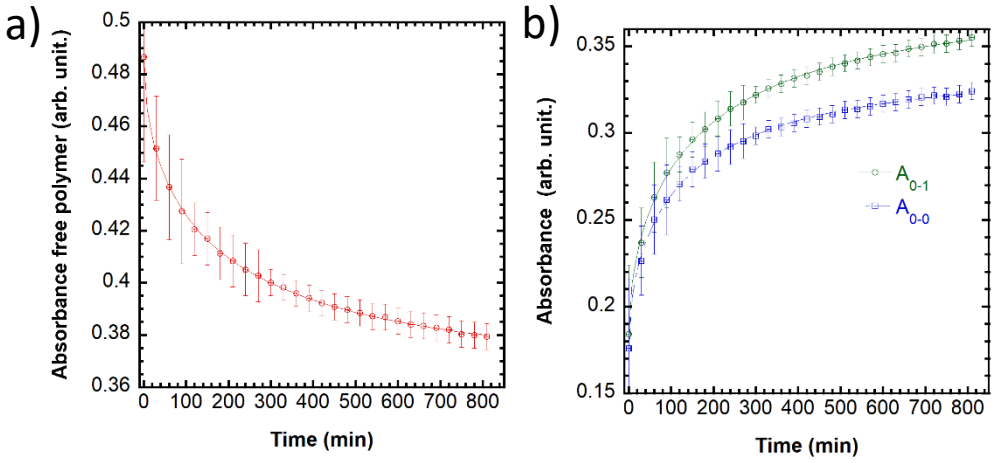

Figure 85: Evolution of the absorption of a) free polymer band at 450 nm and; b) Aggregated polymer peaks ($A_{0\text{-}0}$ at 610 nm and $A_{0\text{-}1}$ at 560 nm, respectively blue and green) with time for a P44@SWNTs solution (SWNTs/P44 ratio = 0.28)

The parameters given by the fits (**Figure 85a** and **b**) are similar (**Table 4**). The parameter α in Avrami's law is usually related to the dimensionality of crystal growth. A value of 1 is expected in this case, as we observe an apparent one dimensional growth of the aggregates. This parameter is supposed to

increase with the dimensionality. Repeating this experiment, we found that, independently of the concentration of polymer and of SWNTs introduced at the beginning of kinetics experiments, values of α are of 0.45 ± 0.11 (**Table 5**), lower than the value expected for a simple one dimensional growth of stacked stretched monodispersed chains. This was also observed for crystallization of P3HT (M_n = 24 kg/mol, Đ = 1.8) on organogelators, but not interpreted.[232]

*Table 4: Parameters of Avrami's fit for the curves shown in **Figure 85**. The last column was obtained by translating the points by 5 min and taking the absorbance of the pure P44 solution as the value at t = 0.*

	450 nm (free polymer)	560 nm(A_{0-1})	610 nm (A_{0-0})	Free polymer (450 nm)*
A_{inf}	0.37 ± 0.04	0.37 ± 0.05	0.33 ± 0.02	0.32 ± 0.04
A_0	0.12 ± 0.04	0.19 ± 0.05	0.16 ± 0.02	0.51 ± 0.10
τ (min)	190 ± 30	180 ± 27	145 ± 23	40 ± 8
α	0.54 ± 0.15	0.57 ± 0.13	0.56 ± 0.13	0.22 ± 0.10

Table 5: Parameters of Avrami's fit (from the variation of the free polymer at 450 nm) for different SWNTs/P44 ratio and for different kind of carbon nanotubes

		τ (min)		α	
	Ratio	Average	Standard error	Average	Standard error
SWNTs	0.14	510	21	0.39	0.05
	0.28	206	90	0.45	0.12
	0.56	91	35	0.46	0.07
DWNTs	0.16	490	80	0.44	0.05
	0.32	370	70	0.45	0.07

We must note that the changes on the fit parameters strongly depend on the time at the initial values. For example, last column of **Table 4** was obtained by using the absorbance value of the pure P44 solution (before addition of SWNTs) and the other points were shifted by 5 min, the estimated time between the end of sonication and the measurement. This results in a strong decrease of α and of the characteristic time The fact that we obtain a good average value between all our experiments means errors are systematic.

Some authors have attributed such kinetics to the to the distribution of molar masses of the polymer, the longer chains aggregating before the smaller ones according to their lower solubility.[178] To test this hypothesis, we performed a kinetic experiment while analyzing the molar mass of the polymer remaining in solution by SEC. **Figure 86** shows the SEC profiles of the starting P44 solution, immediately after sonication with the nanotubes and 24h after beginning of the kinetics. Because of the low concentrations of our solutions, only UV-Visible detection at 450 nm was sensitive enough for

detecting the polymer. The three samples were filtered through a 0.45 µm PTFE filter, so the SEC profiles represent only well dissolved chains.

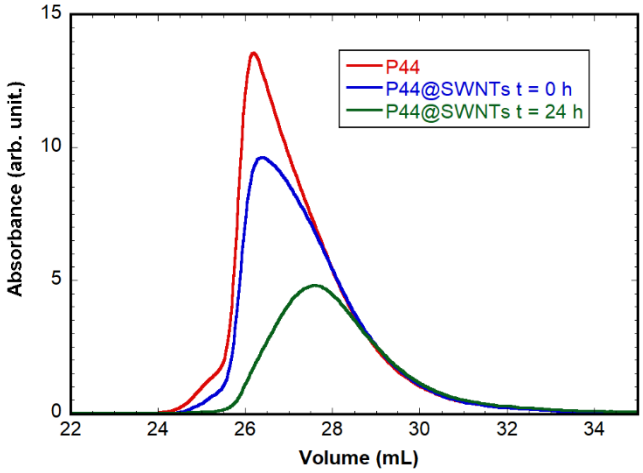

Figure 86: SEC profiles (measurement of optical absorbance at 450 nm) of the soluble (not aggregated) polymer during different phases of our kinetics. The red curve corresponds to the profile before addition of the carbon nanotubes.

These results indicate clearly a polymer fractioning during the aggregation. Immediately after the addition of SWNTs polymers of high molecular weight are present in the solution, their signature decreasing after 24h with respect to shorter chains, in agreement with the interpretation given in ref. 12. (**Table 6**). As for optical absorption, first spectrum has been recorded about 5 minutes after sonication of the mixture, explaining the differences in M_n observed between the pure polymer solution and the time "t=0" suspension.

Table 6: Descriptors of the molar bass for different moments in the kinetic study

Time	M_n	M_w	Dispersity
P44	45256	78879	1.74
P44@SWNTs, t = 0 h	41064	69864	1.7
P44@SWNTs, t = 24 h	24700	48787	1.98

Analyzing the $A_{0\text{-}0}/A_{0\text{-}1}$ ratio, we observe that it corresponds to a relatively high intrachain ordering at the beginning of the kinetics, ratio which decreases with increasing time (**Figure 87**).

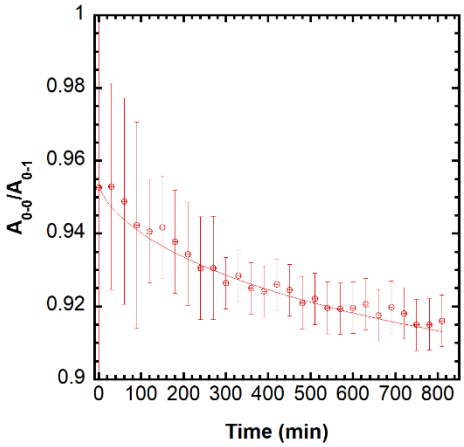

Figure 87: Evolution of the ratio $A_{0\text{-}0}/A_{0\text{-}1}$ calculated from spectra from ***Figure 85b.***

The effect of the distribution of molar masses of the polymer onto the kinetics of aggregation is explained as following: the longer chains aggregate before the smaller ones due to their lower solubility. Moreover, the longer chains have a smaller density of defects (chain-ends) than shorter chains, leading to a high intrachain order at the beginning of the kinetics. As smaller chains integrate to the system, their chain ends act as defects in backbone plane of the aggregate, reducing their J-type character due to the disorder introduced in the backbone plane[178] and impacting the value of the parameter α in Avrami's equation.

However, as reported in chapter 1, above a mass of 10 kg/mol, chains are folded in the aggregates of pure P3HT. Thus, one can reasonably imagine that P44 chains adopt this configuration in the aggregates (the mass of P44 is 44 kg/mol) which could also have an impact on the parameters of the kinetics. Lastly, the absolute values of these have to be taken with care as they strongly depend on the time t=0 of the experiment.

Besides this, the only other tendency is that aggregation is faster when the amount of carbon nanotubes added is higher, due to the increased the number of seeds (as shown by the lower characteristic time τ, **Table 5**).

Finally, for a given mass concentration of carbon nanotubes, the characteristic time for DWNTs is approximatively twice than for SWNTs. This is expected as the number of nucleation sites (related to the specific surface of the tubes) is smaller for DWNTs than for SWNTs. As a consequence, the diameter distribution of the nanotubes (which becomes even larger if we consider that dispersed bundles, that may vary in their own in diameter as well, could also act as seeds) could also contribute to stretched exponential variation of the kinetics in our experiments.

Fluorescence experiments were similarly performed on these systems. Excitation wavelengths were chosen to separate the contribution of the two polymer species.

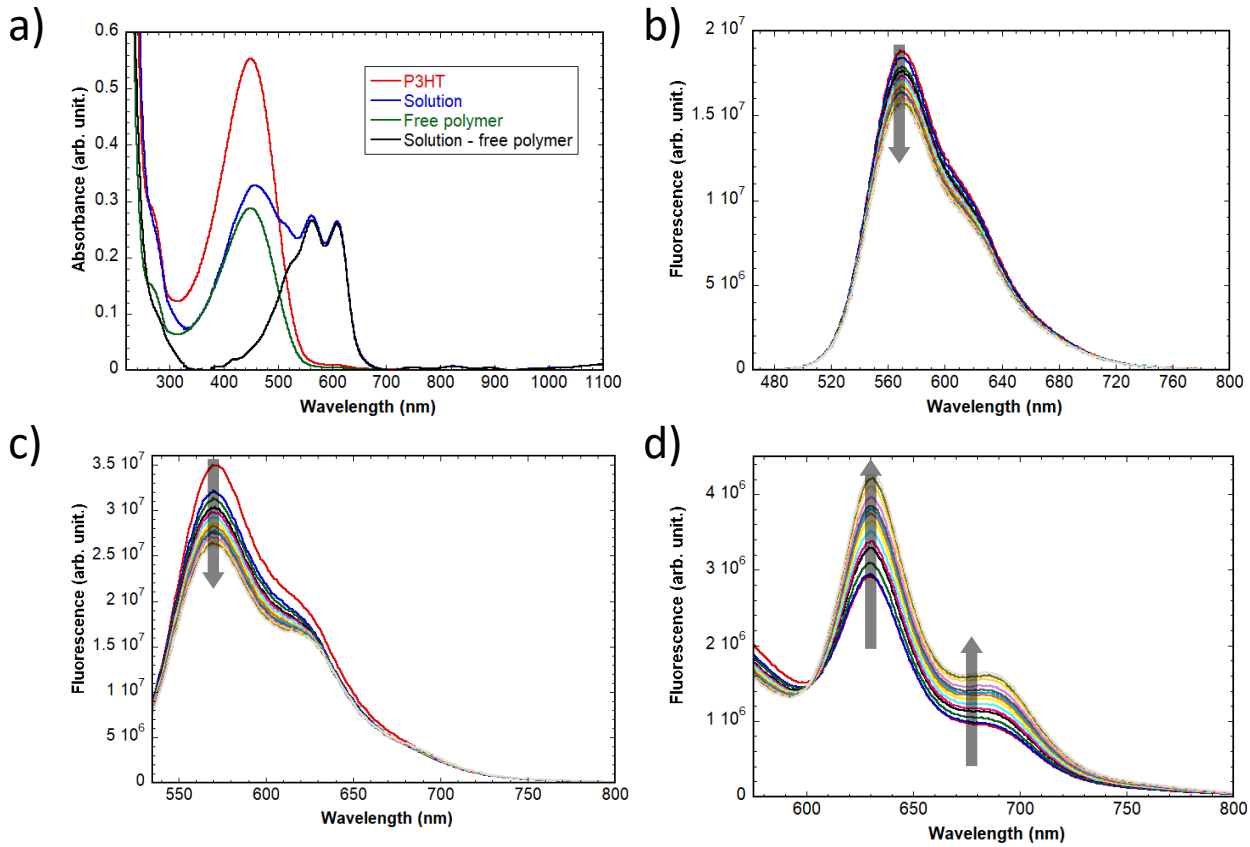

Figure 88: a) Spectral decomposition of a P44@SWNTs suspension; b-d) Emission spectra evolution in time with excitation wavelength of b) 450 nm (free polymer absorption); c) 520 nm (close to the isosbestic point); d) 560 nm (polymer aggregate absorption).

Figure 88b to **d** display the spectra obtained through excitation respectively of the free polymer, close to the isosbestic point wavelength and of the polymer aggregates only. As expected, we observe a decrease of the free polymer emission with time, which is attributed to the decrease of their concentration in the solution when aggregates grow. Contrary to the aggregates in all other P@SWNTs and PC@SWNTs nanohybrids, these ones are emissive, their emission increasing as they grow (**Figure 88d**).

The fact that the aggregates are non-emissive at 570 nm[167] allows for the decomposition of the spectra (**Figure 89a**) and the subtraction of the emission of the free polymer in solution.

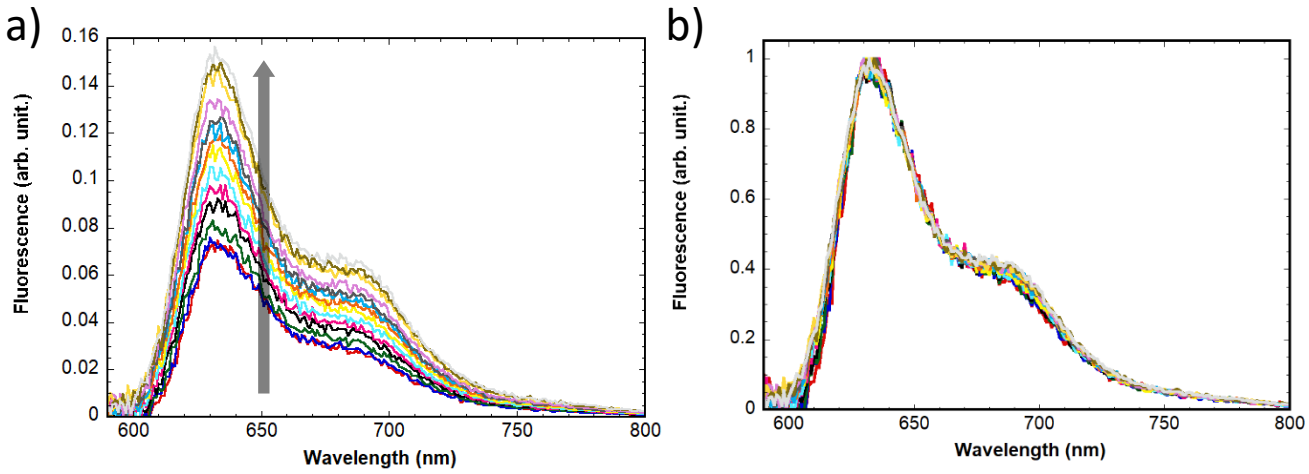

Figure 89: a) Emission kinetics attributed to the aggregates of P44@SWNTs nanohybrids for different times (varying time interval) b) Spectra normalized by its maximum.

A constant I_{PL}^{0-0}/ I_{PL}^{0-1} ratio is observed (**Figure 89b**), while a decrease is expected (from absorbance curves, **Figure 85**). Indeed, an increase of a H-type contribution, suggested by optical absorption experiments, should lead to a decrease of I_{PL}^{0-0} (in pure H-type aggregates this emission is forbidden). This expected decrease could be counterbalanced by the increase of I_{PL}^{0-0} emission due to the superradiance effect in J-aggregates. Actually, the classical manifestation of superradiance follows by recognizing that the radiative decay rate, γ_R, scales as the square of the transition dipole moment. Hence, γ_R in J-aggregates of N chromophores is N-times larger than a single one.[169] Thus, as the aggregates grow, the number of polymer chains increases as do the 0-0 emission. This is a complicated issue as other effects may contribute to such r the emission of exciton localized in defects.[169]

TEM images obtained on samples deposited onto carbon grids show the growth of nanofibers from the carbon nanotubes as time elapses. 20h after sonication (**Figure 90a** and **b**) relatively long fibers can be observed. The presence of short fibers already observable a few minutes after sonication (**Figure 90c**) supports a growth perpendicular to the tubes axis. Sadly, electron diffraction patterns were not observed due to the low density and size of the fibers.

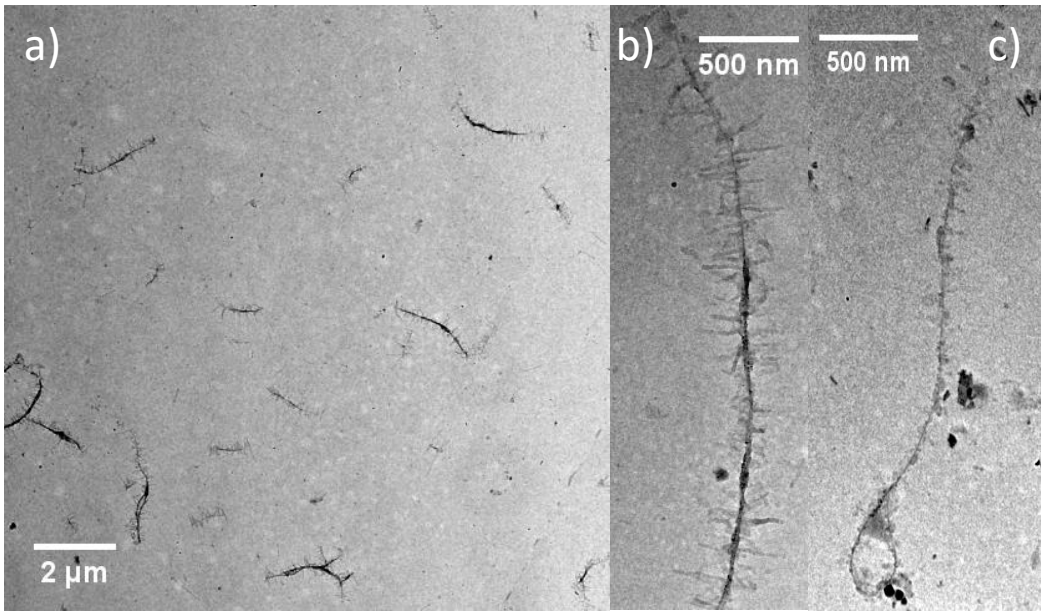

Figure 90: TEM images obtained by deposing P44@SWNTs nanohybrids on a carbon grid at the end of the kinetics (20h after sonication) a and b) Low magnification and high magnification images ; c) High magnification image of nanohybrids deposited a few minutes after sonication.

We conclude that the high molecular weight of P44 leads to the formation of shish-kebab structures even in non-supersaturated solutions. The aggregation of about 40% of the free polymer occurs in the first 5 minutes. This faster kinetics at the beginning suggest that the seeds are formed very rapidly. At the very beginning, a large amount of free polymer densely adsorbs (by a fraction of its chains length) onto the tubes meanwhile the parts of the chains remaining in solution spontaneously aggregates in seeds perpendicular to the chains. This could explain the regular discrete structuration of the aggregates along the tube.

7.2 Study of the kinetics of aggregation for P21

The observed behavior for P44 instigated the search for a similar behavior for P21 in order to better understand the nucleation behavior of the nanotubes on the P3HT aggregation.

Preliminary studies performed at the same conditions do not show any evidence of an evolution of the profile with time. SEC measurements were performed before addition of SWNTs and after addition of SWNTs and subsequent sonication and there is a small fractionation effect – reduction of absorption is relatively higher for larger masses, although there seems to be adsorption onto the tubes for higher molecular weights (**Figure 91**).

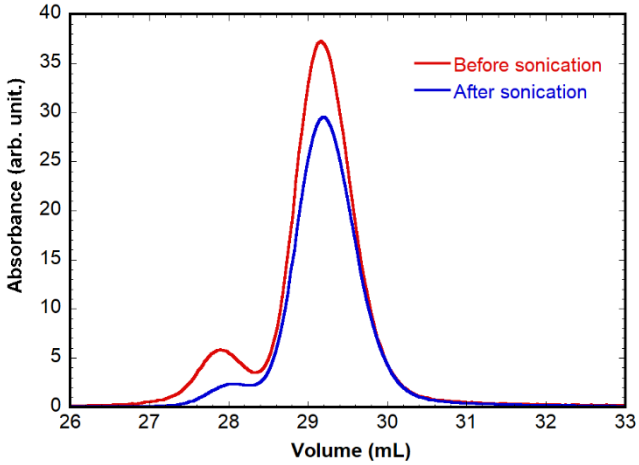

Figure 91: SEC profiles for the polymer P21 remaining in solution before and after addition from nanotubes.

Table 7: Average molecular weight and dispersity of the polymer in solution before and after interaction with the carbon nanotubes

Time	M_n	M_w	Dispersity
Before sonication	20244	25179	1.24
After sonication	20444	22596	1.11

We observe a small reduction of dispersity (1.24 to 1.11, **Table 7**). There is a reduction of M_w that corresponds to the decrease of the higher molecular mass peak, but without an overall change in M_n. The two low molecular mass tails in **Figure 91** almost superpose, suggesting that chains of short length interact weakly with the tubes, in agreement with the results obtained with P7 (**Section 2**).

8. Conclusion on non-covalent nanohybrids

P3HT, is capable of dispersing CNTs when both are sonicated together in an appropriate solvent, forming what we call non-covalent nanohybrids. The behavior of these nanohybrids depends drastically on the polymer molecular weight and solubility.

PHTcoAHT behaves similarly to the homopolymer, the low functionalization rate of its side chains not affecting the observed morphology. It was observed nonetheless that the presence of the aniline at the end of the side chains reduces the dispersibility of the CNTs and lowers intrachain interactions between thiophene units in the aggregate. Increasing the length of the alkyl side chain on the other hand leads to improved solubility of the nanohybrids.

The most interesting property of the interaction of P3HT with the nanotubes is the template effect of the nanotubes on the polymer structure, highly increasing the polymer chain stretching, as observed mainly by optical spectroscopy. This stretching of the polymer chains leads to a J-like type of aggregate, which is usually tricky to synthesized. It is especially interesting that this kind of aggregate forms in good solvents in concentrations that normally promotes the full solubility of the polymer.

This polymer template effect can also be used for forming highly ordered aggregates of shish-kebab structure. Unfortunately, it is difficult to obtain long aggregates due to defects introduced during the fiber growth, for example when incorporating chains with different molecular weight. The ordering is still very good for such a rapid growth process, and optimization of the growth conditions (for example, by slowing its growth through temperature control) could lead to longer highly ordered fibers, which could be of interest in organic electronics.

This high ordering of the polymer chains is accompanied by electronic interactions between the polymer and the carbon nanotubes, notably observed by the quenching of both free polymer and their aggregates wrapped around the tubes and by the red-shift of the optical transitions of the nanotubes. This quenching is caused by energy transfer from the polymer aggregates, intimately adsorbed onto the carbon nanotubes surfaces, to the nanotubes themselves. However, when fibers are grown from the nanotubes, their fluorescence is not completely quenched, due to the less efficient charge transfer from the more distant units

9. Characterization of the covalently functionalized nanohybrids

Covalent nanohybrids were prepared as described in Chapter 2 by using an *in situ* formed diazonium at the end of the PHTcoAHT side chains. The yield of this reaction was low (on the order of a few percent, estimation from optical absorption spectra leading us to a few hundred µg of final nanohybrids (starting from tenths of milligram of carbon nanotubes and few milligrams for the copolymer).

Due to this low overall yield, many characterization techniques which require large amounts of material, such as ATG and XPS, could not be performed on the obtained samples.

9.1 Optical spectroscopy

Optical spectroscopy of the obtained suspensions is not straightforward because of the isoamyl nitrite, which has an absorption band that overlaps that of the copolymer, causing a large saturation below 550

nm in all our samples, preventing the observation of the effect of the functionalization on the metallic nanotubes bands and on the free copolymer band.

The UV-vis spectrum of the covalent nanohybrids and their non-covalent precursors are shown in **Figure 92**. In both cases the peaks are relatively broad, suggesting that bundles are suspended. There is little to no changes in the relative absorption peaks of the SWNTs, which is compatible with the low functionalization rate we expect from the distance between amine groups.[15] Changes in the copolymer/SWNTs ratio did not affect the observed spectra, suggesting that the distance between defects actually is the limiting factor due to steric hindrance.

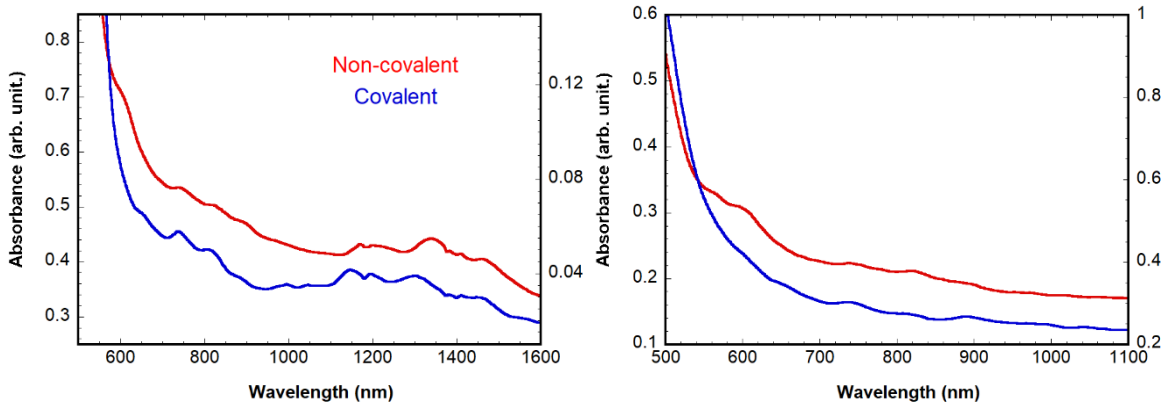

Figure 92: Absorption spectra of covalent and non-covalent nanohybrids; a) CP36@SWNTs; b) CP5@SWNTs. In both cases, red line left scale for non-covalent, blue line right scale for covalent

Unlike non-covalent nanohybrids suspensions, the covalent ones are stable up to two months and cannot be isolated by precipitation in toluene. Using the experimental conditions described above for the functionalization of SWNTs, the UV-vis spectrum of both nanohybrids is saturated by the copolymer absorption below 550 nm (**Figure 92a and b** respectively for CP36 and CP5). This prevents the observation of the effect of the functionalization on the SWNTs absorption bands at this region, particularly in the case of a low covalent functionalization rate, as expected.[7] However, between 1100 and 1500 nm, the SWNTs optical transitions of the non-covalent nanohybrids are red-shifted compared to that of the covalent ones. It indicates that the thiophene units do not stack onto the tubes as easily in the covalent sample as in the non-covalent one. Moreover, the broad band in the range 500 – 600 nm characteristic of thiophene aggregates, present in the UV-vis spectrum of the non-covalent nanohybrids, is absent in that of the covalent one. It shows that covalent functionalization increases the disorder in the copolymer chain packing. These UV-vis results, together with the drastic difference in the stability of the solutions of both nanohybrids, clearly show that the organization of the copolymer in both systems is different.

We could also obtain both CP5@DWNTs and CP36@DWNTs nanohybrids as stable suspensions, while former leads to very unstable non-covalent nanohybrids. **Figure 93** shows the absorption spectra of both types of CP36@DWNTs nanohybrids. The overall behavior was the same as for the SWNTs nanohybrids.

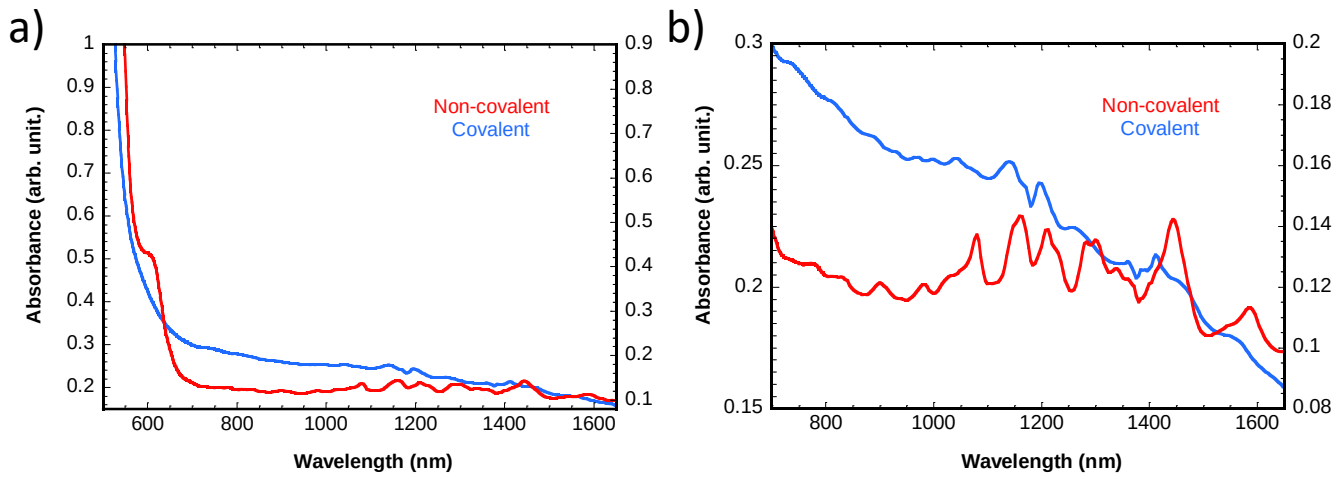

Figure 93: Absorption spectra of covalent and non-covalent nanohybrids of CP36@DWNTs (red line left scale for non-covalent, blue line right scale for covalent); b) zoom on the higher wavelength features

We conclude through these experiments that the covalent bind polymer cannot assume its wrapping conformation, assuming a more disordered conformation instead. These results are similar with those obtained for PFO@graphene, in which the polymer is also attached through its side chains which leads to its adoption of disordered conformation, observed as a blue-shift of its absorption features.[233]

9.2 Raman spectroscopy

Thin films for Raman were prepared by spin coating from a THF solution onto a glass plate then rinsed with THF in order to remove the excess of polymer and isoamyl nitrite.

For non-covalent nanohybrids and whatever their preparation method, the lineshape of the modes around 1380 cm^{-1} and 1450 cm^{-1} (respectively assigned to C-C intra-ring and C=C in-plane symmetric stretching[226,234]) is close to the ones observed on pure polymer thin films as well as those typically reported for "annealed" films in the literature[235] (**Figure 94**). The relative intensities of the peaks of the RBM modes are not significantly different to those of SWNTs.

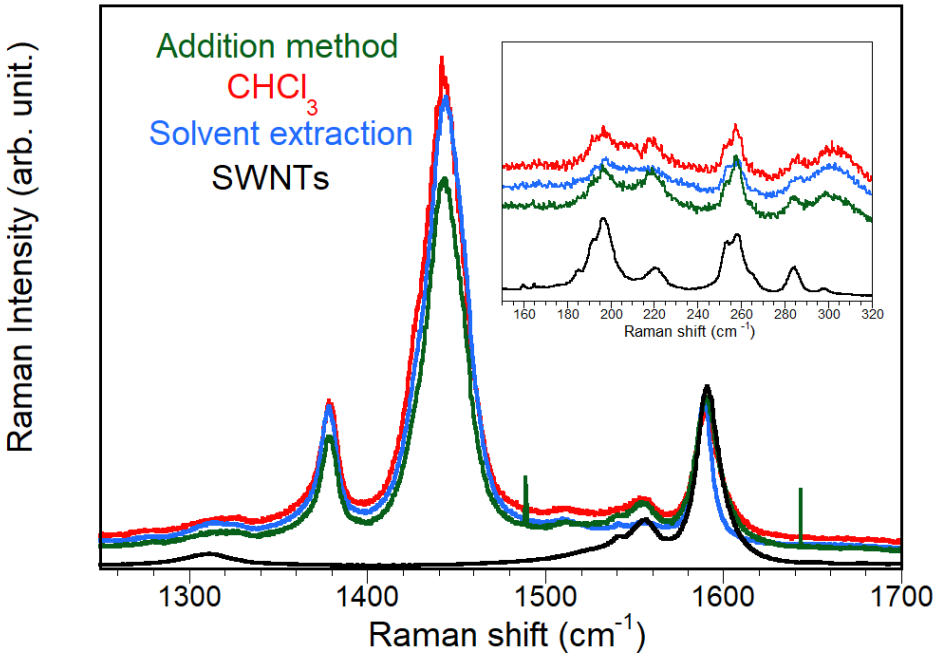

Figure 94: Raman spectra (excitation: 633 nm) of P21@SWNTs nanohybrids obtained from dispersion in $CHCl_3$ (red) or in THF by the addition method (green) and solvent extraction method (blue). Spectrum of the pure SWNTs is shown for reference (black). All the spectra were normalized by the intensity of the G mode. Inset: RBM modes.

Examples of Raman spectra excited at 633 nm of thin films prepared from suspensions of raw (surfactant suspended) and non-covalent (weight ratio of 1.26) and covalent CP36@SWNTs nanohybrids are shown in **Figure 95**.

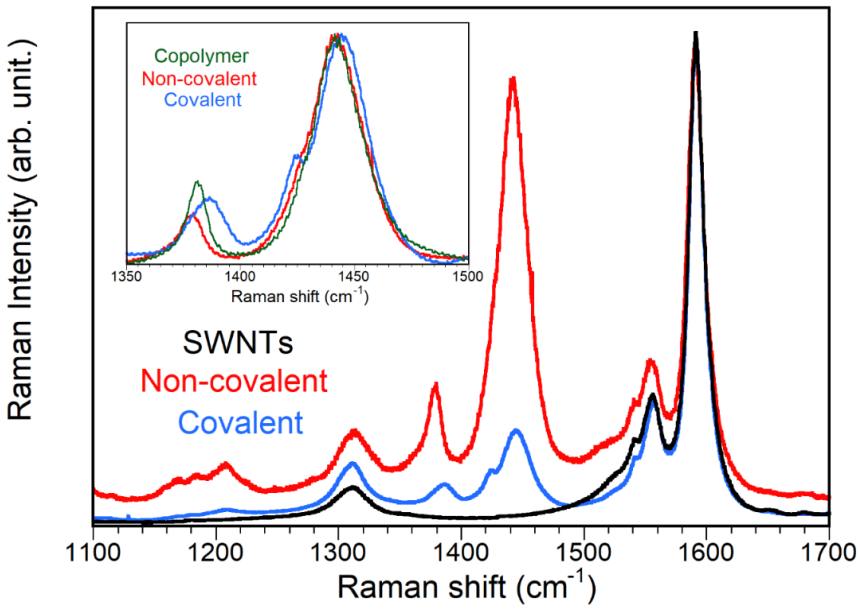

*Figure 95: High frequency range of Raman spectra (excitation wavelength 633nm) of thin films of raw SWNTs (black), **CP36** (green), non-covalent (red) and covalent (blue) SWNT/**CP36** normalized at 1590 cm^{-1}. Inset: zoom of the thiophene C-C and C=C stretching modes in SWNT/**CP36** non-covalent (red) and covalent (blue) nanohybrids; all the spectra are normalized at 1450 cm^{-1}.*

The Raman modes of SWNTs, i.e. the D band around 1320 cm^{-1} and the G modes in the 1500 - 1600 cm^{-1} range, appear close for the three samples with a D/G intensity ratio slightly higher in the covalently functionalized SWNTs (integrated ratio 0.12 ± 0.01 against 0.10 ± 0.01). This is consistent with the expected low amount of covalent grafting (10^{-3} per C atom) corresponding to a large distance between defects, of the order of 2 - 3 nm,[214] and thus negligible changes in D/G ratio.[15,111]

In this way, the polymer peaks became the main reference for studying the effects of functionalization. On non-covalent nanohybrids, the lineshape of the modes around 1380 cm^{-1} and 1450 cm^{-1} (respectively assigned to C-C intra-ring and C=C in-plane symmetric stretching[226,234]) is close from the ones obtained on pure polymer thin films as well as those typically reported for "annealed" films in the literature.[235]

The lineshape of the modes of the PHTcoAHT is different in the non-covalent and covalent samples (Inset **Figure 95)**. These spectral changes indicate clearly that the organization of the copolymer is not the same in both samples. First of all, there is the appearance of a mode at 1425 cm^{-1} in the C=C vibrations range. Second, the C-C band around 1380 cm^{-1} is upshifted and broadened (or there is a splitting with the appearance of a high frequency component). Some similarities can be found with the spectra of regiorandom P3HT (RRa-P3HT).[235] In particular, the mode around 1380 cm^{-1} displays a double peak structure in RRa-P3HT against a single narrow peak in RR-P3HT. This behavior observed for RRa-P3HT is however accompanied by an upshift and a broadening of the C=C band which is dispersive as a function of laser wavelength which is in disagreement with our observations on the covalent SWNT/PHTcoAHT samples.

The position of the C-C mode can be modulated by disorder and chemical modification. However, since no changes were observed on the copolymer for our blank tests (see **Chapter 2 Section 4**), this hypothesis can be rejected. Based on the calculations,[236] a splitting of the C=C mode, with calculated frequency of each component close with our experimental data, is only expected in the so-called torsional packing. This configuration is plausible as a consequence of the covalent link to the SWNTs, the appended aniline acting as a spacer between SWNTs and the PHTcoAHT skeleton.

Similar results were obtained at 532 nm (**Figure 96**). The mode at 1425 cm^{-1} is not as resolved at this wavelength as at 633 nm.

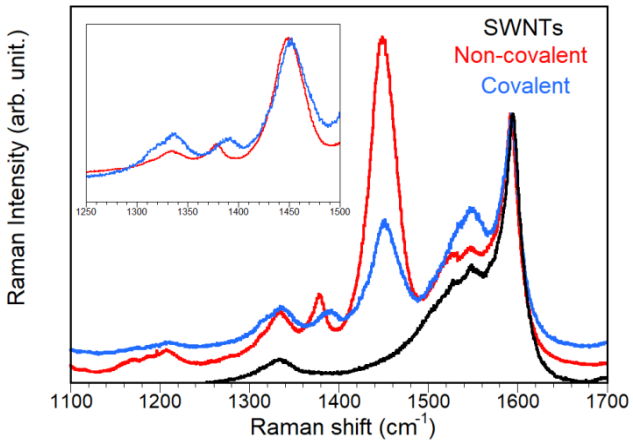

Figure 96: Raman spectra (532 nm) of CP36@SWNTs nanohybrids

The same results were also obtained for CP5@SWNTs (**Figure 97**), suggesting that the molecular weight does not influence the chain ordering after covalent functionalization, the same final conformation being obtained.

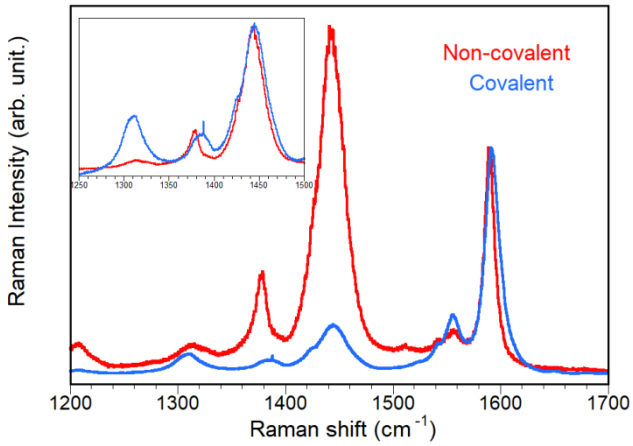

Figure 97: Raman spectra (633 nm) of CP5@SWNTs nanohybrids

Nanohybrids elaborated with DWNTs were analyzed in the same way (**Figure 98**). As for functionalized SWNTs, we observe a broadening of the C=C ring-stretching band as well as its blue-shift. We attribute the broadening as originated by the second mode but not as resolved as for SWNTs. The C-C ring stretching is also slightly broadened and blue-shifted compared to the non-covalent hybrid. Although the effects are less intense than they are for SWNTs, they are still compatible with the adoption of a torsional conformation. The smaller change could be explained by the adoption of a less distorted conformation, possibly due to the larger diameter of the nanotubes.

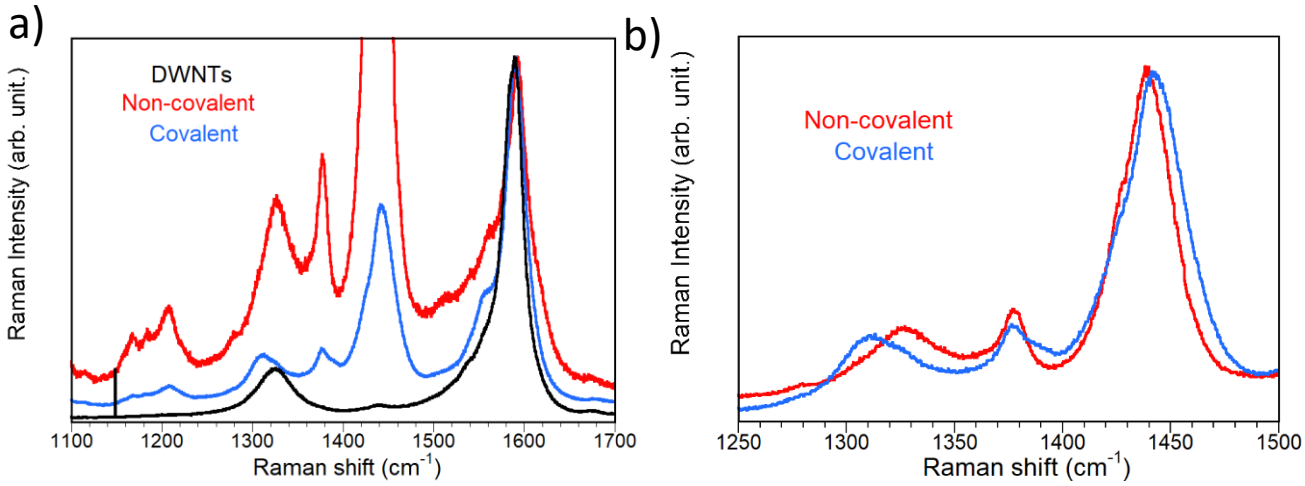

Figure 98: Raman spectroscopy of CP36@DWNTs non-=covalent (red) and covalent nanohybrids (blue) as well as the raw DWNTs (black) normalized by the G mode intensity; b) Raman spectra of the polymer main peaks normalized by the vinylic stretch intensity.

9.3 Conclusion

Despite the small amount of material used in the present study preventing XPS and TGA analysis, the stability of the covalent nanohybrids suspensions and the comparison between both covalent and non-covalent nanohybrids characterizations show that the copolymer organizes differently at the interface with the nanotubes in each case. Due to the covalent grafting by PHTcoAHT side chains, the copolymer adopts a torsional configuration preventing π-interactions between SWNTs and thiophene units and polymer aggregation. This leads to more solvated alkyl side chains and to steric effects leading to the very low grafting rate whatever the copolymer concentration. These results are in full agreement with the effectiveness of the reaction

Chapter 4: Functionalization of field effect devices

Carbon nanotubes are amphoteric materials. However, devices made of carbon nanotubes deposited onto SiO_2 substrates present p-type semiconducting behavior when exposed to air. This comes from the adsorption of water molecules at the CNT-SiO_2 interface, which are reduced upon electron transfer from the tubes.[237] These negative species at the interface CNT-SiO_2 also results in the screening of the applied gate potential. This leads to a hysteresis when measuring the drain-source current (I_{ds}) as a function of the gate voltage (V_{gs}), which alters the device performance, as do charges trapped at defects such as siloxane groups [237]

In this chapter, we aim at looking at the behavior of devices made of our nanohybrids, especially under light irradiation. Indeed, in P3HT-SWNTs nanohybrids, exposure to light of appropriate wavelength will generate electron-hole pairs in the polymer. Due to the expected type II heterojunction between P3HT and SWNTs, an electron transfer is expected from the polymer to the nanotubes, which could induce a photocurrent.

The results presented here are only preliminary, and more studies are planned to the confirm the conclusions presented.

1. Device description

Devices were prepared by Matthieu Paillet and Romain Parret at Laboratoire Charles Coulomb. In short, SWNTs prepared by laser ablation (presenting homogeneity of electronic properties, >1 µm of length and good structural quality) are dispersed in dichloroethane (1 mg/ 20 mL) by ultrasonication. This mother suspension is diluted (1/100x) and centrifuged.[238]

The supernatant is deposited onto a silicon wafer (with a controlled oxide thickness of 20 nm or 100 nm) by spin-coating. This substrate is previously treated in a bath of oxygenated water, ammonium hydroxide and ultrapure water (1:1:5 ratio) at 100 °C, which renders the surface hydrophilic. This leads to non-specific adsorption of the SWNTs and allows for molecular combing by the drying front during the spin-coating process, which leads to radial alignment of the SWNTs on the substrate. [238]

Gold electrodes are then deposited onto the surface by metal evaporation after creating a mask by lithography. The gaps between electrodes can be of 1 µm, 1.5 µm or 2 µm (each line of a cluster displayed in **Figure 99a**). [238]

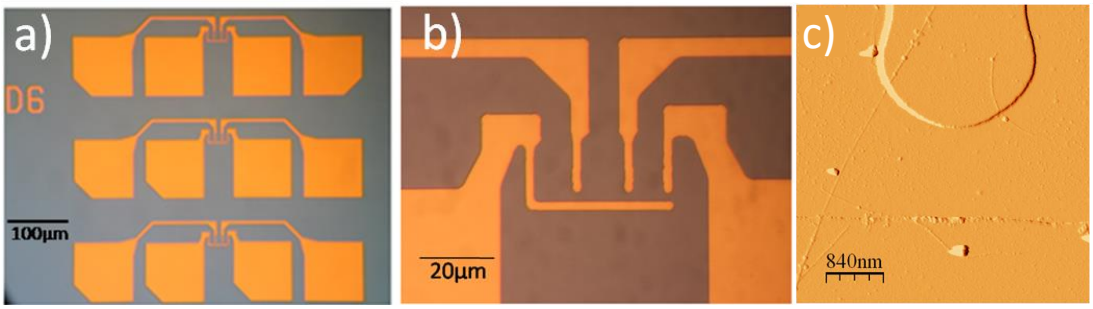

Figure 99: Optical image of a) an elementary cluster in a device. Each cluster is composed of 3 horizontal sets of 4 electrodes. The gap between electrodes is of 1 µm, 1.5 µm or 2 µm for the first, second and third set, respectively; b) The three upper electrodes are used as source (or drain) and the bottom one as drain (or source); c) Amplitude AFM image of a FET device. [238]

Because of the manufacturing method, only about 1/10 electrodes are contacted by carbon nanotubes. Due to the high contact resistance between electrodes and single nanotubes, these are not detectable, and the devices studied were actually contacted by small bundles.

As these bundles have different compositions and more than one bundle can contact the same two electrodes, each individual device show a specific behavior. For example, **Figure 100a** shows the behavior of some of the analyzed devices before functionalization. As it can be observed, these devices present different hysteresis and conductivity. The black flat curve represents the I_{ds} x V_g measurement performed on a metallic bundle, while the other curves represent measurements on semiconducting ones.

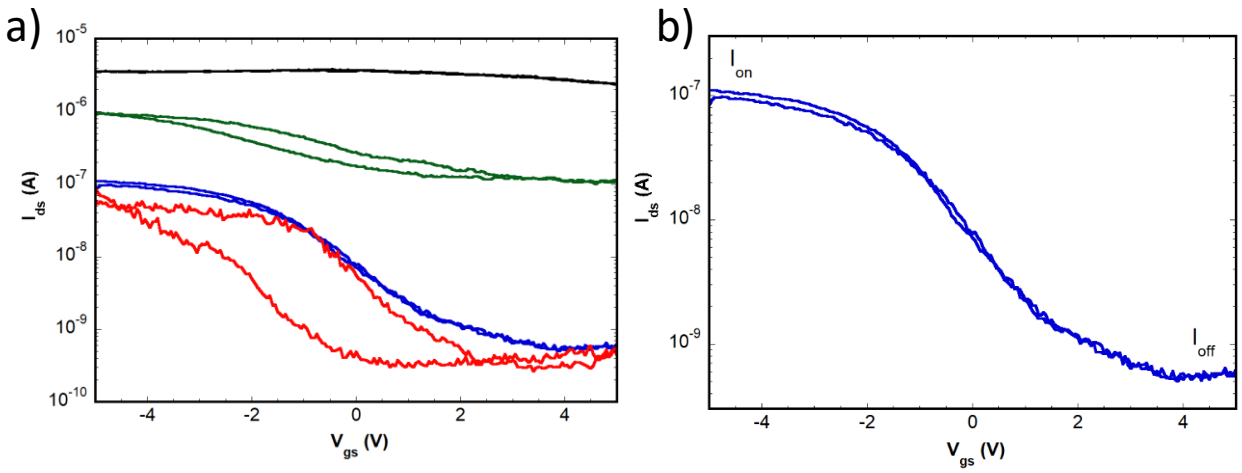

Figure 100 : Typical I_{ds} x V_{gs} curves of some devices showing the diversity of behaviors observed (V_{ds} = 1 V). Black curve represents a metallic bundle. Blue curve represents a semi-conducting bundle with small hysteresis, while green and red curves present a progressively larger hysteresis; b) Curve of a device without hysteresis with indication of the pertinent parameters.

The pertinent parameters in a I_{ds} x V_{gs} curve are (**Figure 100b**):

- I_{on}: saturation current for a given V_{ds} for an open-gate device.

- I_{off}: leakage current, it is the current detected for a given V_{ds} for a closed-gate device.
- I_{on}/I_{off}: represents the classical Figure of merit of a transistor, being independent of the geometry of the device. A higher I_{on}/I_{off} ratio represents a better device performance (maximum current output with minimum leakage current).

Because of this, a statistical analysis was performed on the devices before and after functionalization (between 10 to 25 devices in each wafer). If not mentioned, all I_{ds} x V_{gs} results come from curves obtained with I_{ds} = 1 V.

2. Non-covalent functionalization

Non-covalent functionalization was performed with CP36 and P44. In both cases, the device was plunged in a dilute solution (respectively 0.03 and 0.003 µg/mL) of the polymer for 2 min. It was then quickly plunged in pure THF for removing any excess polymer before being quickly dried under nitrogen flow.

I_{ds} x V_{gs} curves obtained on this sample do not show significant changes compared to those before functionalization. (**Figure 101a**). This suggests that non-covalent functionalization with CP36 does not affect the conductivity of the carbon nanotubes or that non-covalent functionalization was unsuccessful on these devices.

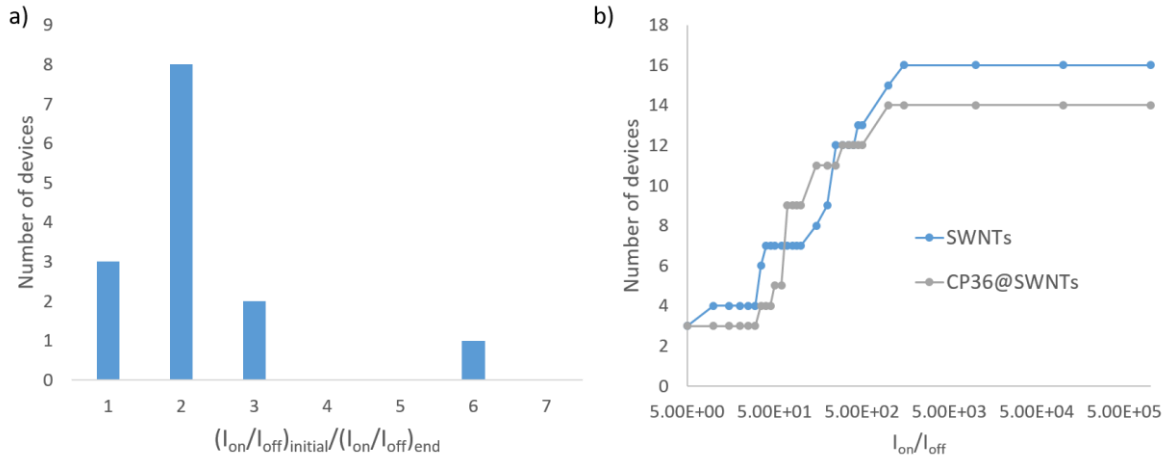

Figure 101: a) Histogram showing the ratio I_{on}/I_{off} (before/after non-covalent functionalization with CP36); b) Cumulated distribution of I_{on}/I_{off} values for the devices before (blue) and after (gray) non-covalent functionalization with CP36. Two devices could not be detected after functionalization.

AFM images (**Figure 102a**) of the devices do not show differences in the height of the nanotubes before and after functionalization. This, complemented by Raman spectroscopy mapping (**Figure 102b to d**)

of the samples, allows one to check the relative position of the carbon nanotubes (G band, **Figure 102c**) and the polymer (ring stretch, **Figure 102d**). It is important to note that only the nanotubes that are in resonance with the laser wavelength appears (for example, only one of the bundles is visible on **Figure 102c**). indication that there seems to be no polymer adsorbed onto the surface of the tubes.

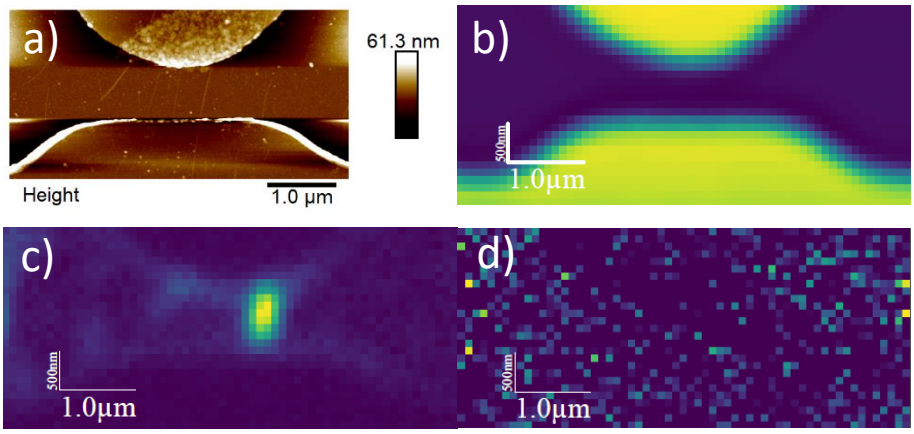

Figure 102: a) AFM image of a device after non-covalent functionalization; b) Optical reflectometry map of the device, displaying the position of the gold contacts; c) Map of the G band mode (excitation 532 nm) signal on the device; d) Map of the ring-stretching mode of P3HT on the device.

For most of the studied devices, no correlation is obtained between the position of the two components. As it can be observed in **Figure 102c**, P3HT appears more or less scattered everywhere in the sample.

The most probable explanation is that non-covalent functionalization with CP36 did not occur because the nanotubes are in contact with the substrate. This configuration hinders the possibility of the polymer to wrap around the carbon nanotubes.

3. Covalent functionalization

Covalent functionalization was performed on the same type of device by plunging the device in a solution of CP36 with added isoamyl nitrite (10 eq.) for 12 h. Two solutions of CP36 were used, one with the same concentration as the one used for non-covalent functionalization (0.03 µg/mL), and a second one about ten times more diluted (0.004 µg/mL).

After covalent functionalization, the characteristics of the devices are different from that of the pristine devices (**Figure 103**). For the more diluted solution, I_{on} is significantly reduced (between 50% and 75 % for 13/19 devices, the others presenting larger reductions).

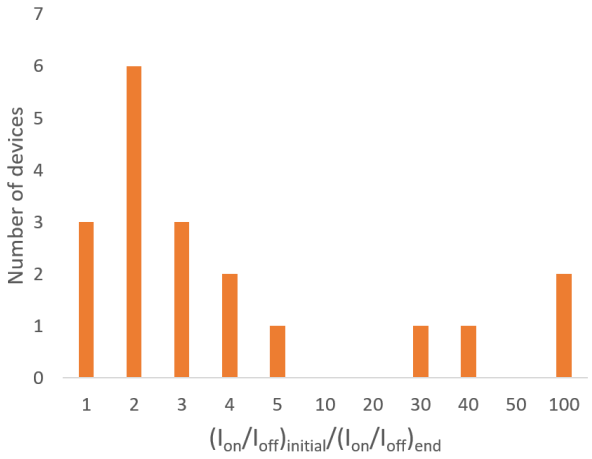

Figure 103: Histogram showing the ratio I_{on}/I_{off} (before/after covalent functionalization with CP36 in diluted conditions)

These are the kind of results expected for a low level of covalent functionalization.[239] However, performing a blank experiment with only THF in the same conditions leads to similar results (**Figure** 104), preventing any clear conclusion.

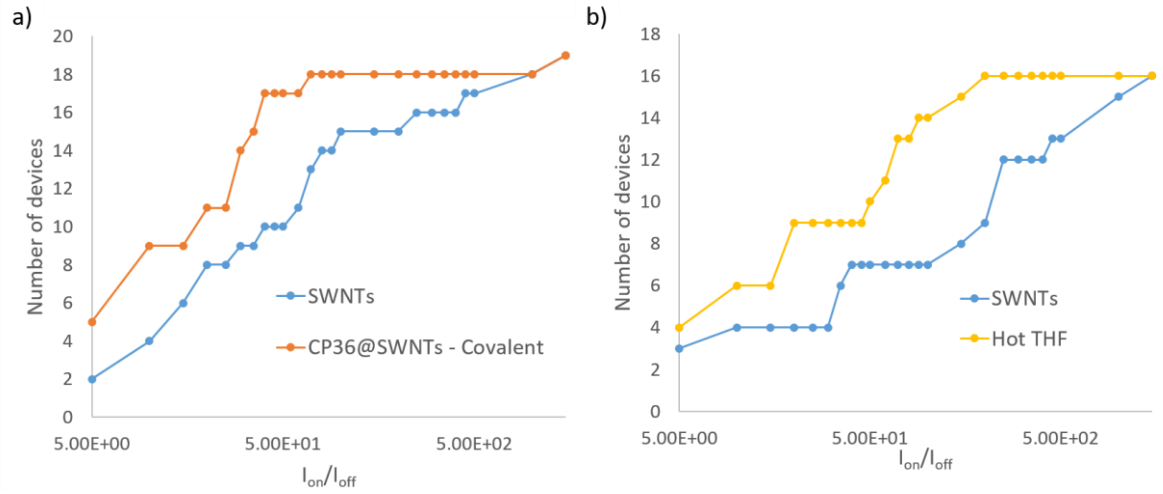

Figure 104: Cumulated distribution of the I_{on}/I_{off} behavior of the devices a) before functionalization (blue) and after covalent functionalization with CP36 in diluted conditions (orange); b) before functionalization (blue) and after exposure to hot THF (yellow)

Hysteresis observed on the I_{ds} x V_g curves increases for the covalent functionalized samples, while it remains constant for non-covalent functionalized samples and for the blank with hot THF. This behavior has been already reported in the literature, but no interpretation was given for such an effect.[239] We are not able to explain these results.

One of the main differences between non-covalent and covalent systems lies in the clear observation of a correlation between the position of the nanotubes and that of the polymer as shown by Raman mapping (**Figure 105**).

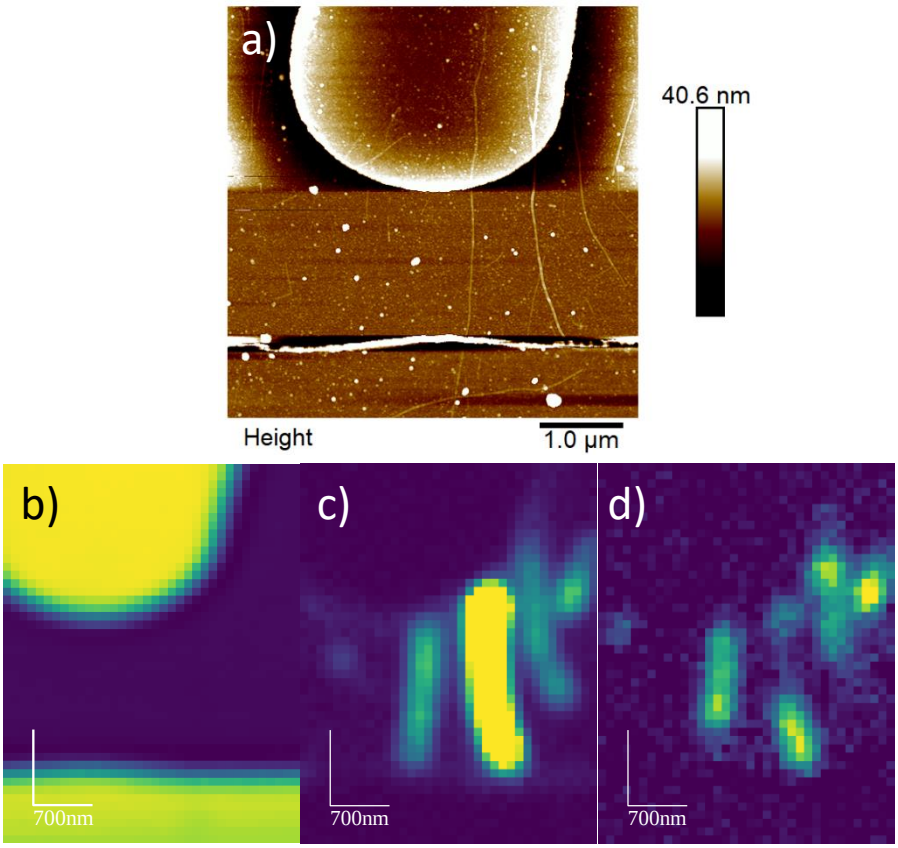

Figure 105: a) AFM image of a device after covalent functionalization with CP36; b) Optical reflectometry map of the device; c) Map of the G band mode (excitation 532 nm) signal on the device; d) Map of the ring-stretching mode of P3HT on the device

On the Raman spectra obtained at 532 nm (**Figure 106**) we observe an up-shift of 10 cm^{-1} the main polymer vibration (C=C in-plane symmetric stretch) as well as an up-shift of the C-C intra-ring vibration compared to the non-covalent nanohybrids. This is in agreement with the more disordered configuration of the covalently functionalized material (**Chapter 3**)

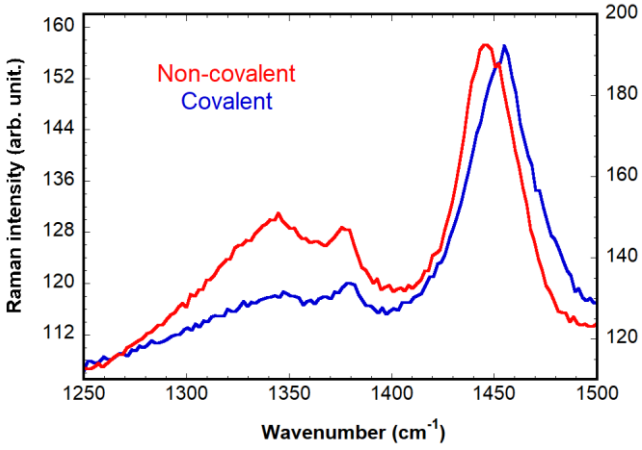

Figure 106: Raman spectra centered in the polymer signal for non-covalent and covalent functionalization . Profiles are normalized by the polymer ring-stretching mode intensity.

4. Photocurrent

Photocurrent tests were performed on both kinds of functionalized devices. These experiments consist in irradiating the sample with a laser (supercontinuum laser for controlling incidence wavelength) focused on a specific point of the device while measuring the current in the device. By scanning the sample with the laser we obtain a photocurrent map.

Photocurrent experiments performed on devices made of non-functionalized carbon nanotubes give poorly reproducible results.[238] Here again, this is related to adsorption of water molecules on the interface between the nanotubes and the silicon oxide layer, which leads to charge trapping. These charges modify the electric field locally, modulating the nanotube resistance, as would do a modification of V_{gs}, masking the observation of photocurrent. Moreover, the kinetics of trapping-detrapping of these charges is slow compared to the creation of photocurrent. Both effects lead to the presence of horizontal lines in the photocurrent maps when making measurements in open-gate conditions or under application of V_{ds} (**Figure 107**). Thus, optimum conditions for observing the photocurrent are V_{ds} = 0 V and V_{gs} = 20 V (closed gate).

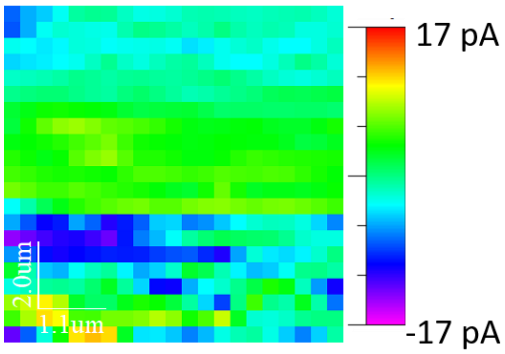

Figure 107: Measurement of photocurrent (irradiation at 500 nm) for an open gated device (V_{gs} = - 20 V) with no applied V_{ds}. A low current is observed on the whole channel region due to charge trapping.

Non-covalently functionalized devices show the same response as non-functionalized ones (**Figure 108a** and **b**). These devices present a photocurrent signal only when the nanotube is irradiated at the contact with the metal. This signal is observed even in the absence of an applied potential between the source and the drain. It is explained by charge separation at the contact nanotube-electrode due to band bending at their interface. This creates a barrier for hole transfer from the valence band of the nanotube into the metal (Schottky barrier), while the electron transfer from the conducting band of the nanotube is possible (**Figure 108c**).

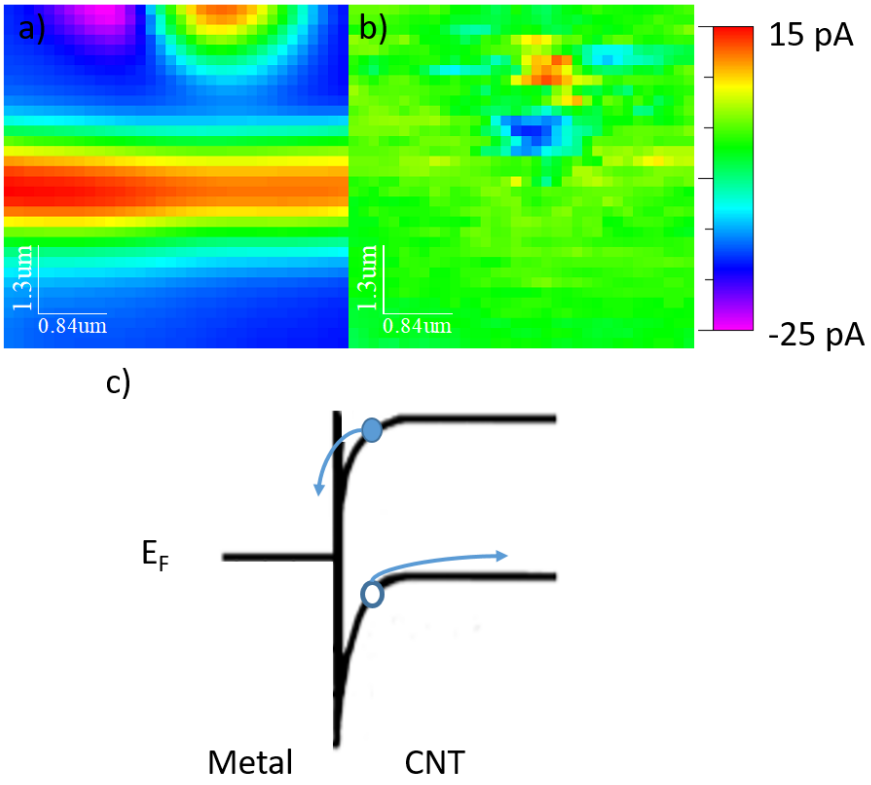

Figure 108: a) Map of the device obtained by reflectivity and b) Photocurrent map of a device (V_{gs} = 20 V, V_{ds} = 0 V) non-covalently functionalized with CP36 (diluted conditions) irradiated at 500 nm; c) Schematic representation of the band diagram of the carbon nanotubes at the interface with the electrode. Excitation close to the contact creates an exciton whose charges are separated by the creation of a Schottky barrier for hole transfer to the metal, while electron transfer is possible. E_F represents the Fermi energy of the metal.

On the other hand, covalent functionalization resulted in photoconductivity not only at the level of the contact, but also on the channel (**Figure 109a** and **b**). We observe different signals of the current on each side of the defects created by the functionalization. These defects induce localized curvatures in the band structure of the nanotubes, which act as points of charge separation (**Figure 109c**).[240]

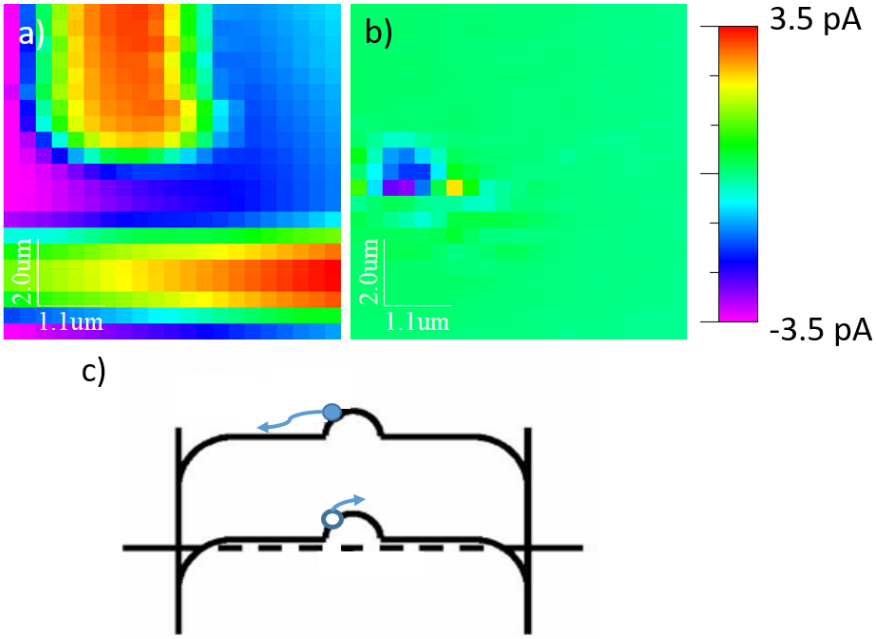

Figure 109: a) Reflectivity and b) Photocurrent signal of a device (V_{gs} = 0 V, V_{ds} = 0 V) covalently functionalized with CP36 (diluted conditions) irradiated at 500 nm; c) Schematic representation of the band structure of carbon nanotubes containing a defect, demonstrating how charge separation happens upon excitation on the defect point. [240]

Note that studies in the literature[240] on the effect of defects are reported on structural defects and not on induced defects as in this work, motivating us for further studies on our systems.

5. Conclusion

As a conclusion, we have observed that non-covalent functionalization cannot be performed directly on carbon nanotube devices used in this study. Since the nanotubes are already deposited on a substrate, the polymer cannot wrap on the carbon nanotubes and non-covalent functionalization is not effective.

On the other hand, the effectiveness of covalent functionalization is shown by the effect on the performance of the devices, decreasing I_{on}/I_{off} for example, and the observation of an induced photocurrent.

General conclusion

This thesis is dedicated to the synthesis and understanding of CNTs-P3HT nanohybrids. Two main types of nanohybrids were synthesized depending on the type of functionalization: non-covalent and covalent nanohybrids. The properties of these were studied by spectroscopic methods (UV-Vis-NIR absorption, fluorescence, photoluminescence and Raman) and TEM. The synthetic method was also used for preliminary studies on the functionalization of carbon nanotubes in field-effect devices.

In a first step, the synthesis of the copolymer PHTcoAHT was performed. The synthesis of this copolymer could not be obtained directly through polymerization and required post-polymerization modification. Because of this, a comonomer containing a bromine group at the end of the hexyl side chain of the thiophene was synthesized. This could be polymerized with 3-hexylthiophene, yielding statistical copolymers. This polymerization happens through a quasi-living mechanism, which allows control of the obtained polymer molecular weight, low dispersity and high regioregularity. Through the same method, fully functionalized polymers and classical P3HT were also obtained.

After obtaining the copolymer, the synthesis of the nanohybrids was considered. As P3HT has been shown to disperse CNTs in THF through the formation of non-covalent nanohybrids, we started by studying the behavior of these. A method described in the literature as the solvent extraction method was one that was especially attractive for our first experiments. In principle, it should lead to isolated nanohybrids, a simple system for further analysis. However, this method presents major inconveniences. All the purification steps lead to loss of knowledge of the system composition, and the method led to only two pure nanohybrids: P21@SWNTs and CP36@SWNTs.

The little control of this method pushed us to use the simple sonication of the two components together in a relatively diluted solution. With this method we gained the control of the system composition and the reproducibility of the results, despite keeping impurities in the system. In contrast with the previous method, nanohybrids could be synthesized independently of the molecular weight of the P3HT (or the copolymer) or the type of the CNTs used.

Elaboration of non-covalent nanohybrids led to the observation of some interesting changes in the optical spectrum of P3HT and the copolymer. These were first evidenced for P21@SWNTs, but many of the conclusions are true for most systems. In fact, the on spectrum of P3HT in the nanohybrids is very similar to those of thin films of pure P3HT or in solutions in which the polymer forms nanofibers, i.e., when the polymer forms aggregates. This in itself suggests strong interactions between the P3HT and CNTs, as P3HT concentration was about one order of magnitude below its limit of solubility in THF for the highest mass used (44000 g/mol), the others being even more soluble). We concluded that the polymer chains organize as aggregates on the carbon nanotubes surfaces driven by the strong π-π and hydrophobic interactions between the two compounds.

Another conclusion deduced from optical absorption spectroscopy was that polymer chains in these aggregates present a very high intrachain order compared to aggregates usually obtained for pure P3HT in THF (such as by reducing the temperature of the solution). This suggests a template effect of the carbon nanotubes in the formation of these highly ordered aggregates. This high intrachain order is linked to better optical and electronic properties of P3HT in thin films. Fluorescence and photoluminescence studies have shown the quenching of the fluorescence of the free polymer which can be completely ascribed to the formation of the aggregates, which emission is quenched as well. However, these also do not emit. In fact, their emission is completely quenched due to energy transfer to the carbon nanotubes, proving the strong interaction between the compounds as well as their proximity. Electron microscopy also confirms this proximity and the wrapping configuration of the polymer chains and aggregates around the carbon nanotubes.

The molecular weight of the polymer, in relation to its solubility, was shown to be an important factor in the elaboration of the non-covalent nanohybrids. Actually, P21 has a molecular weight that optimizes the amount of nanotubes dispersed and the stability of the suspensions, the interactions with the nanotubes counterbalancing the loss of entropy of mixing resulting from the aggregation. This entropy of mixing is more important for shorter chains, resulting in a weaker solubilization of the. On the other hand, chains of higher masses lead to a totally different morphology of the nanohybrids showing polymer fibers organized perpendicularly to the carbon nanotube axis (shish-kebab nanostructures). This morphology was interpreted as resulting from the spontaneous formation of nucleation sites perpendicular to the nanotube axis from which polymer aggregates grow.

Non- covalent functionalization of DWNTs has shown that the increase of the nanotube diameter results in an increasing amount of dispersed nanotubes and stability of their suspensions for polymer of higher masses compared to what observed for SWNTs. This effect of the diameter of the tube is fully consistent with the observed effect of the polymer mass in P3HT@SWNTs nanohybrids. It is the couple (polymer mass – nanotube diameter) which governs the aggregation in the nanohybrids. This behavior led us to perform some tests with graphene (which would represent a nanotube with infinite diameter). The results, still preliminary and not included in the manuscript, support a strong interaction between the polymer and the graphene structure as well as an effect of the latter on the polymer chain ordering. Also, only a single P3HT layer is adsorbed onto the graphene surface. These results offer an interesting perspective for continuing our studies, as they could reveal more information on these hybrid systems.

Covalent functionalization resulted in nanohybrids with a different behavior than the non-covalent ones. Optical and Raman spectroscopy point a more disordered conformation of the polymer chains, with no formation of aggregates. This is probably due to the steric hindering caused by the grafting through the side chain, which prevents π-stacking with the nanotubes. This different conformation increases the

solubility of the nanohybrids, which remain in solution far longer than their non-covalent counterparts. The same results are observed whatever the polymer weight and CNTs type.

Covalent functionalization of nanotube devices was successfully performed, in contrast with the failure of non-covalent functionalization of the same devices. The results obtained so far show that the chemical defects created onto the carbon nanotubes structure seem to generate a charge separation upon light irradiation. This result is very motivating for further investigations.

All the results presented in this manuscript are worthy of being refined by theoretical studies and additional characterization techniques, IR spectroscopy and electron energy loss spectroscopy, as well as DSC, ATG, and XPS, as long as we can prepare these nanohybrids with increased yields. For this reason, in view of the highest solubility of the nanohybrids formed with P3DDT, a copolymer derived from P3DDT has been synthesized with a somewhat different route than the one used for the synthesis of PHTcoAHT, which offers a short time perspective.

Finally, the structure of the covalent nanohybrids could result in a different photophysical behavior compared to the non-covalent ones. For example, it is currently unknown if there is charge or energy transfer from the grafted copolymer into the CNTs. It is also unknown how a possible energy transfer would eventually interact with defect states on the CNTs. These questions could be addressed upon functionalization of simpler systems (such as chirality enriched carbon nanotubes) with our copolymer.

References

1 S. Iijima, *Nature*, 1991, **354**, 56–58.

2 W. Krätschmer, L. D. Lamb, K. Fostiropoulos and D. R. Huffman, *Nature*, 1990, **347**, 354–358.

3 M. Monthioux and V. L. Kuznetsov, *Carbon N. Y.*, 2006, **44**, 1621–1623.

4 R. Saito, M. Fujita, G. Dresselhaus and M. S. Dresselhaus, *Phys. Rev. B*, 1992, **46**, 1804–1811.

5 R. Saito, M. Fujita, G. Dresselhaus and M. S. Dresselhaus, *Appl. Phys. Lett.*, 1992, **60**, 2204–2206.

6 S. Iijima and T. Ichihashi, *Nature*, 1993, **363**, 603–605.

7 D. S. Bethune, C. H. Kiang, M. S. de Vries, G. Gorman, R. Savoy, J. Vazquez and R. Beyers, *Nature*, 1993, **363**, 605–607.

8 M. S. Dresselhaus and P. C. Eklund, *Adv. Phys.*, 2000, **49**, 705–814.

9 A. Loiseau, P. Launois, P. Petit, S. Roche and J.-P. Salvetat, *Understanding Carbon Nanotubes*, Springer Berlin Heidelberg, Berlin, Heidelberg, 2006, vol. 677.

10 C. Aurisicchio, R. Marega, V. Corvaglia, J. Mohanraj, R. Delamare, D. A. Vlad, C. Kusko, C. A. Dutu, A. Minoia, G. Deshayes, O. Coulembier, S. Melinte, P. Dubois, R. Lazzaroni, N. Armaroli and D. Bonifazi, *Adv. Funct. Mater.*, 2012, **22**, 3209–3222.

11 M. Monthioux, *Carbon Meta-Nanotubes: Synthesis, Properties and Applications*, Wiley, 2011.

12 H. Kataura, Y. Kumazawa, Y. Maniwa, I. Umezu, S. Suzuki, Y. Ohtsuka and Y. Achiba, *Synth. Met.*, 1999, **103**, 2555–2558.

13 A. Thess, R. Lee, P. Nikolaev, H. Dai, P. Petit, J. Robert, C. Xu, Y. H. Lee, S. G. Kim, A. G. Rinzler, D. T. Colbert, G. E. Scuseria, D. Tomanek, J. E. Fischer and R. E. Smalley, *Science*, 1996, **273**, 483–487.

14 A. V. Naumov, S. Ghosh, D. A. Tsyboulski, S. M. Bachilo and R. B. Weisman, *ACS Nano*, 2011, **5**, 1639–1648.

15 C. Fantini, M. L. Usrey and M. S. Strano, *J. Phys. Chem. C*, 2007, **111**, 17941–17946.

16 Y. Zheng, S. R. Sanchez, S. M. Bachilo and R. B. Weisman, *J. Phys. Chem. C*, 2018, **122**, 4681–4690.

17 K. Iakoubovskii, N. Minami, T. Ueno, S. Kazaoui and H. Kataura, *J. Phys. Chem. C*, 2008, **112**, 11194–11198.

18 M. J. O'Connell, S. M. Bachilo, C. B. Huffman, V. C. Moore, M. S. Strano, E. H. Haroz, K. L. Rialon, P. J. Boul, W. H. Noon, C. Kittrell, J. Ma, R. H. Hauge, R. B. Weisman and R. E. Smalley, *Science*, 2002, **297**, 593–6.

19 Y. Miyauchi, *J. Mater. Chem. C*, 2013, **1**, 6499–6521.

20 M. Pfohl, D. D. Tune, A. Graf, J. Zaumseil, R. Krupke and B. S. Flavel, *ACS Omega*, 2017, **2**, 1163–1171.

21 N. Nair, M. L. Usrey, W. J. Kim, R. D. Braatz and M. S. Strano, *Anal. Chem.*, 2006, **78**, 7689–7696.

22 D. Shimamoto, H. Muramatsu, T. Hayashi, Y. A. Kim, M. Endo, J. S. Park, R. Saito, M. Terrones and M. S. Dresselhaus, *Appl. Phys. Lett.*, 2009, **94**, 1–3.

23 J. Lefebvre, J. M. Fraser, Y. Homma and P. Finnie, *Appl. Phys. A Mater. Sci. Process.*, 2004, **78**, 1107–1110.

24 F. Wang, G. Dukovic, L. E. Brus and T. F. Heinz, *Science*, 2005, **308**, 838–841.

25 T. G. Pedersen, *Carbon N. Y.*, 2004, **42**, 1007–1010.

26 E. B. Barros, R. B. Capaz, A. Jorio, G. G. Samsonidze, A. G. Souza Filho, S. Ismail-Beigi, C. D. Spataru, S. G. Louie, G. Dresselhaus and M. S. Dresselhaus, *Phys. Rev. B*, 2006, **73**, 241406.

27 P. Avouris, J. Chen, M. Freitag, V. Perebeinos and J. C. Tsang, *Phys. status solidi*, 2006, **243**, 3197–3203.

28 P. Avouris, M. Freitag and V. Perebeinos, *Nat. Photonics*, 2008, **2**, 341–350.

29 T. Koyama, Y. Miyata, Y. Asada, H. Shinohara, H. Kataura and A. Nakamura, *J. Phys. Chem. Lett.*, 2010, **1**, 3243–3248.

30 H. Qian, C. Georgi, N. Anderson, A. A. Green, M. C. Hersam, L. Novotny and A. Hartschuh, *Nano Lett.*, 2008, **8**, 1363–1367.

31 D. I. Levshov, R. Parret, H.-N. Tran, T. Michel, T. T. Cao, V. C. Nguyen, R. Arenal, V. N. Popov, S. B. Rochal, J.-L. Sauvajol, A.-A. Zahab and M. Paillet, *Phys. Rev. B*, 2017, **96**, 195410.

32 M. Paillet, T. Michel, J. C. Meyer, V. N. Popov, L. Henrard, S. Roth and J. L. Sauvajol, *Phys. Rev. Lett.*, 2006, **96**, 1–4.

33 M. S. Dresselhaus, G. Dresselhaus, R. Saito and A. Jorio, *Phys. Rep.*, 2005, **409**, 47–99.

34 D. I. Levshov, H. N. Tran, M. Paillet, R. Arenal, X. T. Than, A. A. Zahab, Y. I. Yuzyuk, J. L. Sauvajol and T. Michel, *Carbon N. Y.*, 2017, **114**, 141–159.

35 P. Petit, C. Mathis, C. Journet and P. Bernier, *Chem. Phys. Lett.*, 1999, **305**, 370–374.

36 S. Suzuki and H. Hibino, *Carbon N. Y.*, 2011, **49**, 2264–2272.

37 J. L. Bahr, E. T. Mickelson, M. J. Bronikowski, R. E. Smalley and J. M. Tour, *Chem. Commun.*, 2001, 193–194.

38 T. Fujigaya and N. Nakashima, *Sci. Technol. Adv. Mater.*, 2015, **16**, 024802.

39 D. Tasis, N. Tagmatarchis, A. Bianco and M. Prato, *Chem. Rev.*, 2006, **106**, 1105–1136.

40 N. G. Sahoo, S. Rana, J. W. Cho, L. Li and S. H. Chan, *Prog. Polym. Sci.*, 2010, **35**, 837–867.

41 J. Liu, Y. Ye, Y. Xue, X. Xie and Y.-W. Mai, *J. Polym. Sci. Part A Polym. Chem.*, 2017, **55**, 622–631.

42 N. Tsubokawa, *Polym. J.*, 2005, **37**, 637–655.

43 P. Liu, *Eur. Polym. J.*, 2005, **41**, 2693–2703.

44 Z. Spitalsky, D. Tasis, K. Papagelis and C. Galiotis, *Prog. Polym. Sci.*, 2010, **35**, 357–401.

45 S. Campidelli, *Curr. Org. Chem.*, 2011, **15**, 1151–1159.

46 Y. Chen, L. Marty and N. Bendiab, *Adv. Mater.*, 2019, **1902917**, 1902917.

47 A. Setaro, *J. Phys. Condens. Matter*, 2017, **29**, 423003.

48 P. Singh, S. Campidelli, S. Giordani, D. Bonifazi, A. Bianco and M. Prato, *Chem. Soc. Rev.*, 2009, **38**, 2214–2230.

49 O. Moradi, M. Yari, K. Zare, B. Mirza and F. Najafi, *Fullerenes, Nanotub. Carbon Nanostructures*, 2012, **20**, 138–151.

50 Z. Abousalman-Rezvani, P. Eskandari, H. Roghani-Mamaqani and M. Salami-Kalajahi, *Adv. Colloid Interface Sci.*, 2020, **278**, 102126.

51 S. D. Stranks, J. K. Sprafke, H. L. Anderson and R. J. Nicholas, *ACS Nano*, 2011, **5**, 2307–2315.

52 C. Roquelet, J. S. Lauret, V. Alain-Rizzo, C. Voisin, R. Fleurier, M. Delarue, D. Garrot, A. Loiseau, P. Roussignol, J. A. Delaire and E. Deleporte, *ChemPhysChem*, 2010, **11**, 1667–1672.

53 C. Roquelet, D. Garrot, J. S. Lauret, C. Voisin, V. Alain-Rizzo, P. Roussignol, J. A. Delaire and E. Deleporte, *Appl. Phys. Lett.*, 2010, **97**, 141918.

54 P. Lutsyk, R. Arif, J. Hruby, A. Bukivskyi, O. Vinijchuk, M. Shandura, V. Yakubovskyi, Y. Kovtun, G. A. Rance, M. Fay, Y. Piryatinski, O. Kachkovsky, A. Verbitsky and A. Rozhin, *Light Sci. Appl.*, 2016, **5**, e16028–e16028.

55 P. Lutsyk, Y. Piryatinski, M. Shandura, M. AlAraimi, M. Tesa, G. E. Arnaoutakis, A. A. Melvin, O. Kachkovsky, A. Verbitsky and A. Rozhin, *J. Phys. Chem. C*, 2019, **123**, 19903–19911.

56 A. Menon, Y. L. Slominskii, J. Joseph, O. P. Dimitriev and D. M. Guldi, *Small*, 2020, **16**, 1906745.

57 W. Feng, A. Fujii, M. Ozaki and K. Yoshino, *Carbon N. Y.*, 2005, **43**, 2501–2507.

58 R. F. Araújo, C. J. R. Silva, M. C. Paiva, M. M. Franco and M. F. Proença, *RSC Adv.*, 2013, **3**, 24535–24542.

59 C. Backes, U. Mundloch, A. Ebel, F. Hauke and A. Hirsch, *Chem. Eur. J.*, 2010, **16**, 3314–3317.

60 J. Ma, F. Yu, L. Zhou, L. Jin, M. Yang, J. Luan, Y. Tang, H. Fan, Z. Yuan and J. Chen, *ACS Appl. Mater. Interfaces*, 2012, **4**, 5749–5760.

61 Y. Almadori, G. Delport, R. Chambard, L. Orcin-Chaix, A. C. Selvati, N. Izard, A. Belhboub, R. Aznar, B. Jousselme, S. Campidelli, P. Hermet, R. Le Parc, T. Saito, Y. Sato, K. Suenaga, P. Puech, J. S. Lauret, G. Cassabois, J. L. Bantignies and L. Alvarez, *Carbon N. Y.*, 2019, **149**, 772–780.

62 L. Alvarez, Y. Almadori, R. Arenal, R. Babaa, T. Michel, R. Le Parc, J. L. Bantignies, B. Jousselme, S. Palacin, P. Hermet and J. L. Sauvajol, *J. Phys. Chem. C*, 2011, **115**, 11898–11905.

63 E. Gaufrès, N. Y. W. Tang, A. Favron, C. Allard, F. Lapointe, V. Jourdain, S. Tahir, C. N. Brosseau, R. Leonelli and R. Martel, *ACS Nano*, 2016, **10**, 10220–10226.

64 K. Yanagi, K. Iakoubovskii, S. Kazaoui, N. Minami, Y. Maniwa, Y. Miyata and H. Kataura, *Phys. Rev. B - Condens. Matter Mater. Phys.*, 2006, **74**, 1–5.

65 S. Van Bezouw, D. H. Arias, R. Ihly, S. Cambré, A. J. Ferguson, J. Campo, J. C. Johnson, J. Defillet, W. Wenseleers and J. L. Blackburn, *ACS Nano*, 2018, **12**, 6881–6894.

66 T. Koyama, K. Fujiki, Y. Nagasawa, S. Okada, K. Asaka, Y. Saito and H. Kishida, *J. Phys. Chem. C*, 2018, **122**, 5805–5812.

67 W. Gomulya, J. Gao and M. A. Loi, *Eur. Phys. J. B*, 2013, **86**, 404.

68 E. R. Waclawik, J. M. Bell, R. G. S. Goh, A. Musumeci and N. Motta, in *BioMEMS and Nanotechnology II*, ed. D. V. Nicolau, Brisbane, 2005, vol. Proc. of S, p. 603607.

69 A. Ikeda, K. Nobusawa, T. Hamano and J. Kikuchi, *Org. Lett.*, 2006, **8**, 5489–5492.

70 R. D. K. Misra, D. Depan, V. S. A. Challa and J. S. Shah, *Phys. Chem. Chem. Phys.*, 2014, **16**, 19122–19129.

71 Y. Luo, F. A. Santos, T. W. Wagner, E. Tsoi and S. Zhang, *J. Phys. Chem. B*, 2014, **118**, 6038–6046.

72 B. J. N. Coleman, A. B. Dalton, S. Curran, A. Rubio, A. P. Davey, A. Drury, B. Mccarthy, B. Lahr and P. M. Ajayan, *Adv. Mater.*, 2000, **12**, 213–216.

73 D. Fong and A. Adronov, *Chem. Sci.*, 2017, **8**, 7292–7305.

74 W. Z. Wang, W. F. Li, X. Y. Pan, C. M. Li, L. J. Li, Y. G. Mu, J. A. Rogers and M. B. Chan-Park, *Adv. Funct. Mater.*, 2011, **21**, 1643–1651.

75 J. S. Moore, Z. X. Zhang, Y. K. Che, R. A. Smaldone, M. A. Xu, B. R. Bunes and L. Zang, *J. Am. Chem. Soc.*, 2010, **132**, 14113–14117.

76 I. Pochorovski, H. Wang, J. I. Feldblyum, X. Zhang, A. L. Antaris and Z. Bao, *J. Am. Chem. Soc.*, 2015, **137**, 4328–4331.

77 F. Toshimitsu and N. Nakashima, *Nat. Commun.*, 2014, **5**, 5041.

78 S. D. Stranks, A. M. R. Baker, J. A. Alexander-Webber, B. Dirks and R. J. Nicholas, *Small*, 2013, **9**, 2245–2249.

79 D. Fong, G. M. Andrews and A. Adronov, *J. Polym. Sci. Part A Polym. Chem.*, 2018, **56**, 2723–2729.

80 T. Lei, I. Pochorovski and Z. Bao, *Acc. Chem. Res.*, 2017, **50**, 1096–1104.

81 J.-Y. Hwang, A. Nish, J. Doig, S. Douven, C. Chen, L.-C. Chen and R. J. Nicholas, *J. Am. Chem. Soc.*, 2008, **130**, 3543–3553.

82 A. Nish, J. Y. Hwang, J. Doig and R. J. Nicholas, *Nat. Nanotechnol.*, 2007, **2**, 640–646.

83 W. Gomulya, J. M. Salazar Rios, V. Derenskyi, S. Z. Bisri, S. Jung, M. Fritsch, S. Allard, U. Scherf, M. C. dos Santos and M. A. Loi, *Carbon N. Y.*, 2015, **84**, 66–73.

84 M. J. Shea, R. D. Mehlenbacher, M. T. Zanni and M. S. Arnold, *J. Phys. Chem. Lett.*, 2014, **5**, 3742–3749.

85 J. Gao, R. Annema and M. A. Loi, *Eur. Phys. J. B*, 2012, **85**, 246.

86 N. A. Rice, A. V. Subrahmanyam, S. E. Laengert and A. Adronov, *J. Polym. Sci. Part A Polym. Chem.*, 2015, **53**, 2510–2516.

87 N. A. Rice and A. Adronov, *Macromolecules*, 2013, **46**, 3850–3860.

88 P. Imin, F. Cheng and A. Adronov, *Polym. Chem.*, 2011, **2**, 1404.

89 W. Gomulya, G. D. Costanzo, E. J. F. De Carvalho, S. Z. Bisri, V. Derenskyi, M. Fritsch, N. Fröhlich, S. Allard, P. Gordiichuk, A. Herrmann, S. J. Marrink, M. C. Dos Santos, U. Scherf and M. A. Loi, *Adv. Mater.*, 2013, **25**, 2948–2956.

90 S. K. Samanta, M. Fritsch, U. Scherf, W. Gomulya, S. Z. Bisri and M. A. Loi, *Acc. Chem. Res.*, 2014, **47**, 2446–2456.

91 F. Jakubka, S. P. Schießl, S. Martin, J. M. Englert, F. Hauke, A. Hirsch and J. Zaumseil, *ACS Macro Lett.*, 2012, **1**, 815–819.

92 D. J. Bindl, N. S. Safron and M. S. Arnold, 2010, **4**, 5657–5664.

93 Y. Kanai and J. C. Grossman, *Nano Lett.*, 2008, **8**, 908–912.

94 A. Nish, J. Hwang, J. Doig and R. J. Nicholas, *Nanotechnology*, 2008, **19**, 095603.

95 J. Gao and M. A. Loi, *Eur. Phys. J. B*, 2010, **75**, 121–126.

96 J. Geng and T. Zeng, 2006, 16827–16833.

97 N. M. Dissanayake and Z. Zhong, *Nano Lett.*, 2011, **11**, 286–290.

98 M. B. Upama, M. A. Mahmud, G. Conibeer and A. Uddin, *Sol. RRL*, 2020, **4**, 1900342.

99 S. Campidelli, B. Ballesteros, A. Filoramo, D. D. Díaz, G. de la Torre, T. Torres, G. M. A. Rahman, C. Ehli, D. Kiessling, F. Werner, V. Sgobba, D. M. Guldi, C. Cioffi, M. Prato and J.-P. Bourgoin, *J. Am. Chem. Soc.*, 2008, **130**, 11503–11509.

100 M. L. Usrey, E. S. Lippmann and M. S. Strano, *J. Am. Chem. Soc.*, 2005, **127**, 16129–16135.

101 C. Fantini, M. A. Pimenta and M. S. Strano, *J. Phys. Chem. C*, 2008, **112**, 13150–13155.

102 P. Salice, E. Fabris, C. Sartorio, D. Fenaroli, V. Figa, M. P. Casaletto, S. Cataldo, B. Pignataro, E. Menna and A, *Carbon N. Y.*, 2014, 73–82.

103 D. Hetemi, V. Noël and J. Pinson, *Biosensors*, 2020, **10**, 4.

104 J. L. Bahr and J. M. Tour, *Chem. Mater.*, 2001, **13**, 3823–3824.

105 M. S. Strano, C. A. Dyke, M. L. Usrey, P. W. Barone, M. J. Allen, H. Shan, C. Kittrell, R. H. Hauge, J. M. Tour and R. E. Smalley, *Science*, 2003, **301**, 1519–1522.

106 L. An, Q. Fu, C. Lu and J. Liu, *J. Am. Chem. Soc.*, 2004, **126**, 10520–10521.

107 C. D. Doyle, J.-D. R. Rocha, R. B. Weisman and J. M. Tour, *J. Am. Chem. Soc.*, 2008, **130**, 6795–6800.

108 C. A. Dyke and J. M. Tour, *J. Am. Chem. Soc.*, 2003, **125**, 1156–1157.

109 C. A. Dyke and J. M. Tour, *Nano Lett.*, 2003, **3**, 1215–1218.

110 L. R. Powell, Y. Piao and Y. Wang, *J. Phys. Chem. Lett.*, 2016, **7**, 3690–3694.

111 Y. Piao, B. Meany, L. R. Powell, N. Valley, H. Kwon, G. C. Schatz and Y. Wang, *Nat. Chem.*, 2013, **5**, 840–845.

112 X. He, K. A. Velizhanin, G. Bullard, Y. Bai, J.-H. Olivier, N. F. Hartmann, B. J. Gifford, S. Kilina, S. Tretiak, H. Htoon, M. J. Therien and S. K. Doorn, *ACS Nano*, 2018, **12**, 8060–8070.

113 A. H. Brozena, M. Kim, L. R. Powell and Y. Wang, *Nat. Rev. Chem.*, 2019, **3**, 375–392.

114 X. He, H. Htoon, S. K. Doorn, W. H. P. Pernice, F. Pyatkov, R. Krupke, A. Jeantet, Y. Chassagneux and C. Voisin, *Nat. Mater.*, 2018, **17**, 663–670.

115 A. Setaro, M. Adeli, M. Glaeske, D. Przyrembel, T. Bisswanger, G. Gordeev, F. Maschietto, A. Faghani, B. Paulus, M. Weinelt, R. Arenal, R. Haag and S. Reich, *Nat. Commun.*, 2017, **8**, 14281.

116 H. Li, F. Cheng, A. M. Duft and A. Adronov, *J. Am. Chem. Soc.*, 2005, **127**, 14518–14524.

117 I. Hijazi, K. Khedhiri and S. Campidelli, *Org. Biomol. Chem.*, 2018, **16**, 6767–6772.

118 L. M. Arellano Castellanos, H. B. Gobeze, M. J. Gómez-Escalonilla, J. L. G. Fierro, F. D'Souza and F. Langa, *Nanoscale*, 2020, 9890–9898.

119 A. Şenocak, E. Nur Kaya, B. Kadem, T. Basova, E. Demirbaş, A. Hassan and M. Durmuş, *Dalt. Trans.*, 2018, **47**, 9617–9626.

120 Y.-P. Sun, K. Fu, Y. Lin and W. Huang, *Acc. Chem. Res.*, 2002, **35**, 1096–1104.

121 A. Gohier, F. Nekelson, M. Helezen, P. Jegou, G. Deniau, S. Palacin and M. Mayne-L'Hermite, *J. Mater. Chem.*, 2011, **21**, 4615–4622.

122 P. R. Marcoux, P. Hapiot, P. Batail and J. Pinson, *New J. Chem.*, 2004, **28**, 302–307.

123 X. L. Wu and P. Liu, *Polym. Lett.*, 2010, **4**, 723–728.

124 C. A. Dyke and J. M. Tour, *J. Phys. Chem. A*, 2004, **108**, 11151–11159.

125 A. Hamdast, S. Agbolaghi, M. Zeighami, Y. Beygi-Khosrowshahi and R. Sarvari, *Polym. Int.*, 2019, **68**, 335–343.

126 B. K. Kuila, K. Park and L. Dai, *Macromolecules*, 2010, **43**, 6699–6705.

127 A. Rahmani, J. L. Sauvajol, S. Rols and C. Benoit, *Phys. Rev. B - Condens. Matter Mater. Phys.*, 2002, **66**, 1–9.

128 S. Rochal, D. Levshov, M. Avramenko, R. Arenal, T. T. Cao, V. C. Nguyen, J. L. Sauvajol and M. Paillet, *Nanoscale*, 2019, **11**, 16092–16102.

129 K. Fujisawa, H. Kim, S. Go, H. Muramatsu, T. Hayashi, M. Endo, T. Hirschmann, M. Dresselhaus, Y. Kim and P. Araujo, *Appl. Sci.*, 2016, **6**, 109.

130 T. Hayashi, D. Shimamoto, Y. A. Kim, H. Muramatsu, F. Okino, H. Touhara, T. Shimada, Y. Miyauchi, S. Maruyama, M. Terrones, M. S. Dresselhaus and M. Endo, *ACS Nano*, 2008, **2**, 485–488.

131 J. H. Kim, M. Kataoka, D. Shimamoto, H. Muramatsu, Y. C. Jung, T. Hayashi, Y. A. Kim, M. Endo, J. S. Park, R. Saito, M. Terrones and M. S. Dresselhaus, *ACS Nano*, 2010, **4**, 1060–1066.

132 T. Koyama, Y. Asada, N. Hikosaka, Y. Miyata, H. Shinohara and A. Nakamura, *ACS Nano*, 2011, **5**, 5881–5887.

133 T. Koyama, Y. Miyata, K. Asaka, H. Shinohara, Y. Saito and A. Nakamura, *Phys. Chem. Chem. Phys.*, 2012, **14**, 1070–1084.

134 O. Postupna, R. Long and O. V Prezhdo, *J. Phys. Chem. C*, 2015, **119**, 12088–12094.

135 A. A. Green and M. C. Hersam, *Nat. Nanotechnol.*, 2009, **4**, 64–70.

136 S. Yang, A. N. Parks, S. A. Saba, P. L. Ferguson and J. Liu, *Nano Lett.*, 2011, **11**, 4405–4410.

137 Y. Miyata, M. Suzuki, M. Fujihara, Y. Asada, R. Kitaura and H. Shinohara, *ACS Nano*, 2010, **4**, 5807–5812.

138 D. Levshov, T. X. Than, R. Arenal, V. N. Popov, R. Parret, M. Paillet, V. Jourdain, A. A. Zahab, T. Michel, Y. I. Yuzyuk and J. L. Sauvajol, *Nano Lett.*, 2011, **11**, 4800–4804.

139 K. Liu, X. Hong, M. Wu, F. Xiao, W. Wang, X. Bai, J. W. Ager, S. Aloni, A. Zettl, E. Wang and F. Wang, *Nat. Commun.*, 2013, **4**, 1–6.

140 V. N. Popov, D. I. Levshov, J.-L. Sauvajol and M. Paillet, *Phys. Rev. B*, 2018, **97**, 165417.

141 M. Kalbac, A. A. Green, M. C. Hersam and L. Kavan, *Chem. Eur. J.*, 2011, **17**, 9806–9815.

142 A. Lopez-Bezanilla, *J. Phys. Chem. C*, 2013, **117**, 15266–15271.

143 H. Muramatsu, Y. A. Kim, T. Hayashi, M. Endo, A. Yonemoto, H. Arikai, F. Okino and H. Touhara, *Chem. Commun.*, 2005, **2**, 2002–2004.

144 D. Bouilly, J. Cabana, F. Meunier, M. Desjardins-Carrière, F. Lapointe, P. Gagnon, F. L. Larouche, E. Adam, M. Paillet and R. Martel, *ACS Nano*, 2011, **5**, 4927–4934.

145 Y. Piao, C. F. Chen, A. A. Green, H. Kwon, M. C. Hersam, C. S. Lee, G. C. Schatz and Y. Wang, *J. Phys. Chem. Lett.*, 2011, **2**, 1577–1582.

146 J. Huang, A. L. Ng, Y. Piao, C. F. Chen, A. A. Green, C. F. Sun, M. C. Hersam, C. S. Lee and Y. Wang, *J. Am. Chem. Soc.*, 2013, **135**, 2306–2312.

147 M. Barrejón, S. Pla, I. Berlanga, M. J. Gómez-Escalonilla, L. Martín-Gomis, J. L. G. Fierro, M. Zhang, M. Yudasaka, S. Iijima, H. B. Gobeze, F. D'Souza, Á. Sastre-Santos and F. Langa, *J. Mater. Chem. C*, 2015, **3**, 4960–4969.

148 M. Vizuete, M. J. Gõmez-Escalonilla, J. L. G. Fierro, P. Atienzar, H. García and F. Langa, *ChemPhysChem*, 2014, **15**, 100–108.

149 L. M. Arellano, L. Martín-Gomis, H. B. Gobeze, M. Barrejón, D. Molina, M. J. Gómez-Escalonilla, J. L. G. Fierro, M. Zhang, M. Yudasaka, S. Iijima, F. D'Souza, F. Langa and Á. Sastre-Santos, *J. Mater. Chem. C*, 2015, **3**, 10215–10224.

150 M. Vizuete, M. J. Gõmez-Escalonilla, S. García-Rodriguez, J. L. G. Fierro, P. Atienzar, H. García and F. Langa, *Chem. Eur. J.*, 2012, **18**, 16922–16930.

151 S. Ludwigs, *P3HT Revisited – From Molecular Scale to Solar Cell Devices*, Springer, Berlin, Germany, 2014.

152 J. Lawrence, E. Goto, J. M. Ren, B. McDearmon, D. S. Kim, Y. Ochiai, P. G. Clark, D. Laitar, T. Higashihara and C. J. Hawker, *J. Am. Chem. Soc.*, 2017, **139**, 13735–13739.

153 R. D. McCullough, R. D. Lowe, M. Jayaraman and D. L. Anderson, *J. Org. Chem*, 1993, **58**, 904–912.

154 R. D. McCullough and R. D. Lowe, *J. Chem. Soc. Chem. Commun.*, 1992, 70.

155 J. A. Lim, F. Liu, S. Ferdous, M. Muthukumar and A. L. Briseno, *Mater. Today*, 2010, **13**, 14–24.

156 K. Rahimi, I. Botiz, N. Stingelin, N. Kayunkid, M. Sommer, F. P. V. Koch, H. Nguyen, O. Coulembier, P. Dubois, M. Brinkmann and G. Reiter, *Angew. Chemie - Int. Ed.*, 2012, **51**, 11131–11135.

157 S. Agbolaghi, S. Abbaspoor, B. Massoumi, R. Sarvari, S. Sattari, S. Aghapour and S. Charoughchi, *Macromol. Chem. Phys.*, 2018, **219**, 1–15.

158 M. Pandey, N. Kumari, S. Nagamatsu and S. S. Pandey, *J. Mater. Chem. C*, 2019, **7**, 13323–13351.

159 I. Osaka and R. D. McCullough, *Acc. Chem. Res.*, 2008, **41**, 1202–1214.

160 R. J. Kline, M. D. McGehee, E. N. Kadnikova, J. Liu, J. M. J. Fréchet and M. F. Toney, *Macromolecules*, 2005, **38**, 3312–3319.

161 R. J. Kline, M. D. McGehee, E. N. Kadnikova, J. Liu and J. M. J. Fréchet, *Adv. Mater.*, 2003, **15**, 1519–1522.

162 S. Agbolaghi and S. Zenoozi, *Org. Electron.*, 2017, **51**, 362–403.

163 J. Clark, J. F. Chang, F. C. Spano, R. H. Friend and C. Silva, *Appl. Phys. Lett.*, 2009, **94**, 2007–2010.

164 H. Yamagata and F. C. Spano, *J. Chem. Phys.*, 2012, **136**, 184901.

165 Y. Yuan, J. Shu, P. Liu, Y. Zhang, Y. Duan and J. Zhang, *J. Phys. Chem. B*, 2015, **119**, 8446–8456.

166 F. C. Spano, *Acc. Chem. Res.*, 2010, **43**, 429–439.

167 J. Clark, C. Silva, R. H. Friend and F. C. Spano, *Phys. Rev. Lett.*, 2007, **98**, 206406.

168 F. C. Spano and C. Silva, *Annu. Rev. Phys. Chem.*, 2014, **65**, 477–500.

169 N. J. Hestand and F. C. Spano, *Chem. Rev.*, 2018, **118**, 7069–7163.

170 M. Kasha, *Radiat. Res.*, 1963, **20**, 55.

171 E. G. McRae and M. Kasha, *J. Chem. Phys.*, 1958, **28**, 721–722.

172 E. E. JELLEY, *Nature*, 1936, **138**, 1009–1010.

173 T. Eder, J. Vogelsang, S. Bange, K. Remmerssen, D. Schmitz, S. S. Jester, T. J. Keller, S. Höger and J. M. Lupton, *Angew. Chemie - Int. Ed.*, 2019, 1–6.

174 F. Paquin, H. Yamagata, N. J. Hestand, M. Sakowicz, N. Bérubé, M. Côté, L. X. Reynolds, S. A. Haque, N. Stingelin, F. C. Spano and C. Silva, *Phys. Rev. B - Condens. Matter Mater. Phys.*, 2013, **88**, 12–14.

175 K. Rahimi, I. Botiz, N. Stingelin, N. Kayunkid, M. Sommer, F. P. V. Koch, H. Nguyen, O. Coulembier, P. Dubois, M. Brinkmann and G. Reiter, *Angew. Chemie Int. Ed.*, 2012, **51**, 11131–11135.

176 K. Rahimi, I. Botiz, J. O. Agumba, S. Motamen, N. Stingelin and G. Reiter, *RSC Adv.*, 2014, **4**, 11121–11123.

177 N. Li, T. Shi, C. Ye, X. Zeng, X. Li, Y. Zhao, W. Wang, B. Zhou, H. Duan and Y. Wang, *EPL (Europhysics Lett.*, 2014, **107**, 28007.

178 F. Panzer, H. Bässler, R. Lohwasser, M. Thelakkat and A. Köhler, *J. Phys. Chem. Lett.*, 2014, **5**, 2742–2747.

179 K. A. Mazzio, A. H. Rice, M. M. Durban and C. K. Luscombe, *J. Phys. Chem. C*, 2015, **119**, 14911–14918.

180 C. Scharsich, R. H. Lohwasser, M. Sommer, U. Asawapirom, U. Scherf, M. Thelakkat, D. Neher and A. Köhler, *J. Polym. Sci. Part B Polym. Phys.*, 2012, **50**, 442–453.

181 E. T. Niles, J. D. Roehling, H. Yamagata, A. J. Wise, F. C. Spano, A. J. Moulé and J. K. Grey, *J. Phys. Chem. Lett.*, 2012, **3**, 259–263.

182 Y. Yuan, J. Shu, P. Liu, Y. Zhang, Y. Duan and J. Zhang, *J. Phys. Chem. B*, 2015, **119**, 8446–8456.

183 Y. Xi, D. S. Li, G. M. Newbloom, W. K. Tatum, M. O'Donnell, C. K. Luscombe and L. D. Pozzo, *Soft Matter*, 2018, **14**, 4963–4976.

184 N. M. B. Neto, M. D. R. Silva, P. T. Araujo and R. N. Sampaio, *Adv. Mater.*, 2018, **30**, 1–8.

185 M. Sapolsky and D. Boucher, *J. Polym. Sci. Part B Polym. Phys.*, 2018, **56**, 999–1011.

186 Y. Martinez-Rubi, Z. J. Jakubek, M. B. Jakubinek, K. S. Kim, F. Cheng, M. Couillard, C. Kingston and B. Simard, *J. Phys. Chem. C*, 2015, **119**, 26605–26610.

187 C. Shen, S. Chai, S. Zou and L. Zhai, *Polymer (Guildf).*, 2018, **144**, 168–178.

188 L. Bu, E. Pentzer, F. A. Bokel, T. Emrick and R. C. Hayward, *ACS Nano*, 2012, **6**, 10924–10929.

189 D. H. Kim, J. T. Han, Y. D. Park, Y. Jang, J. H. Cho, M. Hwang and K. Cho, *Adv. Mater.*, 2006, **18**, 719–723.

190 X. Zhang, N. Yuan, S. Ding, D. Wang, L. Li, W. Hu, Z. Bo, J. Zhou and H. Huo, *J. Mater. Chem. C*, 2017, **5**, 3983–3992.

191 L. Li, D. L. Jacobs, B. R. Bunes, H. Huang, X. Yang and L. Zang, *Polym. Chem.*, 2014, **5**, 309–313.

192 C. Rosu, C. J. Tassone, P. H. Chu, P. L. Balding, A. Gorman, J. L. Hernandez, M. Hawkridge, A. Roy, I. I. Negulescu, P. S. Russo and E. Reichmanis, *Chem. Mater.*, 2017, **29**, 5058–5062.

193 R. ichi Sugimoto, S. Takeda, H. B. Gu and K. Yoshino, *Chem. Express*, 1986, **1**, 635–638.

194 K.-Y. Jen, G. G. Miller and R. L. Elsenbaumer, *J. Chem. Soc. Chem. Commun.*, 1986, **17**, 1346.

195 R. D. McCullough, *Adv. Mater.*, 1998, **10**, 93–116.

196 M. R. Andersson, D. Selse, M. Berggren, H. Järvinen, T. Hjertberg, O. Inganäs, O. Wennerström and J. E. Österholm, *Macromolecules*, 1994, **27**, 6503–6506.

197 X. Qiao, X. Wang, X. Zhao, J. Liu and Z. Mo, *Synth. Met.*, 2000, **114**, 261–265.

198 T. A. Chen and R. D. Rieke, *J. Am. Chem. Soc.*, 1992, **114**, 10087–10088.

199 L. Verheyen, P. Leysen, M.-P. Van Den Eede, W. Ceunen, T. Hardeman and G. Koeckelberghs, *Polymer (Guildf).*, 2017, **108**, 521–546.

200 R. S. Loewe, S. M. Khersonsky and R. D. McCullough, *Adv. Mater.*, 1999, **11**, 250–253.

201 E. E. Sheina, J. Liu, M. C. Iovu, D. W. Laird and R. D. McCullough, *Macromolecules*, 2004, **37**, 3526–3528.

202 M. C. Iovu, E. E. Sheina, R. R. Gil and R. D. McCullough, *Macromolecules*, 2005, **38**, 8649–8656.

203 A. Yokoyama, R. Miyakoshi and T. Yokozawa, *Macromolecules*, 2004, **37**, 1169–1171.

204 R. Miyakoshi, A. Yokoyama and T. Yokozawa, *J. Am. Chem. Soc.*, 2005, **127**, 17542–17547.

205 S. D. Boyd, A. K.-Y. Jen and C. K. Luscombe, *Macromolecules*, 2009, **42**, 9387–9389.

206 R. Tkachov, V. Senkovskyy, H. Komber, J. Sommer and A. Kiriy, *J. Am. Chem. Soc.*, 2010, **132**, 7803–7810.

207 Z. J. Bryan and A. J. Mcneil, *Macromolecules*, 2013, **46**, 8395–8405.

208 A. K. Leone, E. A. Mueller and A. J. McNeil, *J. Am. Chem. Soc.*, 2018, **140**, 15126–15139.

209 R. H. Lohwasser and M. Thelakkat, *Macromolecules*, 2011, **44**, 1–7.

210 J. Yu and S. Holdcroft, *Macromolecules*, 2000, **33**, 5073–5079.

211 I. Tahar-Djebbar, F. Nekelson, B. Heinrich, B. Donnio, D. Guillon, D. Kreher, F. Mathevet and A.-J. Attias, *Chem. Mater.*, 2011, **23**, 4653–4656.

212 F. Ouhib, A. Khoukh, J.-B. Ledeuil, H. Martinez, J. Desbrières and C. Dagron-Lartigau, *Macromolecules*, 2008, **41**, 9736–9743.

213 J. P. Lamps and J. M. Catala, *Macromolecules*, 2011, **44**, 7962–7968.

214 R. Lin, M. Galili, U. J. Quaade, M. Brandbyge, T. Bjørnholm, A. D. Esposti, F. Biscarini and K. Stokbro, *J. Chem. Phys.*, 2002, **117**, 321–330.

215 J.-P. Lamps and J.-M. Catala, *Macromolecules*, 2009, **42**, 7282–7284.

216 M. Sato and H. Morii, *Macromolecules*, 1991, **24**, 1196–1200.

217 M. Loegers, L. E. Overman and G. S. Welmaker, *J. Am. Chem. Soc.*, 1995, **117**, 9139–9150.

218 K. Fasth, G. Antoni and B. Langström, *J. Chem. Soc., Perkin Trans. 1*, 1988, 3081–3084.

219 J. Liu, R. S. Loewe and R. D. McCullough, *Macromolecules*, 1999, **32**, 5777–5785.

220 Z. Bao, H. W. Lee, Y. Yoon, S. Park, J. H. Oh, S. Hong, L. S. Liyanage, H. Wang, S. Morishita, N. Patil, Y. J. Park, J. J. Park, A. Spakowitz, G. Galli, F. Gygi, P. H. S. Wong, J. B. H. Tok, J. M. Kim and Z. Bao, *Nat. Commun.*, 2011, **2**, 541–548.

221 E. Flahaut, R. Bacsa, A. Peigney and C. Laurent, *Chem. Commun.*, 2003, 1442.

222 T. Schuettfort, H. J. Snaith, A. Nish and R. J. Nicholas, *Nanotechnology*, 2010, **21**, 025201.

223 L. Röder, A. J. Nicholls and I. R. Baxendale, *Molecules*, 2019, **24**, 1–18.

224 N. I. of A. I. S. and Technology, SDBS Web, https://sdbs.db.aist.go.jp, (accessed 1 November 2020).

225 R. Czerw, Z. Guo, P. M. Ajayan, Y. P. Sun and D. L. Carroll, *Nano Lett.*, 2001, **1**, 423–427.

226 L. Brambilla, M. Tommasini, I. Botiz, K. Rahimi, J. O. Agumba, N. Stingelin and G. Zerbi, *Macromolecules*, 2014, **47**, 6730–6739.

227 T. Schuettfort, A. Nish and R. J. Nicholas, *Nano Lett.*, 2009, **9**, 3871–3876.

228 Y. Ohno, S. Iwasaki, Y. Murakami and S. Kishimoto, 2007, **4005**, 4002–4005.

229 T. W. J. Gadella, *FRET and FLIM Techniques*, Elsevier Science, 2011.

230 M. Giulianini, E. R. Waclawik, J. M. Bell, M. De Crescenzi, P. Castrucci, M. Scarselli, M. Diociauti, S. Casciardi and N. Motta, *J. Phys. Chem. C*, 2011, **115**, 6324–6330.

231 Q. Peng, I. W. Wyman, D. Han and G. Liu, *Can. J. Chem.*, 2011, **89**, 27–33.

232 M. Diebolt, Université de Strasbourg, 2018.

233 M. Castelaín, G. Martínez, P. Merino, J. Á. Martín-Gago, J. L. Segura, G. Ellis and H. J. Salavagione, *Chem. – A Eur. J.*, 2012, **18**, 4965–4973.

234 S. Wood, J. R. Hollis and J. S. Kim, *J. Phys. D. Appl. Phys.*, , DOI:10.1088/1361-6463/50/7/073001.

235 W. C. Tsoi, D. T. James, J. S. Kim, P. G. Nicholson, C. E. Murphy, D. D. C. Bradley, J. Nelson and J. S. Kim, *J. Am. Chem. Soc.*, 2011, **133**, 9834–9843.

236 B. Sainbileg, Y. B. Lan, J. K. Wang and M. Hayashi, *J. Phys. Chem. C*, 2018, **122**, 4224–4231.

237 C. M. Aguirre, P. L. Levesque, M. Paillet, F. Lapointe, B. C. St-Antoine, P. Desjardins and R. Martel, *Adv. Mater.*, 2009, **21**, 3087–3091.

238 R. Parret, Université de Montpellier II, 2011.

239 D. Bouilly, J. L. Janssen, J. Cabana, M. Côté and R. Martel, *ACS Nano*, 2015, **9**, 2626–2634.

240 M. Freitag, J. C. Tsang, A. Bol, P. Avouris, D. Yuan and J. Liu, *Appl. Phys. Lett.*, 2007, **91**, 031101.

Annex 1: Description of the synthesis

All the reactions were carried out under argon atmosphere with dry freshly distilled solvents under anhydrous conditions unless otherwise noted. Tetrahydrofuran (THF) was distilled from Na/Benzophenone. All other chemicals were purchased from commercial suppliers (Aldrich and ACROS) and used without further purification. Chromatographic separations were carried out with silica gel (Geduran 40-63 μm).

1. Synthesis of monomers

Synthesis of 2-bromo-3-hexyl-5-iodothiophene (1)

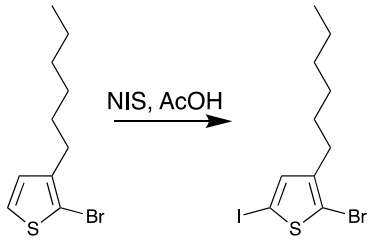

1

Scheme 5: Synthesis of 1

Monomer **1** was synthesized by iodation of the commercially available 2-bromo-3-hexylthiophene (**Scheme 5**).

A solution of 2-bromo-3-hexylthiophene (500 mg, 2.0 mmol) in a $CHCl_3$/AcOH mixture (1/1.6 mL) was stirred at 0°C under Ar and sheltered from light. *N*-Iodosuccinimide (455 mg, 2.0 mmol) was added and the mixture stirred for 2 h at 0°C and for 12 h at 25 °C. The medium is mixed with iced water (10 mL) and extracted with $CHCl_3$. The organic layer is washed with aq. NaOH (0.1 M), with water, dried ($MgSO_4$) and the solvent removed under vacuum. The crude oil is purified by chromatography (SiO_2, cyclohexane) to yield pure **1** as a colorless oil (500 mg, 66% yield):

^{1}H NMR ($CDCl_3$, 400 MHz) δ (ppm): 6.96 (s, 1H, thiophene H4), 2.52 (m, 2H, thiophene-CH_2), 1.57-1.50 (m, 2H, hexyl C2-H_2), 1.48 (m, 2H, hexyl C3-H_2), 1.35-1.26 (m, 4H, hexyl CH_2), 0.88 (t, *J* = 6.8 Hz, 3H, CH_3);

^{13}C NMR ($CDCl_3$, 100 MHz) δ (ppm): 144.4 (thiophene C3), 138.2 (thiophene C4), 111.9 (thiophene C2), 71.1 (thiophene C5), 31.7 (hexyl C4), 29.8 (hexyl C2), 29.3 (hexyl C3), 29.0 (thiophene-CH2), 22.7 (hexyl C5), 14.2 (CH_3);

FTIR (ATR diamond) ν (cm^{-1}): 3082 (vw, aromatic νCH), 2953 (vasCH_3), 2923 (vasCH_2), 2868, 2854 (νsCH_2), 1652 and 1536 (aromatic νCC), 1465 (δCH_2), 1453, 1443, 1403, 1377 (δCH_3), 1354, 1340, 1191, 1095, 995, 975, 909, 826, 724, 650, 580;

MS (ESI): m/z 371.90, 373.84 [M^+ - H];

Anal. calcd. for $C_{10}H_{14}BrIS$: C 32.19, H 3.78; found: C 32.22, H 3.80.

Synthesis of 2-bromo-3-(6-bromohexyl)-5-iodothiophene (2)

Monomer **2** was synthesised according with Scheme S2

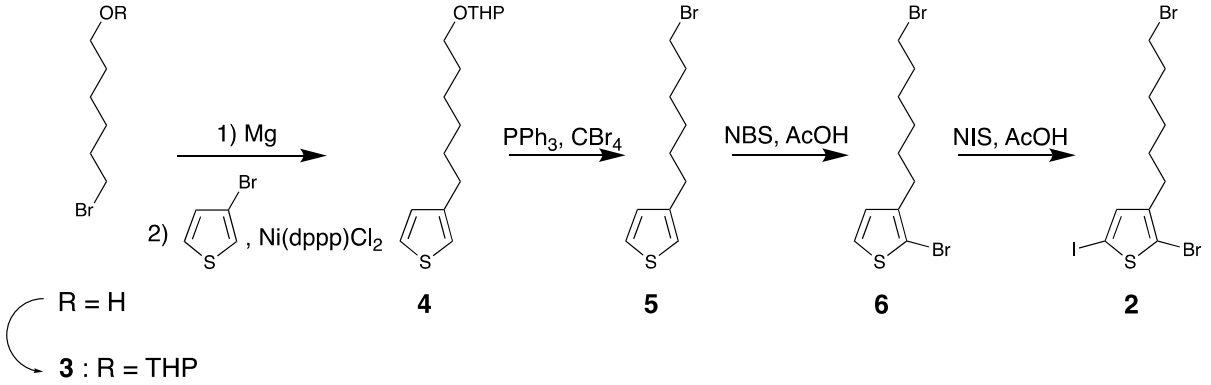

Scheme 6: Synthesis of monomer 2

2-((6-bromohexyl)oxy) tetrahydro-2*H*-pyran (3): Amberlyst 15® resin (2 g) was suspended in a solution of 6-bromohexanol (10.0 g, 55.3 mmol) in CH_2Cl_2 (125 mL) under Ar. 3,4-dihydro-2H-pyran (6.11 g, 72.6 mmol, 1.3 equiv) was added to the suspension that was stirred for 1 hour at 25 °C. The resin was filtered and the medium evaporated under vacuum. The yellow crude oil was purified by chromatography (SiO_2, EtOAc/C_6H_{12} 1/9) to yield pure **3** as a colorless oil (11.20 g, 77% yield).

^{1}H RMN (400 MHz, $CDCl_3$) δ (ppm): 4.58 (dd, *J* = 4.6, 2.7 Hz, 1H, OCHO), 3.84 (m, 1H, pyran C**H**HO), 3.74 (dt, *J* = 9.6, 6.8 Hz, 1H, CH**H**-OTHP), 3.50 (m, 1H, OC**H**H(CH_2)$_4$$CH_2$Br), 3.40-3.34 (m, 3H, CH**H**-OTHP + CH_2Br), 1.89-1.33 (m, 14H, CH_2);

^{13}C RMN (100 MHz, $CDCl_3$) δ (ppm): 98.9 (pyran C2), 67.3 (pyran C6), 62.3 (CH_2-O-), 33.9 (CH_2-Br), 32.7 (**C**H_2-CH_2-Br), 30.7 (pyran C3), 29.6 (**C**H_2-CH_2-O-), 27.9 (**C**H_2-$(CH_2)_2$-O-), 25.5 (C**H₂**-$(CH_2)_2$-Br), 19.7 (pyran C4);

FTIR (ATR diamond) ν (cm^{-1}): 2937 ($\nu_{as}CH_2$), 2860 (ν_sCH_2), 1453, 1440, 1352, 1322, 1259, 1242, 1200, 1184, 1133, 1118, 1076, 1032, 1021, 987, 904, 868, 814, 729, 645 (νCBr), 634, 632, 626, 620, 616;

HRMS (ESI) m/z: $[M + Na]^+$ calcd for $C_{11}H_{21}BrO_2$, 287.0617; found, 287.0613.

3-(6-(tetrahydro-2*H*-pyran-2-oxy)hexyl)thiophene (4): A suspension of magnesium turnings (110 mg, 2.27 mmol, 1.2 equiv) in dry THF (8 mL) was heated at 50 °C and a few drop of dibromoethane were added. 10% of the total amount of **3** (1 g, 1.89 mmol) was introduced and the medium was refluxed for 2h30. When the mixture darkened and the magnesium reacted, the rest of **4** was added dropwise and the mixture refluxed until most of the magnesium had been consumed. The organomagnesium solution was cooled to 25 °C and kept under Ar. In a separate flask, a solution of bromothiophene (558 mg, 3.44 mmol, 1.1 equiv) and Ni(dppp)Cl_2 (54.5 mg, 100 µmol, 0.03 equiv) in dry THF (4 mL) was heated to 60°C for 30 min. The magnesium bromide solution was added dropwise and heated at reflux for 12 hrs. The reaction was quenched with water and extracted with C_6H_{12}/EtOAc (1/1, 3 × 25 mL). The combined organic layers were dried ($MgSO_4$) and concentrated under vacuum. The crude was purified by chromatography (SiO_2, cyclohexane/EtOAc 95/5) to afford pure **5** as an oil (346 mg, 42% yield).

^{1}H RMN (400 MHz, $CDCl_3$) δ (ppm): 7.23 (dd, *J* = 4.9, 3.0 Hz, 1H, thiophene H5), 6.95 – 6.91 (m, 2H, thiophene H2 and H4), 4.56 (dd, *J* = 4.4, 2.7 Hz, 1H, OCHO), 3.85 (m, 1H, pyran C**H**HO), 3.72 (dt, *J* = 9.6, 6.8 Hz, 1H, C**H**H-OTHP), 3.48 (m, 1H, pyran CH**H**O), 3.37 (dt, *J* = 9.6, 6.6 Hz, 1H, CH**H**-OTHP), 2.61 (t, *J*=7.5 Hz, 2H, thiophen-CH_2), 1.89 – 1.79 (m, 1H, THP C3-**H**H), 1.78-1.48 (m, 9H, CH_2), 1.45-1.30 (m, 4H, CH_2);

^{13}C RMN (100 MHz, $CDCl_3$) δ (ppm): 143.1 (thiophene C3), 128.3 (thiophene C4), 125.1 (thiophene C5), 119.9 (thiophene C2), 98.9 (OCHO), 67.6 (pyran C6), 62.3 (**C**H_2-OTHP), 30.9 30.6 and 30.3 (hexyl C1, C2 and pyran C3), 29.8 (hexyl C5), 29.2 (hexyl C3), 26.2 (hexyl C4), 25.6 (pyranC5), 19.8 (pyranC4);

FTIR (ATR diamond) ν (cm^{-1}): 3100 (aromatic νCH), 2930 ($\nu_{as}CH_2$), 2856 (ν_sCH_2), 1536, 1464, 1453, 1440, 1383, 1364, 1352, 1283,1275, 1259, 1200, 1184, 1135, 1119, 1076, 1064,1030, 1021, 988, 904, 882, 834, 814, 771, 731, 683, 661, 632 (νCBr), 575;

HRMS (ESI) m/z: $[M + Na]^+$ calcd for $C_{15}H_{24}O_2S$, 291.1389; found, 291.1388;

Anal. calcd for $C_{15}H_{24}O_2S$: C 67.12, H 9.01; found: C 67.09, H 9.17.

3-(6-bromohexyl)thiophene (5): A solution of **5** (995 mg, 3.71 mmol) and CBr_4 (1.726 g, 5.22 mmol, 1.4 equiv) in anhydrous CH_2Cl_2 (50 mL) is cooled to 0°C under Ar. $P(Ph)_3$ (2.741 g, 10.4mmol, 2.4 equiv) was added and the mixture is warmed to 25 °C and stirred for 3 days. The solvent was evaporated in vacuum and the crude is purified by chromatography (SiO_2, EtOAc/C_6H_{12} 2/98) to afford pure **6** as an oil (760 mg, 83% yield).

^{1}H RMN (400 MHz, $CDCl_3$) δ (ppm): 7.27 (dd, *J* = 4.9 Hz, 3.0 Hz, 1H, thiophene H5), 6.94 (m, 2H, thiophene H2 and H4), 3.43 (t, *J* = 6.8 Hz, 2H, CH_2Br), 2.66 (t, *J* = 7.8 Hz, 2H, thiophene-CH_2), 1.89 (m, 2H, hexyl C5-H_2), 1.67 (p, *J* = 7.7 Hz, 2H, hexyl C2-H_2), 1.53-1.42 (m, 2H, hexyl C4-H_2), 1.41-1.26 (m, 2H, hexyl C3-H_2);

^{13}C RMN (100 MHz, $CDCl_3$) δ (ppm): 143.0 (thiophene C3), 128.3 (thiophene C4), 125.3 (thiophene C5), 120.0 (thiophene C2), 34.1 (CH_2Br), 32.9 (hexyl C5), 30.5 (hexyl C2), 30.3 (hexyl C1), 28.5 (hexyl C3), 28.1 (hexyl C4);

FTIR (ATR diamond) ν (cm^{-1}): 3054 (aromatic νCH), 2928 ($\nu_{as}CH_2$), 2855 (ν_sCH_2), 1536, 1462, 1437, 1410, 1257, 1236, 1152, 1079, 938, 909, 858 and 832, 770, 728 (CH_2rock), 684, 632;

MS (ESI): 246.1, 248.1 [M^+];

Anal. calcd for $C_{10}H_{15}BrS$: C 48.59; H 6.12; found: C 48.26, H 6.12.

2-Bromo-3-(6-bromohexyl)thiophene (6): A solution of **5** (1,00 g, 4.0 mmol, 1 equiv) and AcOH (6mL) in $CHCl_3$ (36 mL) was stirred at 0 °C under Ar. A solution of NBS (721 mg, 4.0 mmol, 1 equiv) in $CHCl_3$ (18 mL) was added in fractions of 5mL spaced by 15 min. After disappearance of **5** (followed by TLC), the solution was neutralised with a 10% NaOH solution, mixed with water (100 mL) and extracted with EtOAc (3 × 40 mL). The organic phases were dried ($MgSO_4$) and concentrated under vacuum. The crude was purified by flash chromatography (cyclohexane) to afford pure **7** as a yellow oil (853 mg, 65% yield):

^{1}H RMN (400 MHz, $CDCl_3$) δ (ppm): 7.20 (d, *J* = 5.6 Hz, 1H, thiophene H5), 6.80 (d, *J* = 5.6 Hz, 1H,thiophene H4), 3.42 (t, *J* = 6.8 Hz, 2H, CH_2Br), 2.58 (t, *J* = 7.7 Hz, 2H, thiophene -CH_2), 1.87 (p, 2H, *J* = 7.0 Hz, hexyl C5-H_2), 1.61 (p, *J* = 7.7 Hz, 2H, hexyl C2-H_2), 1.48 – 1.44 (m, 2H, hexyl C3-H_2), 1.41 – 1.33 (m, 2H, hexyl C4-H_2);

^{13}C RMN (100 MHz, $CDCl_3$) δ (ppm): 141.8 (thiophene C3), 128,3 (thiophene C4), 125.4 (thiophene C5), 109.1 (thiophene C2), 34.0 (CH_2Br), 32.9 (hexyl C5), 30.2 (hexyl C2), 29.6 (hexyl C1), 28.4 (hexyl C3), 28.0 (hexyl C4);

FTIR (ATR diamond) ν (cm^{-1}) 3084 (aromatic νCH), 3003, 2938 ($\nu_{as}CH_2$), 2854 (ν_sCH_2), 1655; 1527 (aromatic νCC), 1463, 1435, 1429, 1394, 1338, 1321, 1281, 1236, 1191, 1059, 1008, 992, 955, 895, 860, 828, 727, 691, 644;

MS (EI): 323.9, 325.9 and 327.9 [M^+].

2-Bromo-3-(6-bromohexyl)-5-iodothiophene (2): A solution of 7 (403 mg, 1.23 mmol) and acetic acid (2.7 mL) in $CHCl_3$ (18 mL) was stirred at 0 °C under Ar. N-iodosuccinimide (275 mg, 1.22 mmol, 1 equiv) was added. When 7 was no longer detected by TLC, the mixture was mixed with aq. NaOH (10%, 100 mL) and extracted with CHCl3 (2 x 40 mL). The organic phase was washed with aq. $Na_2S_2O_3$, dried ($MgSO_4$) and evaporated. The crude was chromatographed (SiO_2, eluent cyclohexane) to yield pure 2 as a solid (417 mg, 75 % yield).

^{1}H NMR ($CDCl_3$, 400 MHz) δ (ppm): 6.97 (s, 1H, thiophene H4), 3.42 (t, 2H, *J* = 6.8 Hz, CH_2-Br), 2.55 (t, *J* = 7.6 Hz, 2H, thiophene-CH_2), 1.87 (p, *J* = 7.0 Hz, 2H, hexyl C5-H_2), 1.57 (p, *J* = 7.6 Hz, 2H, hexyl C2-H_2), 1.48 (m, 2H, hexyl C3-H_2), 1.37 (m, 2H, hexyl C4-H_2);

^{13}C NMR ($CDCl_3$, 100 MHz) δ (ppm): 144.0 (thiophene C3), 138.1 (thiophene C4), 112.0 (thiophene C2), 71.3 (thiophene C5), 34.0 (CH_2-Br), 32.8 (hexyl C5), 29.6 (hexyl C2), 29.1 (hexyl C3), 28.3 (hexyl C4), 28.0 (hexyl C1);

FTIR (ATR diamond) ν (cm^{-1}): 3084 (aromatic νCH), 2923 (νasCH_2), 2854 (νasCH_2), 1655, 1527 and 1463 (aromatic νCC), 1435, 1428, 1394, 1338, 1321, 1281, 1236, 1191, 1059, 1008, 992, 955, 895, 860, 828, 727 (methyl rock), 691, 644;

MS (EI): 453.9, 451.9 and 449.9 [M+];

Anal. calcd. for $C_{10}H_{13}Br_2IS$: C 26.57, H 2.90; found: C 26.43; H 3.15.

2. Polymerization

Poly(3-hexylthiophene-co-3-(6-bromohexyl)thiophene) (A): in a 200 mL reactor equipped with a UV-Vis probe (optical path 151 µm), a solution of dry LiCl (464 mg, 10.9 mmol) in THF (120 mL) was stirred at 0 °C. i-PrMgCl (2 M in THF) was added slowly until the absorption of the organomagnesium between 250 and 270 nm was persistent. 2-bromo-3-hexyl-5-iodothiophene 1 (751 mg, 2.0 mmol) and 2-bromo-3-(6-bromohexyl)-5-iodothiophene 2 (159 mg, 336 µmol) were added. i-PrMgCl (2 M in THF) was added slowly until no more than 90 % of the monomer is metallated. Aliquots of the medium were sampled, quenched with CD_3OD and the amount of metallated monomers measured (singlet at 6.90

ppm). The mixture was heated to 20 °C and Ni(dppp)Cl_2 (68 mg, 127 µmol, 0.04 equiv) was added. Reaction was followed by absorption at 440 nm. The reaction was quenched with two drops of aqueous HCl (2 M). The solution was partially evaporated and the polymer was precipitated in methanol (10 x the volume of the solution). The polymer was separated from supernatant by centrifugation (9500 rpm, 1 h) and dried under vacuum for 24 h to yield pure A (543 mg, 97%). The copolymer was dissolved in $CHCl_3$ and further purified by preparative GPC.

^{1}H NMR (400 MHz, $CDCl_3$): δ (ppm) 6.99 (s, thiophene C4-H), 3.43 (t, *J* = 6.8 Hz, CH_2Br), 2.81 (m, thiophene-CH_2), 1.89 (p, *J* = 6.9 Hz, C**H**$_2$$CH_2Br$), 1.71 (m, hexyl C2-$H_2$), 1.57-1.25 (m, 6H, hexyl C3-H_2, C**H**$_2$$CH_3$ and hexyl C4-H_2), 0.92 (m, 3H, CH_3);

^{13}C NMR (100 MHz, $CDCl_3$) δ (ppm): 140.1 (thiophene C3), 139.7 (bromohexylthiophene C3), 133.9 (thiophene C5), 130.7 (thiophene C2), 128.8 (thiophene C4), 34.0 (CH_2Br), 32.9 (bromohexyl C5), 31.8 (hexyl C4), 30.7 (hexyl C2), 30.5 (bromohexyl C2), 29.6 (hexyl C3), 29.4 (hexyl and bromohexyl C1), 28.8 (bromohexyl), 28.2 (bromohexyl), 22.8 (hexyl C5), 14.3 (CH_3);

FTIR (ATR diamond) ν (cm^{-1}): 3055 (aromatic νCH), 2953 ($\nu_{as}CH_3$), 2920 ($\nu_{as}CH_2$), 2852 (ν_sCH_2), 1562, 1509 and 1453 (aromatic νCC), 1376 (δCH_3), 1261, 818, 723;

Poly(3-hexylthiophene-*co*-3-(6-(4-(diphenylimino)phenoxy)hexyl)thiophene) (B): in a pressure tube, K_2CO_3 (29 mg, 210 µmol, 1.22 equiv) was suspended in a solution of Bu_4NBr (35 mg, 108 µmol, 0.63 equiv) and 4-[(diphenylmethylene)amino]phenol (48 mg, 172 µmol, 1.00 equiv) in DMF (2 mL). A solution of copolymer **A** (204 mg, 1.15 mmol, 172 µmol of bromohexyl) in THF (30 mL) was added and the sealed tube was heated to 95 °C for 4 days. THF was removed in vacuum and the crude was precipitated in ten times its volume of MeOH. The polymer was recovered by centrifugation (9500 rpm) and dried 24 h under vacuum (211 mg, 89% yield).

^{1}H NMR (400 MHz, $CDCl_3$): δ (ppm) 7.70 (d, *J* = 7.2 Hz, imine phenyl), 7.47-7.33 (m, 0.44 H, imine phenyl), 7.25 (m, imine phenyl), 7.10 (m, 0.28 H, imine phenyl), 6.99 (s, 1H, thiophene C4-H), 6.65 (m, 0.57 H, *J* = 8.4 Hz, aminophenol H), 3.87 (t, 0.28 H, *J* = 6.3 Hz, CH_2O), 2.80 (m, 2H, thiophene-CH_2), 1.71 (m, 2H, thiophene-CH_2C**H**$_2$), 1.49-1.40 (m, 2H, hexyl C), 1.35 (m, 4H, CH_2C**H**$_3$ and thiophene-$(CH_2)_3$C**H**$_2$), 0.92 (m, 3H, C**H**$_3$).

^{13}C NMR (100 MHz, $CDCl_3$) δ (ppm): 175.1 (C=N), 155.6 (Aryl C-O), 151.7, 144.4 (Aryl C-N), 140.3 (Ph_2C=N phenyl C1), 140.1 (thiophene C3), 136.8 (Ph_2CN phenyl C4), 135.9 (phenyl , 133.9 (thiophene C5 HTHT). 130.6 (thiophene **C**2), 129.7, 129.3, 128.8 (thiophene **C**4), 128.6, 128.4 (**C**2 thiophene), 128.3, 128.1, 125.7, 122.7, 114.5, 34.4 (**C**H_2-thiophene protected amine). 31.9 (**C**H_2-thiophene hexyl).

30.7 (**C**H_2CH_2-thiophene hexyl), 30.5 (**C**H_2-CH_2-O), 29.6 (**C**$H_2CH_2CH_2$-thiophene hexyl), 29.5, 29.4 (**C**$H_2CH_2CH_3$), 26.1 (**C**$H_2CH_2CH_2$-O), 22.8 (**C**H_2CH_3), 21.3, 14.3 (**C**H_3);

FTIR (ATR diamond) ν (cm^{-1}): 3054 (aromatic νCH), 2953 ($\nu_{as}CH_3$), 2922 ($\nu_{as}CH_2$), 2853 (ν_sCH_2), 1608 (imine νCN), 1564, 1501 and 1453 (thiophene νCC), 1446, 1376 (δCH_3), 1315 (aryl C-N stretching), 1238 (νCO ether), 1166 (νC-O ether), 1104 and 958, 819 (oop thiophene CH), 783 (imine phenyl CH bend), 724 (methyl rock), 693 (imine phenyl CH bend).

Poly(3-hexylthiophene-*co*-3-((4-aminophenoxy)hexyl)thiophene) (PHTcoAHT): a solution of copolymer **B** (58 mg, 280 µmol, 40 µmol of imine) and hydroxylamine (0.1 mL, 33 mmol, 35 equiv) in THF (2 mL) was heated to 50 °C under Ar for 20h. The resulting polymer was precipitated in MeOH, separated by centrifugation (9500 rpm, 1 h) and dried under vacuum for 24 h. A shiny violet solid was obtained (50 mg, 98 % yield) (SI section I-E).

^{1}H NMR (400 MHz, $CDCl_3$) δ (ppm) 6.99 (s, 1H, C**H** thiophene HT-HT coupling), 6.96, 6.73(d, 2H, *J* = 8.2 Hz, phenyl C2-H and C6-H), 6.62 (d, 2H, *J* = 8.2 Hz, C**H** phenyl C3-H and C5-H), 5.02 (s, NH2), 3.89 (t, 2H, *J* = 6.4 Hz, C**H**$_2$O), 2.81 (m, 2H, C**H**$_2$-thiophene HT coupling), 1.71 (m, 2H, C**H**$_2$-CH_2 -thiophene), 1,44 (m, 2H, C**H**$_2$-CH_2 -CH_2 thiophene), 1.35 (m, 2H, C**H**$_2$-CH_2 -CH_2-CH_2 thiophene), 1,27(m, 2H, CH_2C**H**$_3$), 0.93(m, 3H, C**H**$_3$);

^{13}C NMR (400 MHz, $CDCl_3$) δ (ppm): 140.1 (**C**3 thiophene HTHT). 133.9 (**C**5 thiophene HTHT). 130.7 (**C**2 thiophene HTHT), 128.8 (**C**4 thiophene HTHT). 116.6, 115.8, 31.9 (**C**H_3). 30.7(**C**H_2CH_2-thiophene hexyl), 30.5, 29.6 (**C**$H_2CH_2CH_2$-thiophene hexyl), 29.4 (**C**$H_2CH_2CH_3$), 22.8 (**C**H_2CH_3), 14.3 (**C**H_3);

FTIR (ATR diamond) ν (cm^{-1}): 3361 (large, NH stretching), 3053 (CH aromatic stretching), 2953, 2922 and 2853 (aliphatic CH stretching), 1608 (NH bend), 1562 (NH bend), 1510 and 1454 (asymmetric and symmetric ring stretching), 1377 (methyl def.), 1236 (C-O alkyl aryl ether), 819 (aromatic CH out of plan), 724 (methyl rock).

Annex 2: Experimental and Instrumental

Elaboration of the nanohybrids: A typical dispersion procedure for the elaboration of non-covalent nanohybrids consist in adding a given volume of the mother suspension (sonicated for 30 s before use) of the nanotubes into a solution of the desired polymer of known concentration.

Each sonication step is performed directly in the vial for 5 min (tip sonication, 20% of 500 W, Fischer Scientific Model FB-505). This procedure was shown to have no effect on the polymer chain length via SEC.

The reference sample for SWNTs was prepared by dissolving 10.5 mg of sodium dodecyl sulfate (SDS) in 4 mL of D_2O. 1.98 mg of SWNTs were added to this solution and the mixture was sonicated for 5 min then centrifuged (25000 g for 80 min). The supernatant was collected and characterized.

The reference sample for DWNTs was prepared by dissolving 37 mg of sodium cholate in 4 mL of D_2O. 0.83 mg of DWNTs were added to this solution and the mixture was sonicated for 5 min then centrifuged (25000 g for 80 min). The supernatant was collected and characterized.

Covalent functionalization: Typical samples were prepared by Tour's reaction on suspensions of SWNTs/**PHTcoAHT** in THF (weight ratio of 0.2 and 0.05 for **PHTcoAHT 36000** and **5000** respectively to ensure a good dispersion of SWNTs). 10 equiv. of isoamyl nitrite with respect to the amine groups were added to the suspensions and the resulting mixtures were heated at 65 °C for 12 h in a sealed Schlenk's vial. The product of the reaction was centrifuged during 5 minutes at 25000 g and the supernatant was recovered and characterized.

NMR spectra were recorded on a Bruker WH-400 MHz spectrometer in $CDCl_3$ and were reported in δ ppm relative to Me_4Si.

Size exclusion chromatography (SEC): The dry samples (5 mg) were dissolved in THF (5 mL) and few drops of toluene as the flow marker were added and the solution filtered (PTFE, 0.45 µm). 100 µL of the solution was injected on a Shimadzu HPLC equipped with a diode array UV detector (SPD-M20A), an Optilab T-rEX refractometer from Wyatt Technology, and a TREOS light scattering detector from Wyatt Technology. The solution was analyzed with a 4 PL gel mixed C column, thermostated at 35 °C, and calibrated with 15 linear PS standards from Polymer Lab. Preparative SEC was performed on a LaboACE LC-5060 from Japanese Analytical Industries, on a JAIGEL-2HR and JAIGEL-2.5HR columns.

UV – Vis – NIR spectra were recorded with a Varian Cary 5000 or a Perkin Elmer - Lambda 25 spectrometer.

Fluorescence spectra were measured with a Horiba-Jobin-Yvon E348 Fluorimeter. A triangular cell was used allowing the analysis of the same solutions as those characterized by UV-vis by getting rid of possible internal filter effects. A rectangular cell (10mm x 10mm) has been used to characterize low concentrated solutions.

Transmission electron microscopy experiments were performed using a Technai G2 Microscope (FEI) at 200 kV. Images were acquired with an Eagle2K slow-scan charge-coupled device (ssCCD) camera (FEI).

Five microliters of nanohybrids solutions were deposited onto a Lacey-Formvar/carbon-covered copper grid (300mesh) or onto a carbon covered copper grid (300mesh). The deposited droplet is quickly dried with a filter paper.

PL maps were obtained by using a supercontinuum WhiteLase SC400-8 exciting laser, a liquid-nitrogen cooled InGaAs detector and a 300 groove/mm grating. Cutting filters are placed in front of the spectrometer to remove high-order peaks of the laser.

Measurements were performed on the suspensions inside a 5 mm quartz cell. These were obtained with excitation steps of 5 nm.

Raman spectra and maps were recorded using an Acton SP2500 spectrometer fitted with a Pylon CCD detector and a 1800 grooves/mm grating. The samples were excited with a 633 nm (1.96 eV) laser (HeNe, Newport) or a supercontinuum WhiteLase SC400-8 laser calibrated to 633 nm or 532 nm (2.33 eV) through 50x objective (Numerical Aperture 0.5) and 0.1 mW impinging on the sample. The instrument is calibrated by using the peak position of the laser wavelength and silicon peak (520.7 cm^{-1})

Samples for Raman spectroscopy analysis were prepared from the suspensions/solutions via spin-coating. The obtained films were then rinsed with THF for eliminating the excess of polymer.

Field effect transistor devices preparation was briefly described in Chapter 4. Electric measurements were performed with Berillium-Copper contacts and an Agilent B1500A equipped with 3 source measurement units for each terminal (source, drain, gate).

AFM images of the devices were obtained with Nanoscope V (Bruker) instrument in tapping mode using a commercial silicon probe (resonant frequency ~300 kHz and spring constant ~20 N/m) in ambient conditions.

Photocurrent maps were obtained by exciting the sample by using a supercontinuum WhiteLase SC400-8 laser attenuated by a filter of optical density 4.

Résumé de thèse

Cette thèse décrit la synthèse et la caractérisation de matériaux nanohybrides polymère conjugué – nanotubes de carbone. Deux types d'hybrides ont été synthétisés : non-covalents et covalents. Les propriétés physico-chimiques de ces nanohybrides ont ensuite été étudiées par des méthodes de microscopie et spectroscopie. La procédure de synthèse a été aussi utilisée pour la fonctionnalisation de nanotubes de carbone en dispositifs du type transistor à effet de champ, dont les propriétés ont aussi été étudiées.

Le premier chapitre de cette thèse introduit les concepts fondamentaux liés à chacun des composants des nanohybrides. Comme les nanohybrides sont composés de deux matériaux très différents, ce chapitre est divisé en deux sous-parties, chacune centrée sur un de ces composants. Il commence par une description des nanotubes de carbone monofeuillets (SWNTs) et de sa structure électronique. La connaissance de cette structure donne les bases nécessaires pour la compréhension des spectres obtenus le long de la thèse, notamment les résultats des spectroscopies optique, Raman et de fluorescence. Il y est aussi décrit les différentes méthodes de fonctionnalisation des nanotubes de carbone (covalente et non-covalente) et les propriétés des matériaux hybrides résultants. Cette partie finit par une brève description des nanotubes de carbone bifeuillets (DWNTs), aussi utilisés dans cette étude et dont les propriétés sont légèrement changées par rapport à celles des SWNTs à cause de l'interaction entre les deux parois.

La deuxième partie de ce chapitre introduit le poly(3-hexylthiophene) (P3HT), polymère conjugué capable d'interagir avec les nanotubes de carbone. Initialement ses propriétés sont décrites par rapport à la longueur de conjugaison, laquelle est affectée par le solvant, la température, la masse molaire du polymère, sa régiorégularité et des processus de mise en forme. Toutefois, les propriétés de ce polymère ne peuvent pas être décrites seulement en considérant les interactions au sein d'une chaîne de polymère (interactions entre les monomères ou intra-chaîne). En effet, le P3HT forme des agrégats où les différentes chaînes interagissent fortement (interactions inter-chaîne), avec une délocalisation des excitations le long de l'agrégat. La balance entre interactions intra-chaîne et inter-chaîne détermine les propriétés optoélectroniques du polymère et peut être évaluée qualitativement à travers d'une théorie développée dans la littérature et introduite dans ce chapitre.

Le deuxième chapitre de cette thèse commence par la présentation de la voie de synthèse du P3HT et du copolymère PHTcoAHT (**Figure 110** pour les structures), lequel est utilisé pour la fonctionnalisation covalente des nanotubes de carbone. Cette voie a été développée avant le début de cette thèse par Dr. Philippe Mésini and Jean-Philippe Lamps et a été reproduite le long de la thèse pour la synthèse des différents polymères utilisés.

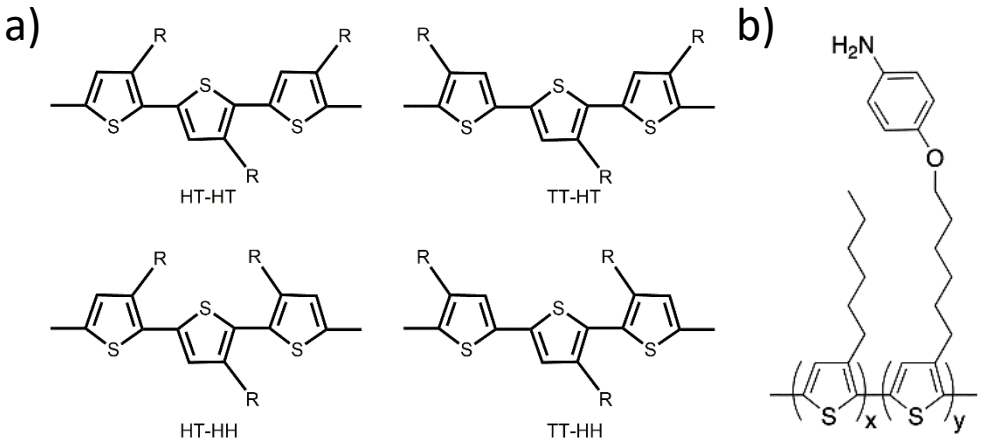

Figure 110: a) Enchaînements possibles des monomères pour des thiophènes substitués en position 3. La triade HT-HT représente l'enchaînement du P3HT dit régioregulier ; b) Structure du copolymère PHTcoAHT.

Cette voie se base sur la polymérisation par transfert de catalyseur de Kumada (KCTP), laquelle résulte en un P3HT avec une masse moléculaire contrôlée et de faible dispersion, ainsi qu'une régiorégularité très élevée (mesurée comme > 99 % par RMN du proton pour les différents polymères et copolymères synthétisés). PHTcoAHT ne peut pas être synthétisé directement par cette méthode, ainsi un copolymère précurseur contenant un brome en fin de chaîne hexyle est synthétisé et modifié postérieurement. Cette copolymérisation via KCTP permet d'obtenir les mêmes avantages que lors de la synthèse de l'homopolymère, ainsi qu'un bon contrôle du taux d'incorporation de chaque comonomère dans la chaîne. Des polymérisations arrêtées à des faibles taux de conversion permettent de prouver que les copolymères obtenus sont statistiques. Cette méthode a permis aussi l'obtention d'un homopolymère complètement fonctionnalisé. Les propriétés des différents polymères et copolymères obtenus sont résumées sur le **Tableau 1**.

Tableau 1 : Caractéristiques des polymères synthétisés.

Nom adopté	Type de polymère	M_n (g/mol)	Đ	Proportion de comonomère fonctionnalisé
P42	P3HT	42000[a]	1.86[a]	0 %
P21	P3HT	21000[a]	1.11[a]	0 %
P7	P3HT	7400[a]	1.34[a]	0 %
CP37	PHTcoAHT	37000[a]	1.41[a]	18 %
CP5	PHTcoAHT	4700[a] [3700][b]	1.29[a] [1.12][b]	14 %
FP17	P3HT amine	17500[a]	1.26[a]	100 %
FP8	P3HT amine	7800[a]	1.47[a]	100 %
PD18	P3DDT[c]	17900[a]	1.02	0 %

[a] Déterminé par chromatographie d'exclusion stérique ; [b] Déterminé par spectroscopie de masse ; [c] Poly(3-dodecylthiophene)

Les groupements brome en fin de chaîne hexyle peuvent être complètement convertis en groupements aniline en deux étapes avec une perte minime de polymère.

Non décrit dans le **Tableau 1**, un copolymère contenant des chaînes dodécyle a pu aussi être synthétisé pendant cette thèse. La méthode a dû être adaptée à cause de difficultés liées à la purification du monomère, et le produit final n'a pu être obtenu qu'en octobre 2020. A cause de cela, la fonctionnalisation de nanotubes de carbone par ce copolymère n'a pas pu être étudiée.

Les polymères et copolymères décrits ci-dessus ont été utilisés pour la synthèse de nanohybrides non-covalents. Ces nanohybrides forment des suspensions stables pendant quelques heures dans du THF, au contraire des nanotubes de carbone seuls qui précipitent immédiatement.

Deux méthodes ont été utilisées pour l'élaboration de ces nanohybrides. La première, dite par extraction par de solvant, permet d'obtenir une suspension de nanohybrides pure. Cette méthode consiste à mélanger les nanotubes avec du polymère dans du THF à l'échelle du milligramme à travers l'utilisation d'ultrasons. La suspension obtenue est centrifugée et le précipité, composé majoritairement de faisceaux de nanotubes non dispersés, est rejeté. Au surnageant on ajoute du toluène, ce qui entraîne la précipitation des nanohybrides, tandis que l'excès de polymère demeure en solution. Cette étape est suivie d'une nouvelle centrifugation et redispersion des nanohybrides, et le processus d'extraction par toluène est répété jusqu'à élimination du P3HT. Le produit final est dispersé dans le THF.

La suspension de nanohybrides obtenue est stable pendant quelques heures. Il est possible d'observer que, en dépit de plusieurs étapes d'extraction (6 en moyenne), une quantité importante de polymère reste en interaction avec les nanotubes (**Figure 111**). La quantité totale de matière en suspension est de l'ordre du dixième de milligramme.

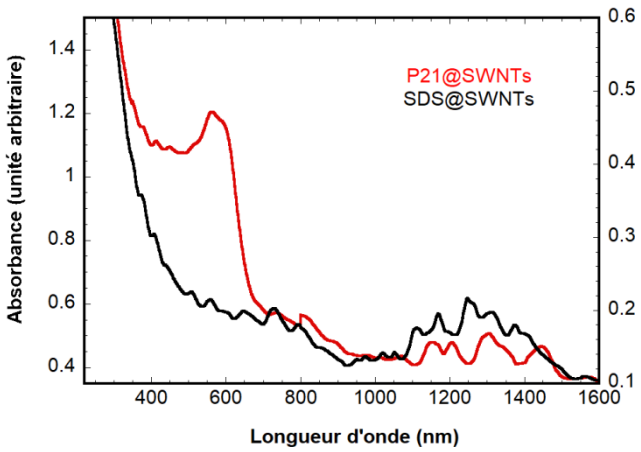

Figure 111 : Spectre d'absorption des nanohybrides SDS@SWNTs dans du D_2O (noir) et P21@SWNTs (obtenus par extraction par solvant) dans du THF (rouge)

Alors que cette méthode s'est montrée effective pour la synthèse de nanohybrides non-covalents P21@SWNTs et CP36@SWNTs, les nanohybrides préparés avec d'autres polymères/copolymères n'ont pas pu être obtenus par cette méthode, très peu ou aucun nanohybride restant en solution après la première centrifugation. De même, les nanohybrides de nanotubes bifeuillets n'ont pas pu être obtenus par de cette méthode. Cette technique a aussi l'inconvénient de ne pas permettre de connaître parfaitement la composition de la suspension finale. Cela limite la reproductibilité de la technique.

Pour obtenir des suspensions très reproductibles et essayer de mieux comprendre les interactions entre les deux composants, des solutions de polymère plus diluées (concentration de l'ordre du dixième du mg/ml) ont été préparées, auxquelles des fractions de nanotubes sont ajoutées jusqu'à ce que les suspensions floculent spontanément après la sonication. Cette méthode a permis d'obtenir des suspensions de nanohybrides à partir de chaque polymère/copolymère (à l'exception de FP17 et FP8, lesquels ont été abandonnées) avec des nanotubes monofeuillets et bifeuillets.

La méthode décrite ci-dessus est dite méthode des ajouts et les résultats obtenus avec elle sont montrés dans la première partie du Chapitre 3. On peut observer un comportement général pour les différents nanohybrides, ce comportement étant d'abord décrit pour le système P21@SWNTs.

Quatre changements sont observés dans le spectre des nanohybrides à mesure qu'on ajoute des nanotubes à la suspension (**Figure 112a**) :

- Une montée de l'absorbance dans tout le spectre. Cela est causé par la résonance des plasmon π des nanotubes et peut être corrigé par une fonction en $1/\lambda$;

- L'apparition de plusieurs pics à λ > 700 nm, qui correspondent aux pics d'absorption des différentes espèces de nanotubes. Ces pics sont légèrement décalés vers le rouge par rapport aux mêmes nanotubes dispersés dans du D_2O à l'aide de SDS. Cela est partiellement causé par un effet du changement de la constante diélectrique du milieu, mais l'amplitude de ce décalage (environ 50 meV) suggère aussi une interaction non-covalente forte (comme les interactions π).
- Une réduction de l'absorption à 450 nm, attribuée au polymère libre (bien dissout). Cette diminution est linéaire pour les premiers ajouts de nanotubes (**Figure 112b**) et permet d'estimer la quantité de polymère qui interagit avec les nanotubes (pour P21@SWNTs, cette quantité est estimée à 1.02 mg P21/ mg SWNT;

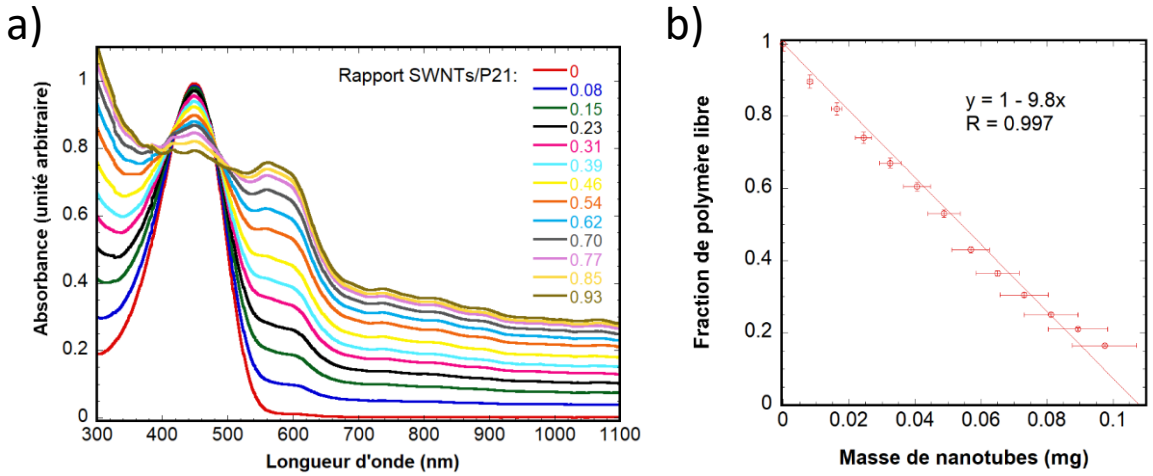

Figure 112 : a) Spectres d'absorption des nanohybrides P21@SWNTs obtenus par ajouts successifs d'une suspension mère de SWNTs dans une solution de P21 ; b) Fraction de polymère libre en solution en fonction de la masse de nanotubes de carbone ajoutée pour les suspension de la ***Figure 112a****.*

- L'apparition d'une bande d'absorption complexe entre 500 et 650 nm (**Figure 113a**). Cette bande est attribuée à des agrégats de P3HT qui se forment sur la surface des nanotubes de carbone.

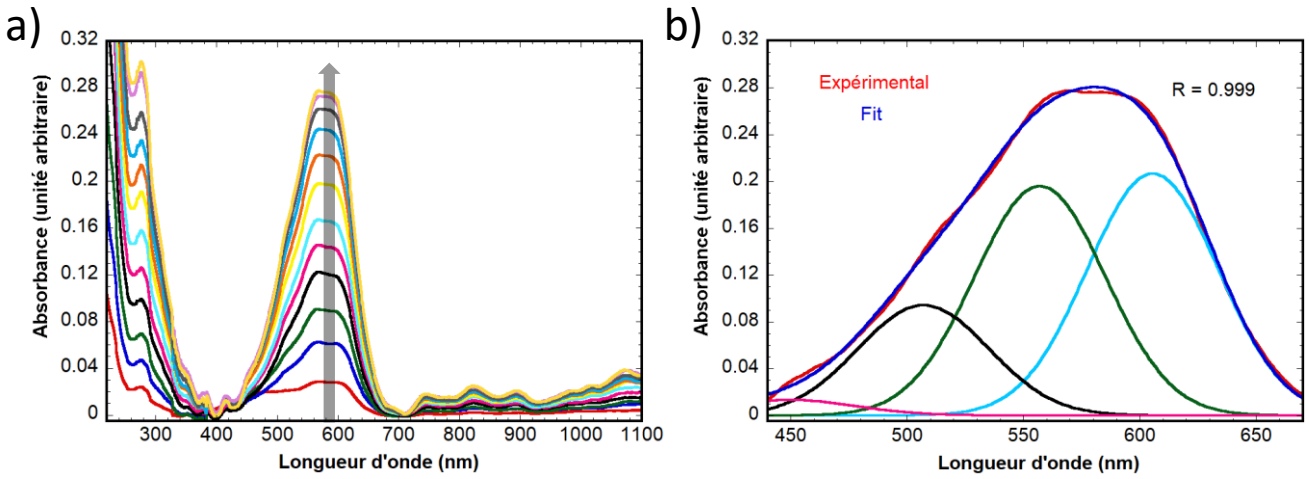

Figure 113 : a) Spectres d'absorption des nanohybrides P21@SWNTs de la ***Figure 112a*** *corrigés de l'absorption des plasmon π des nanotubes de carbone, dont la forme a été ajustée par une fonction en 1/λ, et par l'absorption du polymère libre ; b) Fit du spectre d'absorption des agrégats de polymère.*

Cette bande d'agrégats présente deux particularités qui permettent une évaluation qualitative de sa structure. Premièrement, elle est constituée de trois pics séparés d'approximativement 50 nm (**Figure 113b**, le quatrième pic présent correspondant à du polymère libre non considéré par les corrections antérieures). Ces trois pics sont dus au couplage de l'excitation électronique des agrégats avec la vibration vinylique d'agrégats bien organisés. Le ratio entre l'absorbance des pics à 610 nm et à 560 nm (dits $A_{0\text{-}0}$ et $A_{0\text{-}1}$ respectivement) permet de déterminer le type d'agrégat à l'aide de la théorie de Spano (introduite dans le Chapitre 1). Pour ce système la valeur de $A_{0\text{-}0}/A_{0\text{-}1}$ est très proche de 1, ce qui suggère un comportement J dominant (interactions intra-chaînes dominent la structure électronique du système, ce qui suggère que les chaînes sont étirées).

En deuxième lieu, la résolution des pics est très faible, ce qui est corrélé avec un nombre faible d'unités en interaction. Cela indique que les agrégats sont constitués d'un petit nombre de chaînes en interaction.

Les résultats de spectroscopie d'absorption sont complémentés par ceux de spectroscopie de fluorescence (**Figure 114**). On observe une extinction de la fluorescence au fur et à mesure que les nanotubes sont ajoutés au système. L'émission observée est totalement due au polymère libre en solution, et l'intensité observée est proportionnelle à la valeur de l'absorbance du polymère libre. On n'observe pas d'émission des agrégats.

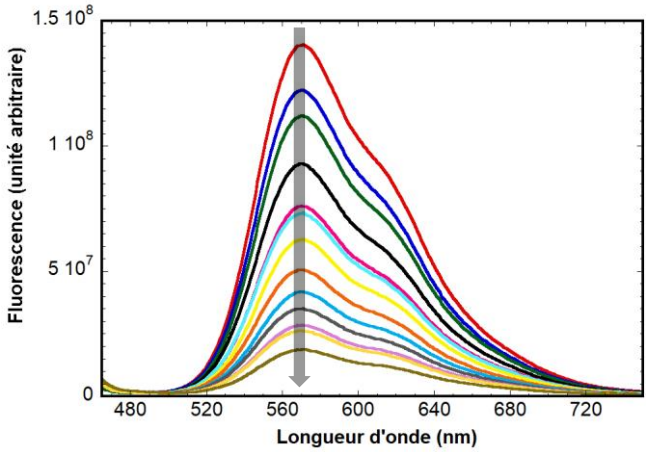

Figure 114 : Spectres d'émission des suspensions de nanohybrides P21@SWNTs correspondant aux spectres de la ***Figure 112a****.*

Utilisant la spectroscopie de photoluminescence (**Figure 115**), on peut observer l'excitation et l'émission des espèces semi-conductrices des nanotubes de carbone monofeuillets. Les longueurs d'onde d'excitation et d'émission de ces espèces sont décalées vers le rouge pour toutes les espèces par rapport aux nanotubes dispersés dans le D_2O avec du SDS, en accord avec ce qui a été observé par spectroscopie optique. Plus important, lorsqu'on excite les agrégats de polymère (entre 500 et 650 nm), toutes les espèces de nanotubes émettent. De plus, cette émission est très intense et dépasse celle obtenue par l'excitation de la transition optique des nanotubes de carbone. Ces résultats suggèrent un mécanisme de transfert d'énergie des agrégats aux nanotubes de carbone via un mécanisme du type FRET (anglais pour transfert d'énergie par résonance de type Förster). Ce mécanisme prédit un transfert d'autant plus efficace que le donneur et l'accepteur sont proches, ce qui est en accord avec la formation des agrégats de polymère sur les nanotubes.

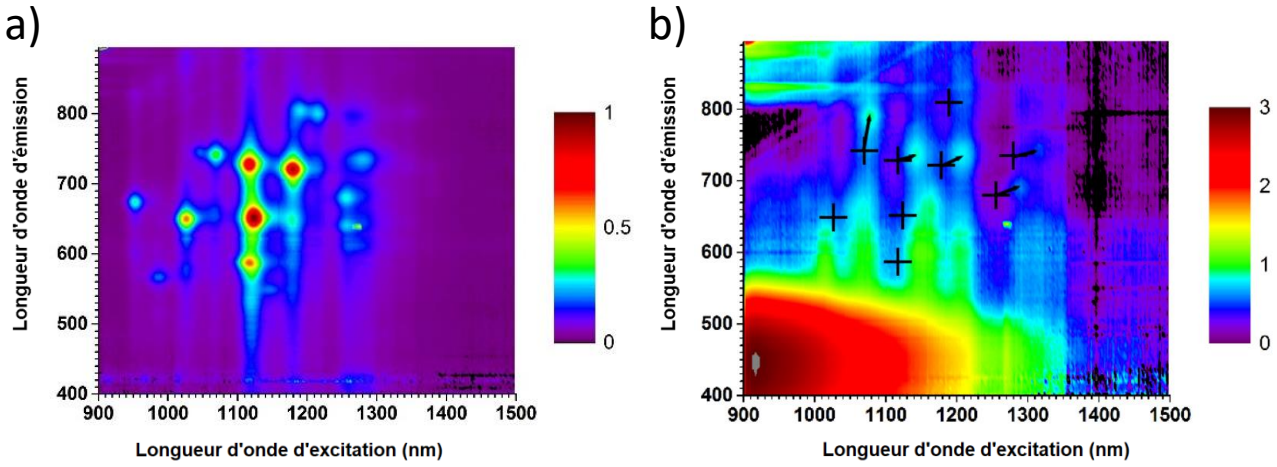

Figure 115 : Spectres de photoluminescence de a) SDS@SWNTs dans du D_2O; b) P21@SWNTs dans du THF.

Les microscopies électronique à transmission (TEM) et Cryo-TEM permettent l'observation directe de la morphologie des nanohybrides obtenus (**Figure 116**). On observe des nanotubes de carbone enrobés

par des chaînes polymères. Cet enrobage est constitué par une ou quelques chaînes de polymère, ce qui est en accord avec ce que nous indique la spectroscopie optique.

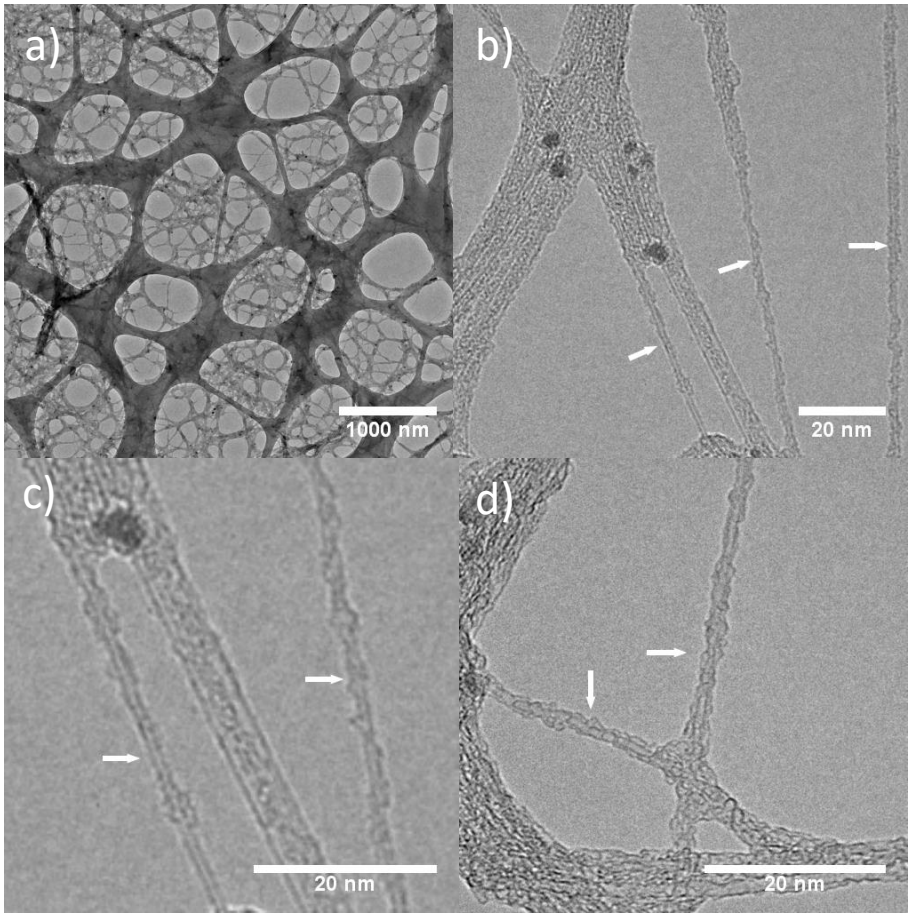

Figure 116 : Images représentatives obtenues par TEM des nanohybrides P21@SWNTs déposés sur une grille à trous. Les flèches pointent vers des nanotubes individuels enrobés de polymère.

L'important ordre intra-chaîne du P3HT dans ces nanohybrides est induit par son interaction avec les nanotubes de carbone. La grande énergie d'interaction entre ces deux composants est due à la présence d'interactions π et d'interactions hydrophobes. Cela permet aux chaînes polymères de compenser la perte d'entropie liée à la diminution de polymère libre dans la solution, permettant ainsi l'enrobage des nanotubes de carbone et la formation des agrégats. Toutefois, cette interaction diminue au fur et à mesure que l'agrégat croît, ce qui limite sa taille.

Comme observé par la méthode d'extraction par solvant, la masse molaire du polymère est un paramètre important pour la formation de nanohybrides. Le **Tableau 2** montre le rapport de masses entre SWNTs et polymère au-delà duquel la suspension de nanohybrides devient instable (floculation immédiate après sonication), ainsi que la quantité de polymère adsorbé par masse de nanotubes de carbone. On observe un optimum de la solubilité des nanohybrides pour le P21. La quantité de matière adsorbée toutefois augmente avec la longueur de la chaîne, ce qui peut être lié la réduction de la solubilité du polymère avec l'augmentation de sa masse molaire.

Tableau 2 : Caractéristiques des suspensions homopolymère @ SWNTs.

Polymère	Rapport massique critique SWNTs/polymère	Polymère adsorbé (mg polymère/mg SWNTs)	Polymère adsorbé (unités hexylthiophène/hexagone de carbone des SWNTs)
P7	0.27 ± 0.12	0.58 ± 0.01	0.25 ± 0.01
P21	2.16 ± 0.10	1.00 ± 0.01	0.44 ± 0.01
P44	0.63 ± 0.08	1.54 ± 0.08	0.67 ± 0.05

P7 et P21 ont un comportement très semblable lors de leur interaction avec les nanotubes de carbone. P44 toutefois, dans les mêmes conditions et même en solutions plus diluées, présente une cinétique d'agrégation sur les nanotubes de carbone (**Figure 117**). Cette agrégation est rapide au début de la cinétique, mais devient plus lente et n'atteint pas l'équilibre même après une journée. De ce fait, la valeur donnée sur le **Tableau 2** n'est qu'indicative et est sous-estimée par rapport à la valeur à l'équilibre. Cette cinétique rapide entraîne la formation d'agrégats plus grands que ceux pour P21, comme cela est mis en évidence par la grande résolution des pics d'absorption de ces agrégats.

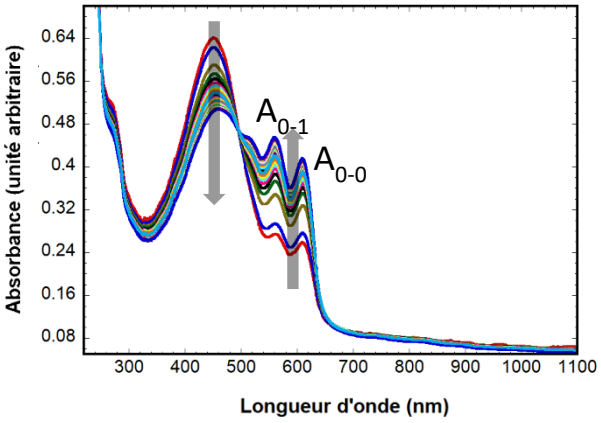

Figure 117 : Spectre d'absorption des nanohybrides P44@SWNTs pris au cours d'une cinétique d'agrégation (intervalle entre les spectres de 15 min)

La cinétique observée suit une fonction exponentielle étirée (**Figure 118**). Cette forme est liée à la distribution de diamètres des nanotubes dans l'échantillon de départ, ainsi qu'à la distribution des masses molaires du polymère. En effet, il est montré par chromatographie d'exclusion stérique, faite sur le surnageant au départ et à la fin de la cinétique, que les chaînes le plus longues s'agrègent en premier en raison de leur plus faible solubilité.

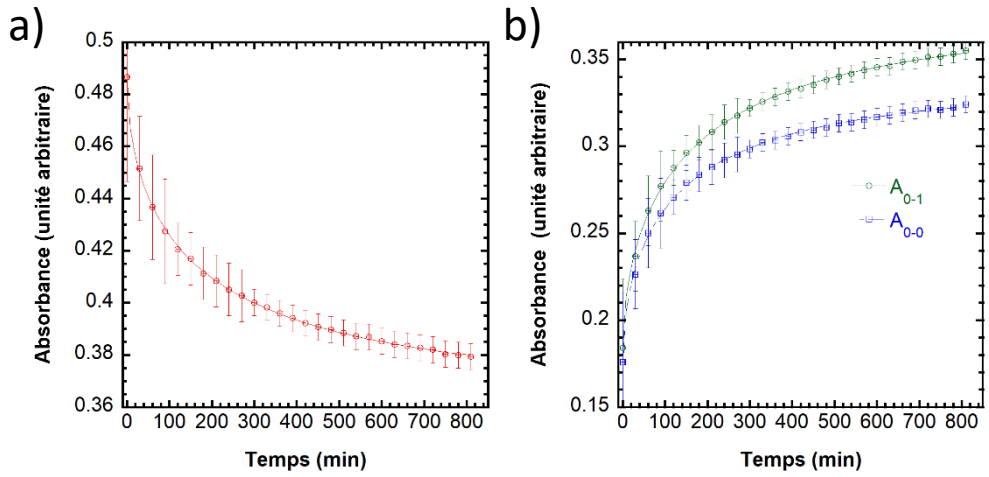

Figure 118 : Cinétique d'agrégation du polymère P44 sur des SWNTs. a) Absorbance du polymère libre, mesurée à 450 nm ; b) Absorbance des agrégats, mesurée à 560 nm ($A_{0\text{-}1}$, vert) et à 610 nm ($A_{0\text{-}0}$, bleu).

L'ajustement de la courbe est très sensible à l'erreur sur la mesure du temps, ce qui doit être pris en compte pour une évaluation absolue des paramètres. Cette erreur est systématique, ce qui permet la comparaison entre différents échantillons.

Le temps caractéristique de cette cinétique est d'autant plus long que le rapport P44/nanotube est faible. Cette variation est attendue et peut être comparée à une cristallisation par nucléation hétérogène. La constante de vitesse (inverse du temps caractéristique) de ce type de cristallisation est proportionnelle au nombre de germes ajoutés au système, ce qui est cohérent avec ce qui a été observé. L'exposant de la loi est toutefois indépendant de la concentration et est inférieur à celui attendu pour une croissance de fibres induite par nucléation hétérogène.

Contrairement aux nanohybrides obtenus avec des polymères plus courts, les agrégats du système P44@SWNTs sont émissifs, l'intensité de cette émission suivant aussi une cinétique (**Figure 119**). La forme du spectre (grand rapport $I_{PL}^{0\text{-}0}$/ $I_{PL}^{0\text{-}1}$) nous montre une dominance du caractère J des agrégats (grande ordre intra-chaîne).

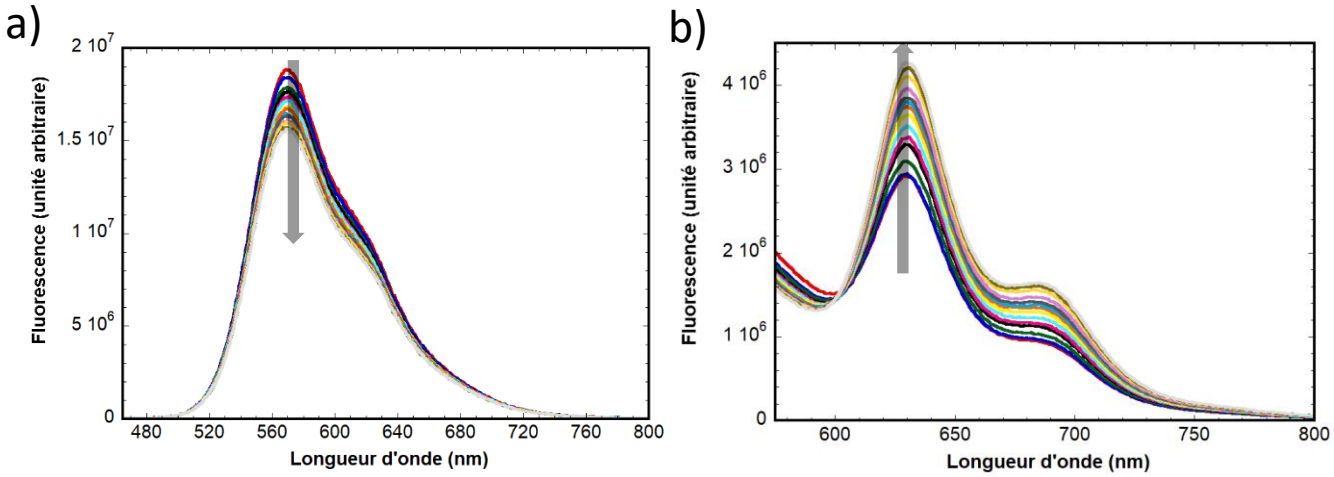

Figure 119 : Évolution des spectres d'émission des nanohybrides P44@SWNTs avec le temps. a) Excitation à 450 nm (correspondante au polymère libre en solution ; b) Excitation à 560 nm (correspondante aux agrégats).

La morphologie des agrégats peut être observée par TEM en déposant la solution sur un film de carbone (**Figure 120**). On observe une morphologie du type shish-kebab, où les nanotubes agissent comme shish et les agrégats de polymère comme kebab. On attribue cette morphologie a un enrobage partiel des longues chaînes de P44 autour des nanotubes, avec une partie des chaînes qui reste en solution à cause de leur longueur et d'un effet stérique entre chaînes voisines. Ces portions de chaînes qui restent en solution induisent une supersaturation locale, causant leur agrégation et formant ainsi des germes pour l'incorporation d'autres chaînes de la solution à ces agrégats.

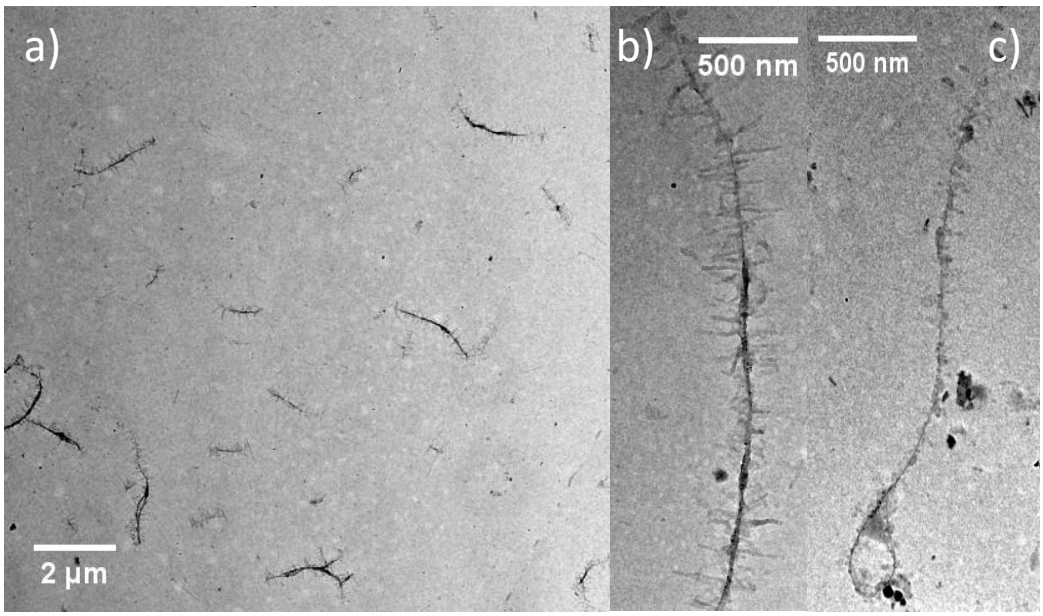

Figure 120 : Images obtenues par TEM de nanohybrides P44@SWNTs déposés sur une grille carbone a) Préparé en fin de cinétique, faible grossissement et ; b) Fort grossissement ; c) En début de cinétique à fort grossissement.

La présence du groupement aniline affecte relativement peu la formation des nanohybrides par rapport à la masse molaire. On observe une réduction du rapport critique de la concentration de nanotubes dispersés par rapport à celle du polymère, ainsi qu'une légère réduction de l'ordre intra-chaîne.

Le remplacement de la chaîne hexyle par une chaîne dodécyle permet une augmentation de la quantité de nanotubes dispersés, même si la quantité de polymère en interaction avec les tubes reste faible. Cette valeur faible peut être en fait liée à la taille plus importante d'un monomère (encombrement stérique). Les suspensions restent instables, floculant après quelques heures, ce qui indique que les chaînes ne sont pas assez longues (ou sont en interaction trop forte avec les nanotubes de carbone) pour une stabilisation stérique efficace de la dispersion.

Le type de nanotube affecte aussi les propriétés des nanohybrides. Les nanotubes bifeuillets ne sont pas dispersés aussi efficacement que les monofeuillets pour la plupart des polymères utilisés, à l'exception de P44. La morphologie des nanohybrides est la même que pour les SWNTs, étant du type shish-kebab pour P44 et du type enrobage pour les autres systèmes. Toutefois, l'ordre intra-chaîne observé est inférieur pour ces nanohybrides que celui obtenus à partir des SWNTs (**Figure 121**).

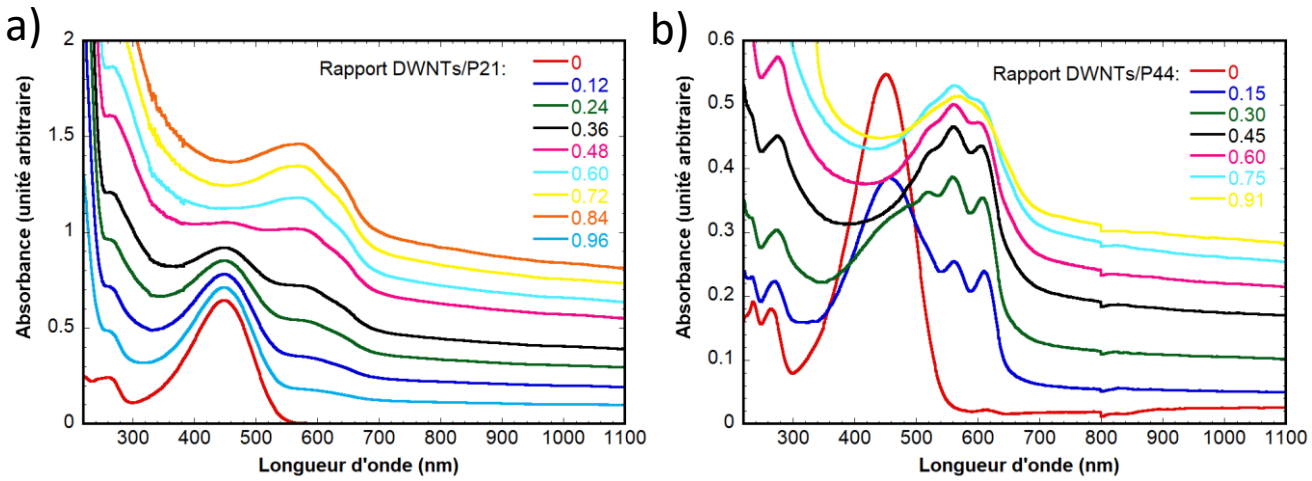

Figure 121 : Spectres d'absorption des nanohybrides a) P21@DWNTs et ; b) P44@SWNTs obtenus avec des masses croissantes de DWNTs ajoutées à une solution du polymère.

En deuxième partie du chapitre 3 sont donnés les résultats de la fonctionnalisation covalente des nanotubes de carbone avec les copolymères CP5 et CP36. Cette fonctionnalisation a été faite en utilisant la réaction de Tour, basée sur la décomposition thermique d'un diazonium formé *in situ* par oxydation de l'aniline par du nitrite d'isoamyle suivi d'un couplage radicalaire (**Schéma 1**).

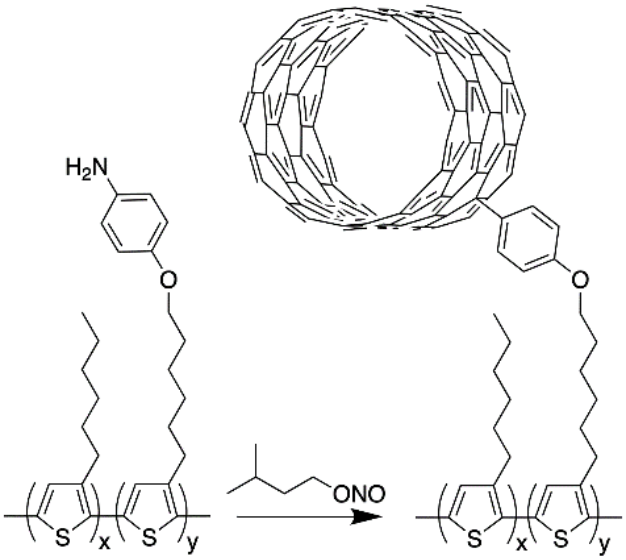

Schéma 1 : Schéma réactionnel de la fonctionnalisation de nanotubes de carbone avec le copolymère PHTcoAHT.

Les nanohybrides covalents ont un comportement différent des non-covalents. Leur solubilité est supérieure à celle des nanohybrides non-covalents. Ils sont stables en solution pendant plus d'un mois. De plus, l'ajout de toluène ne cause pas leur précipitation. Ces résultats indiquent une organisation différente du polymère sur la surface des nanotubes.

La spectroscopie optique permet de visualiser la différence d'organisation du polymère sur les nanotubes (**Figure 122**). Pour ces nanohybrides on n'observe pas les pics correspondants aux agrégats de polymère sur les nanotubes. De plus, les pics des nanotubes de carbone ne sont pas décalés vers le rouge par rapport à ceux dispersés dans le SDS + D_2O. Ceci suggère que la fonctionnalisation empêche les interactions π entre le polymère et les nanotubes.

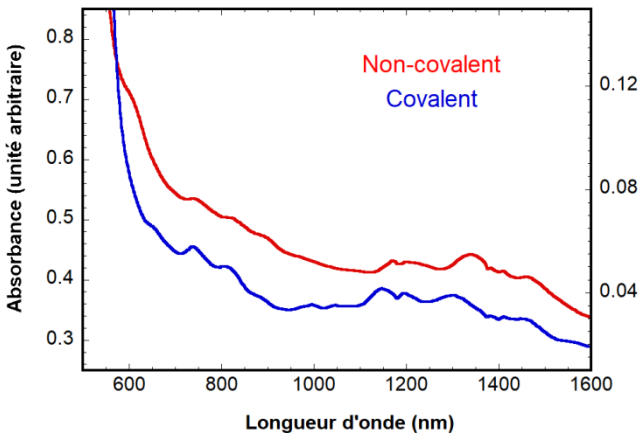

Figure 122 : Comparaison des spectres d'absorption des nanohybrides CP36@SWNTs a) Non-covalent (, rouge, échelle de gauche) et b) Covalent (bleu, échelle de droite).

La spectroscopie Raman confirme ces résultats (**Figure 123**). En effet, le spectre du polymère dans les nanohybrides non-covalents est le même obtenu par du polymère seul lorsque les chaînes sont bien

organisées. Toutefois, pour les nanohybrides covalents, le spectre observé est compatible avec un désordre torsionnel dans chaînes de polymère. Les pics correspondants aux nanotubes de carbone sont peu modifiés, ce qui est en accord avec le faible taux de fonctionnalisation attendu (quelques unités par mille atomes de carbone).

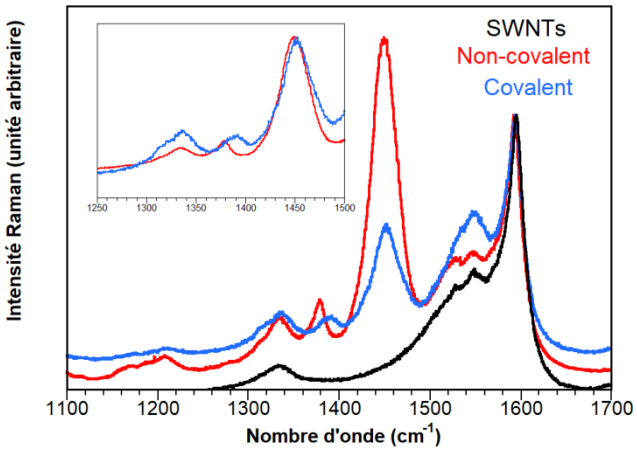

Figure 123 : Spectres Raman excités à 532 nm des SWNTs (noir), nanohybrides CP36@SWNTs non-covalents (rouge) et covalents (bleu) normalises par l'intensité du mode G des nanotubes de carbone (vers 1580 cm^{-1}). Les échantillons ont été déposés sur une plaque en verre par spin-coating et rincés au THF pour éliminer l'excès de polymère libre. Encart : Spectres normalisés à 1450 cm^{-1} (mode d'étirement vinylique du polymère)

Le quatrième et dernier chapitre de cette thèse est consacré à la fonctionnalisation de nanotubes de carbone dans des transistors à effet de champ. Ces transistors sont préparés par déposition de nanotubes de carbone (dispersés dans un solvant organique) sur une surface diélectrique (SiO2), le front de séchage assurant leur alignement. Des électrodes sont alors déposées en utilisant des techniques de lithographie. Enfin, des mesures sur les différentes électrodes déposés permettent l'identification de ceux qui forment un dispositif (**Figure 124**). Cette méthode malheureusement ne permet pas d'identifier des dispositifs connectés par des nanotubes individuels, mais seulement par des faisceaux qui peuvent présenter différents comportements (variabilité en type et nombre de nanotubes).

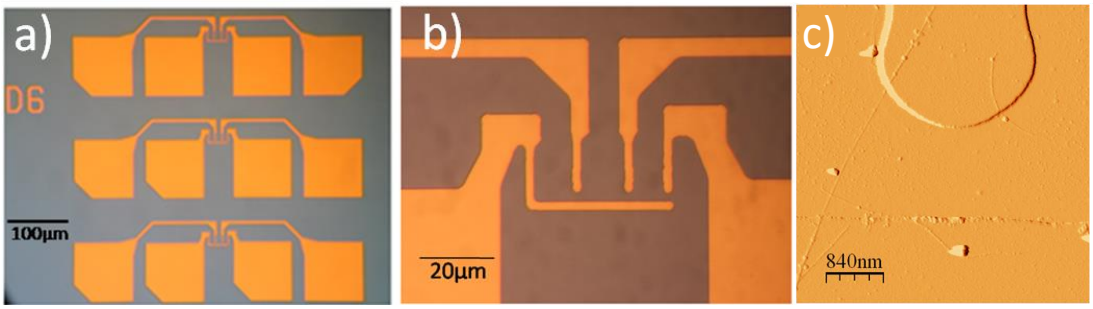

Figure 124 : a) Image optique de trois dispositifs ; b) constitués de 4 électrodes chacun utilisées comme source ou drain ; c) Image AFM d'un dispositif contacté par un faisceau de nanotubes.

Sur chaque transistor, des courbes de courant - tension de grille ont été obtenues, ainsi que des cartographies AFM et Raman. La fonctionnalisation non-covalente sur ce type d'échantillon est ineffective, probablement parce que les nanotubes sont déposés au préalable.

Toutefois, la fonctionnalisation covalente des nanotubes de carbone est efficace sur ces mêmes dispositifs comme le montre les cartographies Raman (**Figure 125**), qui corrèlent la position du signal Raman du polymère et celui des nanotubes. Toutefois, en raison du taux de fonctionnalisation très faible, les variations des propriétés électriques de ces dispositifs sont très difficiles à mesurer avec précision et ne permettent pas des conclusions fortes.

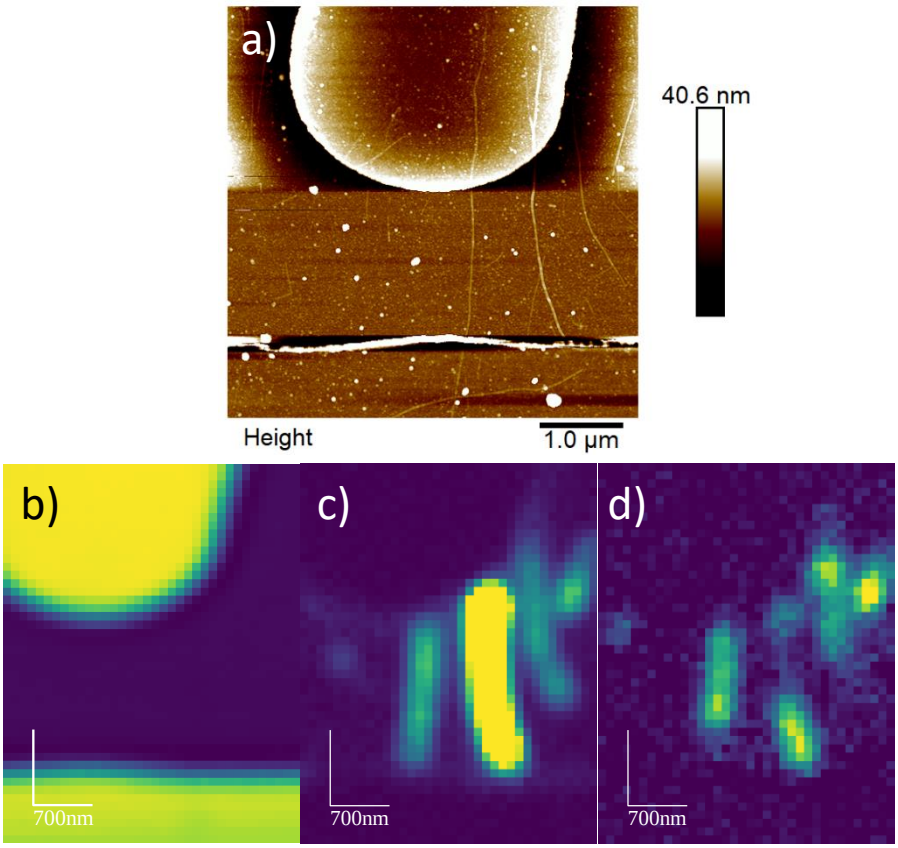

Figure 125 : Image AFM d'un dispositif contacté par quelques faisceaux de nanotubes de carbone; b) Image obtenue par réflectance optique sur le dispositif; c) Cartographie Raman du mode G des nanotubes de carbone; d) Cartographie Raman du mode d'étirement vinylique du polymère.

Des analyses de photocourant ont été effectuées sur les échantillons pour étudier l'effet de la lumière sur les propriétés de conductivité des dispositifs. Pour les échantillons fonctionnalisés de façon covalente, on observe l'existence de défauts créés par la réaction chimique (**Figure 126**). Ces défauts agissent comme points de séparation des charges créés lorsque les dispositifs sont irradiés par un laser, générant un courant électrique. Pour le moment il n'a pas été possible de déterminer l'effet de l'absorption du polymère (en variant la longueur d'onde incidente) sur le courant observé.

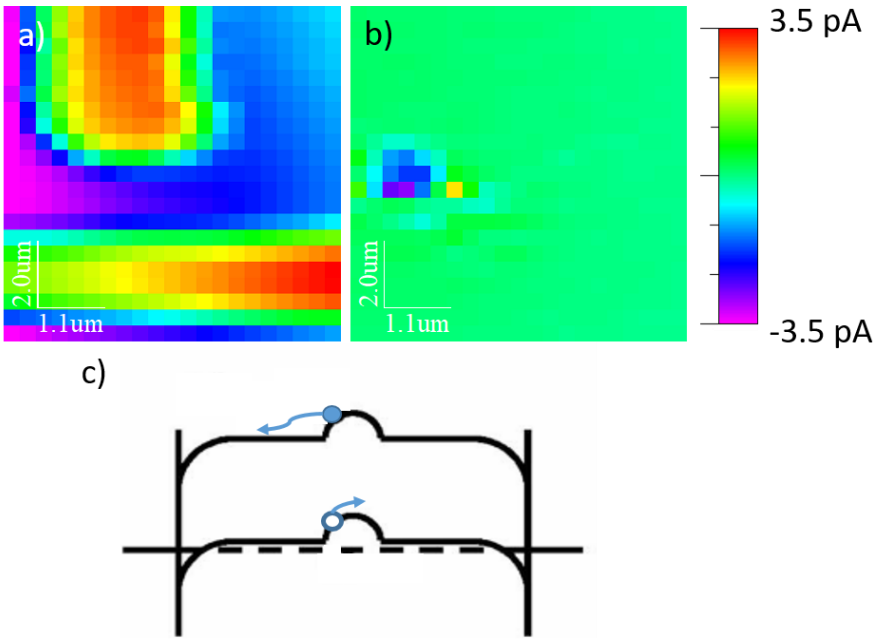

Figure 126 : a) Image de réflectance optique d'un dispositif; b) Cartographie de photocourant obtenue par irradiation du dispositif avec un laser (500 nm). c) Schéma représentant la structure de bande des nanotubes de carbone en contact avec des électrodes métalliques. La courbure des bandes dans le centre de l'image est induite par la formation d'un défaut.

En conclusion, nous avons synthétisé du P3HT régiorégulier de différentes masses molaires, ainsi qu'un copolymère dérivé ayant une composition de comonomères choisie selon une répartition de statistique. Ces matériaux ont été utilisés pour fonctionnaliser des nanotubes de carbone mono et bifeuillets de façon non-covalente et covalente pour le copolymère. La fonctionnalisation non-covalente induit la formation d'agrégats de polymère sur les nanotubes, les propriétés électroniques de ces agrégats étant dominées par un ordre intra-chaîne dominant. Pour la plupart des systèmes, la morphologie de ces hybrides est telle que quelques chaînes de polymère s'enroulent autour des nanotubes en une ou quelques couches. Le polymère de chaîne la plus longue toutefois forme des hybrides du type shish-kebab. La fonctionnalisation covalente quant à elle conduit à la formation d'hybrides dans lesquels les chaînes de polymères sont dans un état de désordre torsionnel induit par l'encombrement des chaînes hexyl portant les groupements aniline qui empêche les interactions π. Des dispositifs électroniques ont été fonctionnalisés de façon covalente avec ce copolymère. Les défauts générés par le greffage agissent comme des points de séparation de charges créés par leur illumination, permettant l'observation d'un photocourant. Ces études restent toutefois préliminaires, plus d'études étant requises pour déterminer l'effet de la fonctionnalisation sur les propriétés des dispositifs.

Felipe WASEM KLEIN

Nanostructures hybrides polymères photoactifs - nanotubes de carbone mono et bi-feuillets

Résumé

L'objectif de cette thèse est la préparation de matériaux hybrides polymères conjugués (P3HT et un copolymère dérivé) - nanotubes de carbone, ainsi que leur caractérisation par des méthodes spectroscopiques et par microscopie électronique.

Des nanohybrides non-covalents sont obtenus par la sonication des deux composants dans le THF. L'interaction entre ces composants entraîne l'enroulement du polymère autour des nanotubes ainsi que la formation d'agrégats de polymère sur leur surface. L'effet de différents paramètres, tels que la masse molaire du polymère, ont été étudiés.

Des nanohybrides covalents sont obtenus en utilisant un copolymère portant une aniline au bout de la chaîne alkyle. Les spectroscopies optique et Raman suggèrent un faible taux de fonctionnalisation ainsi qu'une conformation plus désordonnée des chaînes de polymères par rapport aux nanohybrides non-covalents.

Des études préliminaires montrent que le copolymère peut fonctionnaliser aussi des dispositifs à base de nanotubes de carbone. Le bas taux de fonctionnalisation ne permet pas de conclure sur la modification des propriétés électroniques, mais les défauts induits permettent l'observation d'un photocourant.

Mots-clés : polymères semi-conducteurs, nanotubes de carbone, spectroscopie, agrégats, transfert d'énergie, transistors à effet de champs, photocourant.

Summary

The objective of this thesis is the preparation of conjugated polymers (P3HT and a derivated copolymer) – carbon nanotubes hybrid materials and their characterization through different spectroscopies and transmission electron microscopy.

Non-covalent nanohybrids can be obtained by sonicating both components together in THF. The interaction between both components leads to the wrapping of the polymer around the carbon nanotubes as well as the formation of polymer aggregates on the surface of the nanotubes. The effect of different parameters such as the polymer chain length are described.

Covalent nanohybrids can be obtained using a specially designed copolymer bearing an aniline at the end of its side chain. Optical and Raman spectroscopies indicate a low level of functionalization, and suggest that the polymer chains are in a more disordered state compared to non-covalent nanohybrids.

Preliminary studies show that the obtained copolymer can be used for functionalizing carbon nanotube based devices. Modification of electrical properties of the devices were small and compatible with the low functionalization degree, but the induced defects allow observation of a photocurrent.

Keywords: Semi-conducting polymers, carbon nanotubes, spectroscopy, aggregates, energy transfer, field-effect devices, photocurrent.